PHD

Vibrational anharmonicity and the elastic behaviour of some antiferromagnetic materials

Deni, Mohd Salleh Mohd

Award date:
1988

Awarding institution:
University of Bath

VIBRATIONAL ANHARMONICITY AND THE ELASTIC BEHAVIOUR OF SOME ANTIFERROMAGNETIC MATERIALS.

Submitted by

Mohd. Salleh Mohd. Deni BSc(UKM) MSc(Brunel)

for the degree of PhD

of the University of Bath

1988

ProQuest LLC
789 East Eisenhower Parkway
P.O. Box 1346
Ann Arbor, MI 48106-1346

In The Name Of Allah The Beneficent And The Merciful

Dedicated to

My parents...

My wife-Sharifah

My children-

Shaliza

Shareen

Shahrizal

and UTM.

ACKNOWLEDGEMENTS

This is perhaps the most pleasurable moment in writing this thesis (its last bit!) without the supervision of my supervisor (hopefully). It is difficult for me to express my feeling to depart from the people who have been working together in such a long time, but the time has come for me to say so....

To my supervisor Professor G.A.Saunders my sincere and unreserved gratitude goes to him, whose valued advice and infectious enthusisasm have proved to be a constant source of inspiration and encouragement (....keep trying Salleh, that's called research..). His patience and difficulties in putting me on the right track to the finishing line of writing this thesis in the last six months are very much appreciated.

My thanks to Eddy Lambson for his help with the experimental equipment and to Wendy Lambson for preparing my 'difficult' samples, also to Bob Draper for his immediate action in solving technical problem during my work have contributed to my experimental success. I would like to thanks to Dr.J.E. MacDonald, Dr.N.Hampton and fellow post graduates- Sidek, Nour-Eddine and Ian Collier for various useful discussions.

Finally I warmly acknowledge the Malaysian government (JPA) and my University (UTM) for the financial supports during my stay in England.

ABSTRACT

An investigation into the elastic behaviour and anharmonic characteristics of three materials, namely, uranium nitride (UN), binary γ-Mn-Ni alloys and ternary alloys of γ-Mn-Ni-C which can be antiferromagnetic has been carried out. The effect of hydrostatic pressure on ultrasonic wave velocities have been measured and used to determine the pressure derivatives of the elastic stiffness of single crystal uranium nitride (UN) at room temperature in the paramagnetic state. $\partial C_{44}/\partial P$, and hence the Grüneisen parameter for the transverse mode propagating down an <001> axis, was found to be negative. This behaviour of C_{44} with pressure is often observed in rocksalt structure crystals. The Grüneisen parameters $\gamma_{(p,N)}$ of the acoustic modes obtained in the long wavelength limit, have a pronounced anisotropy which accrues largely from the presence or absence of nearest neighbour repulsive forces.

The temperature dependences of the second order elastic stiffness constants (SOEC) of single crystals of the antiferromagnetic binary alloys γ-Mn-Ni and ternary alloys γ-Mn-Ni-C have been determined both in the antiferromagnetic and the paramagnetic states. The magnetic contribution stiffens the longitudinal acoustic modes but softens the shear modes associated with C_{44} and $C'(= (C_{11}-C_{12})/2)$. Mode softening has been observed for $(C_{11}-C_{12})/2$ over a wide range of temperatures in the antiferromagnetic phase for the ternary alloys (Mn-Ni-C). Measurement of ultrasound velocities under hydrostatic

pressure, over the temperature range 20°C to 170°C, show that the binary alloy $Mn_{73}Ni_{27}$ has a linear dependence of hydrostatic pressure derivatives of the SOEC on temperature. In the antiferromagnetic state $\partial C_{11}/\partial P$ and $\partial C'/\partial P$ increase linearly with temperature whilst $\partial C_{44}/\partial P$ decreases. These are the first measurements of hydrostatic pressure derivatives of the elastic constants on both sides of the Néel temperature made for any antiferromagnetic material. The most noteable behaviour observed in $Mn_{73}Ni_{27}$ was a marked reduction in $\partial[(C_{11}+C_{12}+2C_{44})/2]/\partial P$ and $\partial C_{11}/\partial P$ at the magnetic phase transition temperature, T_N. Above T_N both of these pressure derivatives decrease with increasing temperature. The magnetic disordering showed a small effect on the pressure derivatives of the shear elastic constant with only a small variation at T_N. A nonlinear relationship was observed between $\partial C_{11}/\partial P$ and temperature in the ternary alloy Mn-Ni-C; $\partial C_{11}/\partial P$ has a minimum at approximately 140°C. Positive Grüneisen parameters were obtained in both Mn-Ni and Mn-Ni-C alloys with the longitudinal mode gamma γ_L being the largest as a result of the contribution from nearest neighbour repulsive forces.

CONTENTS PAGE

CHAPTER 1

INTRODUCTION

If the interatomic potential U in a crystal is represented by a quadratic function of interatomic displacement r, such a crystal is said to be purely harmonic (Fig.1.1). Any lattice vibration can be described as the superposition of normal vibrational modes. For a crystal to be stable against any small displacement from equilibrium, the frequency of all normal modes must be non-zero. The frequency of a normal lattice vibration is proportional to d^2U/dr^2; in the harmonic solid the frequencies of such vibrations are independent of vibrational amplitude. Since the effect of temperature is to increase the vibrational amplitude, the mode frequency should be independent of temperature.

In real crystals the interatomic potential is anharmonic in character; i.e. terms higher than second order with respect to interatomic displacement are required for a more exact representation (Fig.1.1). The derivative d^2U/dr^2 is no longer independent of r and consequently the frequency of the normal lattice vibration is temperature dependent.

The second order elastic stiffness constants (SOEC) of a crystal are simply related to the velocities of ultrasound waves propagating in the solid and provide a measure of the stiffness of the crystal lattice.

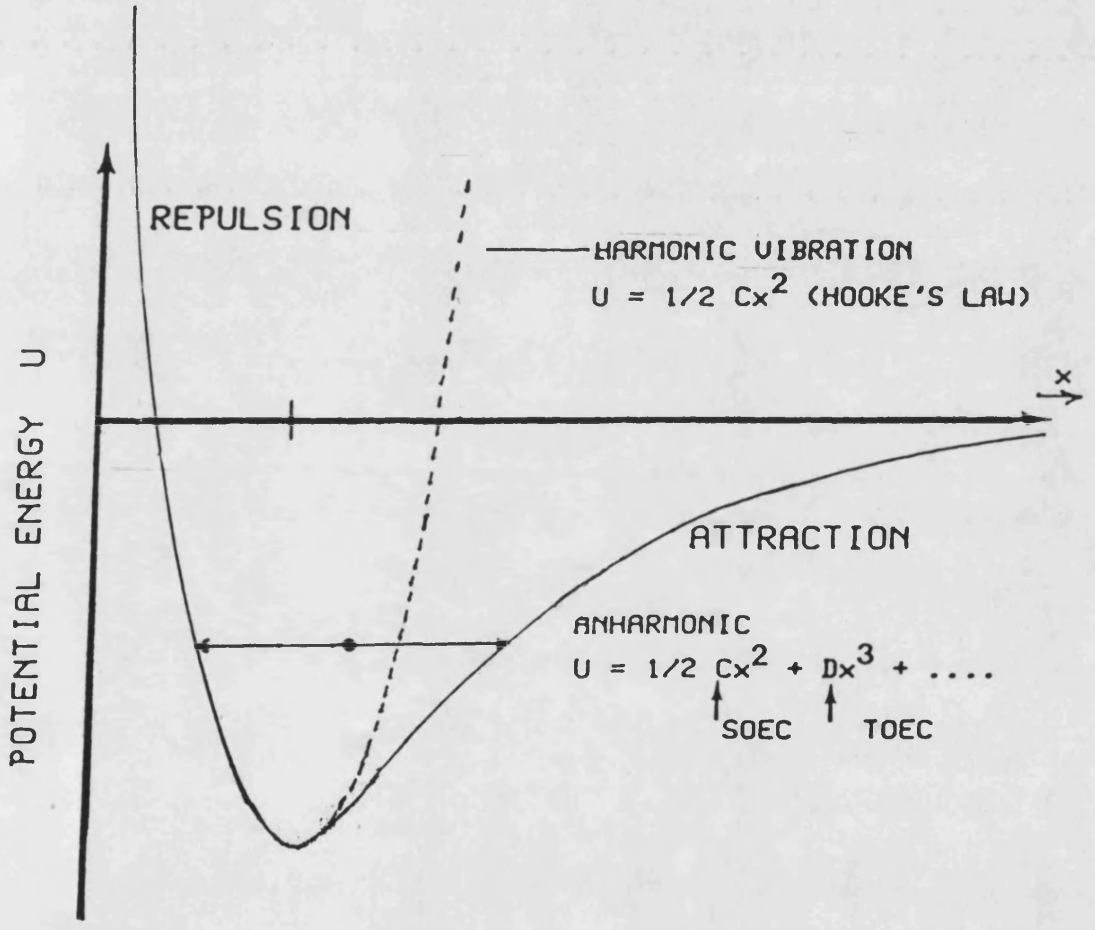

Fig.1.1 Interatomic potential as a function of atomic displacement of an harmonic and anharmonic lattice vibration in solid.

According to the standing wave condition of the Debye model, the frequencies of vibrational modes are proportional to their wave velocities; the stiffer the crystal the higher the frequencies and wave velocities of the normal mode of vibrations. The lattice strain dependences of these wave velocities then characterise the way in which lattice stiffness and mode frequencies vary with interatomic displacement, and consequently give a measure of anharmonicity. Such strain dependences of SOEC define the third order elastic stiffness constants (TOEC) and can be determined experimentally from the stress derivatives of ultrasound velocities.

The main theme of this thesis is to investigate the elastic behaviour of antiferromagnetic crystals when subjected to stress. The destinations are approached by the measurements of the pressure and temperature dependences of the ultrasonic wave velocities. This work begins with the measurement of the effect of hydrostatic pressure on the second order elastic constants for a single crystal uranium nitride at room temperature. Uranium nitride (UN) is one of the group of metallic uranium pnictide compounds which crystallize in the rocksalt structure. In the actinide metals and compounds both 6d and 5f electrons are involved in the chemical bond. This compound is an antiferromagnetic below its Nêel point at about 53K. Results from the measurements of the second order elastic stiffness constants and their hydrostatic pressure derivatives have been compared with those of NaCl and SmS crystals which

have the same structure. The measurements of the hydrostatic pressure dependences of the second order elastic stiffness constants enable the Grüneisen gamma of the acoustic modes in the long wavelength limit to be calculated in uranium nitride. These results are discussed in chapter 5.

As an antiferromagnetic crystal is taken through its Nēel temperature (T_N), changes in the relative alignment of the magnetic moments alter the contribution to the total energy which arise from interatomic magnetic interactions. Since the elastic constants are strain derivatives of the total energy, an intrinsic magnetic contribution to the elastic constants should appear when an antiferromagnetic material is cooled through T_N. To understand the lattice dynamic behaviour of antiferromagnetic materials at elevated temperature, measurements of the elastic constants up to and through the Nēel temperature have been carried out on single crystals of the binary alloys Mn-Ni and the ternary alloys Mn-Ni-C. Using ultrasonic pulse echo overlap, extensive studies have been made on the binary alloys and ternary alloys $Mn_{27}Ni_{27}$ and $Mn_{85}Ni_9C_6$. A complete set of data on temperature dependences of the second order elastic constants in both the antiferromagnetic and the paramagnetic states have been obtained. This data has been used to determine the magnetic contribution to the second order elastic stiffness constants. The magnetic contribution is the difference between the elastic

constants in the antiferromagnetic state and those in the paramagnetic state. This difference can be obtained by taking the difference between the measured values at some temperature below Nēel temperature and the values extrapolated to that temperature from the paramagnetic region. These values characterise the elastic stiffness constants in the antiferromagnetic state for the alloy. To extend the understanding of the behaviour of the interatomic forces in these alloys, particularly when subject to homogeneous strains, the hydrostatic pressure dependences of the SOEC have been measured up to 1.5KBar at several different temperatures. This gives the first and only complete set of data obtained on both sides of the Nēel temperature on any antiferromagnetic material. The results provide information on the Grüneisen parameters and the anharmonic behaviour of the lattice vibrations and the phonon dispersion curve near the Brillouin zone centre on both sides of the magnetic transition temperature. Previously there a set of hydrostatic pressure data has been obtained in a similar way on a ferromagnetic material (Fe-32at.%Ni) by Renaud and Steinemann (1984). There is however some discrepancy in their method of computation of Grüneisen parameters. This has been resolved by consideration of the correct equation to use; it is interesting to note that the magnetic Grüneisen parameters of our samples ($Mn_{73}Ni_{27}$) are of a similar magnitude to those of Fe-32at.%Ni.

A study on the effect of carbon on the SOEC of binary alloys γ-Mn-Ni has been carried out here on the ternary alloy $Mn_{85}Ni_9C_6$. In the ternary alloys of $Mn_{85}Ni_9C_6$ soft modes have been observed through the small shear elastic stiffness $((C_{11}-C_{12})/2)$. This existence of soft modes in Mn-Ni-C alloys is instructive in the understanding of lattice instability in the Mn-Ni-C alloys. The soft mode is associated with decreasing the lattice vibrational frequency. The vibrational mode with zero frequency corresponds to a displacement which never returns to the equilibrium position and would lead to a change in the equilibrium crystal structure. The temperature where this change will take place is called the transformation temperature and a mode whose frequency decrease as the transition temperature is approached is called a soft mode. Hence measurements have been made on the SOEC and their hydrostatic pressure derivatives to examine further mode softening in these manganese alloys.

CHAPTER 2

THE ELASTIC PROPERTIES OF MONOCRYSTALLINE ANTIFERROMAGNETIC Mn-Ni BINARY ALLOYS AND Mn-Ni-C TERNARY ALLOYS.

2.1 Manganese.

Manganese is one of the 3d-transition elements of group (V11a) of the periodic table. The stable phase (α) at room temperature has the face centred tetragonal structure (a= 3.77A , b=3.56A and c/a = 0.094) (Truell 1969). Over the temperature range between 1100 to 1133°C, manganese exists in the γ-phase which has the face centred cubic structure (Zwicker 1951). The electronic configuration of manganese is $[Ar]3d^5 4s^2$ so there is a partially filled 3d subshell: these electrons give rise to a spontaneous spin and orbital alignment which give a single atom an atomic magnetic moment and in crystals produce long range magnetic ordering. For this particular element, spontaneous antiparallel alignment occurs between the spins of nearest neighbours; in its ordered state a crystal possesses no net magnetization. Cade and Young (1980) have calculated the band structure of cubic γ-Mn and concluded that the <111> antiferromagnetic structure has the lowest energy and have suggested that a cubic alloy based on γ-Mn should support the <111> spins

alignment structure illustrated in Fig 2.1b. At the Nēel temperature a phase transition takes place from the antiferromagnetically ordered state to one which is magnetically disordered, the ordered state being below the transition temperature. Zimmerman et al.(1964) have made specific heat measurements in a series of γ-Mn-Cu alloys up to and through the Nēel temperature T_N. Extrapolation of the results back to the value that pure γ-Mn would have given value of T_N for γ-Mn of 540K. However, γ-Mn is unstable at this temperature; this structure is only stable in alloys containing elements such as copper, nickel, iron or zinc.

The Nēel temperature of γ-Mn, as for other transition elements, is determined by the strength of the interaction which is purely electrostatic in origin between electrons in the partially filled 3d-band, for manganese, the electron-electron interaction is sufficiently strong to retain ordering at room temperature. The disordered state is developed when the thermal energy is just sufficient to destroy the magnetic ordering, and in the case of γ-Mn alloys this occurs when the temperature is of the order of 500 K.

The other element which is included in the binary alloys studied here is nickel. Its electronic configuration is $[Ar]3d^8 4s^2$. Pure nickel has a face centred cubic structure with a lattice parameter 3.52 A. It is ferromagnetic, possessing spontaneous magnetization below the Curie temperature of 627K.

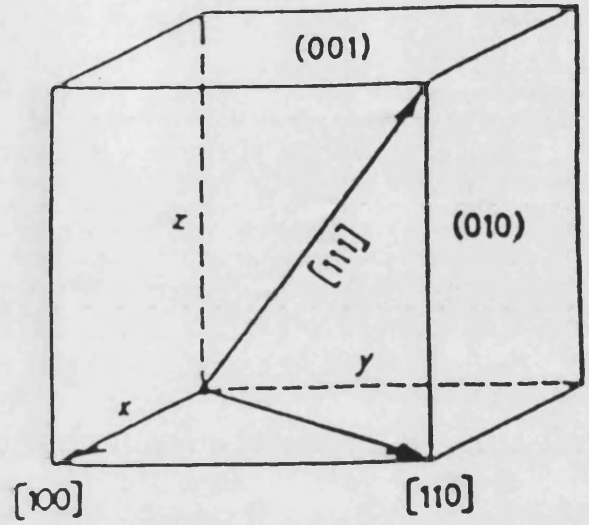

Figure 2.1a Plane and line directions in cubic.

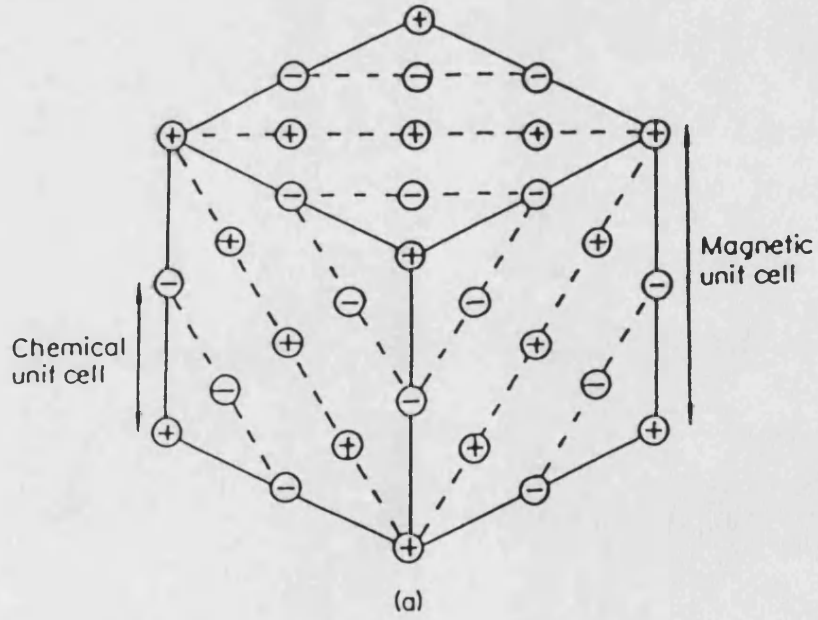

Figure 2.1b Antiferromagnetic spins structure of γ-Mn according to Cade and Young (1980).

When alloyed with manganese, antiferromagnetic binary alloys γ-Mn-Ni can be made which are stable at room temperature.

2.2 Mn-Ni Solid Solution.

The binary Mn-Ni alloys are solid solutions. In a chemical compound the elements combine stoichiometrically (or nearly so), that is in fixed proportions according to the chemical formula. In contrast in a solid solution the chemical combination of the elements is non-stoichiometric; for example γ structure Mn-Ni alloys can be formed over a quite a wide range of nickel content. In the present work solid solutions with composition $Mn_{73}Ni_{27}$ and $Mn_{84}Ni_{16}$ have been used. In such solid solutions, manganese can be thought of as the parent element or solvent, whilst nickel having the smaller percentage in the alloy can be considered as a solute. One of the conditions to form a solid solution is that the crystal structure of the parent element (Mn) does not change when the solute atoms (Ni) are introduced into the structure. The solute atoms are incorporated into the structure substitutionally, and the process is governed by two major conditions (Hume-Rothery rules): (i) the size of the parent atom and that of the solute atom should not differ by more than about 15% in their atomic radii, ii) both elements must have the same crystal structures. In the case of the Mn-Ni alloy system, the atomic radii of γ-Mn and Ni are

1.24A and 1.243A respectively which differ by less than 1% and so comply with this first criterion. The effect of atomic radii in the formations of solid solutions is observed in Cu-Zn and Cu-Cd alloys systems. Only 1.7 atomic percent cadmium (Cd) is soluble in copper (Cu), while for zinc (Zn), up to 38 atomic percent dissolve in copper. The atomic radius for copper is 1.275A and close to zinc (1.375A), but for cadmium (1.48A) it is less favourable. Manganese and nickel are transition metals with similar electronic configurations and can have the same crystal structures (face centred cubic), features which are therefore favourable to formation of substitutional solid solutions. A consequence of the substitutional process is that the allocation of the nickel sites in the manganese crystal is not regular - it occurs at random; thus to describe the concentration of the alloy formed, the average concentration of the whole solid is considered.

2.3 The Phase Diagram of Manganese-Nickel Alloys.

In principle all the face centred cubic Mn-Ni alloys which contain less than 22at.%Ni are subject to structural transformation (Honda et al.1976) and are all unstable below a phase boundary line that runs entirely above 1000C (Tsiuplakis and Kneller 1969). However alloys having the f.c.c. structure can be produced at room temperature and below by quenching; such alloys, exhibit itinerant-electron antiferromagnetism (Asano and

Yamashita 1971; Cade and Young 1980).

A phase diagram has been given by Honda et al.(1976) (Fig 2.2). For nickel concentrations up to about 10at.% the paramagnetic to the antiferromagnetic transition is accompanied by a cubic-to-tetragonal structural transition, just as in Mn-Cu and other alloys. Between 15 and 22at.%Ni the two types of transition occur at different temperatures: the material becomes antiferromagnetic at the Nēel temperature T_N, then at some martensitic temperature T_m below T_N transforms to the tetragonal structure with c>a. Lowde et al.(1981) have made an extensive study on the martensitic transformation in Mn-Ni-C alloys below room temperature (down to approximately 100K) and have suggested that the structural transformation that occurs in ternary alloys $Mn_{85}Ni_9C_6$ at T_m(= 174$\pm$ 2K) is nearly second order. However, the same kind of transformation has not been studied at temperatures higher than room temperature. Thus, the phase diagram shown in Fig 2.2 suggests that above room temperature the martensitic transformation should occur in those Mn-Ni alloys which contain less than 15at.%Ni. Therefore the alloys which are studied here ($Mn_{84}Ni_{16}$ and $Mn_{85}Ni_9C_6$) are expected to undergo both the martensitic and antiferromagnetic transformations first at T_m and then at T_N respectively as these alloys are taken up to and through the Nēel temperature. It is found that the magnetic moment of these alloys varies essentially continuously across the

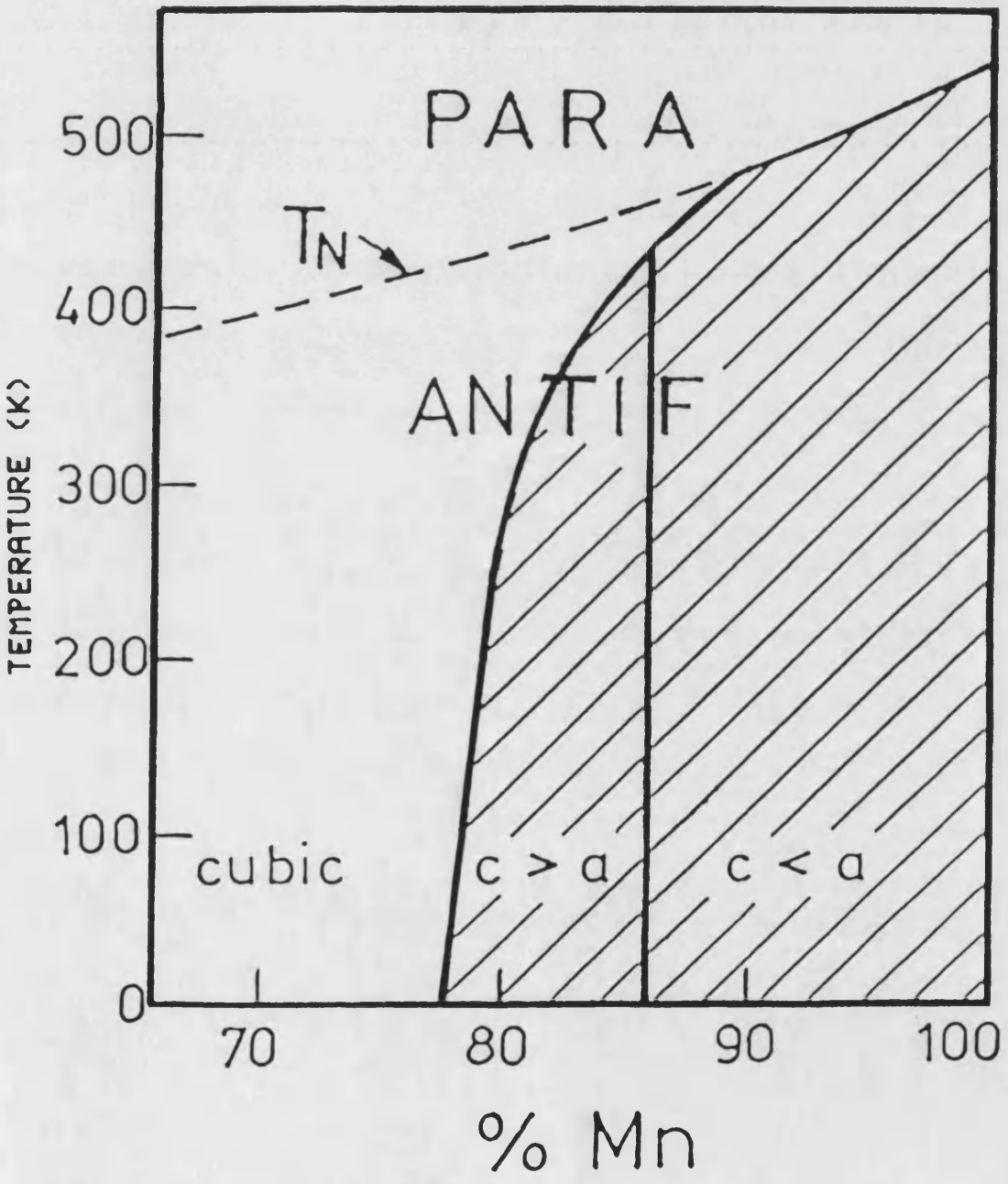

Figure 2.2 Phase diagram of Mn-Ni alloys system showing the boundary line of structural transformation (thick line) and magnetic transformation (broken line) after Honda et al (1976).

structural transition (Yamaoka et al.1974). Therefore to observe the magnetic contribution to the elastic properties of these particular alloys it is only necessary to look into the transformation that occurs at the Nēel temperature. It is considered that the magnetic spin structure of Mn-Ni alloys is of the f.c.c. type I (Fig 2.3a) (Hicks, Pepper and Smith 1968), that is the magnetic moments have their z-components organised so that there are sheets of parallel M_z perpendicular to one selected fourfold axis, the value of M_z alternating in sign from sheet to sheet. On this assumption, any martensitic transition should strictly be called orthorhombic-to-tetragonal; but in practice it is found that (within an accuracy approaching 10^{-4} of lattice dimension) the unit cells of the two phases actually are tetragonal and cubic respectively (Honda et al.1976; Hicks, Pepper and Smith 1968); on this basis any structural transformation can be referred to as tetragonal-to-cubic. However for these particular alloys, the martensitic transformation from tetragonal (c>a) to cubic takes place at much lower temperature than the Nēel temperature; therefore the magnetic transformation takes place in the cubic structure.

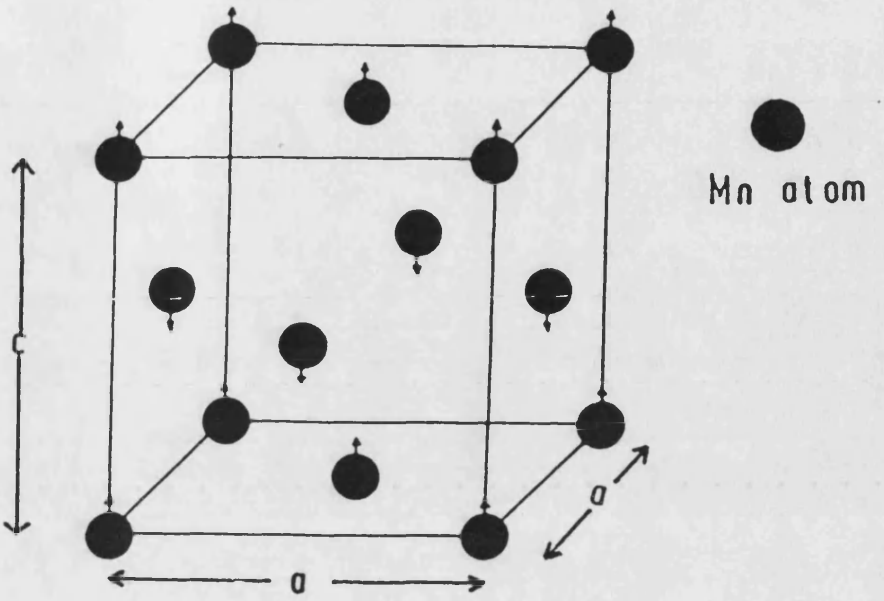

Figure 2.3a Antiferromagnetic spins structure of binary alloy γ-Mn-Ni (Hick et al 1968).

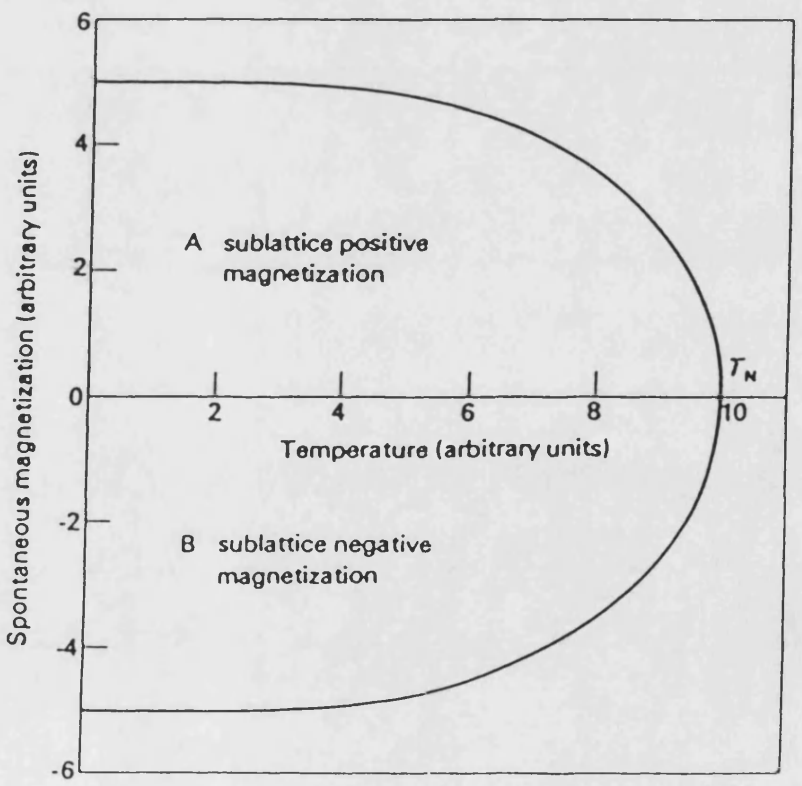

Figure 2.3b Spontaneous magnetization of the sublattices in a simple antiferromagnetic.

2.4 The Introduction of Carbon into Mn-Ni Alloys.

The introduction of carbon atoms in replacing some at.%Ni in the Mn-Ni binary alloys has been used as an alternative approach to studying the magnetic and elastic behaviours of the binary alloy single crystal (Lowde et al.1981). The main idea of adding carbon into the Mn-Ni alloys was to assist the crystallization of alloys containing a minimum amount of nickel. For the ternary Mn-Ni-C alloy system in the present work emphasis has been placed on single crystal of composition $Mn_{85}Ni_9C_6$. One specific reason for employing 9at.% rather than 21at.%Ni is that short-range order based on the Cu_3Au structure tends to be rather pronounced in the binary Mn-Ni alloys, and therefore the hazard of developing uncontrolled effects which are perhaps characteristic of that structural ordering is much more serious in the high-percentage case nickel alloys (Lowde et al.1981). Many of the effects found in binary alloys can also be seen in the ternary alloy $Mn_{85}Ni_9C_6$ single crystal; particularly important are the antiferromagnetic transition above room temperature and the martensitic transformation at T_m at about 174K to a tetragonal structure with c>a. The distribution of carbon atoms in this Mn-Ni-C system has not yet been established: it is not known whether they are located substitutionally or interstitially in the crystal structure. The presence of carbon has a marked influence on the elastic properties

of the alloys; for example in the present work it will be seen that the elastic behaviour of $Mn_{88}Ni_9C_6$ differ substantially from that measured by Hausch (1977) in $Mn_{88}Ni_{12}$. Koh (1978) has shown that the presence of carbon is responsible for altering the phase diagram even when the amount of carbon added is almost negligible (Fig.2.4). Due to carbon content, the structural transformation temperature ofan alloy containing approximately 88at.%Mn is enormously reduced from about 450°K to about 120°K.

2.5 Softening of Phonon Modes in Mn-Ni Alloys.

Understanding of structural phase transitions in solids has been greatly enriched by the idea that they can originate with a soft mode of lattice vibration, the amplitude of which induces a deformation against which the crystal is unstable. This concept was introduced for optic phonons by Anderson (1960) and Cochran (1960) to account for certain ferroelectric transitions. The stability of a material may also be reflected in its elastic constants. A crystal is thermodynamically stable if its elastic energy increases when it is subjected to an infinitesimal strain; work must be expended in order to strain the crystal, otherwise it may undergo a structure transformation which is normally to a lower symmetry structure. Should certain elastic moduli approach zero for any reason for instance as the pressure or temperature is varied, the crystal may become unstable

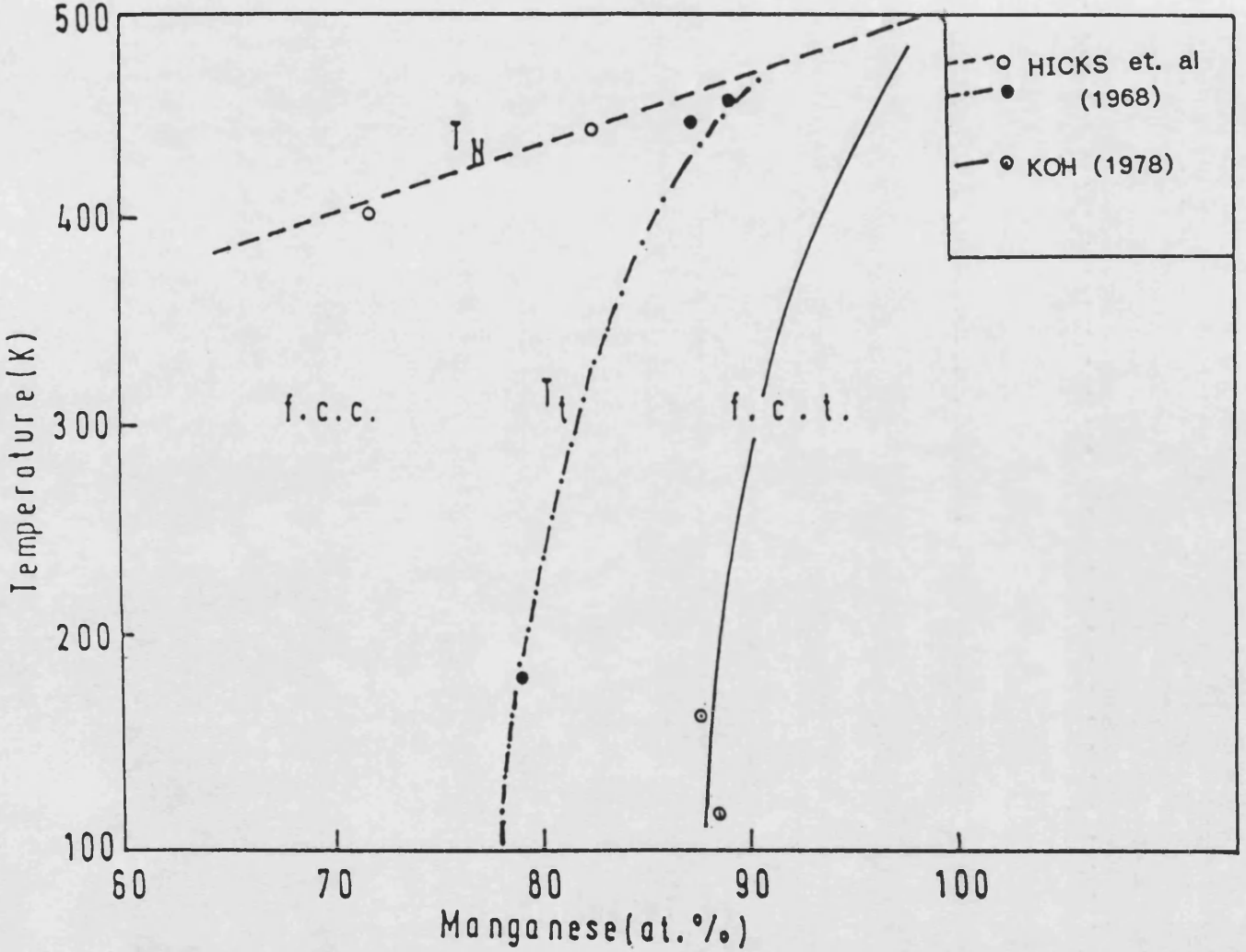

Figure 2.4 The effect of carbon on the structural transformation temperature of γ-Mn-Ni alloys: Thick line showing the new phase boundary with carbon.

to the corresponding strain and deform spontaneously. Thus elastic constant measurements can provide fundamental information about a whole class of lattice instabilities via acoustic phonon mode softening that lead to structural transformation. Such transformation can include some of those of the martensitic type. Lowde et al.(1981) have reported this type of transformation on $Mn_{85}Ni_9C_6$ in which structure transformation occurs from cubic-to-tetragonal at transformation temperature of 174K.

The mode softening is only related to the acoustic phonons with energies restricted to a small volume of wave-vector ($\underline{k}$) space near the zone centre to about $k_{max}/10$ around the Brillouin zone centre (Lowde et al.1981). Group-theoretical considerations require that a structural transformation of the kind considered should be accompanied by reduction of the stiffness parameter $(C_{11}-C_{12})/2$, and by softening of the long wavelength transverse phonons propagating with [110] polarization in the [110] direction (Folk et al.1976). These phenomena were observed by Lowde et al.(1981). This type of transformation has been described by Folk et al.(1976) and Cowley (1976) as second order and they have examined the constraints on such a transformation. Being a second order transformation the limitations are quite severe. However for the structural transformation from a cubic lattice to tetragonal one, there is a cubic invariant in the order parameter so that this type of ferroelastic

phase transition should be first order (Brassington and Saunders 1982). Such a transition occurs via softening of the [110]T_1 acoustic phonon which has the vibrational polarization direction [1$\bar{1}$0]. The corresponding elastic stiffness constant is $(C_{11}-C_{12})/2$, and in a nearly-second-order transition $(C_{11}-C_{12})/2$ would go critically soft. Lowde et al.(1981) have found that C_{11} also softens for $Mn_{85}Ni_9C_6$ although the structural transformation through the softening of the <100> longitudinal acoustic phonon does not occur for the following reason: before C_{11} can reach zero and the transition take place, $(C_{11}-C_{12})/2$ becomes very small and the crystal is obliged to suffer shear distortions in the (110) plane in the [110] direction. The free energy requires that the crystal becomes tetragonal; it can do so because two [110] shears can always be found that superpose to produce a tetragonal end product. Gunton and Saunders (1973) have observed softening of long wavelength acoustic phonons having a wavevector N[110] and polarised U[1$\bar{1}$0] in In-Tl alloys as these alloys are taken towards the cubic tetragonal phase transition. The second order elastic constant associated with this vibrational mode is $(C_{11}-C_{12})/2$ and is a measure of the resistance to deformation of the crystal lattice when a shear stress is applied across a (110) plane in a [110] direction. For indium itself, the small value of this elastic constant and its rapid decrease with increasing temperature strongly suggests that this element should

undergo a transformation to a face-centred cubic from a face centred tetragonal structure at some high temperature. Chung, Gunton and Saunders (1976) have urged that this transformation would occur were it not for the fact that indium melts before the transition temperature is reached. The phonon dispersion curve at room temperature for $Mn_{85}Ni_9C_6$ is shown in Fig.2.5 (Lowde et al.1981). An unusual feature of these alloys is that in the [100] direction low energy longitudinal vibrations propagate more slowly than transverse ones. This feature has been observed in the experimental SOEC data measured by Lowde et al.(1981). Ultrasonic measurements show that the [110] direction the T_1 phonon mode, while behaving in a normal way over the greater part of the wave vector range, approaches the origin anomalously. The abrupt change of slope near T_c is associated to the soft acoustic shear mode $(C_{11}-C_{12})/2$ which has been discussed earlier.

2.6 Invar Properties of Transition Metal Alloys.

The Invar effect was first discovered by Guillaume (1897) who detected that the f.c.c. FeNi alloy at concentration of about $Fe_{65}Ni_{35}$ shows an almost constant- that is "invariant" - thermal expansion as a function of temperature in a broad range centred about room temperature. Since then many workers have discovered other properties of magnetic alloys which have been associated with Invar properties. Some of the physical

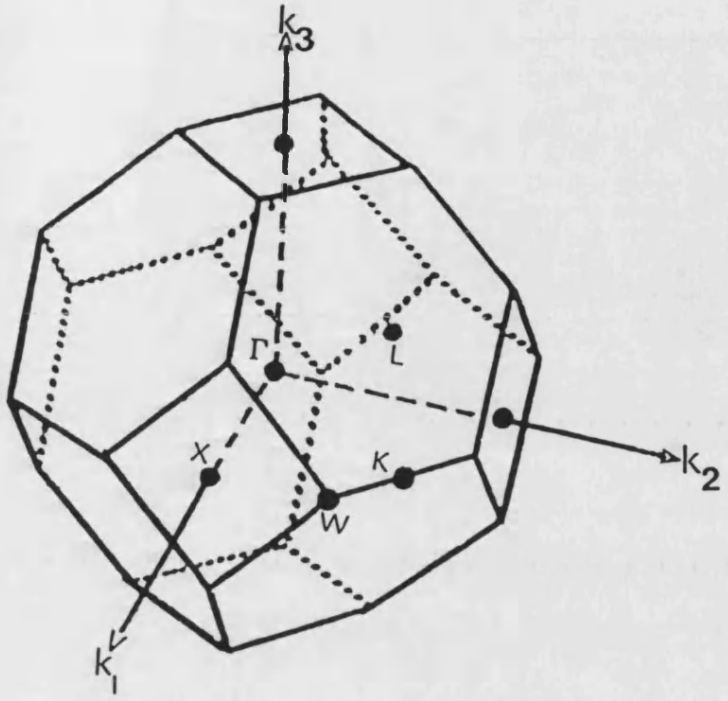

Fig.2.5a The first Brillouin zone for the fcc. crystal structure.

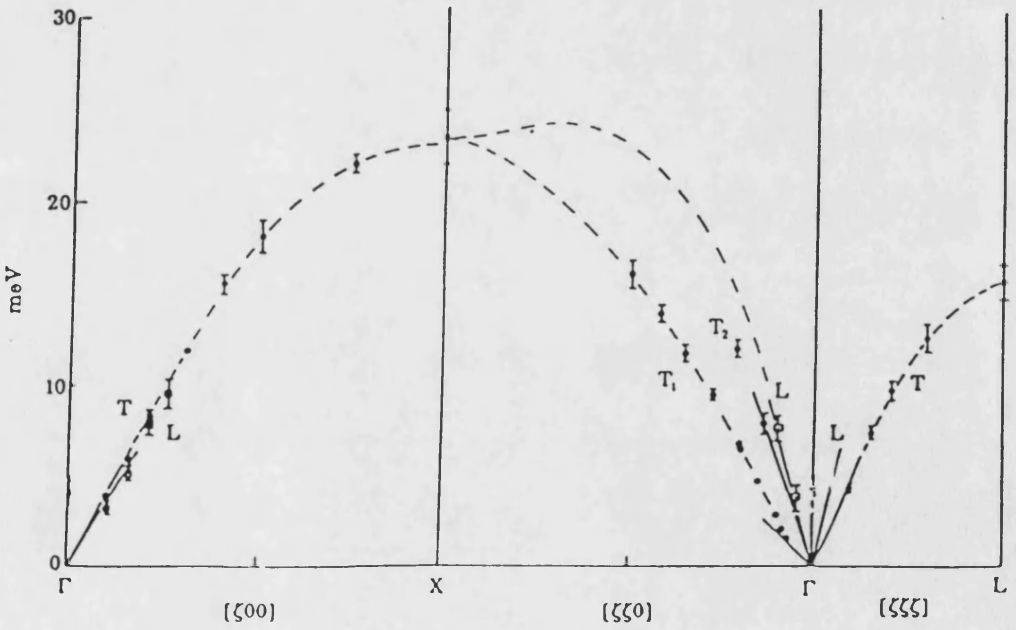

Fig 2.5b Phonon dispersion curve of γ-$Mn_{65}Ni_{19}C_6$ at room temperature (Lowde et al1981). Note in particular: at the left, the low energy associated with [110] longtidunal sound; at the T point on the right-hand side the manner in which the T_1 mode along [110] decends towards the origin. ——— ; Ultrasonics; --- neutrons; , transverse mode; ,longitudinal mode.

properties which shown Invar related effect are listed in Table 2.1. The first two relate directly to this present work on Mn-Ni and Mn-Ni-C alloys system. The objective of this section is to discuss the origin of the Invar properties that lead to the anomalies in the elastic constants, bulk modulus and Young's modulus of crystals. For a Mn-Ni alloy the magnetic transition at the Neel temperature is associated with the transformation of this alloy from the antiferromagnetic to the paramagnetic phase. An assessment of the magnetic contribution to the bulk modulus has been made using a linear extrapolation down to room temperature of the bulk modulus data B_P measured in the paramagnetic phase down to room temperature (Hausch 1977) based on the following equation:

$$B(T)=B_o-DT\exp(-\frac{T_o}{T}) \qquad (2.1)$$

where B and B_o are the bulk modulus at temperature T and OK respectively, D is a constant and T_o is approximately one half of the Debye temperature. Then subtraction of the value of B_P at any temperature from the measured value B_m at the same temperature in the antiferromagnetic state gives the magnetic contribution to the bulk modulus, ΔB_m (= B_m-B_P). Hausch (1977) measured the magnetic induced effects on C_{11}, C_{12} and bulk modulus of a binary alloy $Mn_{85}Ni_{15}$ when the temperature was taken to and through the Nēel temperature. By substracting the measured elastic constants and bulk modulus from the

TABLE 2.1

List of physical properties in which Invar anomalies are observed

Elastic constants	$c_L(T)$, $c_{44}(T)$, $c'(T)$
Young's and Bulk modulus	$E(T)$; $B(T)$
Negative pressure dependence of Curie temperature	$-(dT_c/dp)$
Thermal expansion	$(\Delta l/l)(T)$; $\alpha(T)$
Lattice constant	$a(T)$
Spontaneous volume magnetostriction	$\omega_s = (\Delta V/V)(T)$
Spontaneous volume magnetostriction at T = 0	$\omega_s(T=0) = \omega_{so}$
Excess specific heat at high T, Linear specific heat with large γ-values at low T	$C_V(T)$
Deviation from Brillouin-function in magnetization	$(M/M_o)(T)$
Forced volume magnetostriction	$(\delta\omega/\delta H)(T)$
Large high field susceptibility	$\chi_{HF}(T)$
Negative pressure dependence of magnetization	$-(dM/dp)_{T,H}$

corresponding paramagnetic values, the magnetic part of elasticity at 77K were obtained as:

$$\frac{\Delta B_m}{B_o}=+12\% \qquad \frac{\Delta C_{44}}{C_{44}^o} = -4.8\%$$

The positive sign of $\Delta B_m/B$ shows that there is a magnetic stiffening of the bulk modulus while the negative sign of $\Delta C_{44}/C_{44}^o$ shows that magnetic contribution softens this elastic constant. The sign is in agreement with the prediction of the itinerant electron theory (Wohlfarth 1976, Hausch 1977) which gives

$$\frac{\Delta B_m}{B}=(\frac{5}{3})(3-2\frac{I}{I_b})w_m \qquad (2.2)$$

where w_m is spontaneous volume magnetization; I and I_b are the effective and bare-atomic interactions respectively. The measured value of the bulk modulus should include the effects of volume change result from the spontaneous magnetization. For ferromagnetic materials, Doring (1938) has estimated the correction for the volume change effects of the magnetization as

$$\frac{1}{B_I}=\frac{1}{B_m}-\frac{w^2}{(\frac{dI}{dH})} \qquad (2.3)$$

where w is the volume magnetostriction dV/dH, measurements of which would be very instructive. To extend our knowledge of the magnetic interaction, measurement of the spontaneous volume magnetization would

be invaluable.

Honda, Tanji and Nagasawa (1976) using a similar extrapolation procedure to that used by Hausch (1977) have determined the magnetic contribution to bulk moduli from compressibility data of polycrystalline Mn-Ni alloys. From the temperature dependences of Young's modulus of γ-Mn-Ni alloy of difference concentrations of nickel, Honda et al.(1976) obtained a step-like change at the Nēel points. The size of the steps becomes smaller as the nickel concentration in the alloys is increased: the lower the nickel content of the alloy, the larger the $\Delta E/E_o$ becomes. This implies an increased magnetic interaction strength in the alloys as the manganese concentration is increased. The values of $\Delta E(= E_m - E_p)$ obtained at Nēel temperature plotted as a function of temperature and a smooth curve obtained shows a decrease in ΔE as the at.%Ni is increased (Fig.2.6).

A property of relevance to the present work is the magnitude of the change of Nēel temperature with pressure of γ-$Mn_{95}Cu_5$ (Sawaoka et al.1971). As the pressure is increased from atmospheric pressure to approximately 40 Kbar, the Nēel temperature was observed to decrease at the rate dT_N/dP = -3.25 deg/kbar (Fig.2.7).

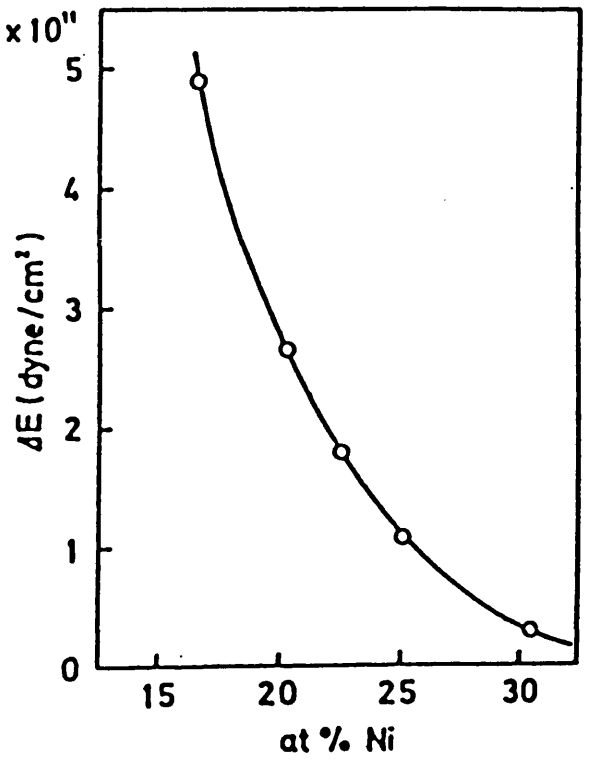

Figure 2.6 Change in Young's modulus at Neel point, ΔE, as a function of alloy composition (Honda, Tanji and Nagasawa (1976)).

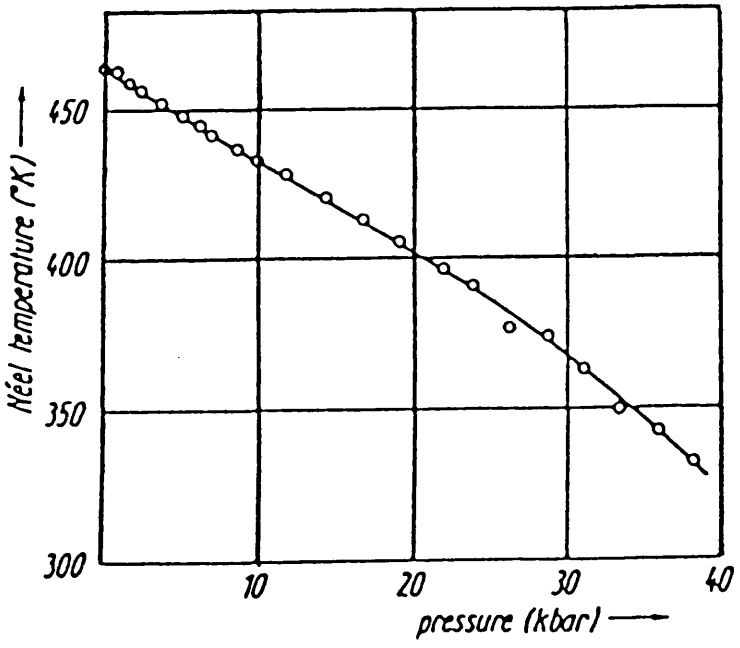

Figure 2.7 Pressure dependence of Néel temperature of γ-$Mn_{88}Cu_5$ alloy (Sawaoka et al. (1971)).

CHAPTER 3

THE DEFINITION AND MEASUREMENTS OF THE SECOND ORDER ELASTIC STIFFNESS CONSTANTS AND ACOUSTIC VIBRATIONAL ANHARMONICITY.

3.1 Introduction

Elastic constants of solids were introduced originally to describe the linear relation observed between stress and strain. This relation is usually written as the generalised Hooke's Law [Nye (1957), Huntington (1958)],

$$\sigma_{ij}=C_{ijkl}\epsilon_{kl} \qquad (3.1)$$

$$(i,j,k,l=1,2,3)$$

where σ_{ij} and ϵ_{kl} are second rank stress and strain tensors respectively while C_{ijkl} is a fourth rank elastic stiffness tensor, the components of which at constant temperature are assumed to be invariant. The components of this fourth rank tensor are termed, for reasons which will be described later, second order elastic stiffness constants (SOEC). It is found that Hooke's Law is only valid for infinitesimal strains, linearity being lost for finite strains. The specification of strain without the simplifying infinitesimal assumption has been considered in detail by Murnaghan (1951) and Wallace (1972). Elastic constants are not inherent properties of a particular material but are dependent on its physical state and on

the conditions under which they are considered. For this reason the definitions of elastic constants are best expressed in thermodynamic terms. These definitions allow for elastic constants of any order. The higher order elastic constants are required to describe the non-linear stress-strain relation observed for finite strains. It is this thermodynamic definition of elastic constants which is described in this chapter and which provides the theoretical basis for their evaluation from experimental ultrasonic data.

3.2 Homogeneous strain

Throughout the following arguments a crystal is considered as a homogeneous anisotropic elastic medium, which when subjected to a uniform stress suffers a homogeneous strain.

Consider a body occupying a space, with every particle referenced to a rectangular Cartesian frame. The position P of a particle in the unstrained state is located at (X_1,X_2,X_3) with its position described by the vector $\underline{X}$. On straining the body this particle moves to a new position Q with coordinates (x_1,x_2,x_3) described by the vector $\underline{x}$. The deformation of the body is known if x_1,x_2,x_3 are known functions of X_1,X_2,X_3,

$$x_i = x_i(X_1,X_2,X_3) \qquad (3.2)$$

It is assumed that the deformation is continuous, a

neighbourhood is transferred into a neighbourhood and that the transformation is one-to-one; ie the functions in 3.2 are singled-valued, continuous and have a unique inverse for every point in the body

$$X_i = X_i(x_1, x_2, x_3) \tag{3.3}$$

As the strain is homogeneous the vectors $\underline{X}$ and $\underline{x}$ are related by a linear transformation according to

$$x_i = \alpha_{ij} X_j \tag{3.4}$$

where α_{ij} is the deformation gradient from the unstrained configuration to the strained configuration. It also follows from the definition of the transformation that

$$\alpha_{ij} = \partial x_i / \partial X_j \tag{3.5}$$

The stress induced displacement from $\underline{X}$ to $\underline{x}$ is described by the displacement vector $\underline{u}$, defined by

$$u_i = x_i - X_i \tag{3.6}$$

with displacement gradients given by

$$u_{ij} = \partial u_i / \partial X_j \tag{3.7}$$

Differentiation of equation 3.6 with respect to X_j, and comparison of the result with equation 3.5 leads to the relation between the transformation coefficients and the displacement gradients,

$$\alpha_{ij} = \delta_{ij} + u_{ij} \tag{3.8}$$

where δ_{ij} is the Kronecker delta.

Our aim is to look particularly into the homogeneous deformation of the solid, ie to exclude body translations and rotations since these do not alter the internal energy of the material. Therefore we require a strain parameter which is zero for a body rotation or translation. By squaring equation 3.4 we obtain

$$\sum_i x_i^2 = \sum_{ijk} \alpha_{ij}\alpha_{ik}X_jX_k \tag{3.9}$$

which may be rewritten as

$$\sum_i x_i^2 = \sum_i X_i^2 + 2\sum_{ij} \eta_{ij}X_iX_j \tag{3.10}$$

where η_{ij} are the elements of Lagrangian strain and are defined as

$$\eta_{ij} = \frac{1}{2}(\alpha_{ki}\alpha_{kj} - \delta_{ij}) \tag{3.11}$$

and are symmetric, $\eta_{ij} = \eta_{ji}$. From equation 3.11 it is clear that $\eta_{ij} = 0$ if α_{ij} represents a body rotation only. In this way the strained state of a crystal may be

completely specified in terms of the initial unstrained state and either the transformation coefficients α_{ij} or the displacement gradients u_{ij}.

3.3 The Thermodynamic Definition of Elastic Constants.

In this discussion the definition of higher order elastic constants will follow the thermodynamic definition introduced by Brugger (1964). The four main thermodynamic potentials are the internal energy U, the Helmholtz free energy F, the enthalpy H and the Gibbs free energy G. Each of these is considered to be a function of two pairs of conjugate thermodynamic variables, one of which is the entropy S and the temperature T. The second pair, analogous to pressure and volume, comprises of the set of thermodynamic tension components t_{ij}, and a set of reduced Lagrangian strain components $(\eta_{ij})/\rho_o$, where ρ_o is the density of the unstrained solid. Assuming that the solid is free from magnetic and electric fields that may contribute to the potentials, and that the material is not piezoelectric then by the first and second law thermodynamics

$$dU = TdS + (\frac{1}{\rho_o})t_{ij}d\eta_{ij} \tag{3.12}$$

$$dF = -SdT + (\frac{1}{\rho_o})t_{ij}d\eta_{ij} \tag{3.13}$$

$$dH = TdS - (\frac{1}{\rho_o})\eta_{ij}dt_{ij} \tag{3.14}$$

$$dG = -SdT - (\frac{1}{\rho_o})\eta_{ij}dt_{ij} \tag{3.15}$$

The potentials and all other expansion variables are taken per unit mass and all the above are summed over repeated indices i and j. The thermodynamic tensions t_{ij} are then given by

$$t_{ij} = \rho_o \left(\frac{\partial U}{\partial \eta_{ij}} \right)_{S,\eta'} = \rho_o \left(\frac{\partial F}{\partial \eta_{ij}} \right)_{T,\eta'} \qquad (3.16)$$

where η' indicates that all other components of η are held constant.

The state functions U and F must be invariant with respect to a body translation or rotation, without deformation. This rotational invariance suggests that U and F depend on the strained configuration x only through the initial unstrained configuration X and rotational-independent strains η_{ij}. Therefore, the functional dependences may be written as

$$U(x,S) = U(X,\eta_{ij}, S) \qquad (3.17)$$

and

$$F(x,T) = F(X,\eta_{ij}, T) \qquad (3.18)$$

Although the strains concerned are finite, they are nevertheless very small, and it is therefore possible to express the strain dependence of the thermodynamic potentials in the form of Taylor series expensions about the state of zero strain. For example,

$$U(S)=U(S,\eta)-U(S,0)$$

$$=\left(\frac{\partial U(S,\eta)}{\partial \eta_{ij}}\right)_{\eta=0}\eta_{ij}+\frac{1}{2!}\left(\frac{\partial^2 U(S,\eta)}{\partial \eta_{ij}\,\partial \eta_{kl}}\right)_{\eta=0}\eta_{ij}\,\eta_{kl}$$

$$+\frac{1}{3!}\left(\frac{\partial^3 U(S,\eta)}{\partial \eta_{ij}\,\partial \eta_{kl}\,\partial \eta_{mn}}\right)_{\eta=0}\eta_{ij}\,\eta_{kl}\,\eta_{mn}+\cdots\cdots \qquad (3.19)$$

but for unstrained crystal in thermodynamic equilibrium,

$$\left(\frac{\partial U(S,\eta)}{\partial \eta_{ij}}\right)_{\eta=0}=\frac{1}{\rho_o}\left(t_{ij}(\eta)\right)_{\eta=0}=0 \qquad (3.20)$$

Elastic coefficients of order n ($n\geq 2$) are defined thermodynamically as the n^{th} partial derivatives of the appropriate thermodynamic potential with respect to the Lagrangian strains, evaluated at zero strain, or with respect to tensions, evaluated at zero tension. Therefore we have the following relations for adiabatic (isentropic) and isothermal cases:

$$C^{S}_{ijkl\cdots\cdots}=\rho_o\left(\frac{\partial^n U}{\partial \eta_{ij}\,\partial \eta_{kl\cdots\cdots}}\right)_{S,\eta=0} \qquad (3.21)$$

$$C^{T}_{ijkl\cdots\cdots}=\rho_o\left(\frac{\partial^n F}{\partial \eta_{ij}\,\partial \eta_{kl\cdots\cdots}}\right)_{T,\eta=0} \qquad (3.22)$$

$$S^{S}_{ijkl\cdots\cdots}=-\rho_o\left(\frac{\partial^n H}{\partial t_{ij}\,\partial t_{kl\cdots\cdots}}\right)_{S,t=0} \qquad (3.23)$$

$$S^{T}_{ijkl\cdots}=-\rho_o\left(\frac{\partial^n G}{\partial t_{ij}\,\partial t_{kl\cdots}}\right)_{T,t=0} \qquad (3.24)$$

The $C^{S}_{ijkl\ldots}$ and $C^{T}_{ijkl\ldots}$ are adiabatic and

isothermal elastic constants respectively and $S^{S}_{ijkl....}$ and $S^{T}_{ijkl....}$ are their corresponding elastic compliances. The energy density of the material can then be written as

$$\rho_o U(S) = (\frac{1}{2})C^{S}_{ijkl}\eta_{ij}\eta_{kl} + (\frac{1}{6})C^{S}_{ijklmn}\eta_{ij}\,\eta_{kl}\,\eta_{mn} + ... \tag{3.25}$$

where

$$C^{S}_{ijkl} = \rho_o \left(\frac{\partial^2 U}{\partial \eta_{ij}\,\partial \eta_{kl}} \right)_{\eta=0}$$

and

$$C^{S}_{ijklmn} = \rho_o \left(\frac{\partial^3 U}{\partial \eta_{ij}\,\partial \eta_{kl}\,\partial \eta_{mn}} \right)_{\eta=0}$$

The first two terms in the above energy expansion are the second and third order contributions of the strain to the elastic energy density. The form of this expansion is similar to the expansion of potential energy in terms of interatomic displacement, and thus it is ultimately possible to relate the elastic constants to the interatomic forces in a solid. Since the strains η_{ij} are symmetric we may employ the Voigt contracted suffix notation; suffices are then allocated according to the scheme,

$$11=1;22=2;33=3;23=4;31=5;12=6,$$

In this contracted notation the strains η_{ij} may be written as η_I. The magnitudes of the η_I are related to

the magnitudes of the η_{ij} by

$$\eta_{ij} = (1+\delta_{ij})\eta_I \qquad (3.26)$$

Also, from Brugger (1964),

$$t_{ij} = t_I$$

In all cases, lower case suffices run from 1 to 3, while upper case run from 1 to 6. Applying this contracted notation to the elastic constants gives

$$C_{IJ} \ldots = C_{ijkl} \ldots \qquad (3.27)$$

Thus the thermodynamic definitions become, for example

$$C^S_{IJK} = \rho_o \left| \frac{\partial^3 U}{\partial\eta_I \, \partial\eta_J \, \partial\eta_K} \right|_{S,\eta=0} \qquad (3.28)$$

The thermodynamic potentials U, F, H and G are extensive properties of the system, and so their n^{th} partial derivatives of the thermodynamic parameters are independent of the order of differentation; ie the strain energy must be independent of the path by which the state of strain is attained. Thus all permutations of the contracted suffices lead to the same constant, so that for second order,

$$C_{IJ} = C_{JI}$$

and for the third order,

$$C_{IJK} = C_{IKJ} = C_{KJI} = C_{KIJ} = C_{JIK} = C_{JKI} \quad (3.29)$$

Therefore the maximum numbers of independent SOEC and TOEC are 21 and 56 respectively. These numbers are further reduced by crystal symmetry . The details of the independent SOEC and TOEC are given by Brugger (1965a) for all of the seven crystallographic systems. For cubic symmetry, there are three independent adiabatic (or isothermal) SOEC and six TOEC. These are

$$C_{11} = C_{22} = C_{33}$$

$$C_{12} = C_{23} = C_{13}$$

$$C_{44} = C_{55} = C_{66}$$

and

$$C_{111} = C_{222} = C_{333}$$

$$C_{112} = C_{322} = C_{133} = C_{311} = C_{122} = C_{233}$$

$$C_{123}$$

$$C_{114} = C_{255} = C_{366}$$

$$C_{166} = C_{155} = C_{266} = C_{244} = C_{344} = C_{355}$$

$$C_{456}$$

All others, except those obtained by the permutation of the suffices in the above, are zero.

3.4 Propagation of Elastic Waves in Crystals.

The second order elastic stiffness constants of a crystal can be determined from the measurements of ultrasonic wave velocities propagating in the solid. The wave motion is assumed to be adiabatic and to cause only infinitesimal displacements of volume elements in the crystal. By Thurston (1964) the equation of motion of such wave can be written as

$$\rho \frac{\partial^2 x_i}{\partial t^2} = \frac{\partial \sigma_{ij}}{\partial x_j} \qquad (3.30)$$

For the wave propagating in an initially unstressed medium this equation becomes, by equation 3.6

$$\rho_o \frac{\partial^2 u_i}{\partial t^2} = \frac{\partial \sigma_{ij}}{\partial X_j} \qquad (3.31)$$

since $\rho = \rho_o$ for infinitesimal strain. Now by equation 3.8 and 3.11 the Lagrangian strain parameter is

$$\eta_{ij} = (u_{ij} + u_{ji} + u_{ki} u_{kj}) \qquad (3.31a)$$

but for infinitesimal strains the product term can be ignored, thus leading to the usual infinitesimal strain definition

$$\epsilon_{ij} = (u_{ij} + u_{ji})/2 \qquad (3.32)$$

By differentating eq (3.1) with respect to $\underline{X}$ equation 3.31 becomes,

$$\rho_o \frac{\partial^2 u_i}{\partial t^2} = C_{ijkl} \frac{\partial^2 u_l}{\partial X_j \partial X_k} \qquad (3.33)$$

The ultrasonic techniques employed in the present study were designed to generate nearly plane wave pulses which may be described by the equation,

$$\underline{u} = \underline{u}_o \exp i\omega(t - \underline{N}.\frac{\underline{x}}{V}) \qquad (3.34)$$

where $\underline{N}$ is a vector in the direction of propagation, u_o is particle displacement amplitude and V is the magnitude of wave velocity. Imposing this into equation (3.33) gives (Brugger 1965a)

$$\rho_o v^2 U_m = C^S_{mnop} N_n N_p U_o \qquad (3.35)$$

where $\underline{U}$ is a unit vector in the direction of polarisation. Equation 3.35 is then solved for V, and there are found to be in general three solutions for each direction of propagation. For certain combinations of $\underline{N}$ and $\underline{U}$, it may be shown (Brugger 1965a) that the propagation modes of the elastic waves are either purely transverse or purely longitudinal. In a cubic crystal, the pure mode directions are of [001], [110] and [111] form and each of these directions is associated with one longitudinal and two transverse modes (although these may be degenerate in velocity). The acoustic mode velocities (v_1, v_2, v_3) can been calculated as the eigenvalues of

the Christoffel equations

$$(L_{ik}-\rho v^2\delta_{ik})\,u_{0k}=0 \quad (i,k=1,2,3), \tag{3.36}$$

where L_{ik} is the Christoffel matrix, u_{01}, u_{02} and u_{03} are the Cartesian components of the unit polarization vector, ρ is the density and v the desired velocity. These equations have a non-trivial solution only when the determinant of the coefficients is zero. For a cubic crystal this condition leads to the determinantal equation

$$\begin{vmatrix} (C_{11}-C_{44})n_1^2+C_{44}-\rho v^2 & n_1n_2(C_{12}+C_{44}) & n_1n_3(C_{12}+C_{44}) \\ n_1n_2(C_{12}+C_{44}) & n_2^2(C_{11}-C_{44})+C_{44}-\rho v^2 & n_2n_3(C_{12}+C_{44}) \\ n_1n_3(C_{12}+C_{44}) & n_2n_3(C_{12}+C_{44}) & n_3^2(C_{11}-C_{44})+C_{44}-\rho v^2 \end{vmatrix} = 0. \tag{3.37}$$

where n_1, n_2, n_3 are direction cosines for the propagation direction.

The three wave velocities were obtained from propagation directions at 1° intervals around the [001] and [110] planes by determining the eigenvalues of the Christoffel equations; at the same time, particle displacement vectors were derived by calculating the eigenvectors. Pure modes solutions, of course, are obtained only for propagation in the crystallographic directions <100>, <110> and <111>.

To obtain a complete set of the SOEC of a cubic crystal it is desirable that the specimen to be cut with two opposed (100) faces and two pairs of faces perpendicular to the [110] direction. The expansions linking the wave velocities and the SOEC for f.c.c. are

listed in Table 3.1. As the elastic stiffness constants obtained from ultrasonic measurements are adiabatic, they may be transformed into isothermal second order elastic constants using the following process. The first step is to transform compliances to stiffnesses:

$$S_{11} = (C_{11} + C_{12})/(C_{11} - C_{12})(C_{11} + 2C_{12}) \quad (3.38)$$

$$S_{12} = - C_{12}/(C_{11} - C_{12})(C_{11} + 2C_{12}) \quad (3.39)$$

$$S_{44} = 1/C_{44} \quad (3.40)$$

and the bulk modulus of the solid is given by

$$B = (C_{11} + 2C_{12})/3 \quad (3.41)$$

The general relation between isothermal and adiabatic compliance(Nye 1957) is

$$S^{T}_{ijkl} = S^{S}_{ijkl} + \frac{\alpha_{ij}\alpha_{kl}T}{\rho_o C_p} \quad (3.42)$$

where T is the absolute temperature, ρ_o is the density in the unstressed state, C_p is the specific heat per unit mass at constant pressure and α_{ij} and α_{kl} are the thermal expansion coefficients. Using S^{T}_{ijkl} obtained from equation (3.42) and substituting into equations (3.38) to (3.40), the isothermal SOEC can be determined. For cubic crystal equation (3.42) becomes

Table 3.1: Expression for $\rho_o V^2$ in face centred cubic crystals.

Mode No	Propagation direction	Polarization direction	$\rho_o V^2 = (\rho_o W^2)$
1.	[001]	[001]	C_{11}
2.	[001]	in (001) plane	C_{44}
3.	[110]	[110]	$(C_{11}+C_{12}+2C_{44})/2$
4.	[110]	$[1\bar{1}0]$	$(C_{11}-C_{12})/2$
5.	[110]	[001]	C_{44}

Table 3.2 Thurston and Brugger Relations for Selected Modes in fcc Crystals.

Mode No	Prop Dir.	Polar Dir.	$W=(\rho_o V^2)_{P=0}$	$(\rho_c W^2)'_{P=0}$
1	[110]	[100]	C_{11}	$-1-2w/3B-(C_{111}+2C_{112})/3B$
2	[100]	in plane	C_{44}	$-1-2w/3B-(C_{144}+2C_{166})/3B$
3	[110]	[110]	$(C_{11}+C_{12}+2C_{44})/2$	$-1-2w/3B-(C_{111}/2+2C_{112}+C_{144}+2C_{166}+C_{123}/2)/3B$
4	[110]	$[1\bar{1}0]$	$(C_{11}-C_{12})/2$	$-1-2w/3B-(C_{111}/2-C_{123}/2)/3B$
5	[110]	[001]	C_{44}	$-1-2w/3B-(C_{144}+2C_{166})/3B$

$B = (C_{11}+2C_{12})/3$

Table 3.1: Expression for $\rho_o V^2$ in face centred cubic crystals.

Mode No	Propogation direction	Polarization direction	$\rho_o V^2 = (\rho_o W^2)$
1.	[001]	[001]	C_{11}
2.	[001]	in (001) plane	C_{44}
3.	[110]	[110]	$(C_{11}+C_{12}+2C_{44})/2$
4.	[110]	$[1\bar{1}0]$	$(C_{11}-C_{12})/2$
5.	[110]	[001]	C_{44}

Table 3.2 Thurston and Brugger Relations for Selected Modes in fcc Crystals.

Mode No	Prop Dir.	Polar Dir.	$w=(\rho_o V^2)_{P=0}$	$(\rho_c W^2)'_{P=0}$
1	[110]	[100]	C_{11}	$-1-2w/3B-(C_{111}+2C_{112})/3B$
2	[100]	in plane	C_{44}	$-1-2w/3B-(C_{144}+2C_{166})/3B$
3	[110]	[110]	$(C_{11}+C_{12}+2C_{44})/2$	$-1-2w/3B-(C_{111}/2+2C_{112}+C_{144}+2C_{166}+C_{123}/2)/3B$
4	[110]	$[1\bar{1}0]$	$(C_{11}-C_{12})/2$	$-1-2w/3B-(C_{111}/2-C_{123}/2)/3B$
5	[110]	[001]	C_{44}	$-1-2w/3B-(C_{144}+2C_{166})/3B$

$B = (C_{11}+2C_{12})/3$

$$S^{T}_{11}=S^{S}_{11}+\frac{\alpha^2 T}{\rho_o C_p}$$

$$S^{T}_{12}=S^{S}_{12}+\frac{\alpha^2 T}{\rho_o C_p} \qquad (3.43)$$

$$S^{T}_{44}=S^{S}_{44}$$

The expressions for cubic crystal (Table 3.2) under hydrostatic pressure imply that the cubic symmetry is retained and from hydrostatic pressure measurements, the three independent combinations of the third order elastic constants ($C_{111}+2C_{112}$), ($C_{144}+2C_{166}$) and ($C_{123}+2C_{112}$) can be determined.

Elastic constant measurements enable the acoustic phonon density of states to be modelled by a Debye distribution function; the excluded optic modes can then be treated separately. The Debye temperature Θ_D^{el} has been obtained as an integral over velocity surface (Saunders et.al.1986)

$$\Theta_D^{el}=\left(\frac{9N}{4\pi V}\right)^{\frac{1}{3}}\left(\frac{h}{k}\right)\left[\int\left(\frac{1}{v_1^3}+\frac{1}{v_2^3}+\frac{1}{v_3^3}\right)\frac{d\Omega}{\pi}\right]^{-\frac{1}{3}}, \qquad (3.44)$$

where N/V is the number of atoms per unit volume V and v_i is the velocity of mode i at low temperature.

3.5 Hydrostatic Pressure Derivatives of the Effective SOEC and of the Bulk Modulus

Thurston and Brugger (1964) defined a 'natural velocity' W as l_o/T where l_o is the length of the unstressed crystal and T is the experimentally measured transit time of ultrasonic waves across the specimen. The product of $\rho_o W^2$ is then evaluated, where ρ_o is the original unstressed density, and the dependence of this product on a single scalar stress parameter P is measured. The parameter P is defined as the force applied to the specimen divided by the unstressed area; thus all experimental parameters are referred back to the original dimensions of the unstressed specimen. The stress derivative is then given by

$$(\rho_o W^2)'_{p=0} = \left\{ \frac{d(\rho_o W^2)}{dP} \right\}_{P=0} \qquad (3.45)$$

The quantity $(\rho_o W^2)'_{P=0}$ does not represent the actual pressure derivative of the SOEC involved since no account is taken of the changes in sample length due to applied pressure. The natural velocity W measured at a pressure P is not equal to the actual sound velocity V in the material at that pressure. Furthermore the density of the solid is also a function of the applied pressure. However Thurston (1965) has shown that the first pressure derivative of 'effective' elastic constants (ρV^2), evaluated at zero pressure, can be calculated from the pressure derivative $(\rho_o W_2)'_{P=0}$ without the need to

calculate the path length and density at any elevated pressure. The equation required (Thurston 1965) is

$$\left[(\rho V^2)' - (\rho_o W^2)'\right]_{P=0} = \rho_o W^2{}_o \left[S^T{}_{kkii} - 2N_k N_m S^T{}_{kmii}\right]_{P=0} \qquad (3.46)$$

where W is the natural velocity, defined as the path length at zero pressure divided by the wave transit time at a pressure P. W_o is the natural velocity at P=0 (W_o=V at P=0). The term in the parentheses on the right is the volume compressibility X^T minus twice the linear compressibility in the propagation direction $\underline{N}$. These terms correspond to the effects of changes of density and path length respectively. It is the isothermal compliance constants which appear here since pressure derivatives are measured at constant temperature. For cubic crystals, the linear compressibility $N_k N_m S^T{}_{kmii}$ is equal to $X^T/3$, for all propagation directions $\underline{N}$. Thus

$$\left[\rho V^2\right]'_{P=0} = \left[\frac{\partial C^S_{IJ}}{\partial P}\right]_{P=0} = \left[(\rho_o W^2)'_{P=0} + \frac{C^S_{IJ}}{3B^T}\right]_{P=0} , \qquad (3.47)$$

since $B^T = 1/X^T$. Thurston (1965) has shown that the bulk modulus at any pressure is related to the effective elastic coefficients for wave propagation at that pressure by the same formula as at zero pressure. Hence the correct derivative of the bulk modulus B is obtained by differentiating the appropriate relationship, interpreting the derivatives as derivatives of the effective elastic coefficients. Therefore,

$$\left(\frac{\partial B}{\partial P}\right)_{P=0} = \frac{1}{3}\left(\frac{\partial C_{11}}{\partial P} + 2\frac{\partial C_{12}}{\partial P}\right)_{P=0} \qquad (3.48)$$

The pressure derivative of the thermodynamic second order elastic stiffness constants (SOEC), B_{IJ} is defined as

$$B_{IJ} = \frac{\partial C^{S}_{lkmn}}{\partial P} = -S^{T}_{ijhh}C_{lkmnij} \qquad (3.49)$$

The difference between the two sets of pressure derivatives has been discussed by Thurston (1964). He then concludes that the difference is expressible in terms of the second order elastic stiffness constants and the second order elastic compliances as shown in Table 3.3 which refers to each of the crystal symmetries except for those belonging to monoclinic and triclinic systems. In the analyses of the ultrasonic data in conjunction with other thermodynamic data, the $\partial C_{IJ}/\partial P$ used most commonly can be deduced from two channels: by the use of equation (3.47) or indirectly by first finding the B_{IJ}'s and then applying the relations in Table 2.3 to obtain the pressure derivatives of the effective SOEC. These dimensionless parameters B_{IJ} and $\partial C_{IJ}/\partial P$ have the values in the range $\sim 10^{-2}$ to 0.5×10^{2}; negative pressure derivatives often imply the softening of acoustic vibrational modes.

Table 3.3 Pressure derivatives of thermodynamic and effective elastic constants.

$$B_{11} = \frac{\partial C_{11}}{\partial p} + 1 - (S_2 + S_3 - 3S_1)C_{11}$$

$$B_{12} = \frac{\partial C_{12}}{\partial p} - 1 - (S_3 - S_1 - S_2)C_{12}$$

$$B_{13} = \frac{\partial C_{13}}{\partial p} - 1 - (S_2 - S_1 - S_3)C_{13}$$

$$B_{14} = \frac{\partial C_{14}}{\partial p} - S_1 C_{14}$$

$$B_{15} = \frac{\partial C_{15}}{\partial p} - (S_2 - 2S_1)C_{15}$$

$$B_{16} = \frac{\partial C_{16}}{\partial p} - (S_3 - 2S_1)C_{16}$$

$$B_{22} = \frac{\partial C_{22}}{\partial p} + 1 - (S_3 + S_1 - 3S_2)C_{22}$$

$$B_{23} = \frac{\partial C_{23}}{\partial p} - 1 - (S_1 - S_2 - S_3)C_{23}$$

$$B_{24} = \frac{\partial C_{24}}{\partial p} - (S_1 - 2S_2)C_{24}$$

$$B_{25} = \frac{\partial C_{25}}{\partial p} + S_2 C_{25}$$

$$B_{26} = \frac{\partial C_{26}}{\partial p} - (S_3 - 2S_2)C_{26}$$

$$B_{33} = \frac{\partial C_{33}}{\partial p} + 1 - (S_1 + S_2 - 3S_3)C_{33}$$

$$B_{44} = \frac{\partial C_{44}}{\partial p} + 1 - (S_1 - S_2 - S_3)C_{44}$$

$$B_{45} = \frac{\partial C_{45}}{\partial p} + S_3 C_{45}$$

$$B_{46} = \frac{\partial C_{46}}{\partial p} + S_2 C_{46}$$

$$B_{55} = \frac{\partial C_{55}}{\partial p} + 1 - (S_2 - S_1 - S_3)C_{55}$$

$$B_{56} = \frac{\partial C_{56}}{\partial p} + S_1 C_{56}$$

$$B_{66} = \frac{\partial C_{66}}{\partial p} + 1 - (S_3 - S_1 - S_2)C_{66}$$

3.6 Compression of the Crystalline Solids

An important quantity in theoretical and experimental studies of the physical properties of magnetic materials under pressure is the compression $V(P)/V_o$, the ratio of the volume $V(P)$ at pressure P to that V_o at atmospheric pressure. Although the dependence of ultrasonic wave velocity upon pressure can be measured with precision, the pressure range is limited. The compression at high pressure can be evaluated from the elastic constants and their hydrostatic pressure derivatives by using an equation-of-state such as that of Murnaghan (1944). This rests upon the assumption that the isothermal and adiabatic bulk moduli depend linearly upon pressure

$$B^T(P)=-V\left(\frac{\partial P}{\partial V}\right)_T=B_o^T+P\left(\frac{\partial B^T}{\partial P}\right)_{P=0,T} \qquad (3.50)$$

$$B^S(P)=-V\left(\frac{\partial P}{\partial V}\right)_S=B_o^S+P\left(\frac{\partial B^S}{\partial P}\right)_{P=0,T} \qquad (3.51)$$

Then integration leads to the Murnaghan equation-of-state:

$$P = \frac{B^T}{B^S}\left[\left(\frac{V_o}{V(P)}\right)^{B^{'T}}-1\right] \qquad (3.52)$$

or in the more easily used form

$$\ln\left[\frac{V_0}{V(P)}\right]=\frac{1}{B'^{T}_0}\ln\left[B'^{T}_0\left(\frac{P}{B^{T}_0}\right)+1\right]. \qquad (3.53)$$

which describes compression of many solids well (Anderson 1966).

Ultrasonic pulse echo measurements lead to adiabatic moduli, so to use this equation-of-state it is necessary to transform the data to isothermal moduli. The adiabatic and the isothermal bulk moduli are related by

$$B^{S}_0=B^{T}_0(1+\alpha\gamma T) \qquad (3.54)$$

γ is the thermal Gruneisen parameter.

The isothermal hydrostatic pressure derivatives ($\partial B^{T}_0/\partial P$) ($= B'^{T}_0$) can be obtained from (Overton 1962, Anderson 1966).

$$B'^{T}_0=B'^{S}_0+T\alpha\gamma\left(\frac{B^{T}_0}{B^{S}_0}\right)\left[1-\frac{2}{\alpha B^{T}_0}\left(\frac{\partial B^{T}_0}{\partial T}\right)_P-2B'^{S}_0\right]+\left[T\alpha\gamma\left(\frac{B^{T}_0}{B^{S}_0}\right)\right]^2\left[B'^{S}_0-1-\frac{1}{\alpha^2}\left(\frac{\partial\alpha}{\partial T}\right)_P\right], \qquad (3.55)$$

where $(\partial B^{T}_0/\partial T)_P$ can be obtained from

$$\left(\frac{\partial B^{T}_0}{\partial T}\right)_P=\left(\frac{\partial B^{S}_0}{\partial T}\right)\Big/(1+T\alpha\gamma)-\frac{B^{S}_0}{T}\frac{T\alpha\gamma}{[1+T\alpha\gamma]^2}\left\{1+\frac{(\partial\alpha/\partial T)_P}{\alpha/T}\right\} \qquad (3.56)$$

The compression up to the theoretical hydrostatic pressure of about 100KBar has been obtained in this work.

3.7 Temperature Dependences of the SOEC

The temperature dependences of the SOEC have been discussed in great details by Tu Hailing (1982). The thermal variations of the SOEC for most crystals which can be regarded as normally behaved are characterised by two general features:

i) linear decreases with increasing temperature.

ii) as temperature approaching zero Kelvin (0K) the SOEC-temperature curve will have a zero slope region.

Thurston (1974) deduced a general relation for the temperature dependences of the SOEC and obtained an equation for cubic crystal as

$$\left[\partial C_{ij}/\partial T \right]_{P=0} = C_{ij}^{0} \left[2/f_{0}(\partial f/\partial T)_{P=0} - \alpha_{v}/3 \right]_{T} \qquad (3.57)$$

where α_v is the volume thermal expansion coefficient, f is overlapping frequency, C_{IJ}^{o} are the SOEC at ambient condition and subscript 0 indicates that quantities are evaluated at some fixed temperature T and at zero pressure. $\partial C_{ij}/\partial T$ comprises two contributions: one from elastic anharmonicity and the other from the volume expansion. In order to discuss the pure anharmonic

lattice contribution which has the physical significance to temperature dependence of the SOEC, $(\partial C_{ij}/\partial T)_V$, the volume effect must be separated from the measured value of $(\partial C_{ij}/\partial T)_P$ from a fundamental thermodynamic relation (Fritz 1974),

$$\left[\partial \ln \Phi/\partial T\right]_P = -\left[K/\alpha\right]^{-1}\left[\partial \ln \Phi/\partial P\right]_T + \left[\partial \ln \Phi/\partial T\right]_V \qquad (3.58)$$

one arrives at an approximation formula:

$$\left[\partial C_{ij}/\partial T\right]_V = \left[\partial C_{ij}/\partial T\right]_P + \left[K/\alpha\right]^{-1}\left[\partial C_{ij}/\partial P\right]_T \qquad (3.59)$$

where K and α are the volume compressibility and volume thermal expansion coefficient respectively.

The temperature derivatives of the SOEC are also useful for an estimation of the magnitude of the fourth order elastic constants (FOEC) if one considers that the central force model may be reasonable for the higher order repulsive interactions in rocksalt and zincblende structure crystals in which case the eleven FOEC would reduce to C_{1111}, C_{1112} and C_{1113}.

3.8 Grüneisen Parameters

One important application of the measured hydrostatic pressure derivatives of the SOEC is that they can be used to determine the mode Grüneisen parameters of the long wavelength acoustic phonon modes alone, and hence enable a separate assessment of the influence of the vibrational anharmonicity of these particular modes on the physical properties of solids. In the Grüneisen approach to anharmonicity the thermal expansion α is used to obtained a thermal Grüneisen parameter γ^{th}

$$\gamma^{th} = \alpha V B^T / C_v = \alpha V B^S / C_p. \tag{3.60}$$

where α is the coefficient of volume thermal expansion, V is the volume, B^T is isothermal bulk modulus and C_v and C_P are specific heats at constant volume and constant pressure respectively. This parameter comprises a weighted average of the individual mode (i) Grüneisen gammas

$$\gamma^{th} = \frac{\sum C_i \gamma_i}{\sum C_i} \tag{3.61}$$

and

$$\gamma_i = -\frac{d\ln\omega_i}{d\ln V} \tag{3.62}$$

where C_i and ω_i are the Einstein heat capacity and lattice frequency of the i^{th} vibrational mode. At high

temperature ($T>\Theta_D$) the thermal expansion and specific heat include contributions from phonons having wavevectors which span the whole Brillouin zone. A link between thermal properties and the stress dependence of the acoustic mode velocities can be forged by calculating the long wavelength acoustic mode Grüneisen parameters and then obtaining a weighted average for these alone. Knowledge of the $\partial C_{ij}/\partial P$ allows the calculation of the mode Grüneisen gamma γ_i of the acoustic branch in the long wavelength limit. These particular γ_i, especially those for the lower-lying transverse vibrations, are expected to dominate the thermal Grüneisen parameter at low temperatures where only the lowest energy modes are excited so that optic modes and modes well away from the Brillouin zone centre can be neglected. In the anisotropic continuum model only the acoustic modes are considered and their dispersion is ignored. Then the volume dependence of the individual mode frequencies for the acoustic modes in the long wavelength limit can be related to the measured pressure dependences of the elastic constants. The mode Grüneisen parameters $\gamma_{(p,N)}$ where p denotes the branch and N is the unit vector in the propagation direction, are given for a cubic crystal by (Brugger and Fritz 1967):

$$\gamma(p,\underline{N})=-(\frac{1}{6w})\ [3B+2w+k]$$

$$w(p,\underline{N})=C_{11}K_1+C_{44}K_2+C_{12}K_3,$$

$$
\begin{aligned}
k(p,\underline{N}) &= C_1K_1+C_2K_2+C_3K_3 \\
K_1(p,\underline{N}) &= N_1^2U_1^2+N_2^2U_2^2+N_3^2U_3^2 \\
K_2(p,\underline{N}) &= (N_2U_3+N_3U_2)^2+(N_3U_1+N_1U_3)^2+(N_1U_2+N_2U_1)^2 \\
K_3(p,\underline{N}) &= 2(N_2N_3U_2U_3+N_3N_1U_3U_1+N_1N_2U_1U_2) \\
C_1 &= C_{111}+2C_{112} \\
C_2 &= C_{144}+2C_{166} \\
C_3 &= C_{123}+2C_{112}
\end{aligned}
\qquad (3.63)
$$

Here N_i and U_i are the direction cosines for the propagation and polarization directions. The mode Grüneisen gammas for any chosen propagation direction N have been computed by solving the Christoffel equations (equation 3.36) to obtain the polarisation directions U_i as the eigenvectors and the mode velocities as the eigenvalues.

A high temperature and low temperature average acoustic Grüneisen gamma can be obtained from the mode Grüneisen gammas. At low temperature each acoustic mode will be excited by an amount proportional to the specific heat C(p,N) of that mode, which in turn is proportional to the inverse cube of the mode Debye temperature. Hence to obtain the low temperature acoustic Grüneisen parameter $\bar{\gamma}^{el}$ it is only necessary to weight $\gamma_{(p,N)}$ by $\nu^{-3}_{(p,N)}$

$$\bar{\gamma}_{o}^{el} = \frac{\Sigma\int \gamma(p,\underline{N})\nu^{-3}(p,\underline{N})d\Omega}{\Sigma\int \nu^{-3}(p,\underline{N})d\Omega} \qquad (3.64)$$

To calculate the high temperature acoustic gamma, $\bar{\gamma}_{\infty}^{el}$, a Debye sphere is assumed, and at $T>>\theta_D$ all modes are excited classically; the weighted factors become equal and the high temperature gamma can be calculated as an unweighted mean of $\gamma_{(p,N)}$, that is

$$\bar{\gamma}_{\infty}^{el} = \frac{1}{3}\Sigma\int \gamma(p,\underline{N})\frac{d\Omega}{4\pi} \qquad (3.65)$$

$\bar{\gamma}^{el}$ is a measure only of the contribution of the zone-centre acoustic mode to the anharmonicity, whereas γ^{th} takes into account contribution from all modes on both acoustic and optic branches. At low temperatures only the zone centre acoustic phonons corresponding to the long wavelength limit are excited; of these modes, the transverse branches are characteristically the lowest in energy.

CHAPTER 4

EXPERIMENTAL METHODS

4.1 Introduction

Measurement of the temperature dependences of the hydrostatic pressure derivatives of wave velocity and hence the temperature and pressure dependences of the elastic vibrational modes is the major interest of this work. One method of making measurement of the second order elastic stiffness constants (SOEC) of a crystal is by measuring the absolute pulse transit time of a specified ultrasonic wave propagating through the solid. In this chapter the ultrasonic pulse echo overlap technique applied to measure the velocities and their pressure dependences for elastic waves propagated in single crystals of binary and ternary alloys of MnNi and MnNiC will be described. Techniques for controlling, measuring and varying the sample temperature and pressure throughout the experimental programme will also be described. To obtain the temperature dependences of the SOEC of these alloys, measurements have been made from room temperature up to about 50 degrees above the Nēel point so that the elastic behaviour of these materials in both the antiferromagnetic and paramagnetic states can be observed within this temperature range. The hydrostatic pressure derivatives have been obtained at fixed temperatures in this range.

4.2 Measurements of Ultrasonic Wave Velocities in the Single Crystals.

The pulse echo overlap method is one of the basic techniques for measuring ultrasonic wave velocity. It is particularly useful for determining changes induced in velocity by the application of pressure or variation of temperature. The technique employed here is the single ended configuration by which a pulse propagates into a crystal and then the reflected pulse is detected from the same side as the incident pulse. A piezoelectric transducer is used both as a transmitter and a receiver; it converts the high voltage radio frequency pulses into mechanical vibrations. On reaching the other side of the sample this is reflected back towards the transducer. As a result a series of reflected echoes of equal distances appears as an echo train on the screen of an oscilloscope. The echo train show an exponential decay due to a sum of all the attenuation mechanism. The interval between any two successive echoes represents the transit time in the unit of the time base scale of the oscilloscope. As the propagation of this wave is essentially a plane wave, the uniform propagation velocity is determined by the distance between the two sample faces and by the transit time of the two successive chosen echoes.

4.3 Sample Preparation.

A plane wave with a uniform propagation velocity can only be obtained from a sample which has a high degree of parallelism of the two end faces. In normal practice most of the crystals employed have been cut with a typical values of non-parallelism and misorientation of less than 10^{-4} and 0.5° respectively. Non-parallelism would effect the measurement of thickness and the acoustic path length; hence the accuracy of the velocity measurement also depends on the parallelism of the two faces. For a sample with larger values of misorientation and non-parallelism the following effects could occur:

i) Interference Effect

Non-parallelism would result in the path of an ultrasonic wave being diverted away from its original direction after repeated reflections causing an interference effect as a result of the transducer receiving different phases of the wave across its diameter. The echo train would then suffer non-exponential loss affecting the accuracy of the transit time measurements.

ii) Diffraction effect and acoustic mode conversion.

These effects can arise from the misorientation of the sample direction from the required crystallographic direction. In this circumstance the wave

propagated in the crystal will not be pure. Then two or more waves of allowable polarizations can be created. These waves will interfere to produce a velocity different from that of the pure mode.

Several processes are needed to prepare sample for ultrasonic wave velocity and SOEC measurements which are discussed below.

i) Determination of Crystal Orientation.

When the crystal is cut so that wave propagation is along the [110] direction, it is possible to measure three combinations of elastic constants using each of the three possible modes of propagation: $(C_{11}+C_{12}+2C_{44})$, C_{44} and $(C_{11}-C_{12})/2$. When cut along the [001] direction , it is possible to measure just C_{11} and C_{44}. The advantages of having both cuts are that: (i) the measurements on C_{44} can be compared, (ii) C_{11} can be measured by itself on the four fold sample.

Crystal orientations have been determined using Laue back reflection X-ray photographs. The crystals are mounted on a three arc goniometer (Fig 4.1) which is placed onto the X-ray set where the Laue photograph is taken. The first experiment is to take a series of Laue photographs at different points on the crystal to determine whether the sample is a single crystal and does not have polycrystalline regions in the area to be cut out for the sample. Any twinning within the crystal can be observed as split diffraction spots on the

photographs. Then the desired symmetry axis can be located and centred. The exact crystal orientation is established after a series of Laue photographs, from each photograph the orientation is improved with the use of a Greniger net. In normal practice the process is repeated three or four times before the orientation to within $\pm 0.5^{0}$ can be obtained.

ii) Sample Cutting and Polishing

When the desired crystal orientation has been established, the goniometer with the crystal mounted on it are transferred onto a spark machine (type SMD, Metal Research Limited, Cambridge.) for cutting. The cutting process is carried out under paraffin, it is a strain free cutting procedure. The crystal and the goniometer are located directly under a spark erosion metal blade and a high tension voltage is applied between the metal blade and the crystal. By setting a suitable voltage between the two, sparks are produced and the crystal is cut so as to have a pair of parallel faces perpendicular to the symmetry axis.

The orientation of each crystal is rechecked after cutting. To do this the crystal is mounted on a spring loaded goniometer with the cut faces held perpendicular to the X-ray beam (Fig 4.2). An X-ray photograph is taken and examined. When the final alignment is satisfactory, the whole process is repeated for the next pair of cuts. With this process pairs of

Fig.4.1 THREE ARC GONIOMETER

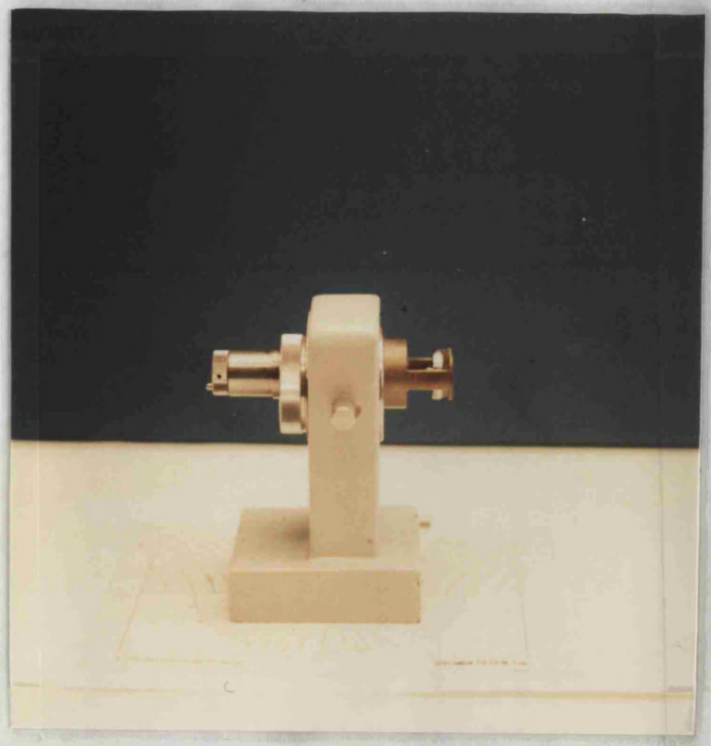

Fig.4.2 SPRING LOADED GONIOMETER

parallel faces perpendicular to the [110] and in some cases [001] directions have been obtained. Using a digital micrometer the thickness of the crystal has been measured at different points; from this the parallelism has been found to be better than 10^{-4} rad.

4.4 Piezeoelectric Quartz Transducers

A transducer is a device used for converting energy from one form to another. In this work a quartz transducer is used which acts as a piston source for generating a wave which is essentially planar in nature with a width equal to the diameter of the piston up to a distance r given by

$$r = a^2 / \lambda \qquad (4.1)$$

where a is the transducer radius and λ is the wave length of the plane wave. The fundamental frequency of the transducers used here is 10MHz. Transducers are designed with the thickness being half of the wavelength of the sound wave in quartz at the resonance frequency (Bateman 1966).

Two types of quartz transducers have been employed. X-cut transducers having a thickness of 0.29 ± 0.02 mm have been used for generating longitudinal waves, while Y-cut transducers have a thickness of 0.19 ± 0.02 mm have been used for generating shear waves. Transducers of different diameters (4mm, 6mm and 10mm) are available. To

ensure that the vibration produced is a plane wave, the diameter of the transducer should be at least ten times the wavelength of sound wave in the crystal. To avoid side wall reflections, the diameter of the transducer needs to be somewhat smaller than the sample diameter (Fig. 4.3). These criteria have been obeyed.

4.5 Bonding Materials for High Temperature Velocity Measurements

To attach a transducer to a specimen, a bonding material is required so that the acoustic energy generated by the quartz transducer can be coupled into the specimen.

The following two bonding materials have been used:

i) Dow Resin 276-V9 (Dow-Corning Corp) which is used particularly for ultrasonic velocities measurements at room temperature. With this bonding material, a good echo train can be produced for the longitudinal mode up to 350°C

ii) Du Pont Thick Film Conductor Composition 9770 (Du Pont UK Ltd) is usually employed for coupling of both shear and longitudinal waves for high temperature measurements. Before bonding, the specimen and transducer faces are freed from grease and dirt by washing them with acetone. A suitable quantity of bonding agent is then put onto the surface of the specimen: the transducer is then placed on this bond and gently rotated. By this rotation

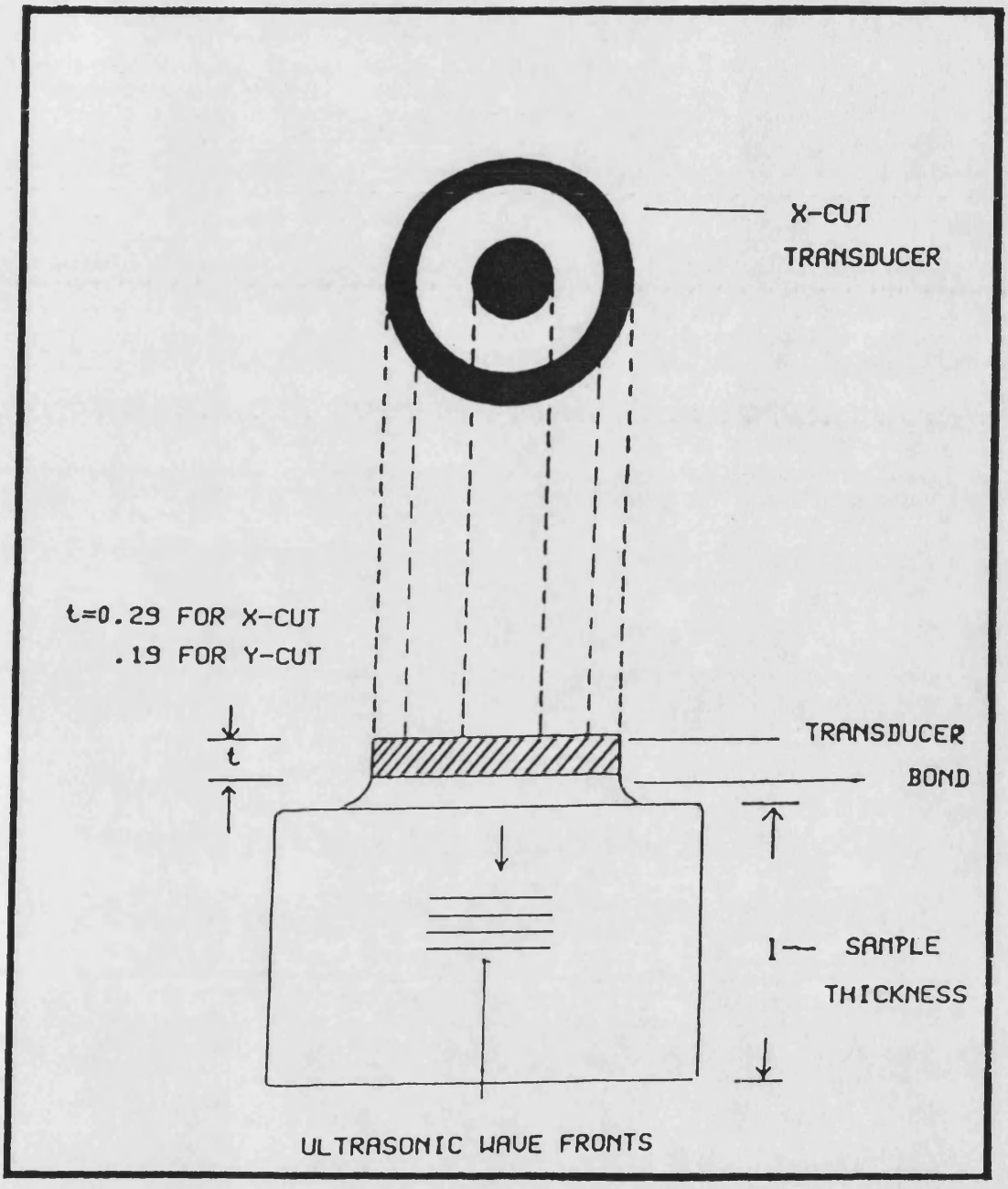

Fig.4.3 SCHEMATIC REPRESENTATION OF SPECIMEN AND QUARTZ TRANSDUCER WITH GOLD PLATED ELECTRODES.

a uniform and thin bond to about 3 μm can be produced (Fig.4.3). It is desirable to obtain a thin and uniform layer of bonding agent that adheres to both transducer and specimen and gives a clear, large amplitude and exponential echo train over a wide temperature range. For an X-cut transducer, a bond of this material can produce a reasonably good echo train at room temperature without heating. However to propagate a shear wave through a crystal, the bond needs to be dry; to ensure this, the orientation of the transducer is first determined by Dow-resin 276-V9 and then reattached with the Dupont material. The specimen is then put into a sample holder and transferred to a furnace (see sections 4.7). The temperature of the furnace is gradually increased to about 90°C and then left for 12 hours before it is brought back to room temperature. The sample is now ready for the ultrasonic wave velocity measurements.

Both bonding agents are stable and resisted erosion when immersed in the silicone fluid used in hydrostatic pressure experiments. After the completion of the experiment the transducer is removed by immersing the specimen into a small quantity of acetone for about 10 minute to dissolve the bond.

4.6 The Pulse Echo Overlap Technique.

Fig 4.4 shows the block diagram of the pulse echo overlap technique employed here. The details of the circuit connections and the electronic networks are not

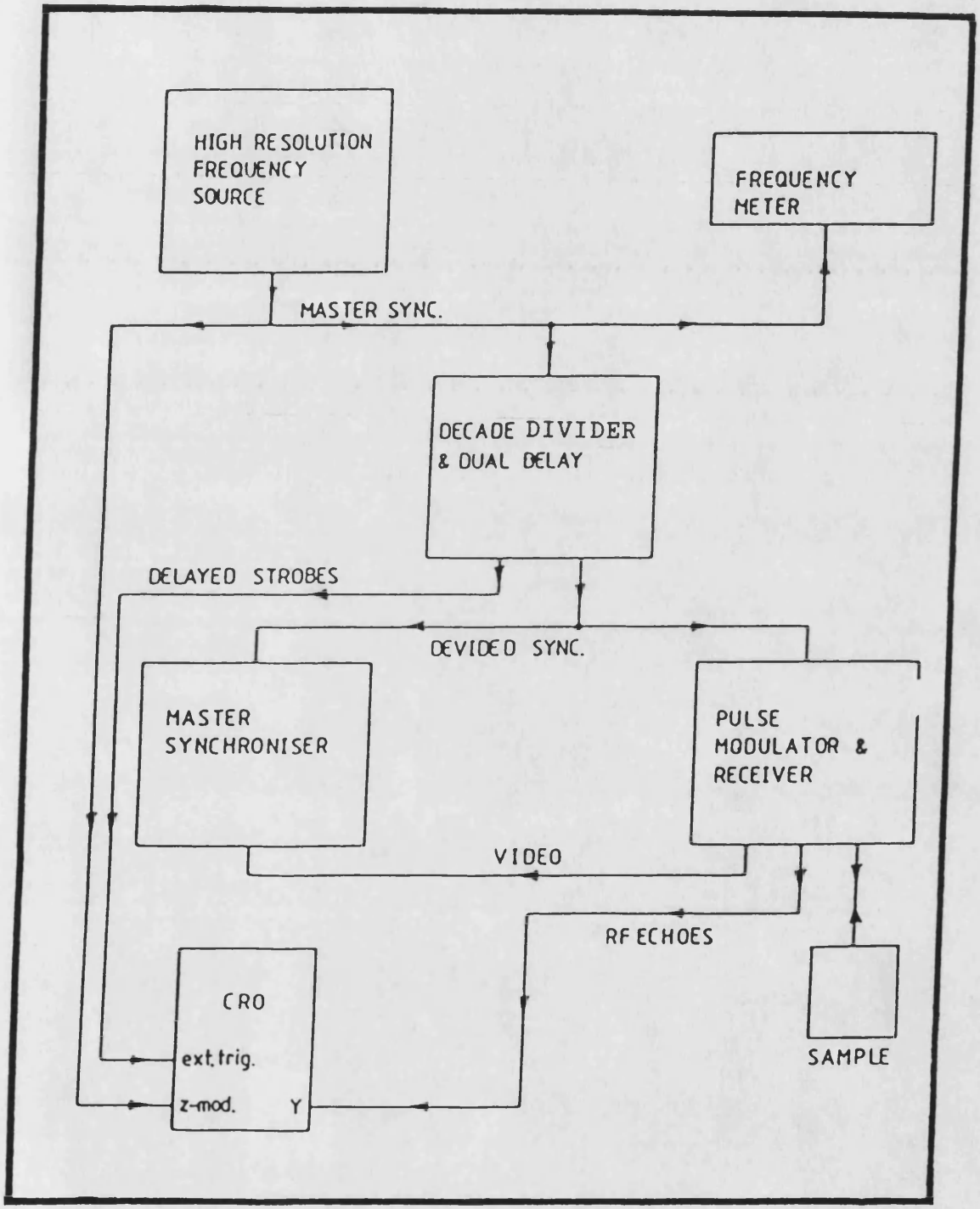

Fig.4.4 BLOCK DIAGRAM OF PULSE ECHO OVERLAP APPARATUS.

discussed here but the function of each component (Fig 4.5) is. The pulse echo unit consists of a radio frequency (r.f.) pulse generator (Matec 6600) which generates the 10MHz r.f. pulse. The repetition rate of this pulse is controlled by a master synchroniser (Matec 122A). This master synchroniser produces a trigger source (in this case it is a square wave) with a frequency similar to the frequency of the sine wave produced by a signal generator (Matec 110). The frequency of the square wave is reduced by dividing by a factor of 10 and is used to trigger the pulse generator. With this triggering process only the pulse with this final repetition frequency will propagate into the crystal. Each triggered pulse consists of an r.f. burst which is in turn transformed by the quartz transducer into a mechanical vibration within the crystal.

After a series of reflections within the crystal, the successive echoes are detected by the transducer and amplified by a receiver. The r.f. echoes are displayed on the oscilloscope in their entirety (Fig 4.6). The Matec 122A also functions as a double delay strobe generator ie to generate two square wave pulses when linked to Z-mode of an oscilloscope it intensifies any two echoes of the same echo train. The intensity of the oscilloscope is then reduced until only these two intensified echoes are observed on the screen. The oscilloscope is then triggered with the master synchroniser at a rate equivalent to the delay between the chosen echoes, and

Fig.4.5 PULSE ECHO ULTRASONIC APPARATUS

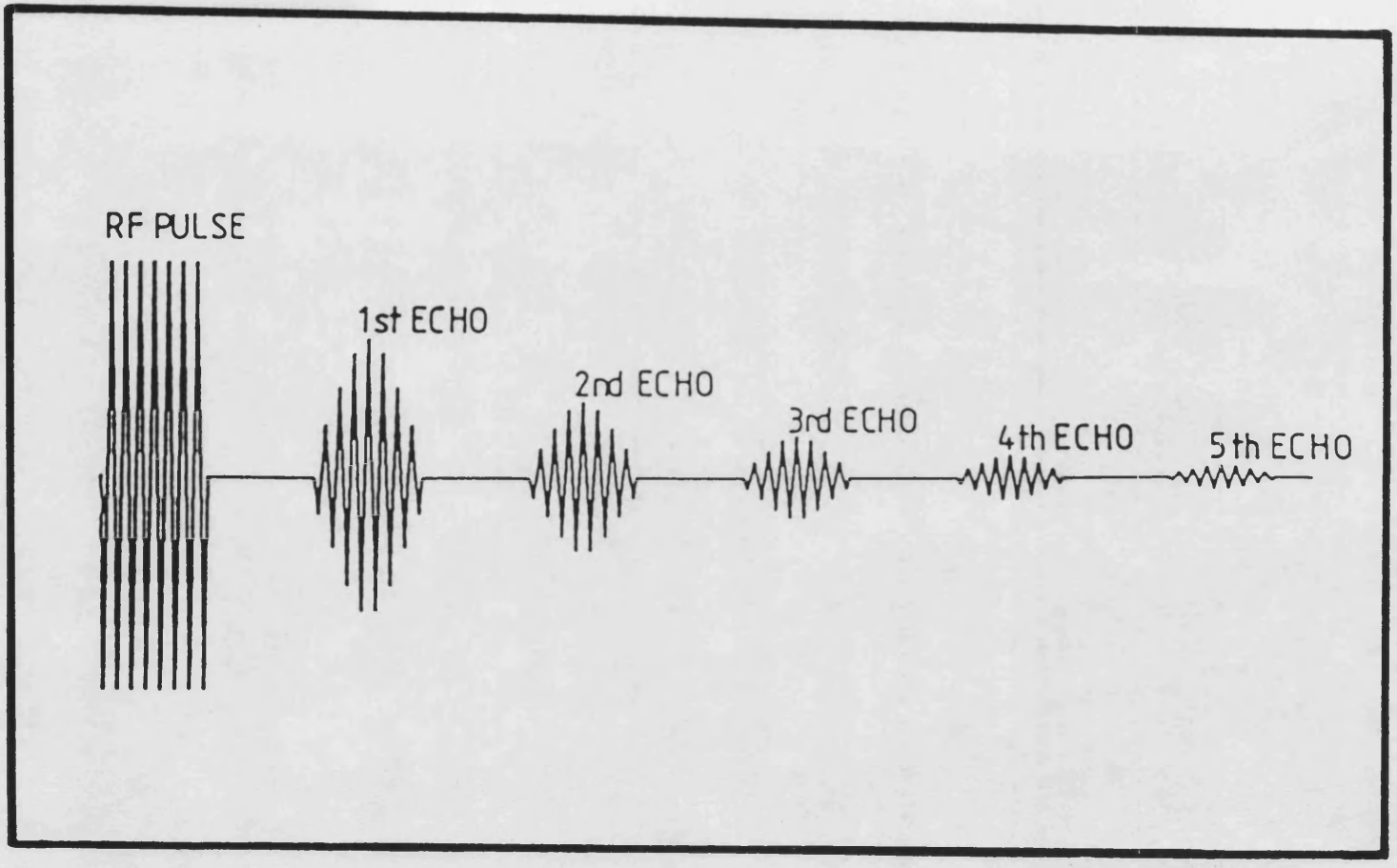

Fig.4.6 ECHO TRAIN AS SEEN ON THE OSCILLOSCOPE FROM A SINGLE PULSE.

the intensified echoes can now be overlapped and visualised. By fine adjustment of the master synchroniser frequency, cycle-to-cycle matching can be achieved. The waveforms associated with this operation are illustrated in Fig 4.7.

4.7 High Temperature Ultrasonic Wave Velocity Measurements.

The temperature dependences of the second order elastic stiffness constants measurements for MnNi and MnNiC alloys have been measured up to and through their Nêel temperatures (above about 50°C) by means of a suitable high temperature sample holder located in a electrically heated furnace (Fig 4.8b).

A brass sample holder (Fig 4.8a) which can sustain temperature up to 400°C has been constructed for this work. It is mounted on one end of an aluminium tube of 45cm length and 1cm in diameter. A spring is attached to the sample holder so that the gap where the specimen is to be placed can be varied according to the specimen thickness. To the opposite end of the aluminium tube is attached a cylindrical brass support 2cm thick and 2.5cm in diameter used to hold an r.f. socket. Inside the aluminium tube two identical ceramic pipes run parallel from the brass support to the sample holder: one is to lead a thermocouple wire from specimen to a digital thermometer for recording temperature of the sample and the other holds the r.f. wire used to transmit and

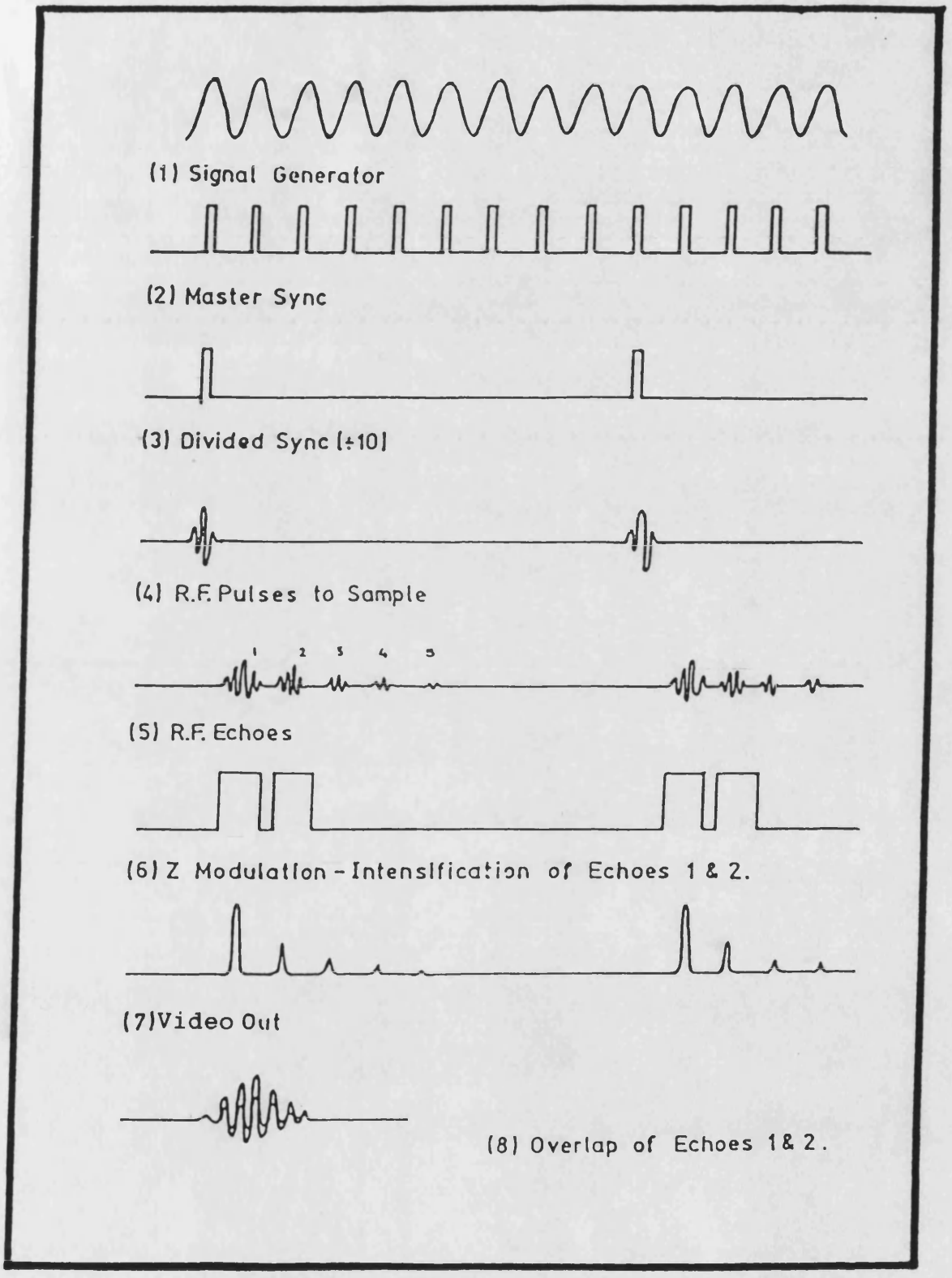

Fig. 4.7 PULSE ECHO OVERLAP WAVEFORMS

receive r.f pulses. The two ceramic pipes have also been used to protect both the r.f. wire and thermocouple wire from damage and to insulate them.

A stainless steel cylinder of 0.75cm thick and closed at on end is introduced into the furnace to reduce temperature fluctuation. After the sample has been inserted into the holder and connected to the pulse echo system, it is then transferred into this steel cylinder (Fig 4.8b): a variac is employed for supplying a suitable current to the furnace. By varying the output voltage from the variac the desired temperature of the specimen can be obtained at the required rate of heating. The specimen temperature is recorded by a digitron digital thermometer having an accuracy of 0.1°C. The schematic diagram of the apparatus used for the temperature dependences of the SOEC experiments is shown in Fig.4.9.

Fig.4.8a

HIGH TEMPERATURE

SAMPLE HOLDER

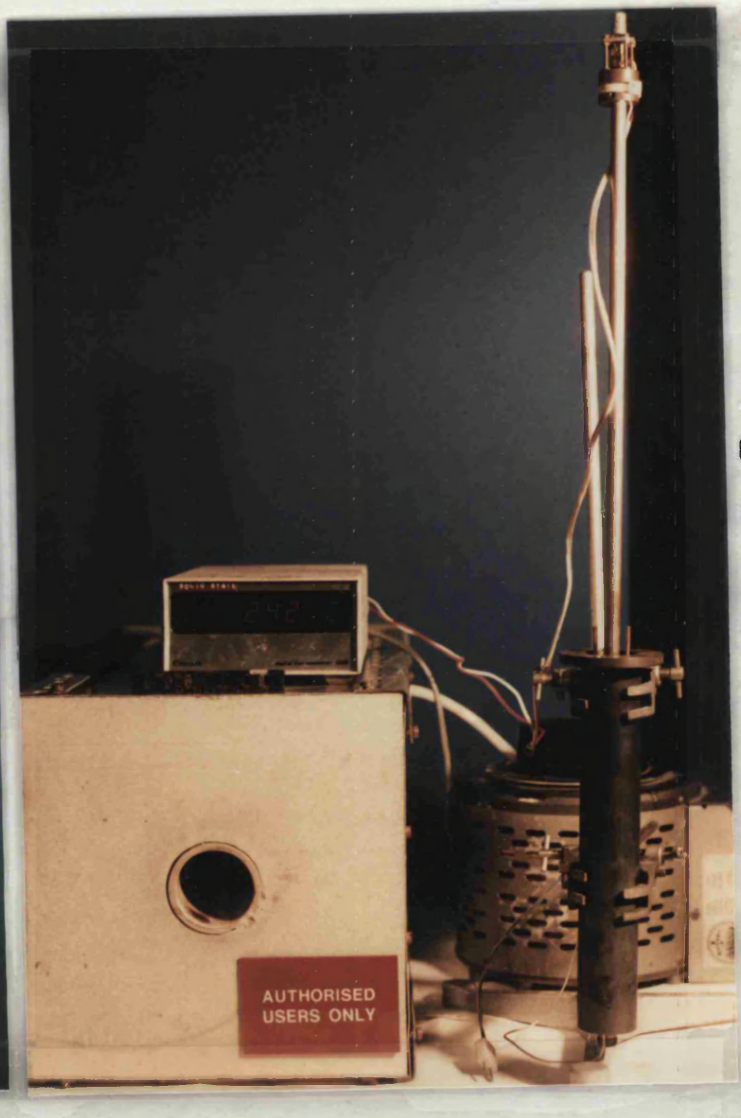

Fig.4.8b

COMPONENTS FOR TEMPERATURE

DEPENDENCES OF THE

SOEC EXPERIMENTS

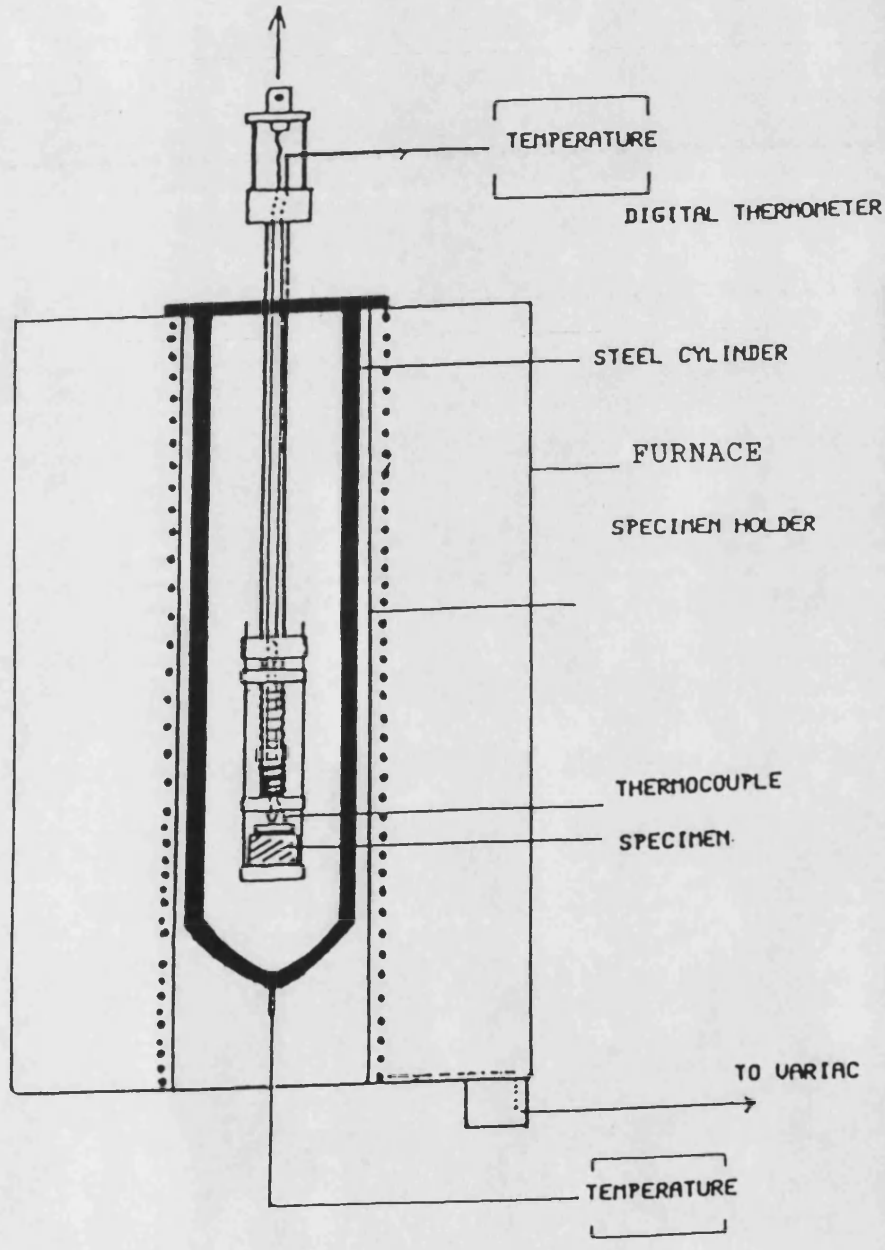

Fig.4.9 SCHEMATIC REPRESENTATION OF THE APPARATUS USED FOR THE HIGHER TEMPERATURE EXPERIMENTS OF THE SOEC.

4.8 Hydrostatic Pressure System

The hydrostatic pressure system employed in this work has already been described in detail by Yogurtcu (1980) and Brassington (1982). With this system a pressure up to 10Kbar can be generated. It consists of a metal cylinder made of EN26 nickel alloy carbon steel (the specifications are given in Table 4.1) having dimensions 115mm high and 127mm in diameter. A bore of 25.4mm in diameter is made along the axis of the cylinder. Two pistons of the same material as the cylinder are inserted from opposite sides of the bore (Fig 4.10) so that they can move in opposite directions to each other. The lower piston is fixed while the upper piston is allowed to move freely (Fig 4.11).

To prevent any leakage from the cavity between the two pistons at high pressure, a PTFE ring and a neoprene O-ring are attached to the leading section of each piston. The maximum operating temperature of these rings is 200°C. The cavity between these two pistons is filled with fluid which acts as the pressure transmitting medium. Several different fluids have been employed in this work:

i) Castor oil for pressures less than 3kbar,

ii) Plexol-244 oil for higher pressures (from 3 Kbar to 10 Kbar) and

iii) Silicone fluid (Dow Corning 200/1000 CS produced by Dow Corning Coop. Michigan USA) for combined higher pressures and temperatures. Unlike Castor oil and

TABLE 4.1 SPECIFICATION OF EN26 NICKEL CARBON STEEL

Principal Alloying Elements (%)

C	Si	Mn	Ni	Cr	Mo	UTS
0.26-0.44	0.10-0.35	0.4-0.7	2.3-2.8	0.5-0.8	0.4-0.7	1.2 GPa

Young's Modulus 195 GPa.

Linear Thermal Expansion Coefficient 12-13 x 10^{-6} $^{o}C^{-1}$

Fig.4.10 PISTON-CYLINDER HYDROSTATIC PRESSURE CELL AND ITS COMPONENTS

Plexol-244 oil, silicone fluid has a higher boiling point and does not contain carbon molecules; the other oils cause a black stain on the cylinder and the pistons.

There are several conical holes through the upper piston. These holes are filled with beryllium copper plugs insulated with ceramic to avoid any metal contact between the plugs and the sample holder. On top of the upper piston is mounted a sample holder and a manganin coil resistance. The resistance of this coil is used as a gauge to measure the hydrostatic pressure exerted on the sample (Fig 4.11). To avoid any damage caused by the fluid at high temperature, PTFE covered thermocouples and wires are employed. The electrical connections for the manganin coil resistance, thermocouple and r.f. wire from the sample holder to their respective meters and the pulse echo system are made through the beryllium copper plugs. All the electrical connections to the beryllium copper plugs are made with a high temperature soldering material. The external pressure is exerted by a 50 tons hydraulic press made by Bishop Lifting Services, Bristol, England. For safety reasons the pressure cell and the press are enclosed in a 6mm steel cabinet having a dimension 82mm x 79mm x 32mm; the door of the cabinet is always locked shut whenever the pressure unit is in operation.

The quality of the transducer-specimen bond and leakage at the seal are examined by gradually increasing the pressure to the maximum required and holding it for

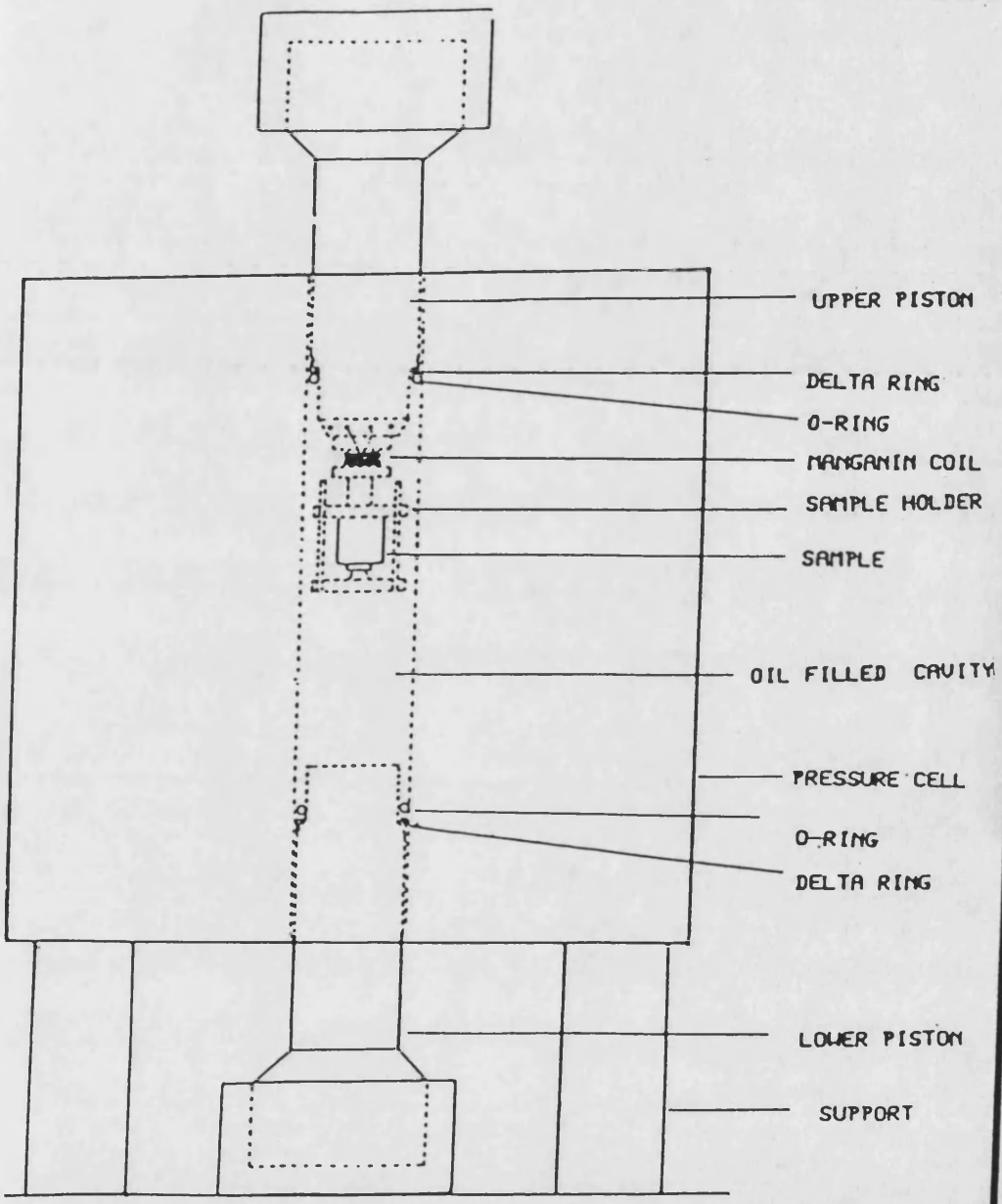

Fig.4.11 SCHEMATIC DIAGRAM OF HYDROSTATIC PRESSURE CELL.(WITH ELECTRICAL CONNECTIONS)

30 minutes. Any leakage can be detected from the external pressure gauge. The pressure is then released and the system is left for 30 minutes to regain thermal equilibrium. This hydrostatic pressure system is now ready for data acquisition.

When the pressure is changed, the temperature inside the cavity alters: an increase in applied pressure by 0.1-0.2kbar results in a significant increase (1^{o}) in temperature. A period of approximately ten minutes is required to allow the cell to return to its thermal equilibrium temperature before ultrasonic measurements can be made.

4.9 Techniques Used to Make Hydrostatic Pressure Measurements of Ultrasonic Wave Velocities at High Temperatures.

The pressure cylinder, which is made of EN26 Nickel Alloy Carbon Steel, has been used up to approximately 180°C. At a higher temperature ($\backsim$ 200°C) this steel undergoes a phase transition which can weaken it. The basic set-up used for the high temperature measurements is similar to that used at room temperature described in section 4.8. Sound velocity pressure dependences of all the three modes of propagation along the [110] direction of Mn-Ni and Mn-Ni-C alloys are first measured at room temperature. The temperature of the cylinder is then increased gradually in steps of

approximately 20°C . This is done by using a temperature controller (Eurotherm Ether type 17-19B) connected to a cylindrical heating element which is tightly clamped around the external wall of the pressure cylinder [Fig 4.12(b)]. A NiCr/NiAl thermocouple is inserted between the external wall of the cylinder and the heating element and used to sense the temperature. If the temperature recorded by the thermocouple is lower than the preset value, the controller will supply current to the heater until the cylinder reaches the preset temperature. When the cylinder cavity reaches the temperature required, the current from the controller is reduced automatically since only the heat losses need to be overcome. Fig 4.13 shows the schematic diagram of the temperature controller for experiments made at elevated temperatures. The temperature of the external wall of the cylinder is held steady to within a few degrees Celsius by this control system but the temperature oscillates about 3°C throughout an experiment. Due to the thermal mass of the cylinder, the oscillation amplitude within the centre of the cell is reduced to about 0.3°C. The temperature oscillations within the centre of the cylinder have to be reduced as far as possible because the ultrasonic wave velocity and hence the echo transit time is sensitive to temperature changes of 0.3°C. The temperature of the internal cell is a few degrees lower than the external value and is empirically related to the preset temperature by:

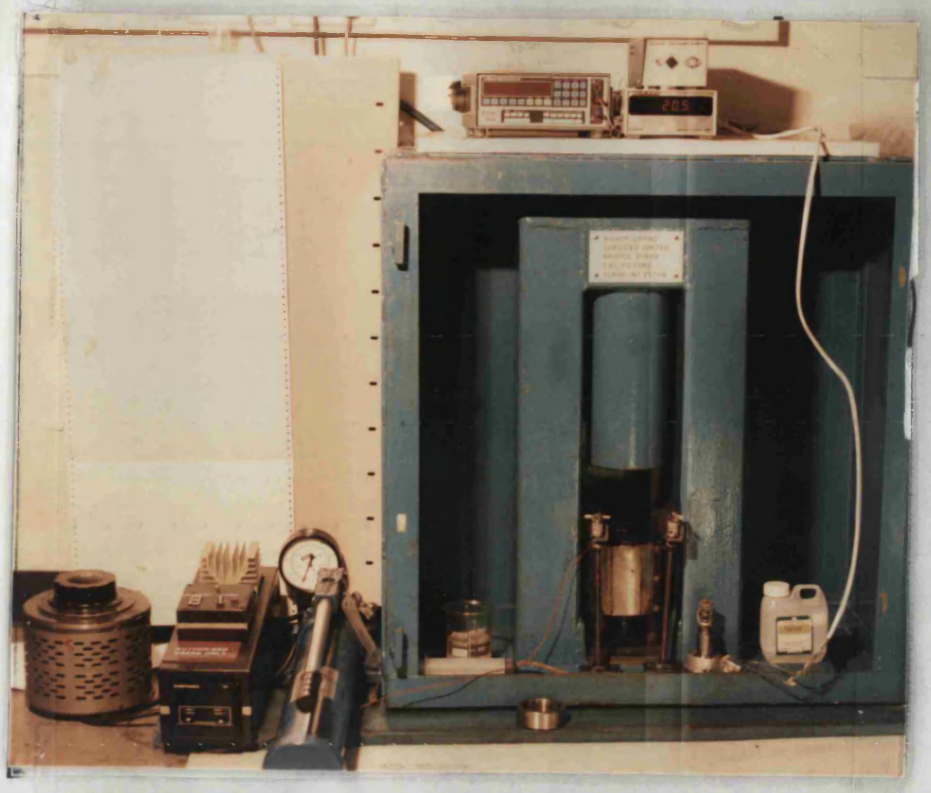

50 TON HYDRAULIC PRESS CELL ASSEMBLY WITH TEMPERATURE CONTROLLER FOR ELEVATED TEMPERATURE

Fig.4.12a

Fig.4.12b CLOSE-UP OF THE HYDROSTATIC PRESSURE CELL

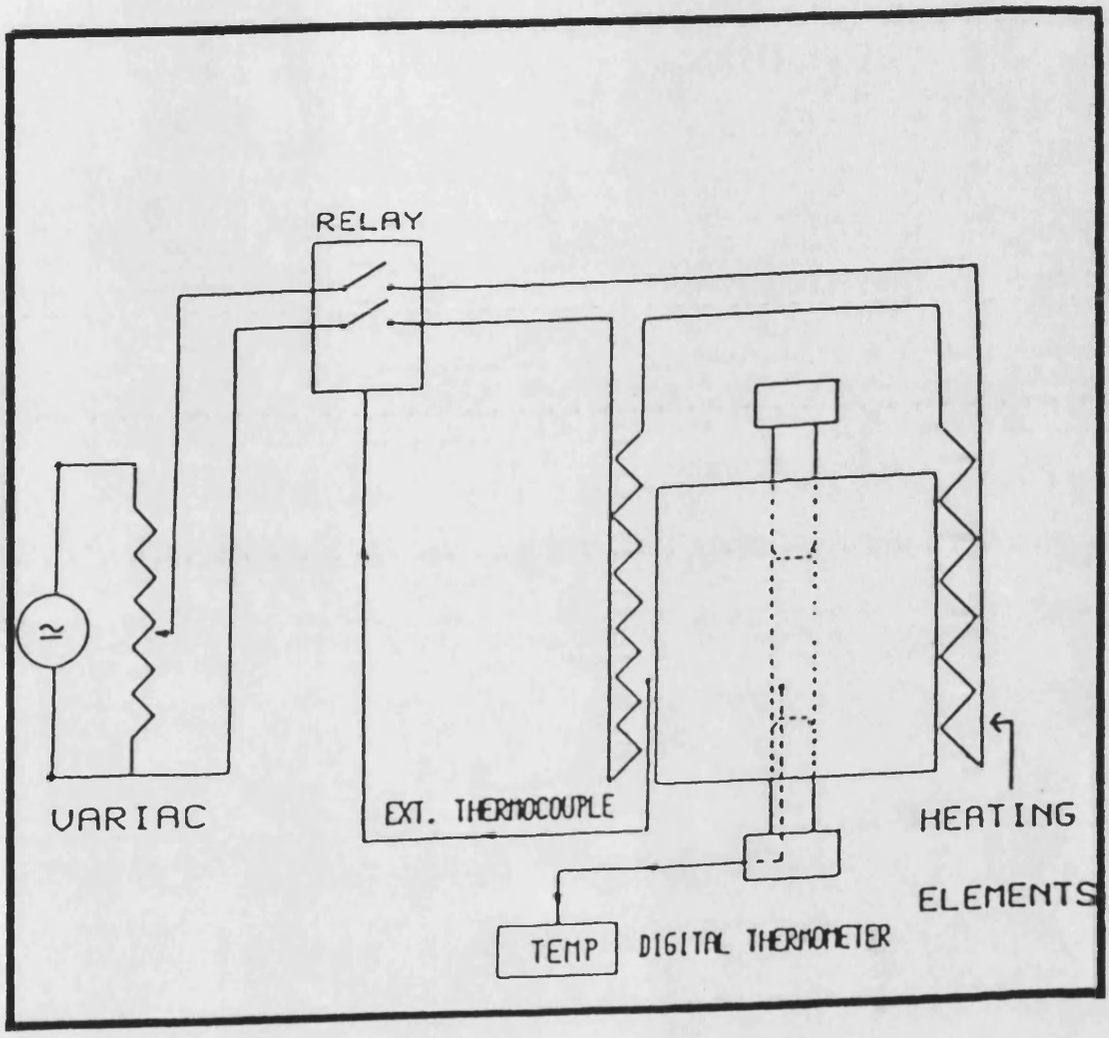

Fig.4.13 TEMPERATURE CONTROLLER OF HYDROSTATIC PRESSURE CELL FOR ELEVATED TEMPERATURES.

$$T_i = 0.9T_e + 1.3 \qquad (4.2)$$

where T_i is the temperature inside the cavity and T_e is the temperature of the external wall. The calibration curve is shown in Fig.4.14: this is useful for setting the temperature at which the measurements are to be made.

4.10 Manganin Coil as a Pressure Gauge

Manganin is a Cu-Mn-Ni alloy which is used in high pressure experiments as a pressure gauge to allow accurate and continuous pressure measurements up to about 100kbar at both room and elevated temperatures (Samara and Giardini 1964). The principle of its operation is based on the nearly linear dependence of resistance of manganin on pressure (Bridgman 1911). The electrical resistivity of this alloy is highly sensitive to pressure but less sensitive to temperature. Its use to measure hydrostatic pressure depends on the fact that application of a small pressure can produce a measurable change in the resistance of a manganin wire gauge; as an example, for an applied pressure of 0.1kbar the resistance changes by about 0.04%. The gauge is particularly useful in piston-cylinder, multianvil and other relatively large volume pressure apparatus. The gauge used here consists of 0.1mm diameter manganin wire wound non-inductively on a pyrophyllite core. Pyrophyllite is a soft natural

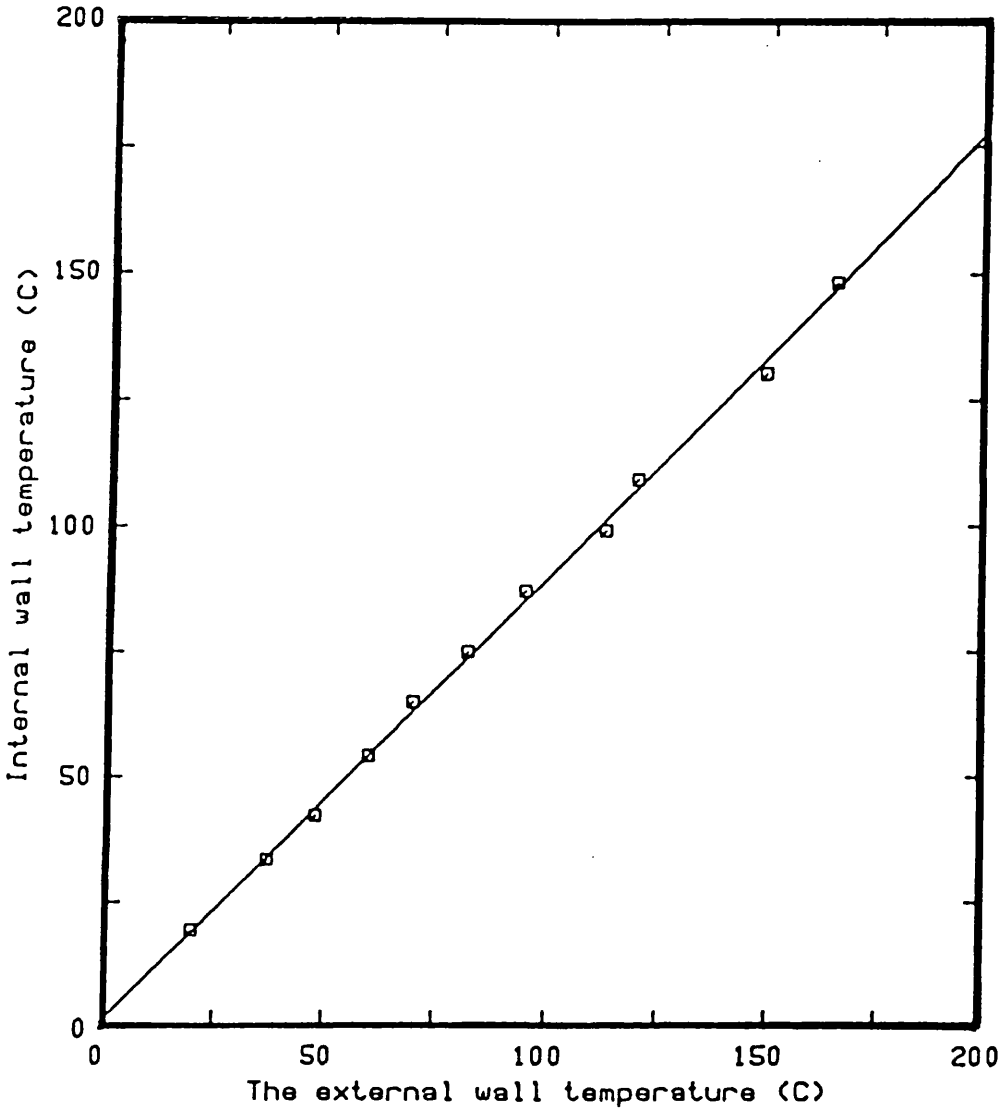

Fig.4.14 THE TEMPERATURE RELATION BETWEEN THE EXTERNAL AND THE INTERNAL WALLS OF THE PRESSURE CYLINDER.

material which after heat treatment is transformed into a hard ceramic-like substance with good insulating properties. Each manganin gauge is put through a Bridgman cycle of pressure-temperature seasoning before it is used; the coil is heated to about 200°C for several hours followed by quenching in liquid nitrogen. This process is repeated several times before the final seasoning by pressurising the gauge to the highest operating pressure (3kbar) for several hours. The thermal treatment eliminates localised strain regions and hence improves uniformity, while the pressure treatment stabilises the pressure coefficient of resistance (Bridgman 1911).

The pressure coefficient of resistance used to obtain the hydrostatic pressure in these experiments is $2.4X10^{-3}$ $kbar^{-1}$ (Samara and Giardini 1964), thus the pressure P inside the cell is given by:

$$P = (\Delta R/R_{atm})/2.4x10^{-3} \text{ kbar} \qquad (4.3)$$

where $\Delta R/R_{atm}$ is equal to $(R_P - R_{atm})/ R_{atm}$ and R_P and R_{atm} are resistances at pressure P and atmospheric pressure respectively. The typical resistance of a gauge at atmospheric pressure is about 100 to 120 Ohms. Using a digital multimeter, resistance is measured with a sensitivity of 1 part in 10^{-5} ohm which in turn leads to the measurement of hydrostatic pressure to a sensitivity of 0.5%.

4.11 Experimental Errors and Corrections.

The precision to which the hydrostatic pressure and the SOEC can be determined depends predominantly on the accuracy to which basic quantities such as crystal density and its dimension can be estabilished. The errors of the density and sample thickness make a direct contributions to the error at the SOEC whilst the errors in the resistance measured on the manganin coil give a direct contribution to the error in the hydrostatic pressure. Some of these errors can be corrected (at least in part) and some can only be estimated.

4.11.a Measurements of Crystal Density and Thickness.

Crystal densities are needed to determine the SOEC. The densities have been measured using Archimedes' principle. The mass of the sample is measured with an accuracy 1 part in 10^4 whilst the density of water is taken from The International Bureau of Weight and Measures 1910. For this work the room temperature densities have been used for the measurements at at higher temperatures. Hausch (1977) and Honda et al.(1976) have measured the change in lattice spacing of Mn-18.5% Ni between 23°C to 250°C by x-ray method. They found a change of only 0.021A in 230°, which gives a 0.5% (0.001A) increase from the room temperature value of 3.695A. This change of 5 parts in 10^3 in lattice

parameter leads to a decrease in the density of 1.5%. Hence the use of the room temperature density, and the sample thickness, are reasonable approximations to use in the determination of the high temperature SOEC. It can be seen that the effects of increasing the sample thickness and decreasing the density on the elastic constant ($C_{ij} = \rho V^2$) serve to balance each other out. The net result is that the elastic constant is underestimated by about 0.5% between room temperature and the Neel temperature.

4.11.b Transit Time Errors.

The accuracy to which the time interval can be measured is limited by factors such as the quality of the bond and the transducer thickness. The time interval between successive echoes increases with transducer thickness. The accuracy can be improved if either a thin transducer or a long sample are used. These two prerequisites cannot be satisfactorily fulfilled since the samples used in this work are only several mm. thick and quartz transducers with higher fundamental frequencies than 10MHz are thin and are fragile. Acoustic impedances of both the sample ($\rho_1 V_1$) and the transducer ($\rho_2 V_2$) where ρ is density and V is sound velocity, are the characteristics that determine the amount of reflection of the ultrasonic wave at the sample-transducer interface. Due to the difference in the

densities and also the velocities of ultrasonic wave in both media, their acoustic impedances are different; this result in an acoustic impedance mismatch between the transducer and the sample. The internal reflections between the two parallel faces of the transducer lead to a considerable distortion of the pulse envelope which develops further with an increasing number of echoes (Kittinger 1977). Eventually the received echo will be delayed by a certain amount of time. Errors introduced by this effect in the measured echo transit time are particularly large for a sample having low acoustic impedance.

The reflection coefficient at the sample-quartz transducer interface can be defined by

$$r_{12} = (\rho_2 V_2 - \rho_1 V_1) / (\rho_2 V_2 + \rho_1 V_1) \qquad (4.4)$$

where $\rho_1 V_1$ is the acoustic impedance of the sample, and $\rho_2 V_2$ is the acoustic impedence of the transducer. This equation has been used by Kittinger (1977) to plot a curve of transit time error (in the unit of reciprocal fundamental transducer frequency) versus reflection coefficient for X-cut quartz transducers of various fundamental frequencies (Fig 4.15). From this curve Brassington (1982) generated an equation for transit time error as a function of reflection coefficient r_{12} of the following form:

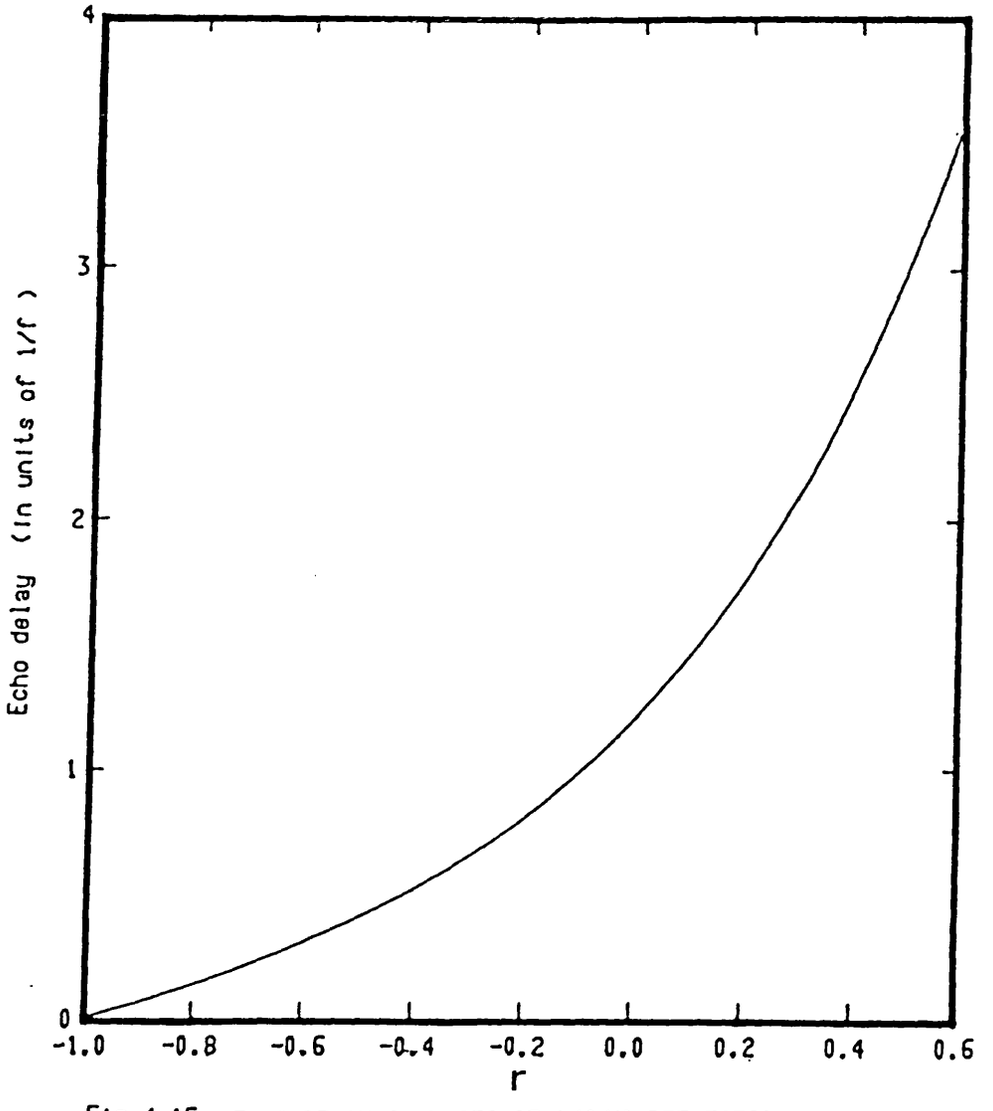

Fig.4.15 ECHO DELAY IN UNITS OF 1/f VS REFLECTION COEFFICIENT r AT THE SAMPLE-TRANSDUCER BOUNDARY (KITTINGER 1977)

$$t_c = [\ 0.1602 \exp(1.831\ (r_f + 1))]\ /f_c \qquad (4.5)$$

where r_f is the reflection coefficient of the sample-transducer boundary, and f_c is the carrier frequency (the resonance frequency of the transducer). Taking the acoustic impedances of the transducer for longitudinal and shear waves as $15.2 \times 10^{-6} Nm^{-1}s$ and $10.3 \times 10^{-6} Nm^{-1}s$ respectively, the transit time errors have been estimated, and by subtracting from the measured transit times (t), the amount of the corresponding transit time errors, corrections on the ultrasonic wave velocities have been made. This equation is found to represent well the results of Kittinger (1977) for $-0.6 < r_f > +0.6$. On this basis the transit time corrections obtained for our particular experimental results lie between -0.5% to +2.0%.

4.11.c Diffraction and Non-Parallelism.

Any non-parallelism of the transducer faces can cause interference in the echo pattern. This effect has been discussed by Taylor and Pointon (1969) on the basis of the piezeoelectric properties of the transducer: the reflected ultrasonic wave front (from the transducer-specimen interface) when it returns to the free face of the transducer, will in general, be at an angle to this free end surface. Thus as the wave is reflected to and fro between the slightly non-parallel

end faces of a transducer, the angle of incidence of the wavefront increases and the echo pattern envelope exhibits a number of maximum and minimum. Thus to avoid this effect and obtain an exponential echo train, the end of the quartz transducer faces must be polished flat to about one-fifth of the wavelength at the resonance frequency of the quartz transducer and must be parallel to within only a few seconds of arc.

When this ultrasonic energy reaches the sample, the beam, which is being diverged by the diffraction field in the transducer can eventually touch the side walls of the sample and then be reflected from this side wall and returned to the main beam. There is always some mode conversion at the side walls which produce intermediate echoes. Truell et al.(1969) have suggested that when the ulrasonic waves are propagated along two- or four-fold crystallographic symmetry directions of a specimen, the transit time errors due to diffraction are of the order of 0.01%, provided that the misalignment of the crystal orientation is not more than 0.5° and the area of the transducer is smaller than the area of the sample.

4.11.d Errors in Temperature Fluctuations.

From the measurements of the pulse echo overlapping frequency as a function of temperature it can be seen that a change by 0.3°C in specimen temperature will lead to the significant change in the ultrasonic

wave velocity. Since this frequency is the major factor in the measurement of the SOEC (and the density and thickness changes are negligible), a constant temperature is required for accurate measurement of ultrasonic wave velocities and their pressure derivatives. In these experiments the temperature of the sample is recorded by a thermocouple in contact with it. The dimensions of the sample are normally much larger than the dimensions of the thermocouple; therefore for temperature dependences of elastic constant experiments, the overlapping frequency at a particular temperature is taken at a time long enough for the sample and thermocouple junction to have reached the same equilibrium temperatures. In pressure work, when external stress is applied to the sample, due to friction and energy convertion, heat is generated inside the cell of the cylinder and temperature of the cell increases. Data acquisition can only be carried out when the system has returned to its equilibrium temperature.

CHAPTER 5

HYDROSTATIC PRESSURE MEASUREMENTS OF SECOND ORDER ELASTIC STIFFNESS CONSTANTS AND VIBRATIONAL ANHARMONICITY OF URANIUM NITRIDE

5.1 Introduction

This chapter presents the experimental results of the second order elastic stiffness constants and their hydrostatic pressure derivatives for single crystal uranium nitride (UN). These measurements of the second order elastic stiffness constants at room temperature under hydrostatic pressure lead to further understanding of the elastic behaviour of UN: knowledge of the elastic constants and their hydrostatic pressure derivatives enable the Gruneisen parameters of the acoustic modes in the long wavelength limit to be calculated. The compression of UN has been determined using the Murnaghan equation-of-state and the results are compared with those of alkali halides and group IV-VI compounds. The results have shed some light on the problem of the interatomic binding forces in uranium compounds.

5.2 Physical Properties of UN

The actinide compound uranium nitride (UN) crystallizes in the f.c.c. rocksalt structure with a lattice constant of 4.89A (Muromura and Tagawa 1979). Below

the Néel temperature it is antiferromagnetic of a group I configuration (Fig 5.1) with a Néel temperature (T_N) of 53.1±0.2K (Muromura and Tagawa 1979). The pressure dependence of the Néel temperature of UN is given in Fig.5.2. It was observed that T_N decreased rapidly under pressure in the manner expected for a band antiferromagnetic (Fournier et al.1979). In UN, and related compounds, both 6d and 5f electrons are involved in chemical bonding leading to mixed-ionic covalent (or perhaps metal-like binding). At the Néel temperature there is a small distortion from f.c.c. to face centred tetragonal giving c/a as 0.99935 at 4K (van Doorn et al.1977). The temperature dependences of the SOEC of UN have been measured by earlier workers (van Doorn et al.1977 and Yoshizawa 1985). These measurements showed that, in the vicinity of T_N, all the elastic stiffness constants exhibited steplike discontinuities which are reminiscent of those which can occur at a structural phase transition (Fig 5.3). van Doorn et al.(1977) have measured all the three vibrational mode velocities in the [110] direction but could not obtain a complete curve for the temperature dependence of the shear mode $(C_{11}-C_{12})/2$ (Fig 5.3). This problem has been overcome by Yoshizawa et al.(1985) who also measured all the three mode velocities in the [110] direction in UN from room temperature to approximately 4K, and observed a pronounced attenuation for the [1$\underline{1}$0] mode at T=180K. For the [110] longitudinal mode there is simultaneous occurrence of large

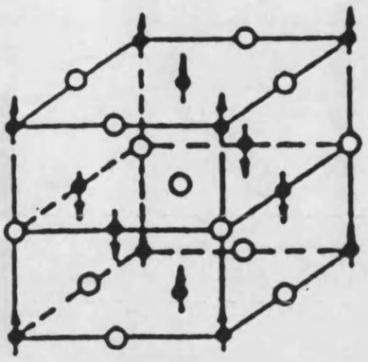

AFM-I

Fig 5.1 Types of magnetic ordering in NaCl-type actinide compound. Full circle: magnetic actinide ion. Empty circle: anion. Arrow: average direction of magnetic moment.

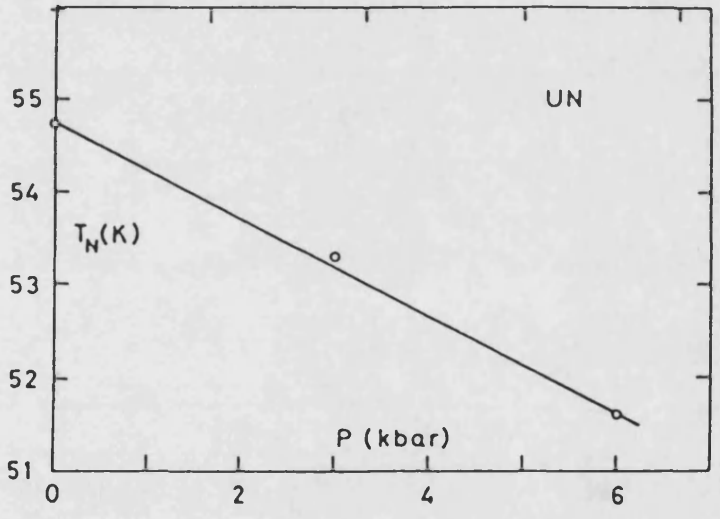

Fig 5.2 Pressure dependences of Néel Temperature (bottom and left scales, full line) of UN (Marples et al. 1975)

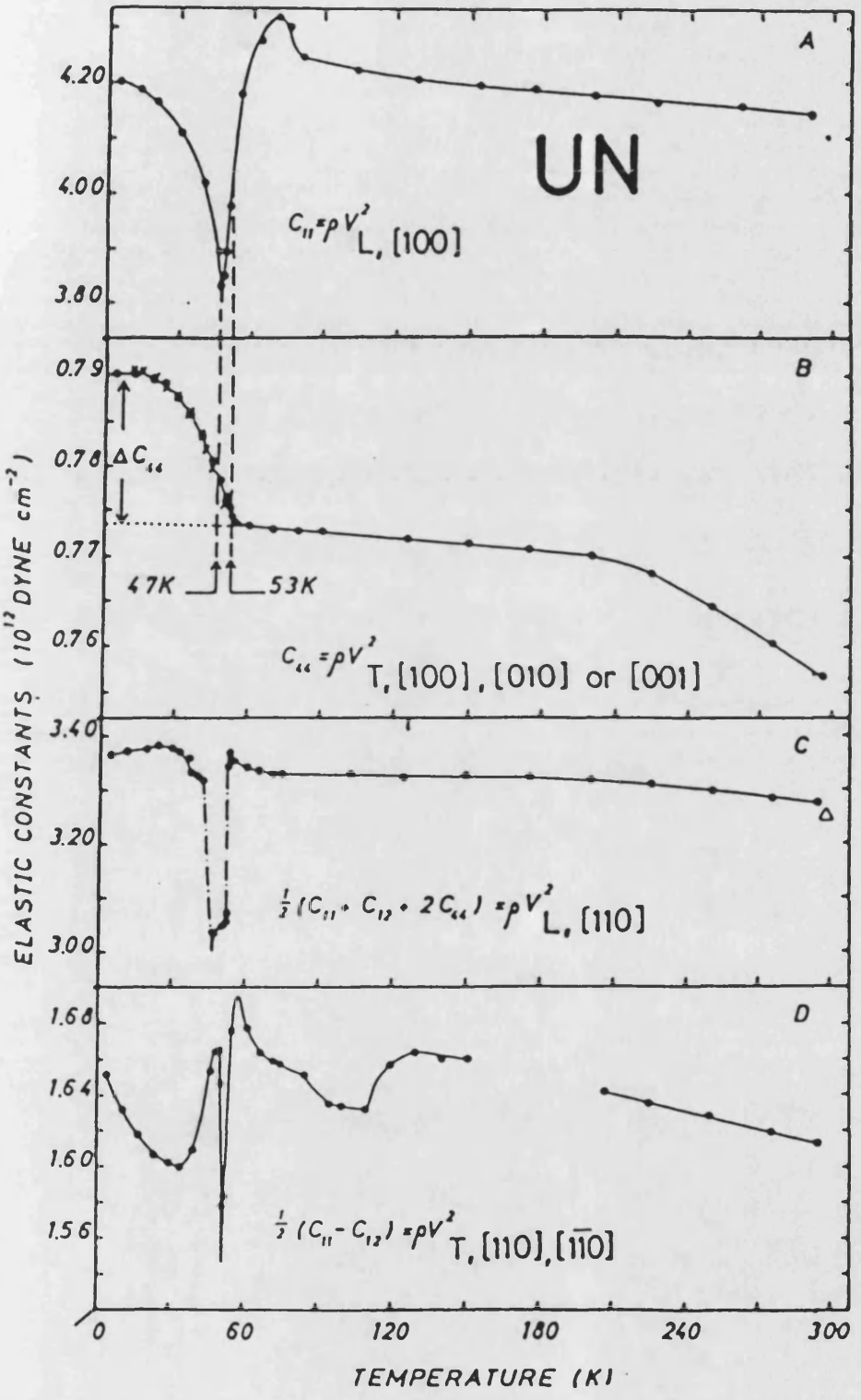

Figure 5.3 A, B, C, D: Different combinations of elastic constants C_{IJ} as measured by the transverse (T) or longitudinal (L) sound velocities V, in certain crystallographic direction (subscripts [klm]) vs temperature T of single crystal UN.

(after van Doorn and du Plessis (1977))

attenuation and large velocity changes just below T_N.

5.3 Experimental Procedure

Ultrasonic wave velocities have been measured by the ultrasonic pulse echo overlap technique at room temperature on a single crystal specimen having a pair of (110) faces polished flat and parallel to better than 1 part in 10^4. To establish the hydrostatic pressure dependence of the ultrasonic wave velocities, measurements have been made for pressures up to about $2x10^8$Pa in the piston and cylinder apparatus using Plexol 201 as the pressure transmitting medium.

5.4 Experimental Results

The elastic stiffness constants obtained from these measurements are in reasonable agreement with those measured previously (van Doorn and du Plessis 1977, Yoshizawa et al.1985). The SOEC of UN are much greater than those of alkali halides [for NaCl C_{11}^S = 4.93, C_{12}^S = 1.3, C_{44}^S = 1.28, C'^S = 1.82 and bulk modulus B_o^S = 2.51 in units of $10^{10}Nm^{-2}$ (Hart 1968)], the mixed covalent-ionic bonded lead and tin chalcogenide [for PbTe C_{11}^S = 10.53, C_{12}^S = 0.72, C_{44}^S = 1.322 , C' = 4.91, B_o^S = 3.976 in units of $10^{10}Nm^{-2}$ (Miller et al.1981)], or even for the rare earth chalcogenide SmS, which like UN contains a strong element of d- and f-binding [C_{11}^S = 12.7, C_{12}^S = 1.2, C_{44}^S = 2.69, C' = 5.75, B_o^S = 5.03 in units of $10^{10}Nm^{-2}$ (Tu Hailing et al.1984)], refer also to

Table 5.1. Since the SOEC of a solid are a measure of the samples' resistance to strain, which is in turn related to the bond strength, large values of the SOEC indicate that the interatomic bonding forces in UN are particularly strong. In common with that of other rocksalt-structure crystals, C_{11}, which includes large contributions from the nearest-neighbour forces, is several times larger than C_{44}. For nearly ideal ionic crystals (such as NaCl) the forces are central so that the Cauchy relation ($C_{12}=C_{44}$) holds. The deviation, traditionally associated with covalency or a metal-like binding, using this relation, is not particularly large in the case of UN.

The acoustic mode velocities, found by solution of Christoffel equations (equation 3.36) are plotted as a function of mode propagation direction in Fig 5.4. These provide a visual indication of the anisotropy of the elastic properties of UN.

5.5 Hydrostatic Pressure Derivatives of the SOEC of UN.

To study the vibrational anharmonicity in this mixed ionic-covalent bonded solid, the pressure dependences of the elastic stiffness constants of UN have been measured. The velocities of the longitudinal and the two shear modes that are polarized in the [001] and the [1$\bar{1}$0] directions and propagated in the [110] direction are found to be linearly dependent upon the applied hydrostatic pressure (up to about 2×10^8Pa). The

Table 5.1 The second order elastic stiffness constants (SOEC) of single crystal UN at 290K in comparison with NaCl, PbTe and SmS.

	UN	NaCl•	PbTe••	SmS•••
Density ϱ_0 (kg m^{-3})	14 333			
Lattice parameter a_0 ($\times 10^{-10}$ m)	4.89			
Elastic stiffness constants				
C_{11} ($\times 10^{10}$ Nm^{-2})	42.39 ± 0.06	4.93	10.53	12.7
C_{12}	9.81 ± 0.09	1.30.	0.70	1.2
C_{44}	7.57 ± 0.02	1.28	1.322	2.69
C' [$=\frac{1}{2}(C_{11} - C_{12})$]	16.29 ± 0.01	1.82	4.91	5.75
Anisotropy ratio C'/C_{44}	2.15			
Bulk modulus B^S ($\times 10^{10}$ Nm^{-2})	20.67 ± 0.08	2.51	3.976	5.03
Volume compressibility χ^S ($\times 10^{-12}$ m^2 N^{-1})	4.82 ± 0.02			
Linear compressibility ($\times 10^{12}$ m^2 N^{-1})	1.61			
Elastic compliance constants				
S_{11} ($\times 10^{-12}$ m^2 N^{-1})	2.34			
S_{12}	−0.72			
S_{44}	1.32			

• HART (1968)
••MILLER, SAUNDERS and YOGURTCU (1981)
•••Tu HAILING, SAUNDERS and BACH (1984)

Table 5.2 The hydrostatic pressure derivatives of the SOEC and bulk modulus of UN at room temperature (290K) and atmospheric pressure.

$\partial C_{11}/\partial P$	9.97 ± 0.11
$\partial C_{12}/\partial P$	3.81 ± 0.14
$\partial C_{44}/\partial P$	−(0.74 ± 0.05)
$\partial C'/\partial P$	3.08 ± 0.25
$\partial B/\partial P$	5.86 ± 0.13
B_{11}	11.35
B_{12}	2.90
B_{44}	0.33
$C_{111} + 2C_{112}$	-72.3×10^{11} Nm^{-2}
$C_{123} + 2C_{112}$	-53.9×10^{11} Nm^{-2}
$C_{144} + 2C_{166}$	-2.4×10^{11} Nm^{-2}
Debye temperature θ_D^{el}	282 K
Mean Grüneisen parameter $\bar{\gamma}_H^{el}$	0.71
Thermal Grüneisen parameter γ^{th}	1.98

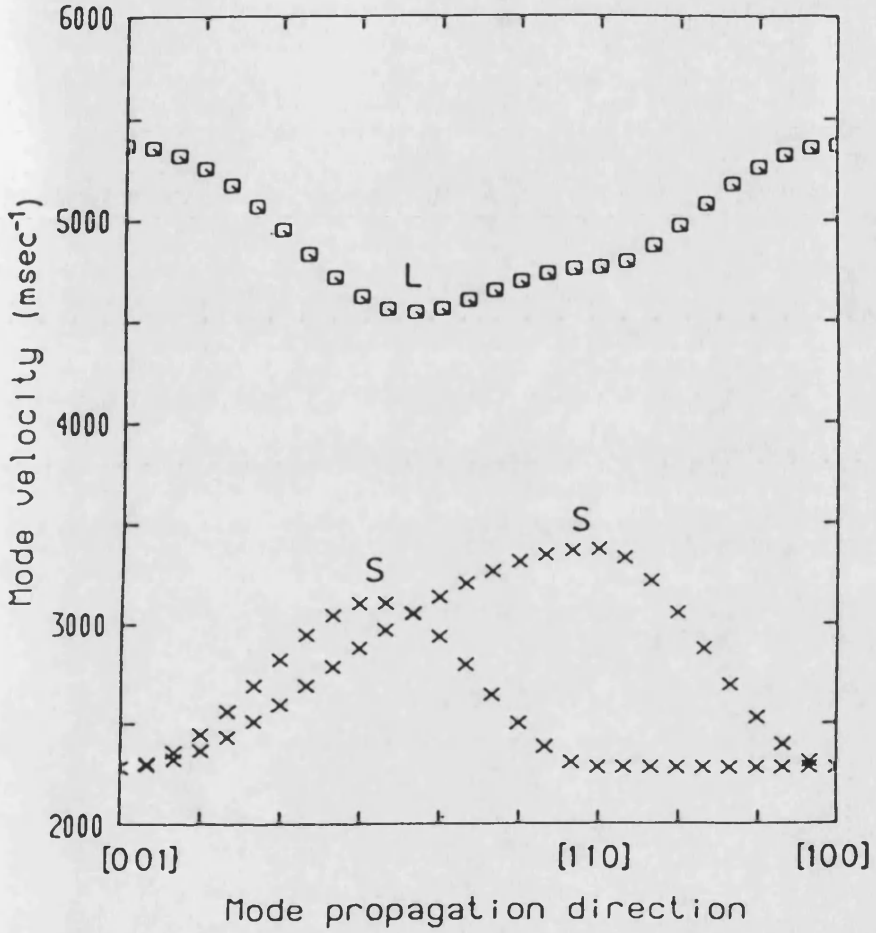

Figure 5.4 Acoustic mode velocity of single crystal UN as a function of mode propagation direction.

hydrostatic pressure derivatives of the elastic stiffness constants C_{IJ} are given in Table 5.2. These were calculated from the experimental data in the form of "natural" velocities W (Thurston and Brugger 1964), using equation 3.47. Also given in Table 5.2 are the hydrostatic pressure derivatives B_{IJ} of the thermodynamic second order elastic stiffness constants. In general for the rocksalt structure compounds (the alkali halides and IV-VI compounds) the pressure derivatives $(\partial C_{IJ}/\partial P)_{T,P=0}$ follow the trend $\partial C_{11}/\partial P > \partial C'/\partial P > \partial C_{12}/\partial P > \partial C_{44}/\partial P$ (Miller, Saunders and Yogurtcu 1981). For UN as for other crystals with this crystallographic structure, $\partial C_{11}/\partial P$ is by far the largest pressure derivative; this is because it is dominated by a large contribution of nearest neighbour repulsive terms and attractive terms including that from the Madelung energy. The normal trend is not followed in that $\partial C_{12}/\partial P > \partial C'/\partial P$. However in all rocksalt structure compounds, including UN, $\partial C_{44}/\partial P$ is the smallest pressure derivative. The negative values of $\partial C_{44}/\partial P$ for UN is not an anomaly - it is also negative for RbBr, KCl and KBr (but positive for NaCl, NaF and LiF). A negative $\partial C_{44}/\partial P$ reflects the negative sign for the Gruneisen parameter of the transverse mode propagated in the [001] direction, which can be accounted for structurally (see later).

To determine the effect of pressure on the volume, lattice parameter and nearest U-U distance, the

Murnaghan (1944) equation-of-state has been used in the logarithmic form given in equation 3.53. Since ultrasonic measurements give adiabatic moduli, the data need to be transformed into isothermal moduli. The isothermal bulk modulus B_0^T has been obtained from the adiabatic bulk modulus B_0^S using equation 3.54. Here γ^{th} is taken as 1.98 (Momin et al.1979), and linear thermal expansion coefficient α_1 is given by (Momin et al.1979)

$$\alpha_1 = 8.695\text{x } 10^{-6} + 12.343\text{x}10^{-10} \text{ (T-298)}, \qquad (5.1)$$

so that the volume thermal expansion at 290K is $26.06\text{x}10^{-6}K^{-1}$ (Table 5.3). Using these values, the isothermal bulk modulus B_0^T has been obtained as $20.36\text{x}10^{10}$ Nm^{-2}. The temperature derivative $(\partial B_0^T/\partial T)_P$ and the hydrostatic pressure derivative $(\partial B_o^T/\partial P)_T$ $(= B_0'^T)$ of the isothermal bulk modulus have been calculated using equations 3.55 and 3.56 respectively. These results are shown in Table 5.3. The isothermal compression of UN calculated using the Murnaghan (1944) equation-of-state (3.53) is plotted in Fig.5.5. Previously the band structure and electronic properties for UN have been computed in the lattice parameter range 4.75 x 10^{-10} to 4.90 x 10^{-10}m (Overton 1962 and Brooks and Glotzel 1980); using the compression obtained here, it is now possible to convert those results to the more experimentally direct effect of pressure on the uranium f and d, the nitrogen valence p electrons and the Madelung

Table 5.3 Primary thermodynamic data for UN at 290K used for adiabatic (S) to isothermal (T) transformations

Bulk modulus $B_0^S = 20.67 \times 10^{10}\,Nm^{-2}$;	$B_0^T = 20.36 \times 10^{10}\,Nm^{-2}$
$\frac{\partial B_0^S}{\partial T} = -5.47 \times 10^{7}\,Nm^{-2}K^{-1}$;	$\frac{\partial B_0^T}{\partial T} = -6.47 \times 10^{7}\,Nm^{-2}K^{-1}$
$\frac{\partial B_0^S}{\partial P} (= B_0'^S) = 5.86$;	$\frac{\partial B_0^T}{\partial P} (= B_0'^T) = 6.06$
Volume thermal expansion coefficient $\alpha = 2.61 \times 10^{-5}K^{-1}$	$\frac{\partial \alpha}{\partial T} = 3.70 \times 10^{-9}$
Thermal Grüneisen parameter $\gamma^{th} = 1.98$[•]	

• MOMIN and KARKHANAVALA (1979)

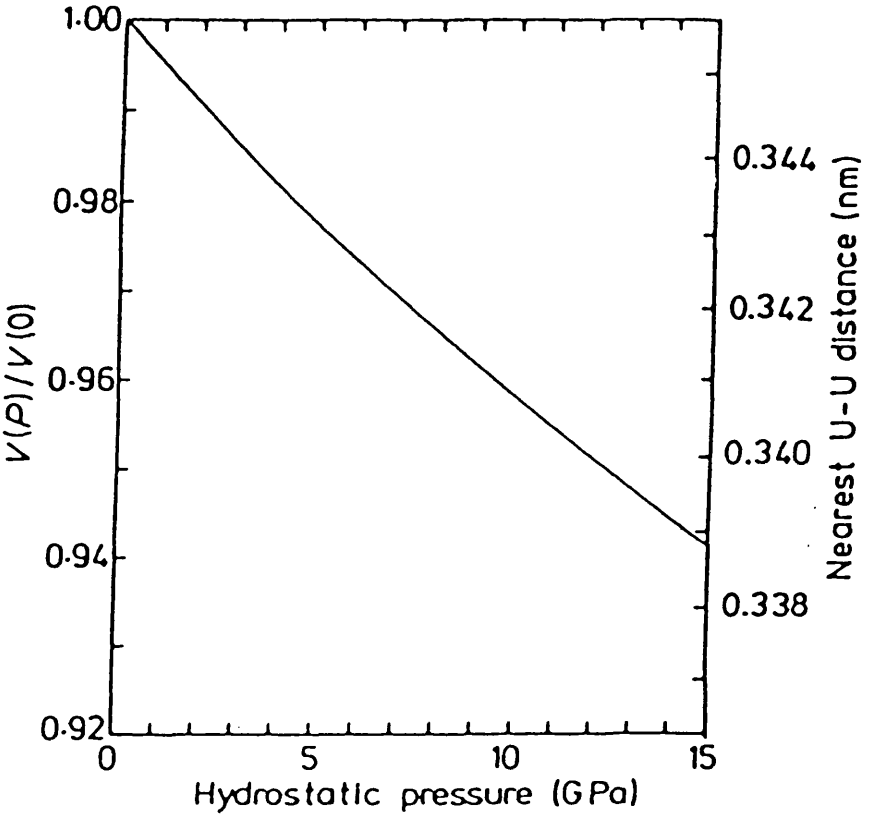

Figure 5.5 The isothermal compression of UN computed on the basis of the Murnaghan equation-of-state.

energy contributions to the band structure energy.

In accord with its much stronger interatomic binding as evidenced by its much greater stiffness C_{IJ}, UN ($\Delta V/V_0$ = 1.84% at 40 x 10^8 Pa) has a much smaller compression than the mixed covalent-ionic lead chalcogenides ($\Delta V/V_0$ = 8% at 40 x 10^8 Pa for PbTe).

From the hydrostatic pressure derivatives of SOEC, the three combinations (C_{111} + C_{112}), (C_{123} + $2C_{112}$) and (C_{144} + $2C_{166}$) of the third order elastic constants (TOEC) are obtained (Table 5.2). The values show the same trends as the rocksalt structure alkali halides and IV-VI compounds (Table 5.2) (Miller 1981) indicating that for UN, as for the other isostructural materials, C_{111} by far the largest third order elastic constant. For an ionic Born-Mayer model with interaction potential between ions

$$\phi_{\mu\nu}(r) = (-Z^2e^2/r) + A \exp(-r/\varrho). \qquad (5.2)$$

the forces would be central and the third order Cauchy relation (Cousins 1971) would be obtained giving

$C_{123} = C_{456} = -10.4 \times 10^{11}$ Nm^{-2}

$C_{112} = C_{166} = -4.0 \times 10^{11}$ Nm^{-2}

Although an ionic model cannot hold strictly for UN, it gives a useful indication of the relative magnitudes of the third order constants: C_{111} would be

about -64 X 10^{11} Nm^{-2} . Including the contributions of repulsive terms up to second nearest neighbours, the TOEC C^0_{IJK} at 0K are (Thakur 1980)

$$
\begin{aligned}
C^0_{IJK} &= (C^0_{IJK})_{\text{attractive}} + (C^0_{IJK})_{\text{repulsive}} \\
C^0_{111} &= 10.2639\,\frac{Z^2e^2}{r_0^4} - \frac{\psi(r_0)}{\varrho}\left(\frac{3}{r_0^2} + \frac{3}{\varrho r_0} + \frac{1}{\varrho^2}\right) \\
&\quad - \frac{\psi(2^{1/2}r_0)}{2\varrho}\left[\frac{3(2)^{1/2}}{r_0^2} + \frac{6}{\varrho r_0} + \frac{2(2)^{1/2}}{\varrho^2}\right] \qquad (5.3) \\
C^0_{112} &= C^0_{116} = -1.2086\,\frac{Z^2e^2}{r_0^4} - \frac{\psi(2^{1/2}r_0)}{4\varrho} \\
&\quad \times \left[\frac{3(2)^{1/2}}{r_0^2} + \frac{6}{\varrho r_0} + \frac{2(2)^{1/2}}{\varrho^2}\right] \\
C^0_{123} &= C^0_{456} = C^0_{144} = 0.6784\,\frac{Z^2e^2}{r_0^4}
\end{aligned}
$$

where $\psi(r_o)$ is the repulsive potential between two ions of distance r_o .

In the case of C^0_{111} the second term, due to nearest neighbour repulsion, is about two orders of magnitude greater than the third term, which results from repulsion between next nearest neighbours, and can be neglected. Hence C_{111} has a large and negative value because it is dominated by the nearest-neighbour repulsion. In the ionic model the nearest-neighbour term does not contribute to the other third order elastic constants, so that these are much smaller than C_{111} .

5.6 Long Wavelength Acoustic Mode Grüneisen Parameter of UN.

The acoustic mode Grüneisen parameters $\gamma(p, N)$ have been computed as a function of mode propagation direction using equation 3.63. $\gamma(p, N)$ in directions in the symmetry planes normal to the two-fold and four-fold symmetries are plotted in Fig.5.6. These Grüneisen parameters quantify the first order anharmonicity of the acoustic modes at the Brillouin zone centre for UN. The marked anisotropy of these $\gamma(p, N)$ can be understood in term of the acoustic modes which can propagate in the rocksalt structure and their relationship to the interionic forces, in particular when the nearest-neighbour repulsion plays a role. Consider for example the $\gamma(p, N)$ for modes propagating along a four-fold <001> direction. Inspection of the mode gamma equations show that the longitudinal mode $\gamma(p, N)$ has a comparatively large positive value (+2.2) because the third order elastic constant combination $(C_{111} + 2C_{112})$ $= C_1 = -72.3 \times 10^{11}$ Nm^{-2} (Table 5.2) is large and negative. Hence $C_1K_1 = -72.3 \times 10^{11}$ Nm$_{-2}$ (K_1 being for the longitudinal mode) is much greater than $w(= C_{11}K_1 = +4.239 \times 10^{11}$ Nm^{-2}), and so dominates $\gamma(p, N)$. Now $(C_{111}+ 2C_{112})$ is in turn largely determined by C_{111}: nearest-neighbour repulsion is responsible for the substantial value of $\gamma(p, N)$ for the longitudinal q[001] acoustic mode. In contrast C_{111} is not involved in the Grüneisen gamma for the shear acoustic wave propagated

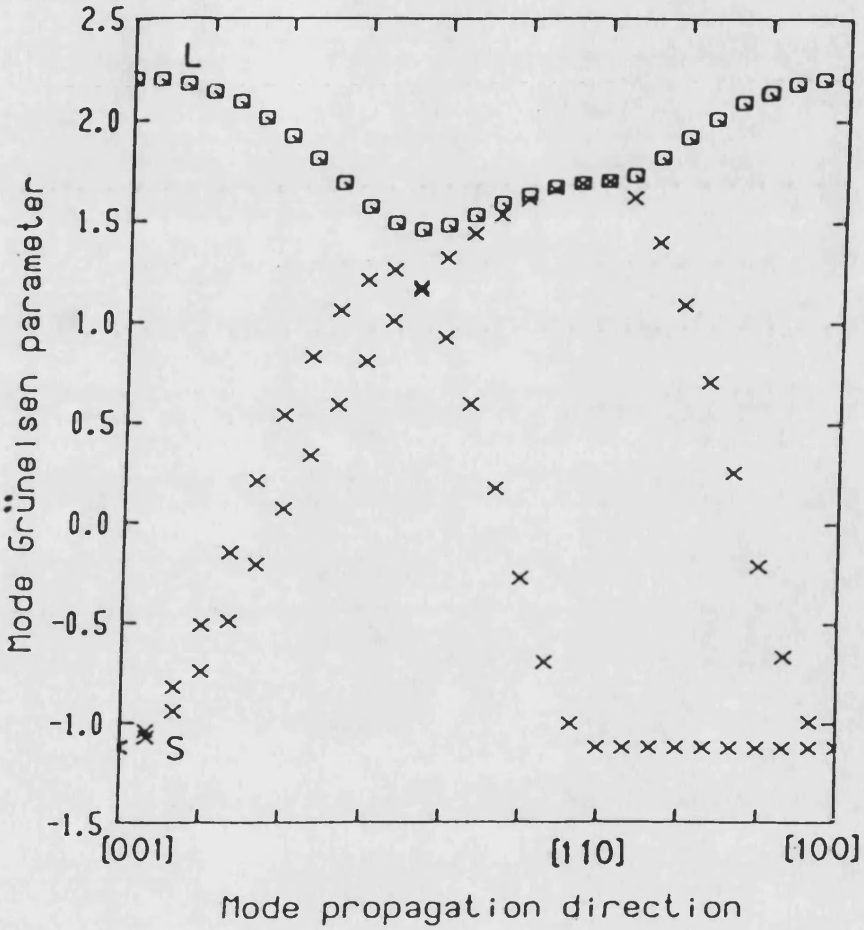

Figure 5.6 The acoustic mode Grüneisen parameter $\gamma(p,N)$ in the long wavelength limit as a function of mode propagation directions in single crystal UN.

along an [001] direction - for this mode nearest-neighbour forces do not come into play. This mode comprises a vibration in which the (001) planes of atoms vibrate almost as a unit perpendicular to the direction of the nearest-neighbour bonds, and since all the changing bond lengths increase, the Grüneisen parameter is negative (Fig.5.6). The thermodynamic properties of the crystal at low temperature (including the thermal expansion) should be determined by the dominance of the phonon population in this transverse low lying branch. In general application of the principle that when C_{111} is involved then the nearest-neighbour repulsion will be important in determining the vibrational anharmonicity accounts for the marked anisotropy of the acoustic mode Grüneisen parameter of UN.

To obtain a mean high temperature acoustic mode Grüneisen parameter $\bar{\gamma}_{\infty}^{el}$, the expression

$$\bar{\gamma}_{\infty}^{el} = \frac{1}{3N}\Sigma\gamma(p, N) \qquad (5.4)$$

has been summed over a grid of 10288 points in velocity space for equal elements of solid angle centered on each propagation vector N. At room temperature UN nears the high temperature limit [$T > \Theta_D$ = 282K (Table 5.2)] so equation 5.4 is a reasonable approximation. The value of $\bar{\gamma}_{\infty}^{el}$ (=0.71) obtained (Table 5.2) is substantially smaller than the thermal Grüneisen parameter γ^{th} (=0.98), which indicates that the mean of the Grüneisen

parameter for optic mode and for acoustic modes away from Brillouin zone centre is much larger than that for the zone centre acoustic modes.

Thus the measurements of the hydrostatic pressure dependences of the SOEC in UN have provided further understanding on the interatomic repulsive forces in rocksalt structure materials in general and in the uranium compounds in particular. The pressure dependence of C_{44} has been found to be negative, this is reflected in the value of the Gruneisen parameter $\gamma_{(p,N)}$ associated with C_{44} which is also negative. A large value of Gruneisen parameter of this material is for the longitudinal acoustic mode vibrational frequency, and this is largely determined by C_{111}; nearest-neighbour repulsive forces are responsible for the substantial value of $\gamma_{(p,N)}$ of this mode.

CHAPTER 6

RESULTS OBTAINED FROM ULTRASONIC VELOCITY EXPERIMENTS MADE ON BINARY ALLOYS Mn-Ni AND TERNARY ALLOYS Mn-Ni-C.

6.1 Introduction

In this chapter the results of the ultrasonic wave velocity measurements performed on single crystal Mn-Ni and Mn-Ni-C alloys by means of the pulse echo overlap technique are presented both as a function of temperature and hydrostatic pressure. The central objective of these experiments has been to obtain all the elastic constants and their pressure derivatives in both the antiferromagnetic and the paramagnetic states of these alloys. The results obtained for two binary alloys Mn-Ni ($Mn_{73}Ni_{27}$ and $Mn_{84}Ni_{16}$) and two ternary alloys Mn-Ni-C (Mn_{85} Ni_9C_6 - sample C2 and $Mn_{85}Ni_9C_6$- sample F) form the major original contributions given in this thesis. The experimental results are presented in two separate sections: Section 6A for the measurements made on the binary alloys $Mn_{73}Ni_{27}$ and $Mn_{84}Ni_{16}$, Section 6B for the measurements made on ternary alloys Mn-Ni-C ($Mn_{85}Ni_9C_6$).

6.2 Crystal Dimensions and Orientations.

The single crystals of Mn-Ni and Mn-Ni-C alloys

were grown commercially by the Bridgman method. Samples have been obtained by spark cutting and have parallel and flat faces normal to the ultrasonic wave propagation direction. The crystallographic orientation has been obtained using a conventional Laue back reflection technique with molybdenum as an x-ray source. Other available sources [copper (Cu), nickel (Ni) and cobalt (Co)] are not suitable for x-ray work on Mn-Ni alloy because Mn-Ni fluoresces which then raises the background intensity and may obscure weak reflections. This problem in general arises if the source and the target are in the same row in the periodic table (Azaroff 1971). The final orientation of the crystals has been obtained to an accuracy of $\pm 0.5^{\circ}$ (section 4.3). The samples were cut normal to the [110] direction (for $Mn_{73}Ni_{27}$ and $Mn_{85}Ni_9C_6$ both samples C2 and F) and the [001] direction (for $Mn_{84}Ni_{16}$ and $Mn_{85}Ni_9C_6$ - sample F) (details of the crystal orientations used are given in Table 6.1a and 6.1b). The final surfaces of the samples were flat and parallel to 1 part in 10^4 (see section 4.3).

6.3 Experimental Data

6.3.1 Velocity Measurements

The results of the measurements made on sample dimensions and densities are given in Table 6.1a and 6.1b. Using these results and the measured overlap

frequency, the ultrasonic wave velocities at room temperature can be obtained. Velocity corrections, required due to multiple internal reflections at the transducer specimen boundary, are determined as the delay transit time t_c given by equation 4.6. The corresponding corrected ultrasonic wave velocity V_c is then determined using

$$V_c = (2l)/[(1/f)-t_c)] \tag{6.1}$$

where l is sample thickness, f is the measured overlap frequency and t_c is the delay transit time in unit of reciprocal transducer frequency. The errors have been calculated on this basis using a computer program "TRANS-CORR" which is given in appendix A. The corrected ultrasonic wave velocities for each mode at room temperature are presented in Table 6.2a and 6.2b.

6.3.2 The Second Order Elastic Stiffness Constants(SOEC)

The SOEC for each mode of propagation at room temperature have been obtained and given in Table 6.2a and 6.2b. The elastic constants determined for each mode from room temperature to approximately 50 degrees above the Nēel temperature are plotted in the following chapter.

The adiabatic compliances S^S_{ij} of these samples can be determined from second order elastic constants using equations 3.36 to 3.38. These adiabatic compliances can then be converted into the isothermal elastic compliances using equations 3.40 and 3.41. For the conversion purposes of the adiabatic SOEC into the isothermal SOEC, the values of the specific heat C_p and linear thermal expansion have been obtained from other work on binary Mn-Ni alloys: the value of the specific heat is taken as that for $Mn_{80}Ni_{20}$ single crystal measured by Uchishiba (1971) and the coefficient of linear thermal expansion α is taken as that measured for $Mn_{85}Ni_{15}$ single crystal by Hausch (1977). The results of the measurements of the SOEC and the data derived from the SOEC measurements for both the binary and ternary alloys at selected temperatures are shown in Tables 6.3a - 6.12a and 6.3b - 6.14b respectively. These data are also presented graphically in Figs.6.1a - 6.14a for binary alloys Mn-Ni and Figs.6.1b - 6.15b (sample C2) and Figs.6.1c-6.10c (sample F) of ternary alloys Mn-Ni-C respectively.

6.3.3. Pressure Derivatives of the SOEC and some of the TOEC Combinations.

The change of ultrasonic wave velocity under hydrostatic pressure in these alloys has been measured using the pulse echo ultrasonic system to a maximum pressure 1.5 kbar. The measurements have been carried out

in step of about 20°C up to the maximum temperature of approximately 170°C. In the interests of clarity the data taken on increasing pressure is plotted except in cases where hysteresis is apparent and in this case the average gradient is taken from data obtained both on increasing and on decreasing pressure. The change of ultrasonic wave frequency with respect to hydrostatic pressure is given by

$$\Delta W/W_0 = (W_{(P)} - W_0)/ W_0 \qquad (6.2)$$

where $W_{(P)}$ is velocity at pressure P and W_0 the ultrasonic wave velocity at zero pressure. The pressure derivatives of the SOEC are obtained using equation 3.44 taking B^T as

$$B^T = (C_{11}^T + 2C_{12}^T)/3. \qquad (6.3)$$

At each fixed temperature a complete set of ultrasonic data has been obtained. The results of hydrostatic pressure measurements versus temperature on the SOEC and the data derived from the SOEC are given in Table 6.13a to 6.18a and Table 6.15b to 6.18b respectively. These data are presented graphically in Fig 6.15a to 6.42a for binary alloys Mn-Ni and Figs.6.16b-6.39b (sample C2) and Figs.11c-13c (sample F) for ternary alloys Mn-Ni-C respectively.

Discussions on experimental results are given in

Chapter 7.

SECTION A. EXPERIMENTAL RESULTS OBTAINED ON BINARY ALLOYS $Mn_{73}Ni_{27}$ AND $Mn_{84}Ni_{16}$.

Table 6.1a. The basic parameters and crystal orientations of binary Mn-Ni alloy single crystals on which ultrasonic velocity measurements have been made.

	Thickness (mm)	density (kgm^{-3})	Neel Temp.(C)	Associated SOEC	Mode($\underline{N}$) Direction	Polarisation Vector($\underline{U}$)
$Mn_{73}Ni_{27}$	4.03	7453	140	C_L	[110]	[110]
				C'	[110]	[110]
				C_{44}	[110]	[001]
$Mn_{84}Ni_{16}$	4.43	7314	170	C_{11}	[001]	[001]
				C_{44}	[001]	in (100) plane
$Mn_{85}Ni_{15}$ (Hausch 1977)	-	7285	192	C_L	[110]	[110]
				C'	[110]	[110]
				C_{44}	[110]	[001]

Table 6.2a. The room temperature second order elastic stiffness constants of binary alloy Mn-Ni single crystals.

N	U	C_{IJ}	f(khz)	observed velocity (ms^{-1})	corrected velocity (ms^{-1})	ρV^2 ($10^{10}Nm^{-2}$)
$Mn_{73}Ni_{27}$						
[110]	[110]	C_L	644	5190	5250	20.1
[110]	[110]	C'	235	1894	1920	2.7
[110]	[001]	C_{44}	449	3626	3640	9.8
$Mn_{84}Ni_{16}$						
[001]	[001]	C_{11}	367	3245	3256	7.8
[001]	in (110) plane	C_{44}	444	3947	3965	11.4
$Mn_{85}Ni_{15}$						
[110]	[110]	C_L				18.0
[110]	[001]	C_{44}				11.1
					(Hausch 1977)	
$Mn_{80.5}Ni_{19.5}$						
[110]	[110]	C_L				19.1
[110]	[110]	C'				3.3
[110]	[001]	C_{44}				11.0
					(Saunders 1985)	

Table 6.3a. Temperature dependences of the second order elastic stiffness constants and elastic compliances of binary alloy $Mn_{73}Ni_{27}$ single crystal. C' is $(C_{11}-C_{12})/2$

Temp. (°C)	C_{11}	C_{12}	C_{44}	C'	S_{11}	S_{12}	S_{44}
		(10^{10} Nm^{-2})			($10^{-11}m^2N^{-1}$)		
20	12.9	7.73	9.80	2.61	1.37	-0.51	1.02
35	12.9	7.52	9.76	2.67	1.37	-0.50	1.02
50	12.7	7.49	9.67	2.60	1.40	-0.52	1.03
65	12.6	7.43	9.63	2.59	1.41	-0.52	1.04
80	12.6	7.43	9.58	2.56	1.42	-0.53	1.04
95	12.5	7.43	9.50	2.52	1.44	-0.54	1.05
105	12.5	7.42	9.45	2.51	1.45	-0.54	1.06
130	12.3	7.35	9.37	2.49	1.46	-0.55	1.07
140	12.5	7.17	9.33	2.65	1.38	-0.50	1.07
150	12.5	7.11	9.24	2.68	1.37	-0.50	1.08
160	12.4	7.05	9.20	2.65	1.38	-0.50	1.09
170	12.3	7.04	9.12	2.63	1.40	-0.51	1.10

Table 6.4a. Temperature dependences of the second order elastic stiffness constants of binary alloy $Mn_{84}Ni_{16}$ single crystal.

Temp. (°C)	C_{11} ($10^{10}Nm^{-2}$)	C_{44}
20	7.75	11.4
40	7.68	11.3
55	7.60	11.2
70	7.51	11.1
90	7.25	11.0
120	7.25	10.8
155	7.13	10.5
175	7.06	10.4
190	7.27	10.2
200	7.31	10.1

Table 6.5a. Temperature dependences of bulk modulus and compressibilities of binary alloy $Mn_{73}Ni_{27}$ single crystal.

Temp. (°C)	Anistropic ratio	Bulk Modulus ($10^{10}Nm^{-2}$)	Volume compress. ($10^{-10}m^2N^{-1}$)	Linear compress.
20	0.27	9.38	0.107	0.036
35	0.27	9.30	0.108	0.036
50	0.27	9.22	0.108	0.036
65	0.27	9.15	0.109	0.036
80	0.27	9.14	0.109	0.036
95	0.27	9.11	0.110	0.037
105	0.27	9.10	0.110	0.037
130	0.27	9.01	0.111	0.037
140	0.28	8.94	0.112	0.037
150	0.29	8.89	0.112	0.037
160	0.29	8.82	0.113	0.038
170	0.29	8.79	0.114	0.038

Table 6.6a The second order elastic stiffness at 20°C in both the antiferromagnetic and the paramagnetic* states of binary alloy $Mn_{84}Ni_{16}$ single crystal. (* from the back extrapolation of the paramagnetic data)

	C_{11}	C_{44}
	(10^{10} Nm^{-2})	
Magnetically ordered	7.78	11.3
Paramagnetic	7.62	11.9

Table 6.7a. The second order elastic stiffness and bulk modulus at 20°C in both the antiferromagnetic and the paramagnetic* states of binary alloy $Mn_{73}Ni_{27}$ single crystal.

(* the back extrapolation of the paramagnetic data)

	C_L	C'	C_{44}	C_{11}	C_{12}	Bulk Modulus
			($10^{10}Nm^{-2}$)			($10^{10}Nm^{-2}$)
Magnetically ordered	20.1	2.67	9.80	12.9	7.60	9.38
Paramagnetic	19.8	2.66	9.92	12.5	7.38	9.05

Table 6.8a. Temperature derivatives of the SOEC in the antiferromagnetic and the paramagnetic states of binary alloys Mn-Ni.

	Antiferromagnetic ($\times 10^7$ Nm^{-2} K^{-1})	Paramagnetic ($\times 10^7$ $Nm^{-2}K^{-1}$)
$Mn_{73}Ni_{27}$		
$\partial C_L / \partial T$	-7.91	-6.87
$\partial C' / \partial T$	-1.63	-2.64
$\partial C_{44} / \partial T$	-3.92	-5.37
$\partial C_{11} / \partial T$	-5.55	-2.00
$\partial C_{12} / \partial T$	-2.3	-2.13
$Mn_{85}Ni_{15}$		
$\partial C_L / \partial T$	-7.31	-6.94
$\partial C_{44} / \partial T$	-3.84	-5.68
$Mn_{84}Ni_{16}$		
$\partial C_{11} / \partial T$	-4.9	-4.67
$\partial C_{44} / \partial T$	-5.3	-8.01

Table 6.9a. Temperature dependence of bulk modulus B of Mn-Ni alloys.

	$(\partial B/\partial T)$ $(Nm^{-2}K^{-1})$	$1/B(\partial B/\partial T)$ (K^{-1})
Single crystal $Mn_{73}Ni_{27}$	-3.93×10^{7}	-4.2×10^{-4}
Polycrystalline $Mn_{74.9}Ni_{25.1}$ (Honda et al 1976)	-5.10×10^{7}	-7.4×10^{-4}

Table 6.9a1. The dependence of the magnetic contribution to the nickel concentration of the bulk modulus of γ-Mn-Ni alloys. (The polycrystalline data is obtained from Honda (1976) and Hausch (1977))

Alloy	$(\Delta B_m/B)_{20}$
Single crystal 27 at.%Ni	3.6%
Polycrystalline 25.1 at.%Ni	3.7% *
Polycrystalline 22.6 at.%Ni	5.4% *
Polycrystalline 20.4 at.%Ni	6.4% *
Polycrystalline 15 at.%Ni	12% (at 77K)**

* Honda et al.(1976)

** Hausch (1977)

Table 6.10a. The Young's modulus and their temperature dependences in both the antiferromagnetic and the paramagnetic states of $Mn_{73}Ni_{27}$ single crystal.

	[111] direction	[110] direction	[001] direction
Young's Mod. E(10^{10} Nm^{-2})			
E_{anti}	19.4	14.5	7.32
E_{para}	19.5	15.0	7.73
$\Delta E_m/E$	-0.5%	-3.9%	-5.6%
$(\partial E/\partial T)_{anti}$ ($10^7 Nm^{-2}K^{-1}$)	-8.61	-5.93	-4.96
$(\partial E/\partial T)_{para}$ ($10^7 Nm^{-2}K^{-1}$)	-8.90	-7.27	-4.80
$(1/E)(\partial E/\partial T)_{anti}$ ($10^{-3}K^{-1}$)	-0.44	-0.49	-0.68
$(1/E)(\partial E/\partial T)_{para}$ ($10^{-3}K^{-1}$)	-0.46	-0.48	-0.62

Table 6.11a. Magnetic contribution to the second order elastic stiffness constant and bulk modulus at 20°C of binary alloy Mn-Ni single crystals.

	$Mn_{73}Ni_{27}$	$Mn_{84}Ni_{16}$	$Mn_{85}Ni_{15}$
$\Delta C_L/C_L$	+1.3%	-	+1.0% **
$\Delta C'/C'$	-3.9%	-	-
$\Delta C_{44}/C_{44}$	-4.2%	-5.3%	-4.8% (at 77K)**
$\Delta C_{11}/C_{11}$	+3.6%	+2.1%	-
$\Delta C_{12}/C_{12}$	+4.6%		
$\Delta B/B$	+4.1%	-	+12% (at 77K)**

** Hausch (1977)

Table 6.12a. Debye temperatures of $Mn_{73}Ni_{27}$ single crystal:

1) At several experimental temperatures

Temp. (°C)	θ_D (K)
20	383
35	382
50	379
65	378
80	377
95	375
105	374
130	372
140	378
150	377
160	376
170	374

11) At absolute zero

	Extrapolated θ_D(K)	Calculated θ_D(K)
Magnetically ordered (antiferromagnetic)	410	396
Paramagnetic	413	415

Table 6.13a. Temperature dependences of pressure derivatives of the SOEC of $Mn_{73}Ni_{27}$ single crystal. C' is $(C_{11}-C_{12})/2$

Temp (°C)	$\partial C_{11}/\partial P$	$\partial C_{12}/\partial P$	$\partial C_{44}/\partial P$	$\partial C'/\partial P$	$\partial B/\partial P$	B_{11}	B_{12}	B_{44}
20	5.19	3.24	3.48	0.97	3.89	6.65	2.51	4.83
35	6.65	3.99	3.23	1.33	4.67	7.51	3.26	4.63
50	8.64	6.55	3.15	1.05	7.25	10.1	5.82	4.50
65	11.5	9.37	2.95	1.05	10.1	12.9	8.64	4.30
80	13.2	11.0	2.88	1.09	11.7	14.7	10.3	4.23
95	15.1	12.8	2.68	1.13	13.6	16.6	12.1	4.03
105	16.7	14.4	2.62	1.16	15.2	18.2	13.7	3.96
130	21.9	19.5	2.27	1.2	20.3	23.4	18.8	3.61
140	6.26	3.58	4.25	1.34	4.47	7.72	2.85	5.60
150	5.62	2.94	4.32	1.34	3.83	7.09	2.20	5.67
160	5.15	2.50	4.49	1.34	3.38	6.61	1.76	5.84
170	4.55	1.93	4.59	1.31	2.81	6.02	1.20	5.94

Table 6.13a1. The hydrostatic pressure derivatives of the second order elastic stiffness constants of f.c.c. transition metals in comparison with $Mn_{73}Ni_{27}$ single crystal at room temperature. C' is $(C_{11}-C_{12})/2$

	$\partial C_{11}/\partial P$	$\partial C_{12}/\partial P$	$\partial C_{44}/\partial P$	$\partial C'/\partial P$
Cu*	6.19	5.15	2.37	0.52
Pd**	6.05	5.19	1.86	0.86
Ni***	5.92	4.74	2.44	1.18
$Mn_{73}Ni_{27}$	5.19	3.24	3.48	0.98

* Daniels and Smith (1958)

** Weinmann and Steiemann (1974)

*** Salama and Alers (1968)

Table 6.14a. Temperature dependences of the TOEC combinations measured at several different temperatures of $Mn_{73}Ni_{27}$ single crystal. Also included is the γ_{mean} acoustic mode Gruneisen parameter.

Temp. (°C)	$C_{111}+2C_{112}$	$C_{144}+2C_{166}$ ($10^9 Nm^{-2}$)	$C_{123}+2C_{112}$	γ_{mean}
20	-1871	-1360	-706	1.55
35	-2095	-1291	-908	1.58
50	-2795	-1246	-1611	1.8
65	-3552	-1180	-2372	2.00
80	-4016	-1159	-2821	2.16
95	-4529	-1102	-3312	2.31
105	-4958	-1081	-3727	2.45
130	-6318	-977	-5079	2.85
140	-2070	-1500	-763	1.94
150	-1892	-1512	-588	1.90
160	-1750	-1544	-467	1.90
170	-1587	-1566	-316	1.88

Table 6.15a. The mode Grüneisen parameters at the long wave length limit for γ-Mn-Ni alloys at 20°C

	$\bar{\gamma}_o^{el}$	$\bar{\gamma}_\infty^{el}$	γ^{th}
Mn-19.5at.%Ni	0.78	1.12	0.72
Mn-27at.%Ni	0.65	0.87	0.97

Table 6.16a. Magnetic contribution to acoustic mode Grüneisen parameters in the long wavelength limit for the $Mn_{73}Ni_{27}$ and $Fe_{68}Ni_{32}$ single crystals.

Mode	Grüneisen parameter					
	$Mn_{73}Ni_{27}$			$Fe_{68}Ni_{32}$*		
	$(\gamma_A)_{20C}$	$(\gamma_P)_{20C}$	γ_{ma}	$(\gamma_A)_{20C}$	$(\gamma_P)_{20C}$	γ_{ma}
C_L	1.13	3.11	-1.98	3.8	6.0	-2.2
C'	1.54	2.38	-0.84	7.7	4.7	+2.8
C_{44}	1.50	1.12	+0.38	3.00	1.8	+1.2

* Renauld and Steinemann (1984).

$(\gamma_A)_{20C}$ = Grüneisen parameter obtained from ultrasonic velocity measurements at 20°C these data correspond to the antiferromagnetic state.

$(\gamma_P)_{20}$ = Grüneisen parameter obtained from extrapolation to 20°C of measurements made in the paramagnetic state.

$\gamma_{ma} = (\gamma_A)_{20C} - (\gamma_P)_{20C}$ is the magnetic contribution to the Grüneisen parameter at 20°C.

Table 6.17a. Mode Grüneisen parameter for the $Mn_{73}Ni_{27}$ single crystal of the three mode of propagations.

Temp. (°C)	20	35	45	65	95	105	130	140	150	160	170
C_L	1.08	1.62	2.02	2.94	3.73	4.11	5.27	1.97	1.85	1.78	1.67
C'	1.54	1.60	1.73	1.86	1.90	2.01	2.07	2.06	2.05	2.04	2.03
C_{44}	1.46	1.37	1.31	1.21	1.09	1.05	0.90	1.85	1.88	1.95	2.04

* $C_L = (C_{11}+C_{12}+2C_{44})/2$

$C' = (C_{11}-C_{12})/2$

Table 6.18a. The elastic stiffness constants and their hydrostatic pressure derivatives of $Mn_{80.5}Ni_{19.5}$ and $Mn_{73}Ni_{27}$ at 20°C.

Unit of C_{IJ} and C_{IJK}:GPa

	$Mn_{80.5}Ni_{19.5}$	$Mn_{73}Ni_{27}$
C^S_{11}	113	129
C^S_{12}	48	77
C^S_{44}	110	98
C'	32	26
B	70	94
$\partial C_{11} / \partial p$	4.2	5.2
$\partial C_{12} / \partial p$	3.8	3.2
$\partial C_{44} / \partial p$	4.9	3.5
$\partial C' / \partial p$	0.2	0.9
$\partial B / \partial p$	3.9	3.9
$C_{111} + 2C_{112}$	-1200	-1870
$C_{144} + 2C_{166}$	-1300	-1360
$C_{123} + 2C_{112}$	-600	-706
C_{111}	-2100	
C_{112}	+460	
C_{123}	-1600	
C_{144}	-170	
C_{166}	-500	
C_{456}	0	

(Saunders,G.A. private communication 1985)

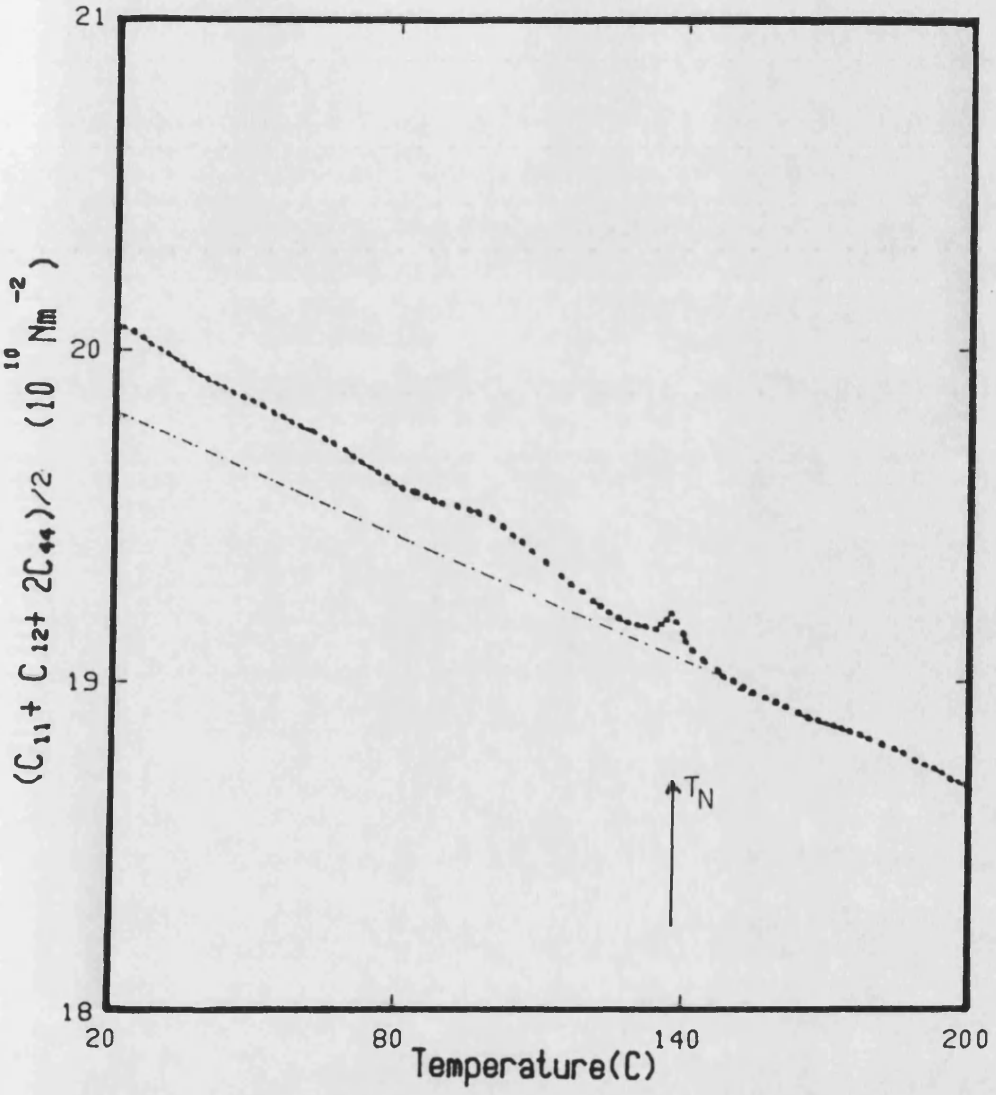

Temperature dependence of the second order elastic stiffness of Mn(73)Ni(27) single crystal for a longitudinal acoustic wave propagates in the [110] direction.

Fig 6.1a

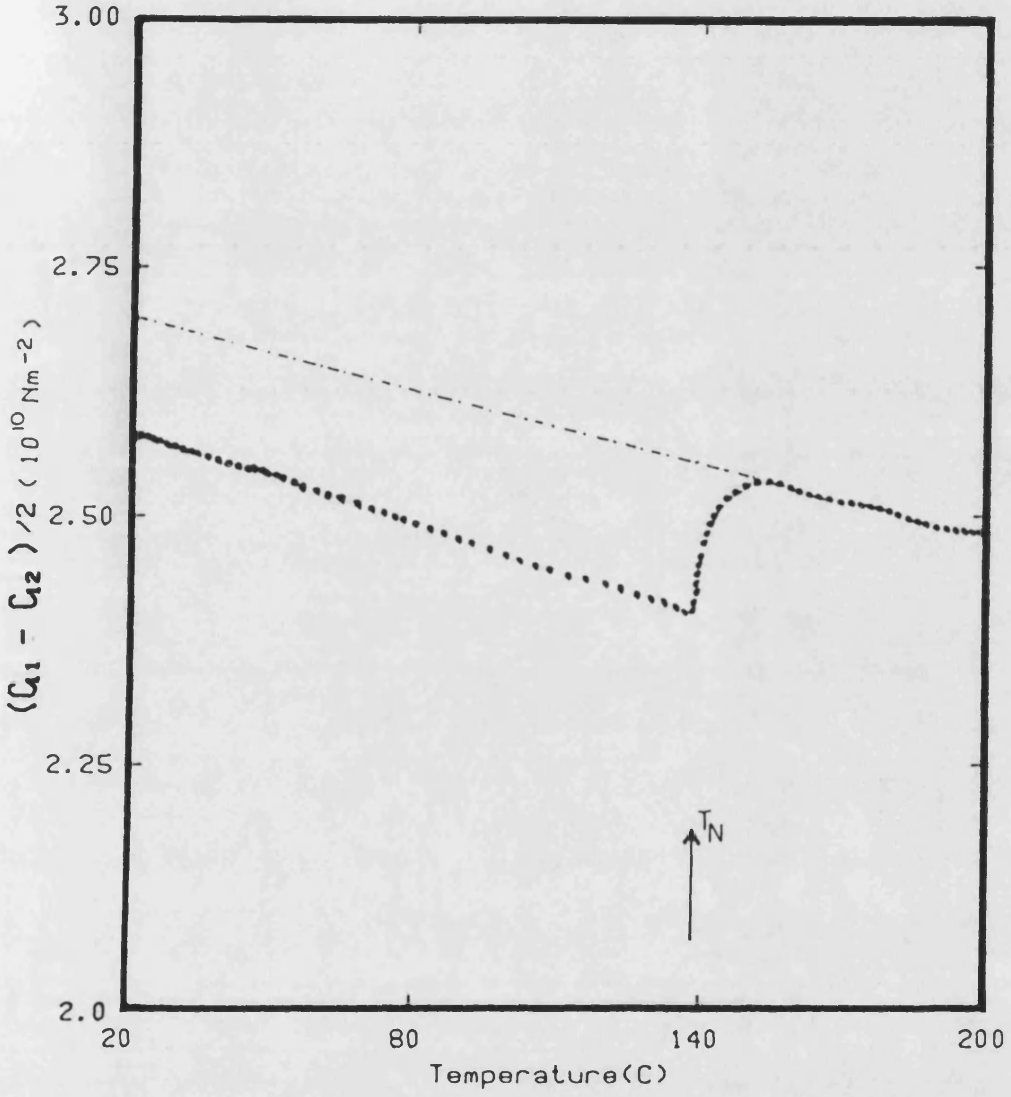

Temperature dependence of the second order elastic stiffness of Mn(73)Ni(27) single crystal for a shear acoustic wave propagates in the [110] direction.

Fig 6.2a

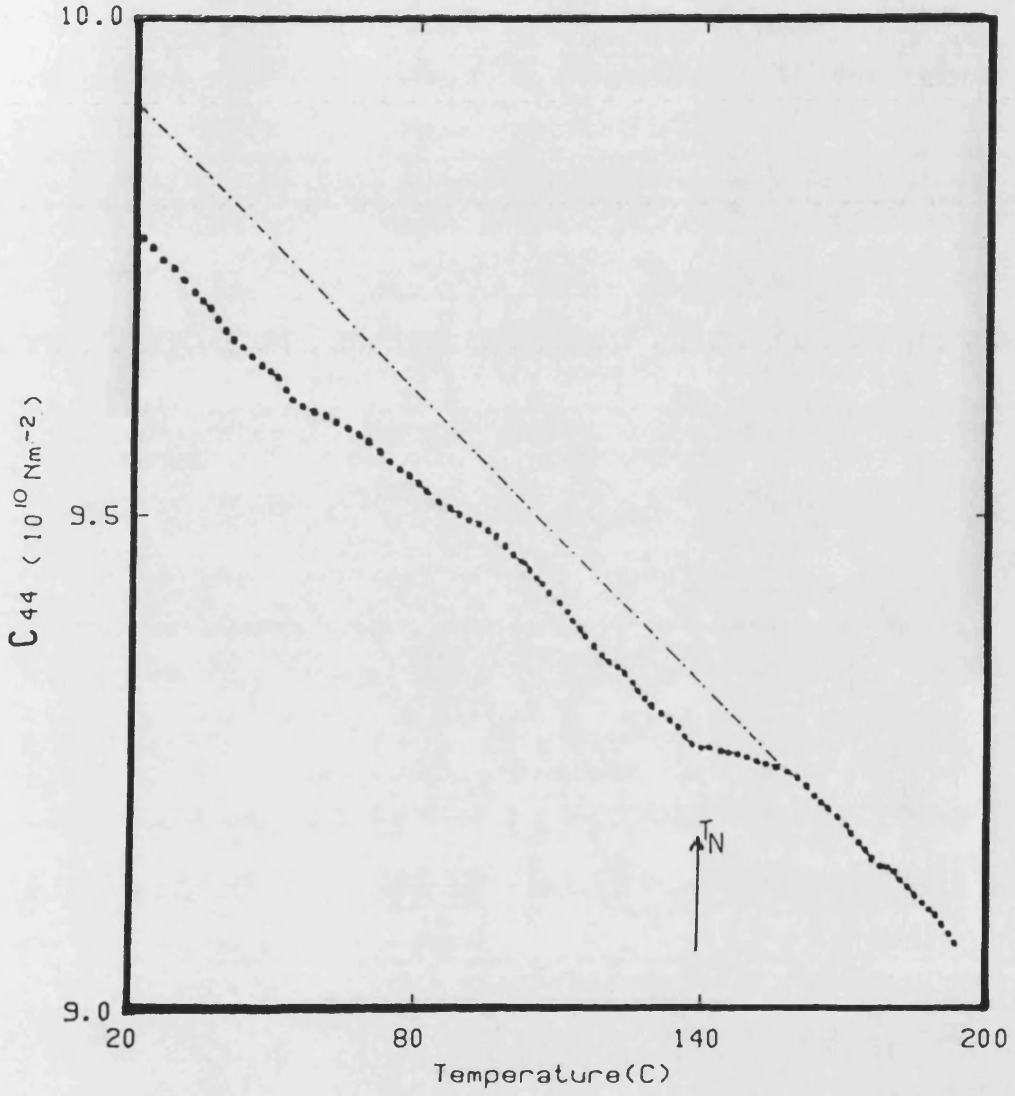

Temperature dependence of the second order elastic stiffness of Mn(73)Ni(27) single crystal for a shear acoustic wave propagates in the [110] direction.

Fig 6.3a

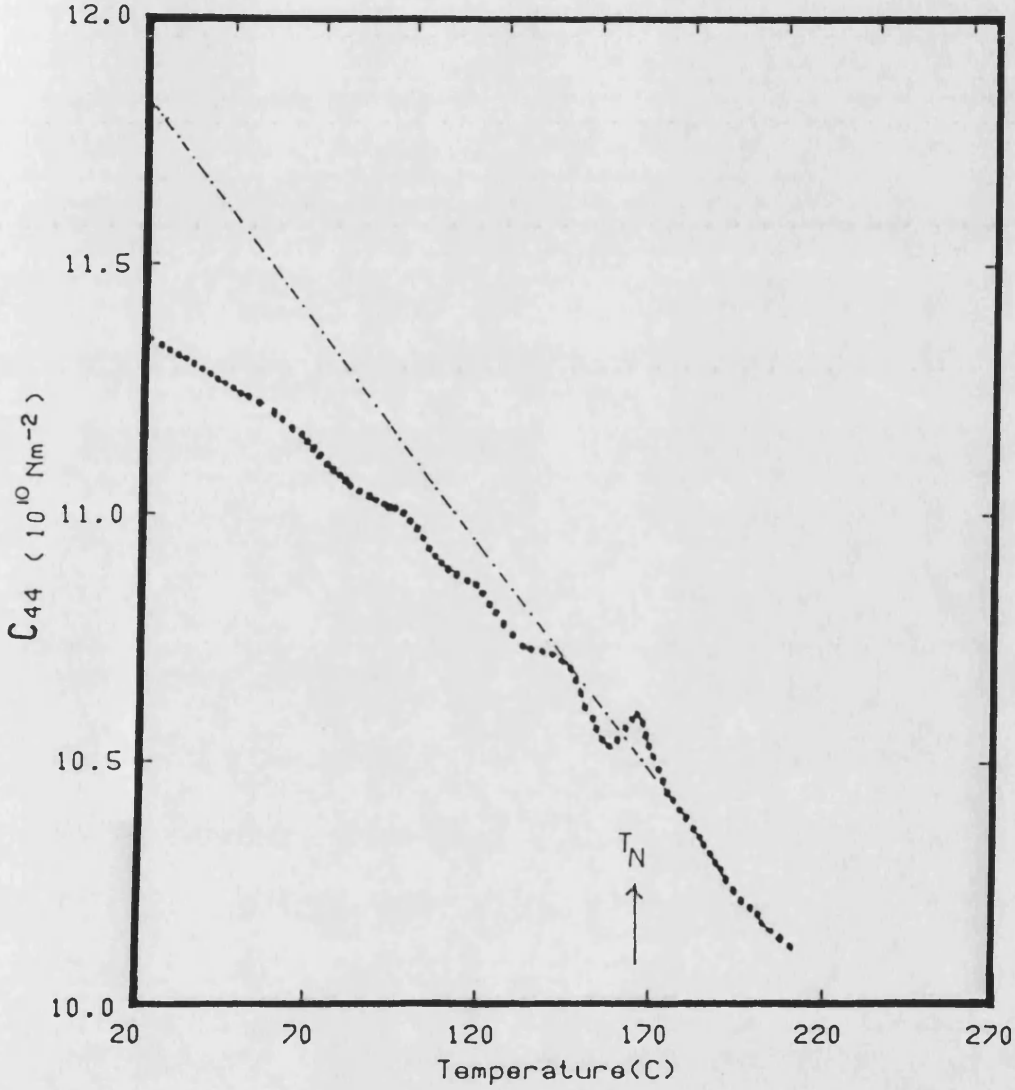

Temperature dependence of the second order elastic stiffness (C44) of Mn(84)Ni(16) single crystal.

Fig 6.3a(1)

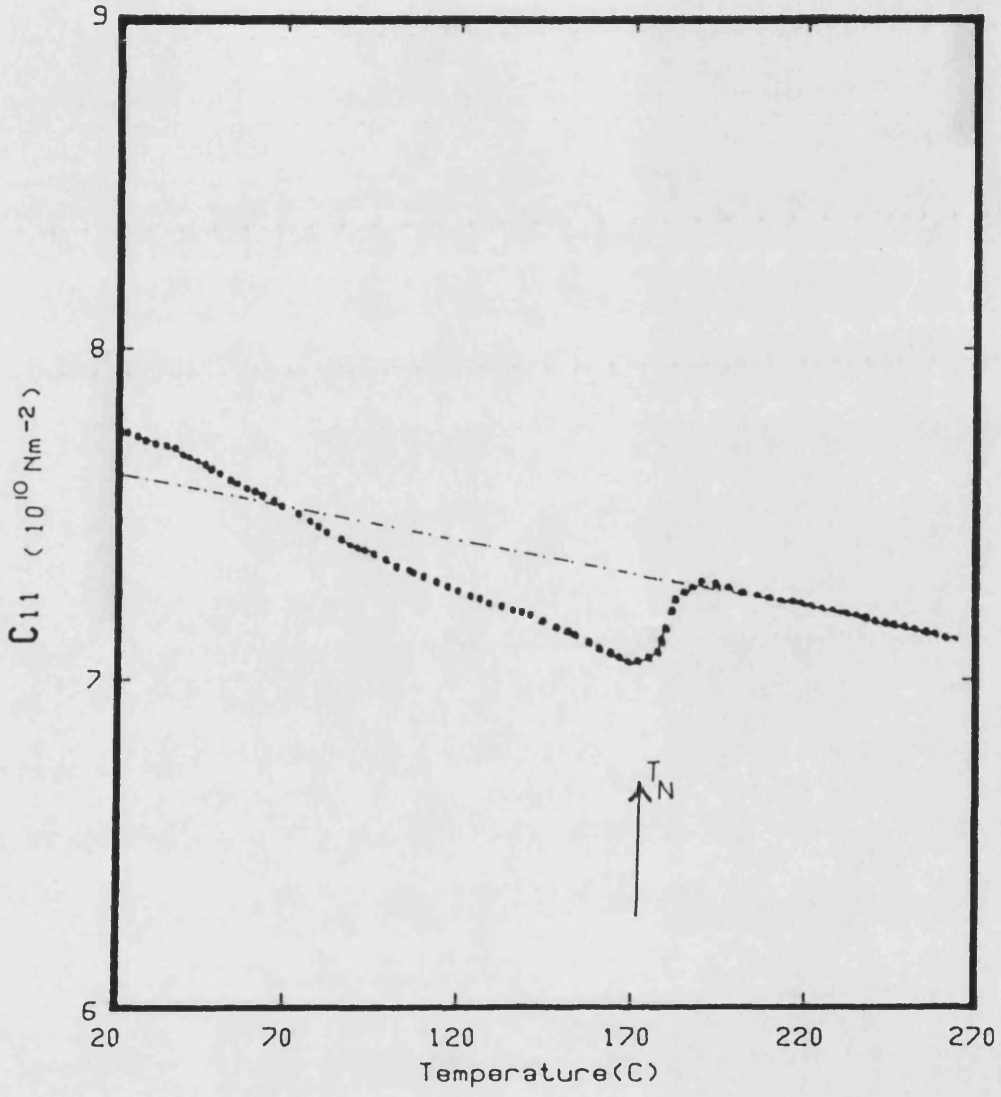

Temperature dependence of the second order elastic stiffness (C_{11}) of Mn(84)Ni(16) single crystal.

Fig 6.4a(1)

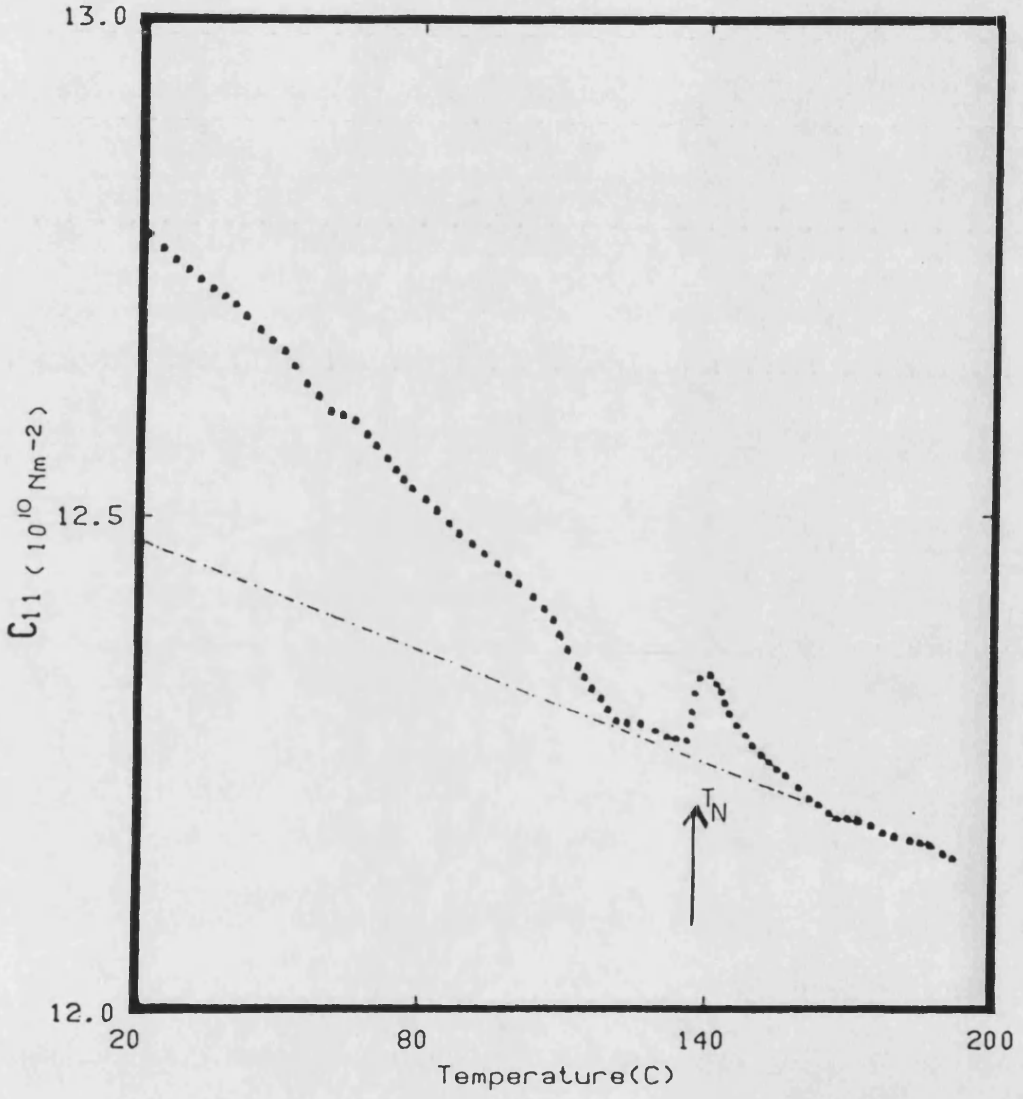

Temperature dependence of the second order elastic stiffness of Mn(73)Ni(27) single crystal for a longitudinal acoustic wave propagates in the [001] direction.

Fig 6.4a

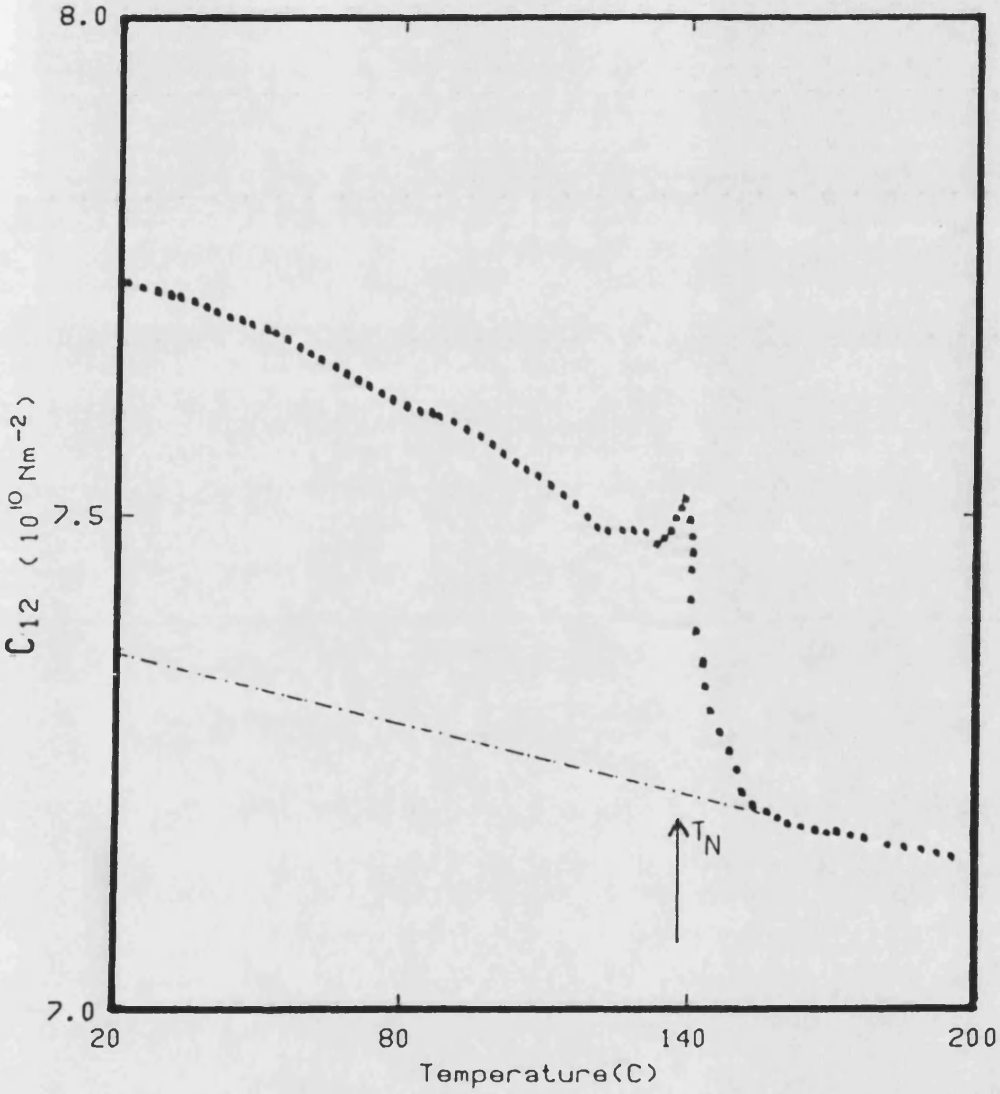

Temperature dependence of the second order elastic stiffness (C_{12}) of Mn(73)Ni(27) single crystal.

Fig 6.5a

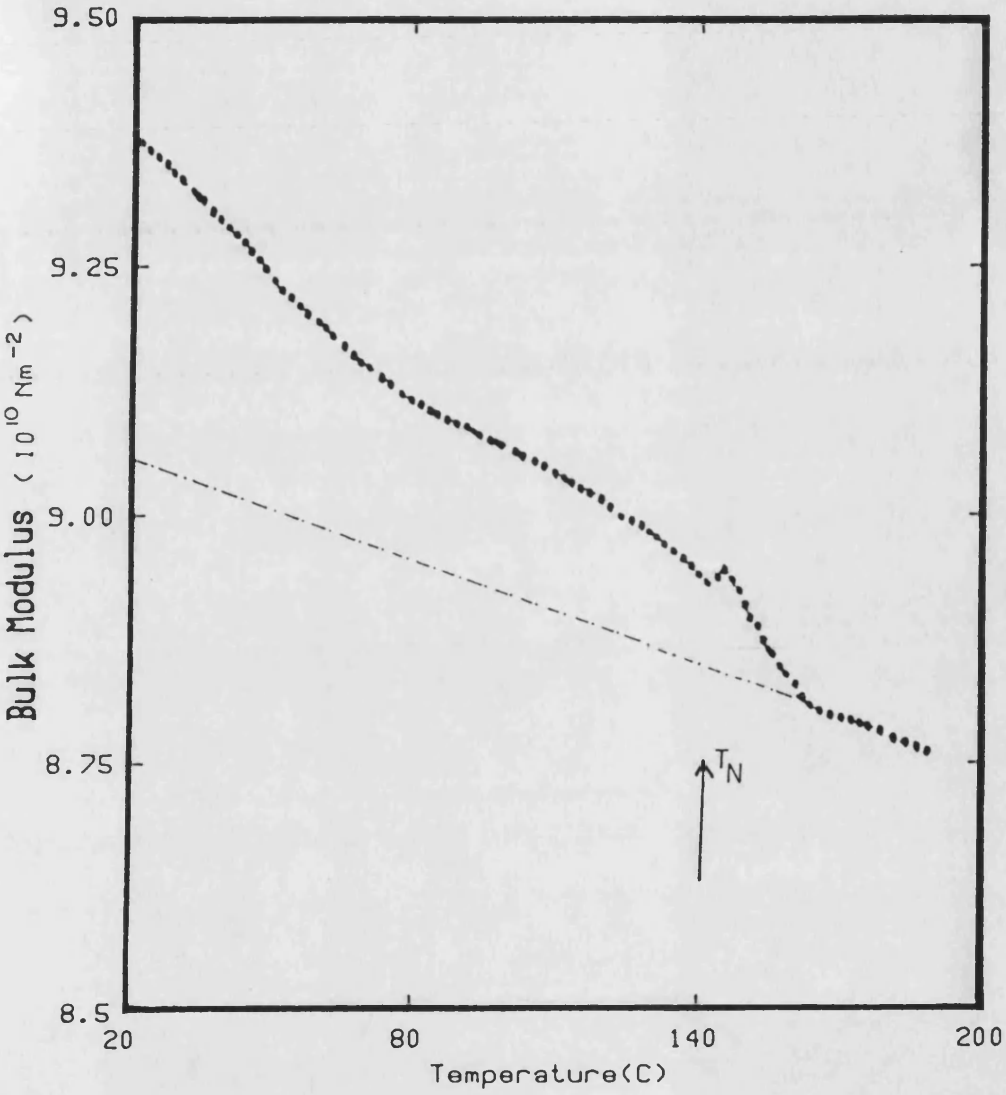

Temperature dependence of bulk modulus of Mn(73)Ni(27) single crystal in the antiferromagnetic and paramagnetic phases.

Fig 6.6a

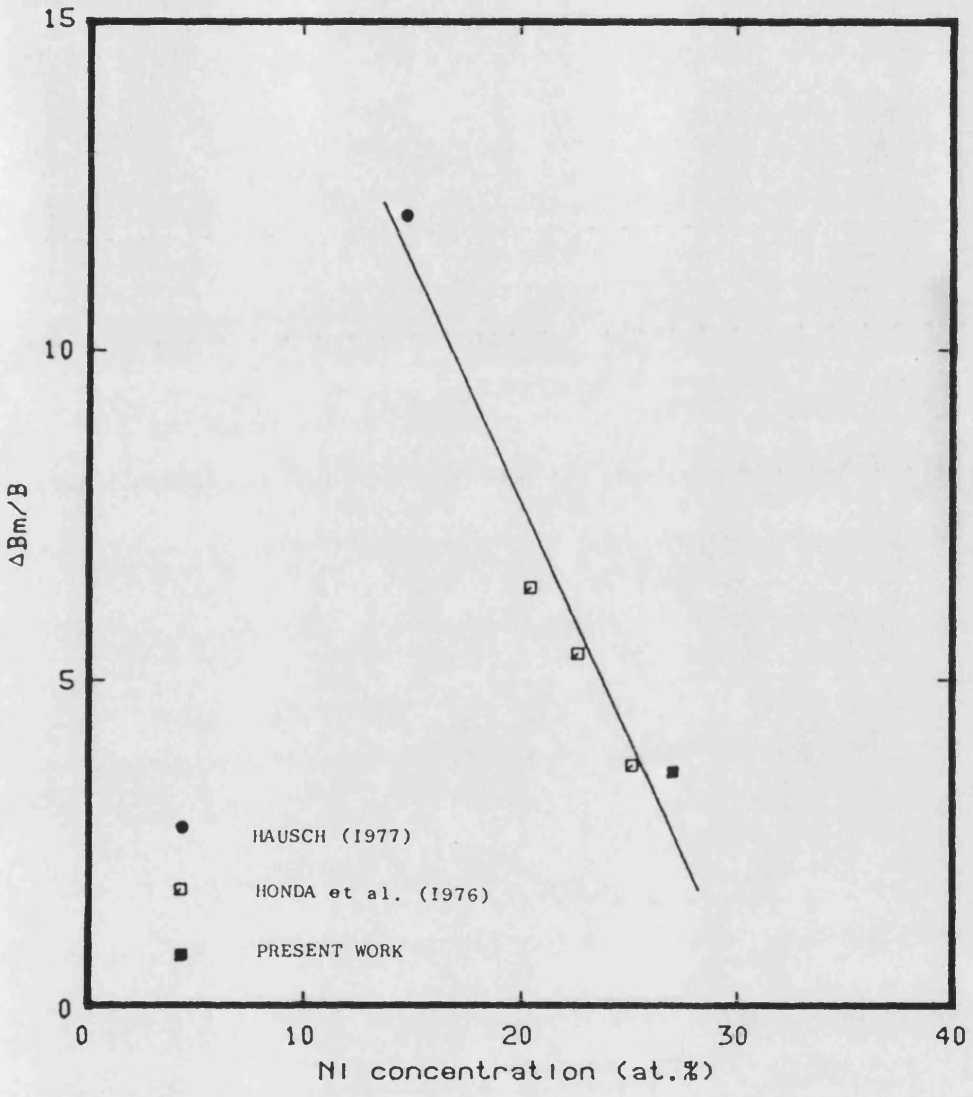

The variation of magnetic contribution ΔBm/B of γ-manganese-nickel alloys with nickel concentration.

Fig 6.6a1

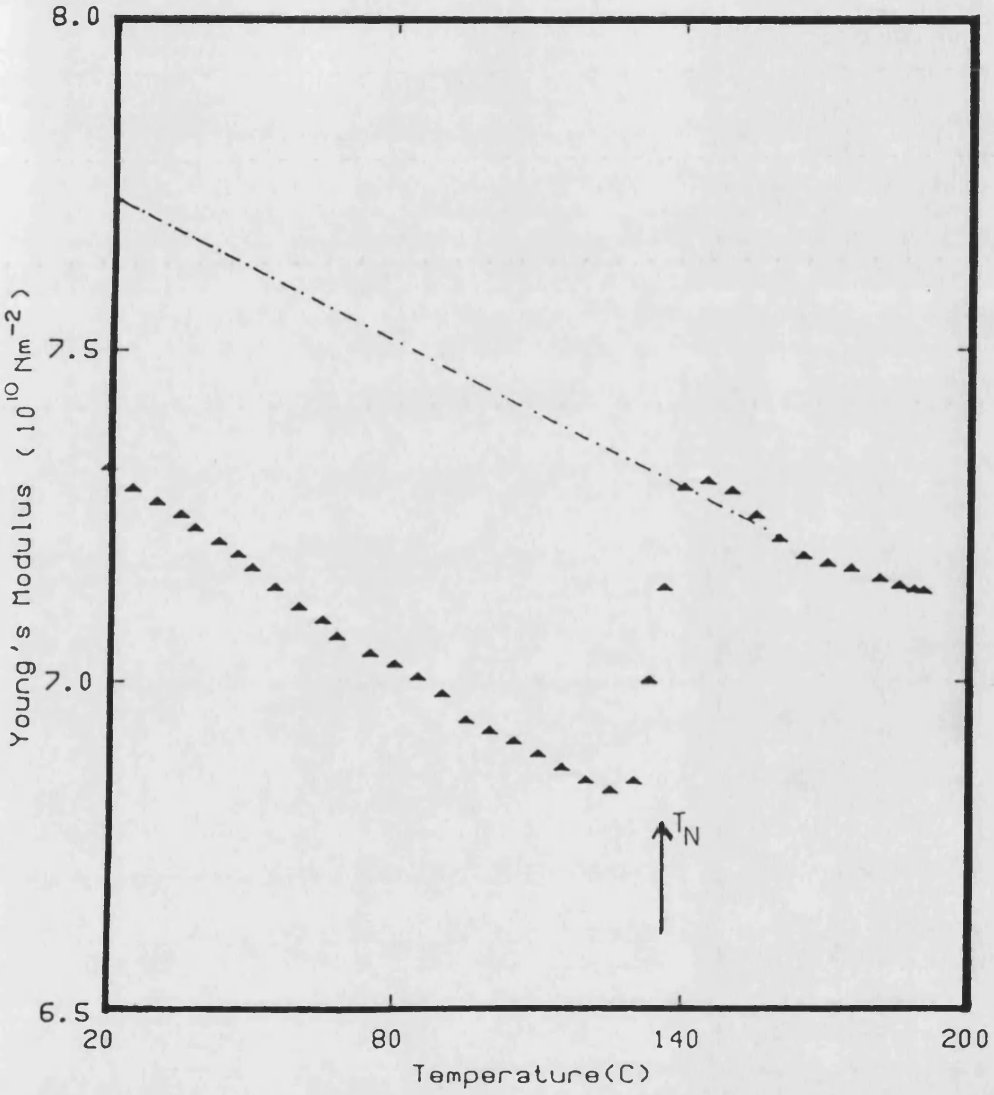

The temperature dependence of Young's modulus in the [001] direction of Mn(73)Ni(27) single crystal.

Fig 6.7a

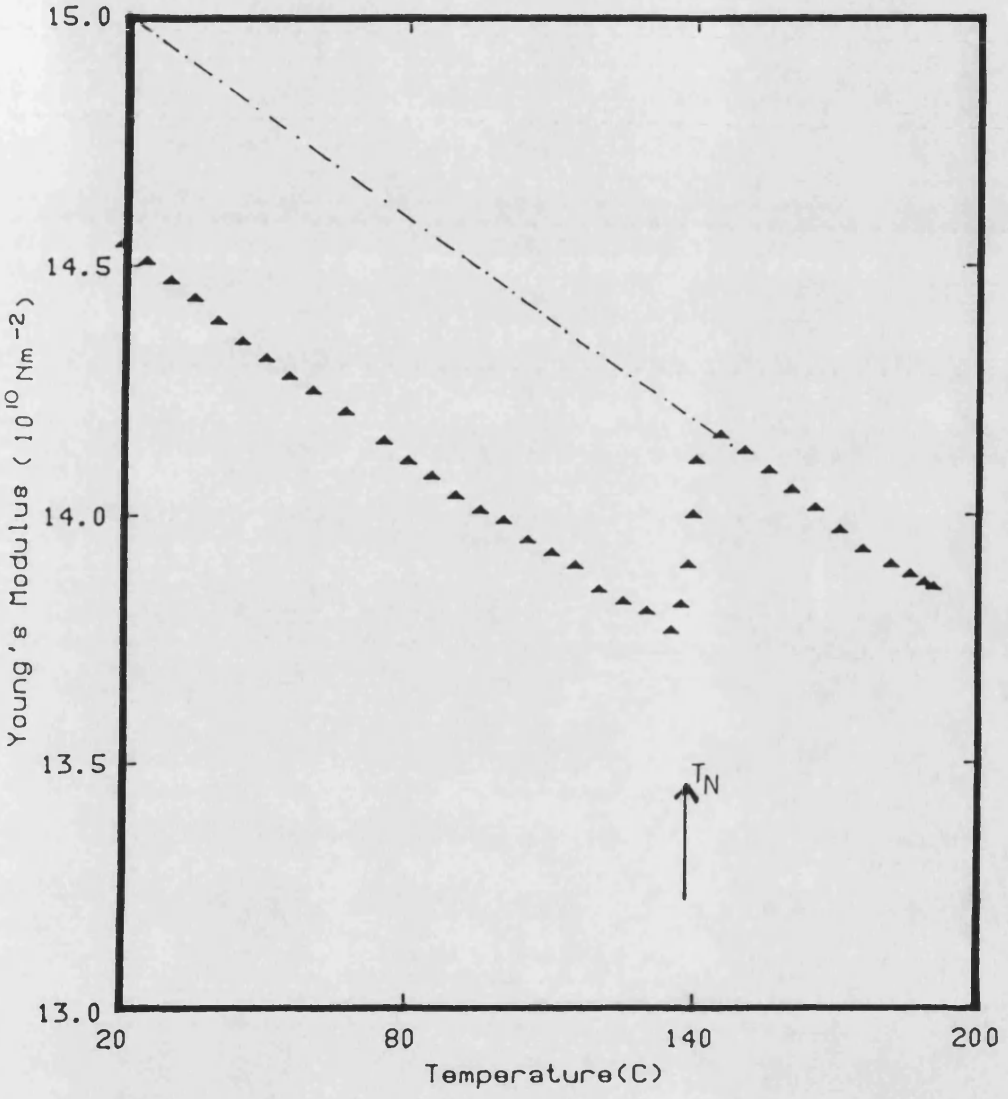

The temperature dependence of Young's modulus in the [110] direction of Mn(73)Ni(27) single crystal.

Fig 6.8a

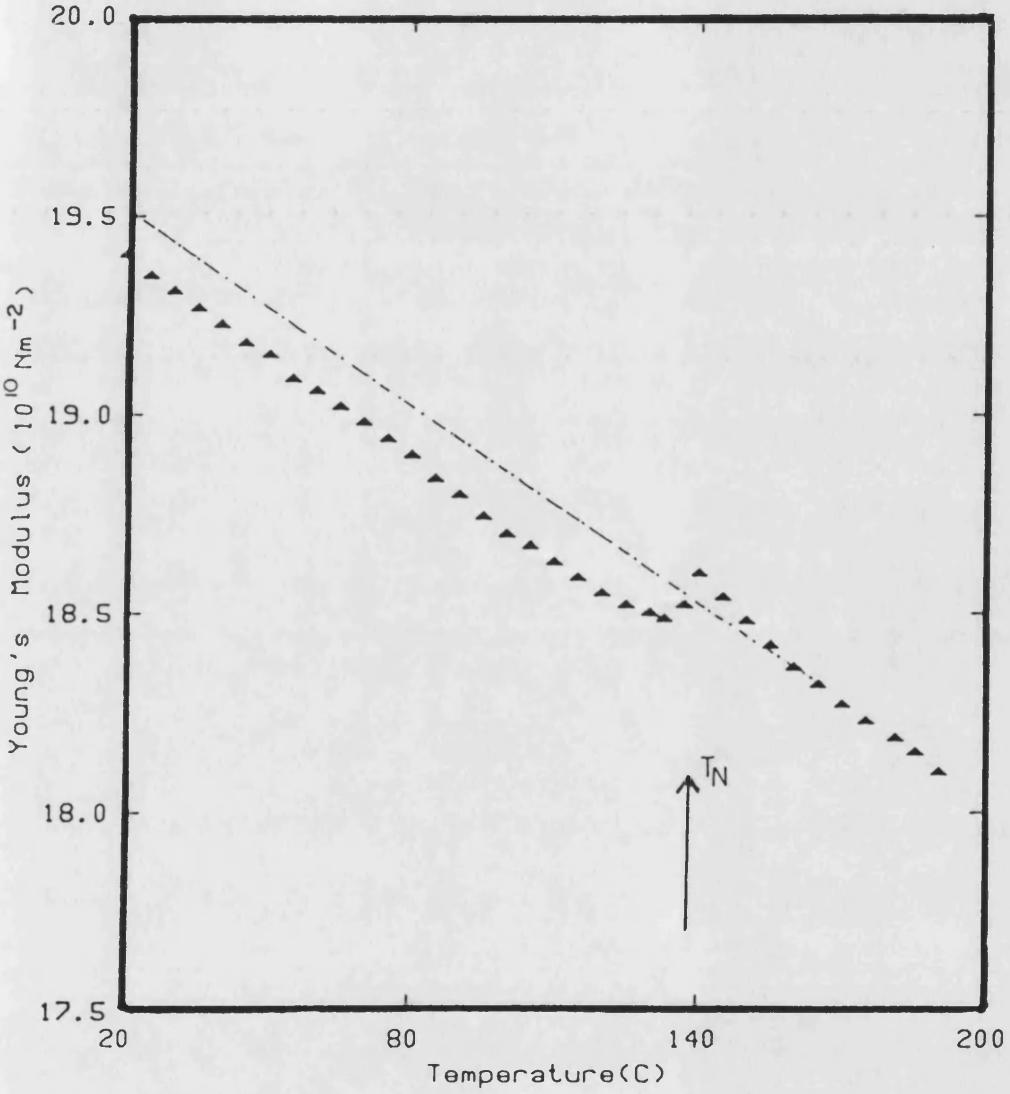

The temperature dependence of Young's modulus in the [111] direction of Mn(73)Ni(27) single crystal.

Fig 6.9a

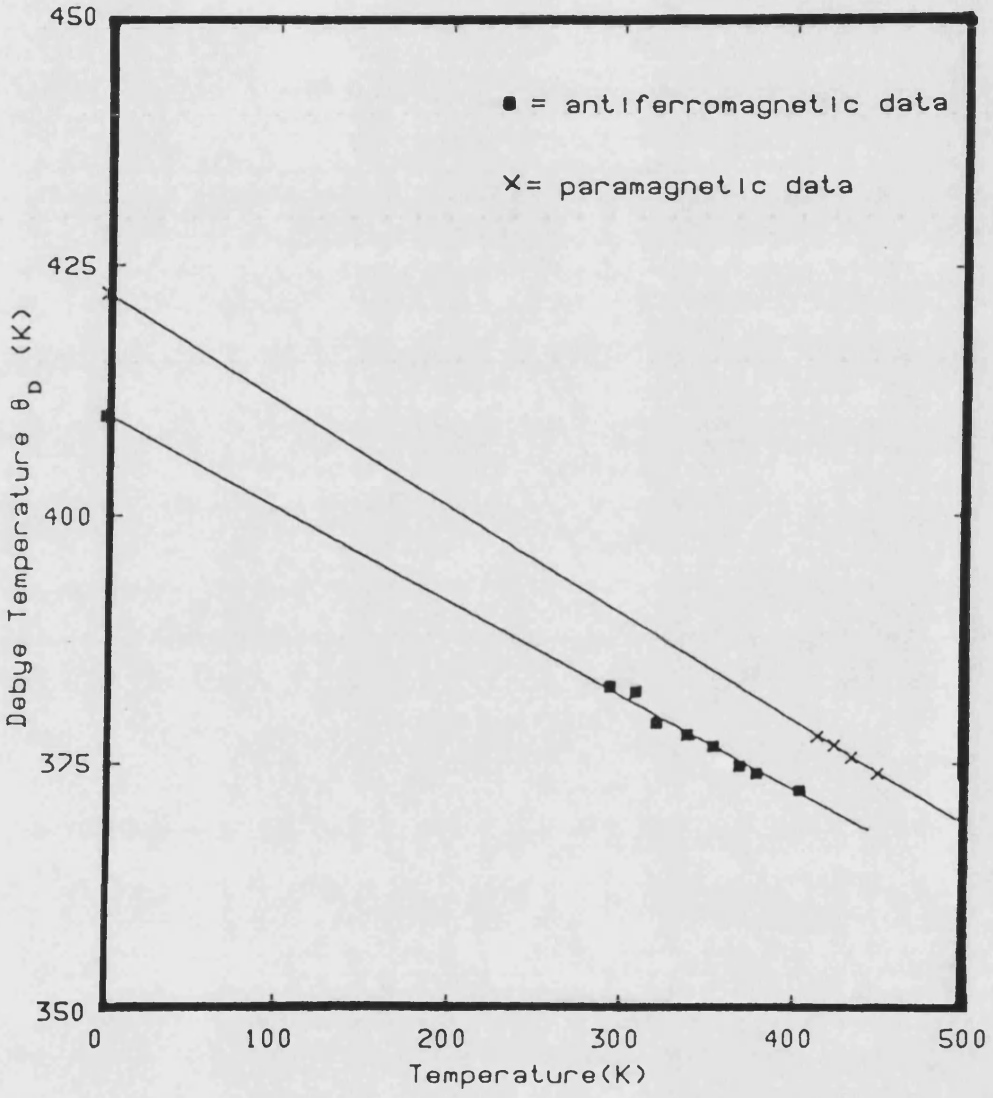

Estimating Debye temperature θ_D of Mn(73)Ni(27) single crystal at 0K by extrapolating the experimental data to 0K

Fig 6.10a

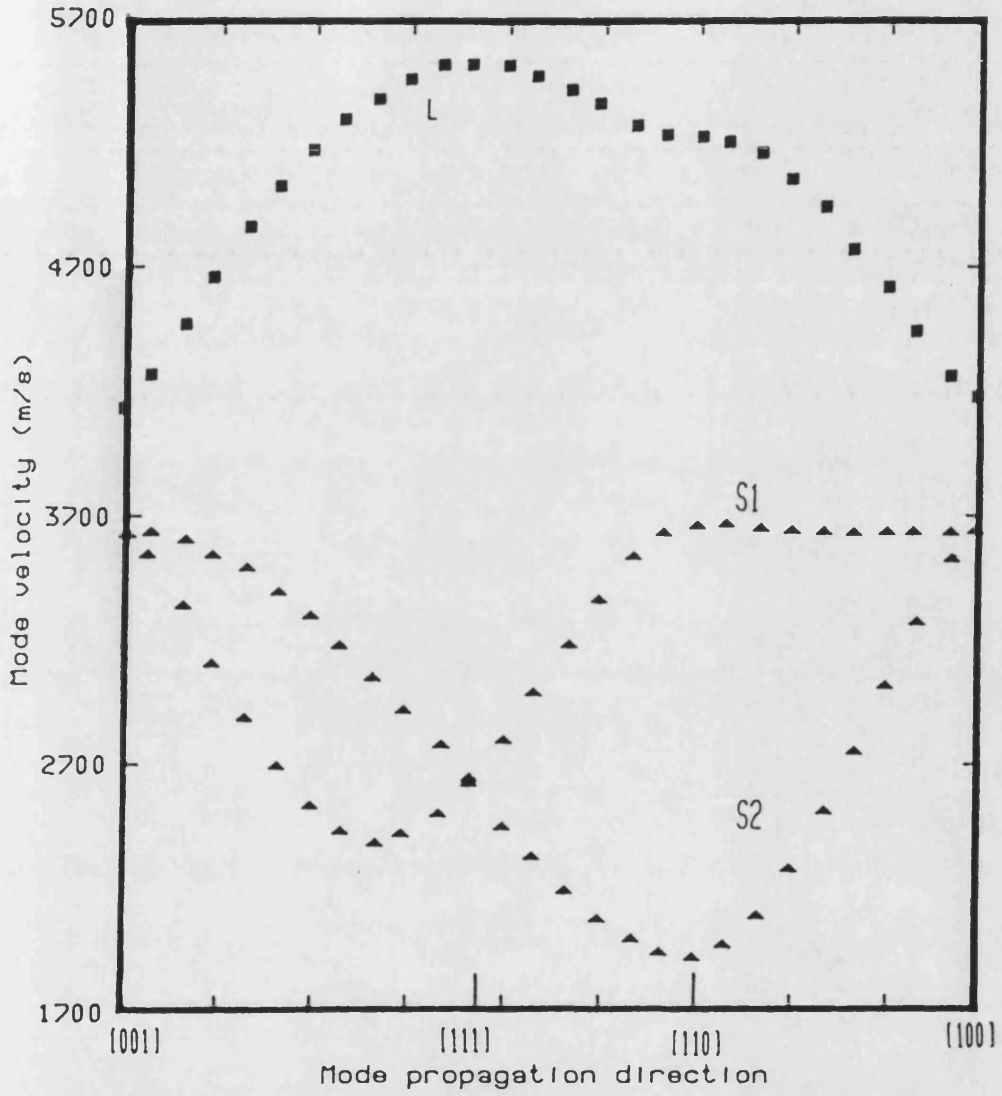

Directional dependence of long wavelength acoustic mode velocities of the Mn(73)Ni(27) single crystal at 20C

Fig 6.11a

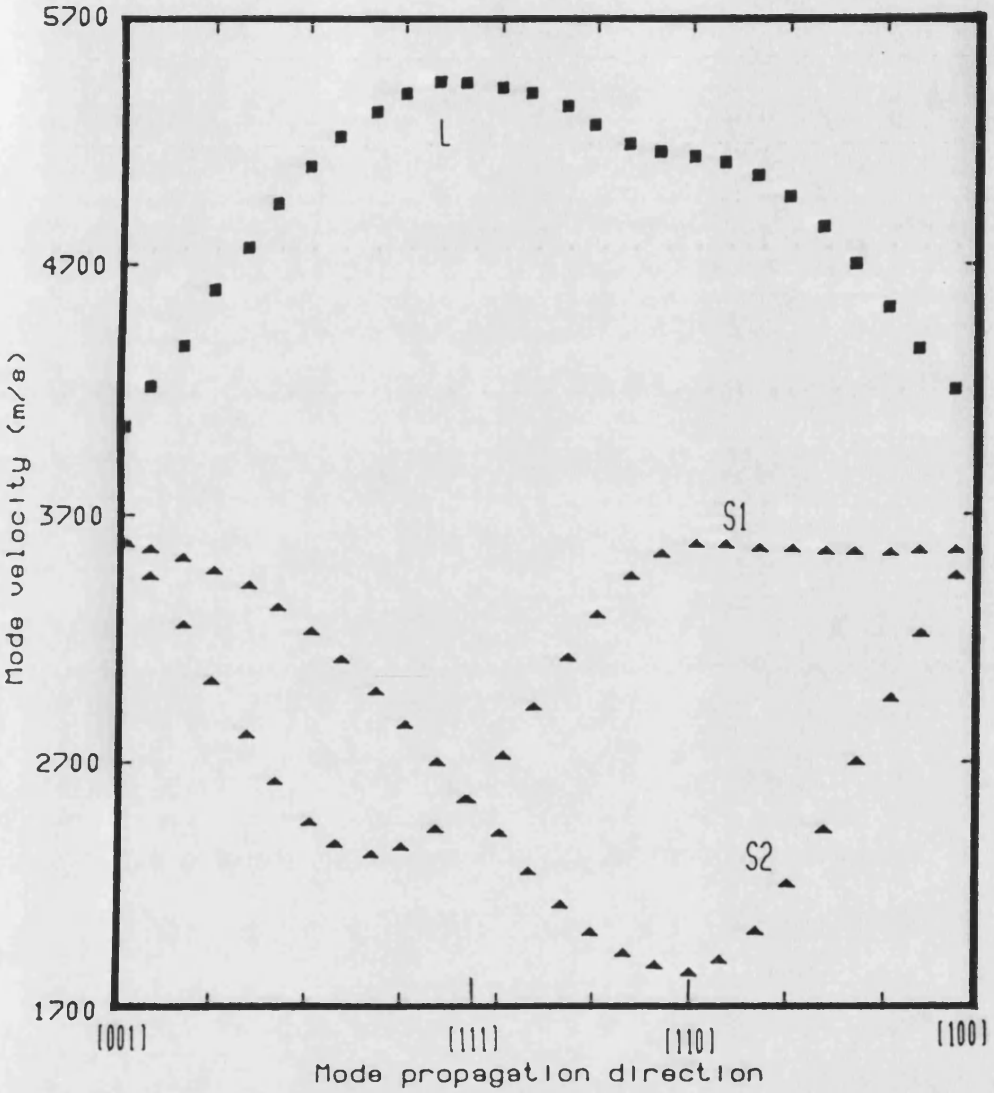

Directional dependence of long wavelength acoustic mode velocities of the Mn(73)Ni(27) single crystal at 130C.

Fig 6.12a

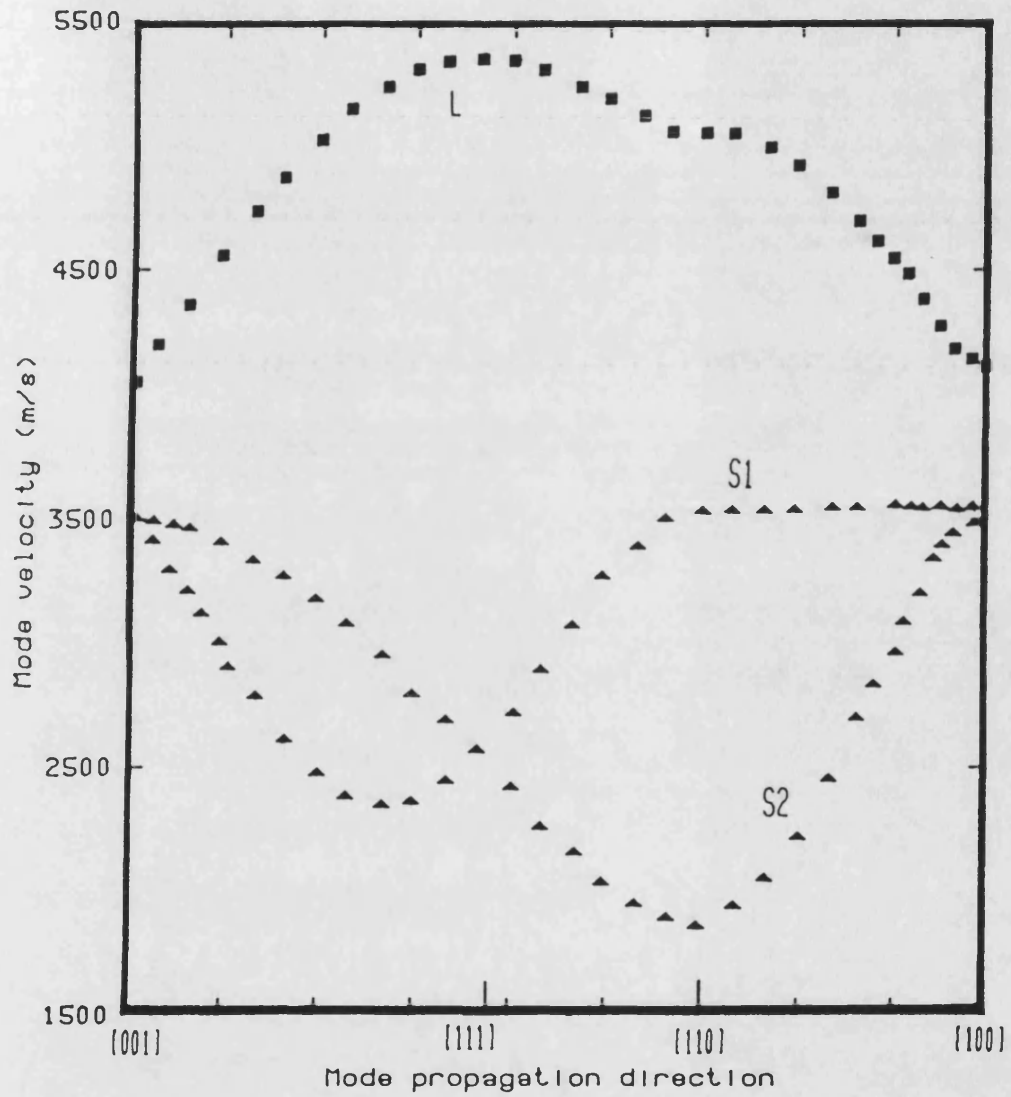

Directional dependence of long wavelength acoustic mode velocities of the Mn(73)Ni(27) single crystal at 150C

Fig 6.13a

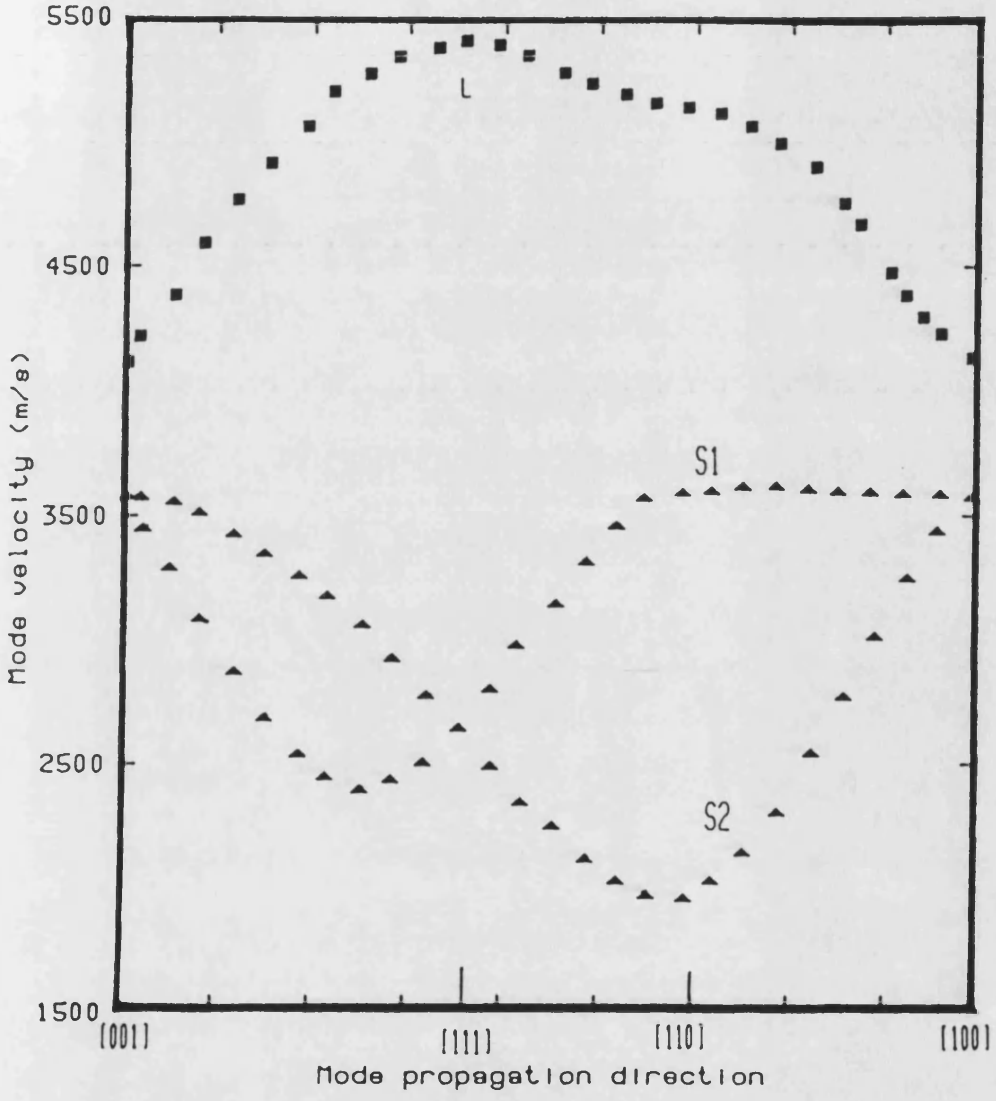

Directional dependence of long wavelength acoustic mode velocities of the Mn(73)Ni(27) single crystal at 170C

Fig 6.14a

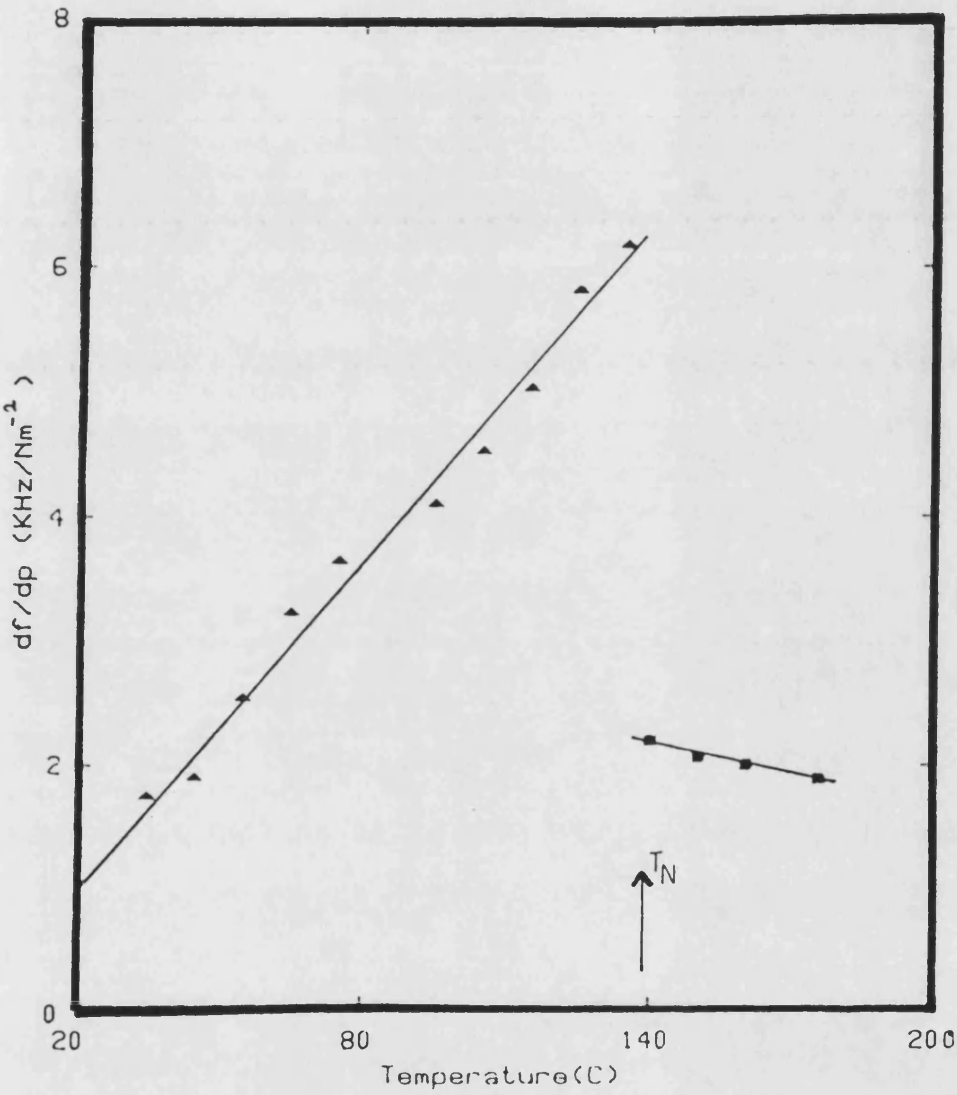

Temperature dependence of the pressure derivatives of long wavelength acoustic mode frequency propagates in the [110] direction and polarises in the [110] direction of Mn(73)Ni(27) single crystal.

Fig 6.15a

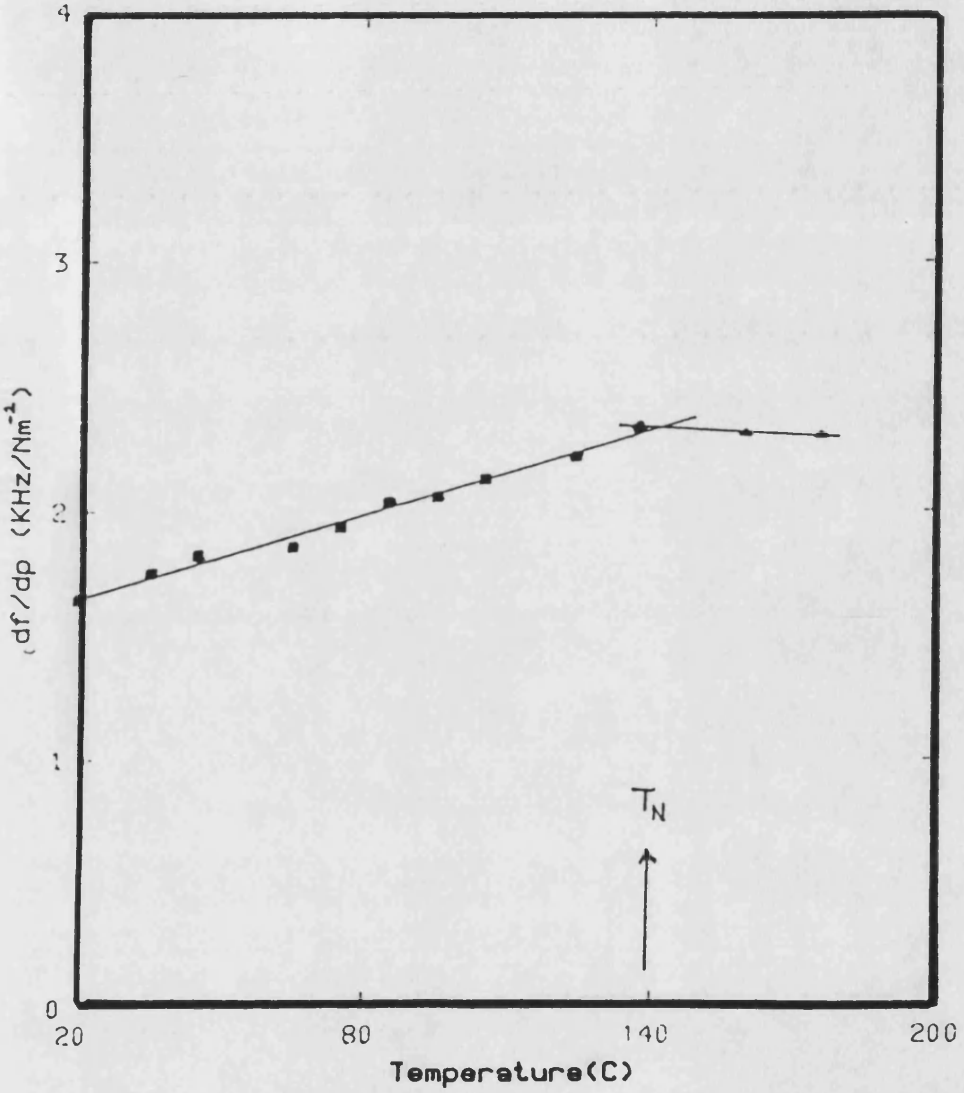

Temperature dependence of the pressure derivatives of long wavelength acoustic mode frequency propagates in the [110] direction and polarises in the [1$\bar{1}$0] direction of Mn(73)Ni(27) single crystal.

Fig 6.16a

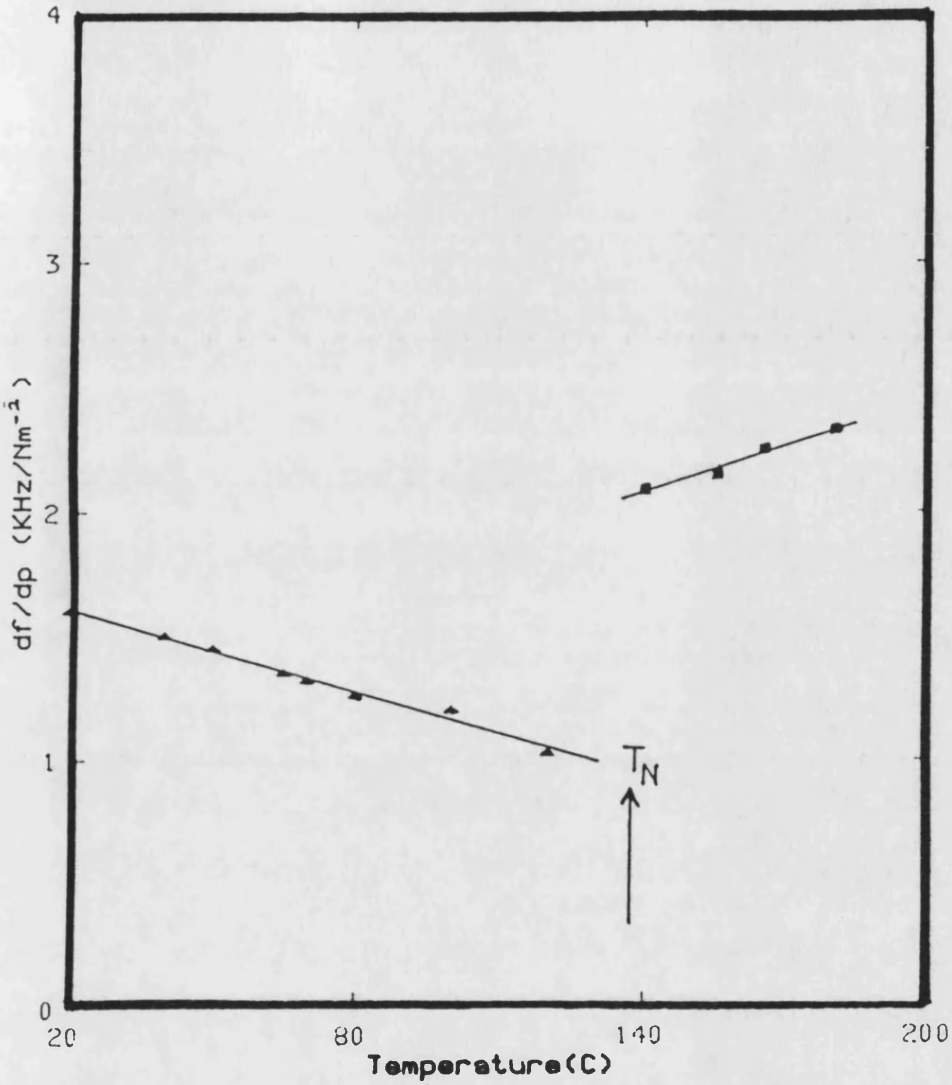

Temperature dependence of the pressure derivatives of long wavelength acoustic mode frequency propagates in the [110] direction and polarises in the [001] direction of Mn(73)Ni(27) single crystal.

Fig 6.17a

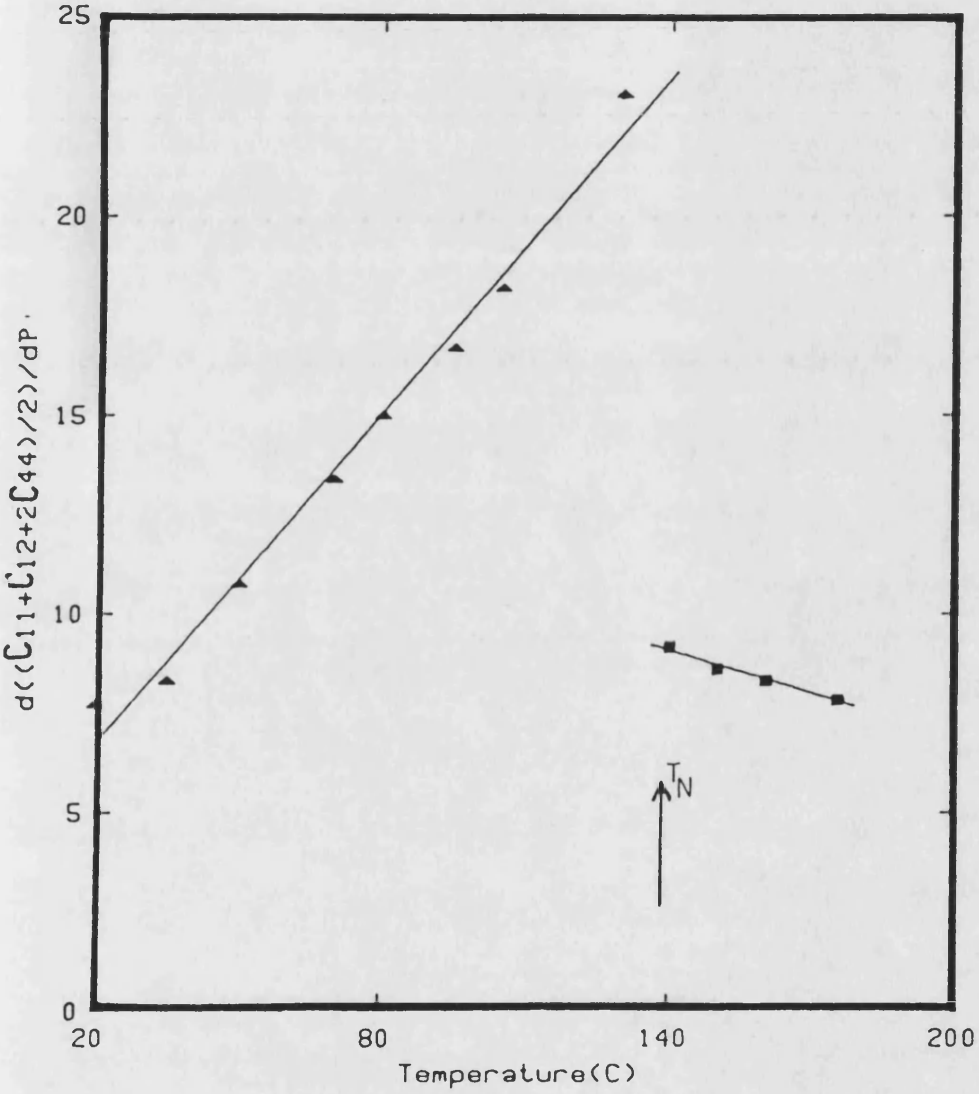

Temperature dependence of hydrostatic pressure derivatives of second order elastic stiffness of Mn(73)Ni(27) single crystal for longitudinal acoustic wave propagates in [110] direction.

Fig 6.18a

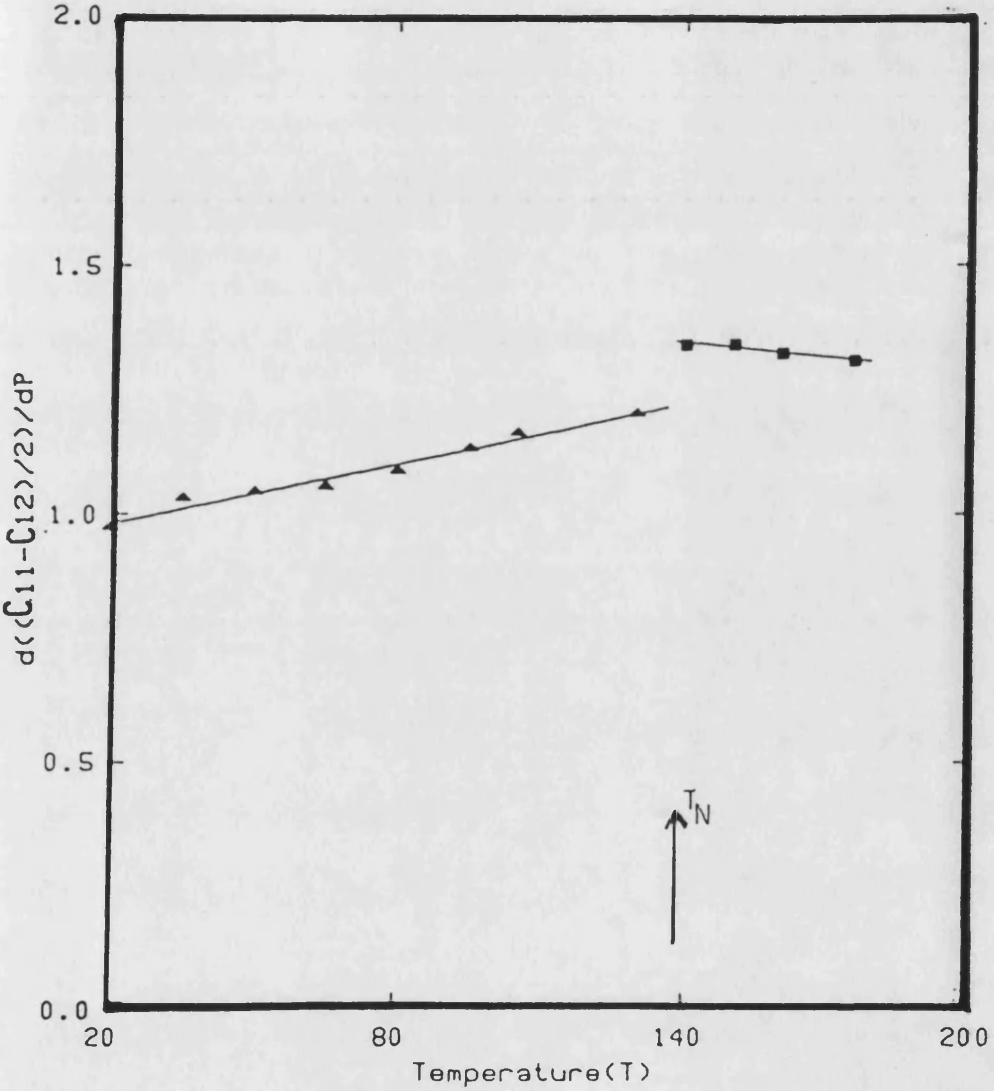

Temperature dependence of hydrostatic pressure derivatives of second order elastic stiffness of Mn(73)Ni(27) single crystal for a shear acoustic wave propagates in the [110] direction.

Fig 6.19a

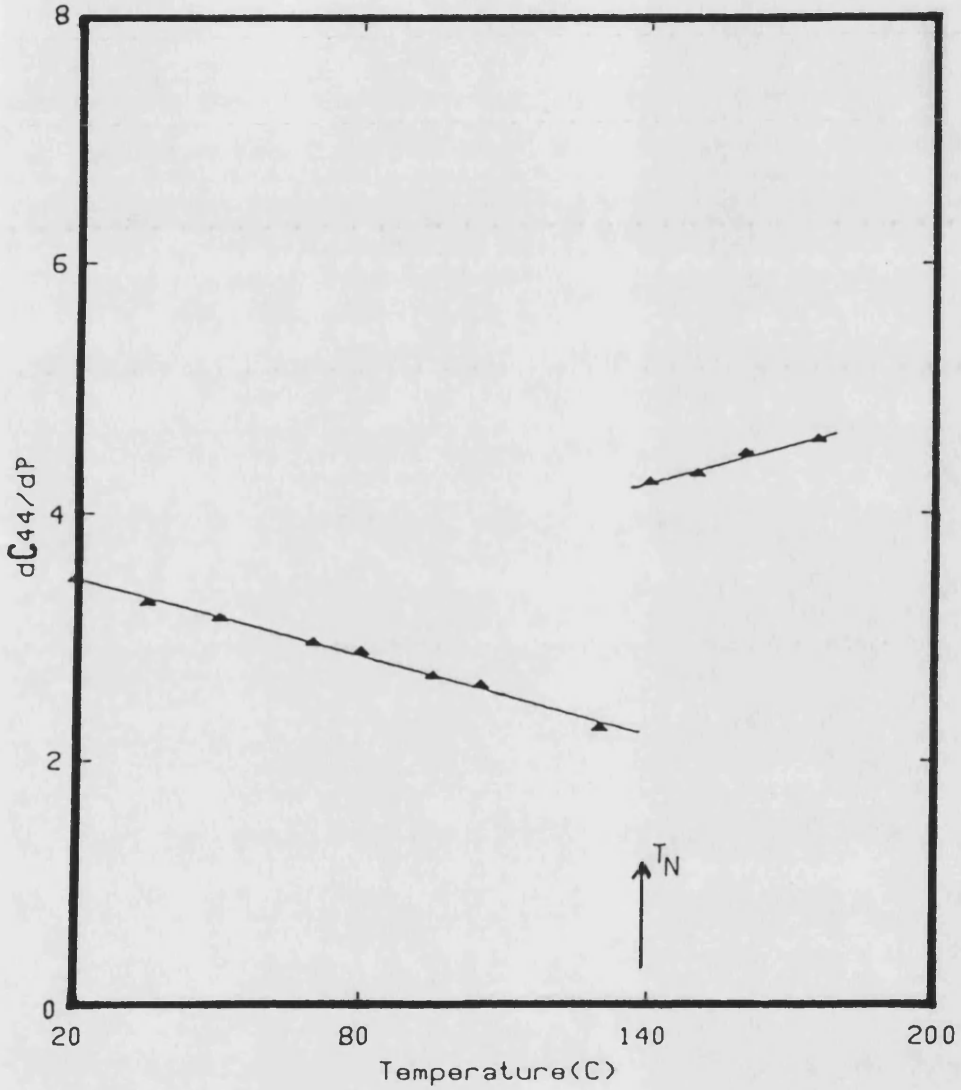

Temperature dependence of hydrostatic pressure derivatives of second order elastic stiffness of Mn(73)Ni(27) single crystal for a shear acoustic wave propagates in the [110] direction.

Fig 6.20a

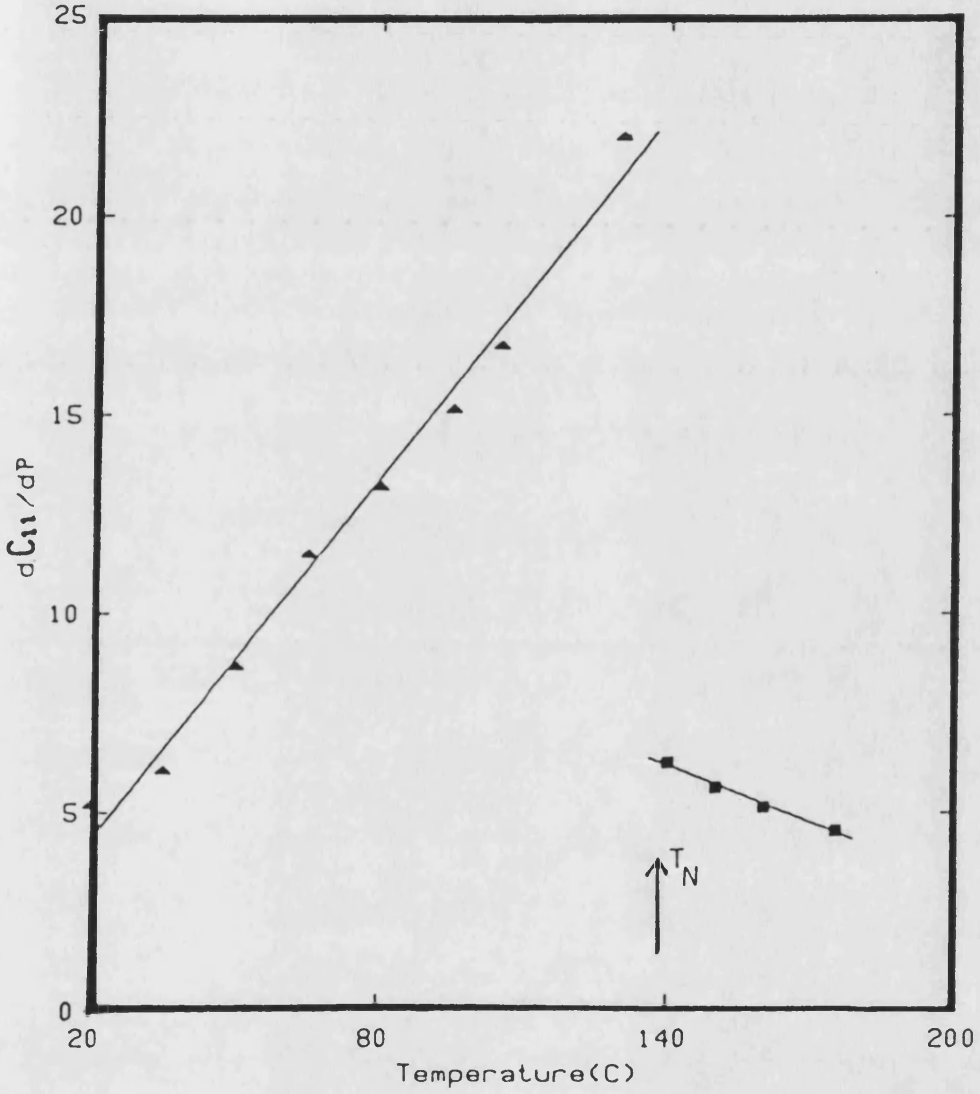

Temperature dependence of hydrostatic pressure derivatives of second order elastic stiffness (C_{11}) of Mn(73)Ni(27) single crystal.

Fig 6.21a

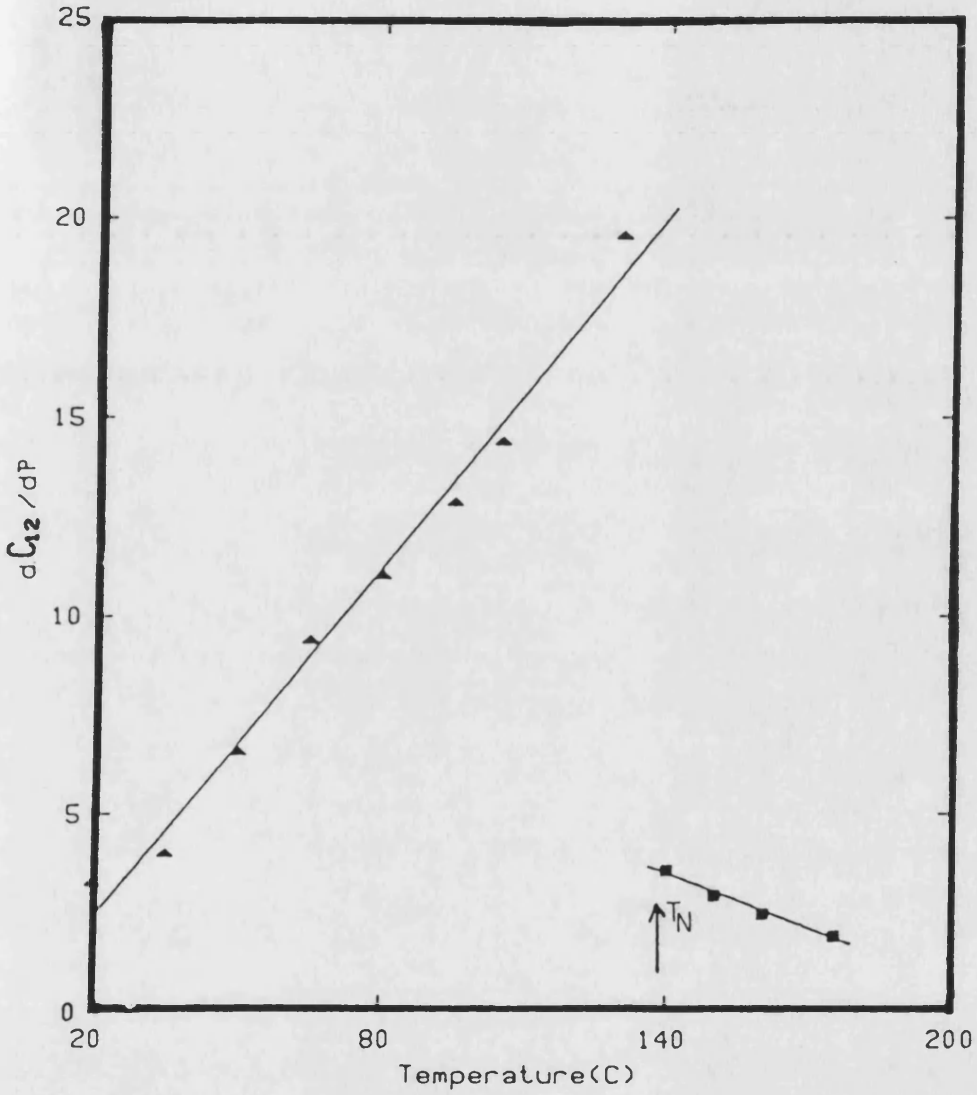

Temperature dependence of hydrostatic pressure derivatives of second order elastic stiffness (C_{12}) of Mn(73)Ni(27) single crystal.

Fig 6.22a

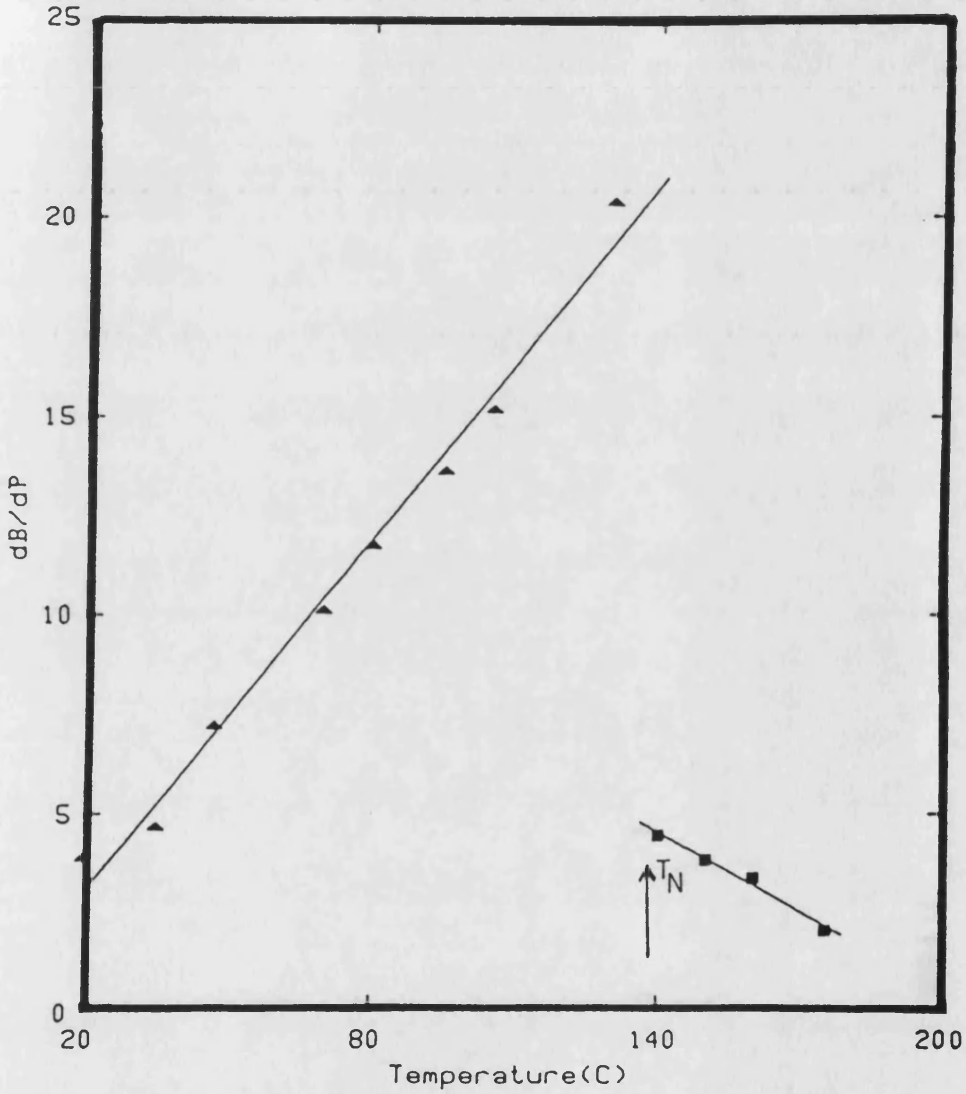

Temperature dependence of the pressure derivatives of bulk modulus of Mn(73)Ni(27) single crystal.

Fig 6.23a

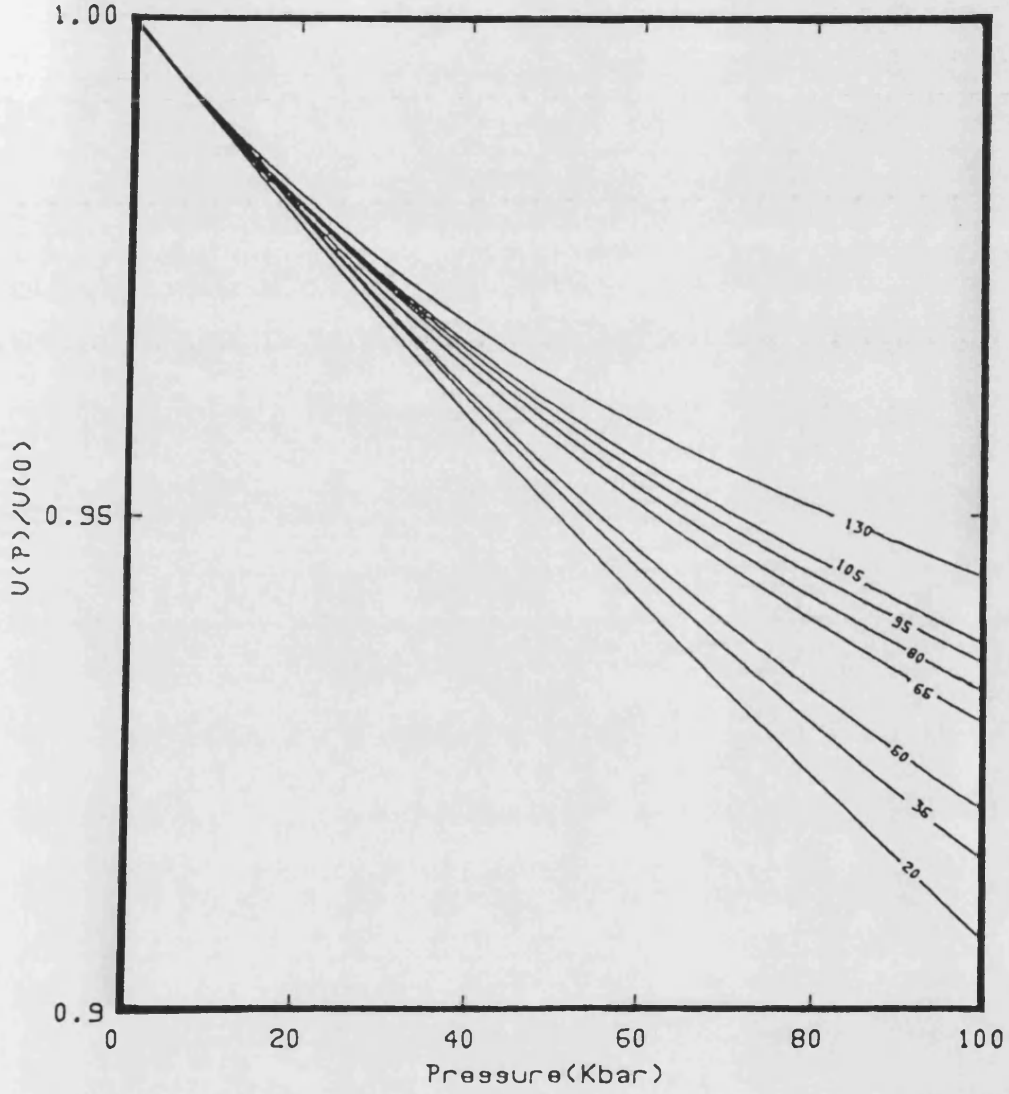

The compression V(P)/V(0) of Mn(73)Ni(27) single crystal in the anti-ferromagnetic phase based on the Murnaghan equation-of-state.

Fig 6.24a

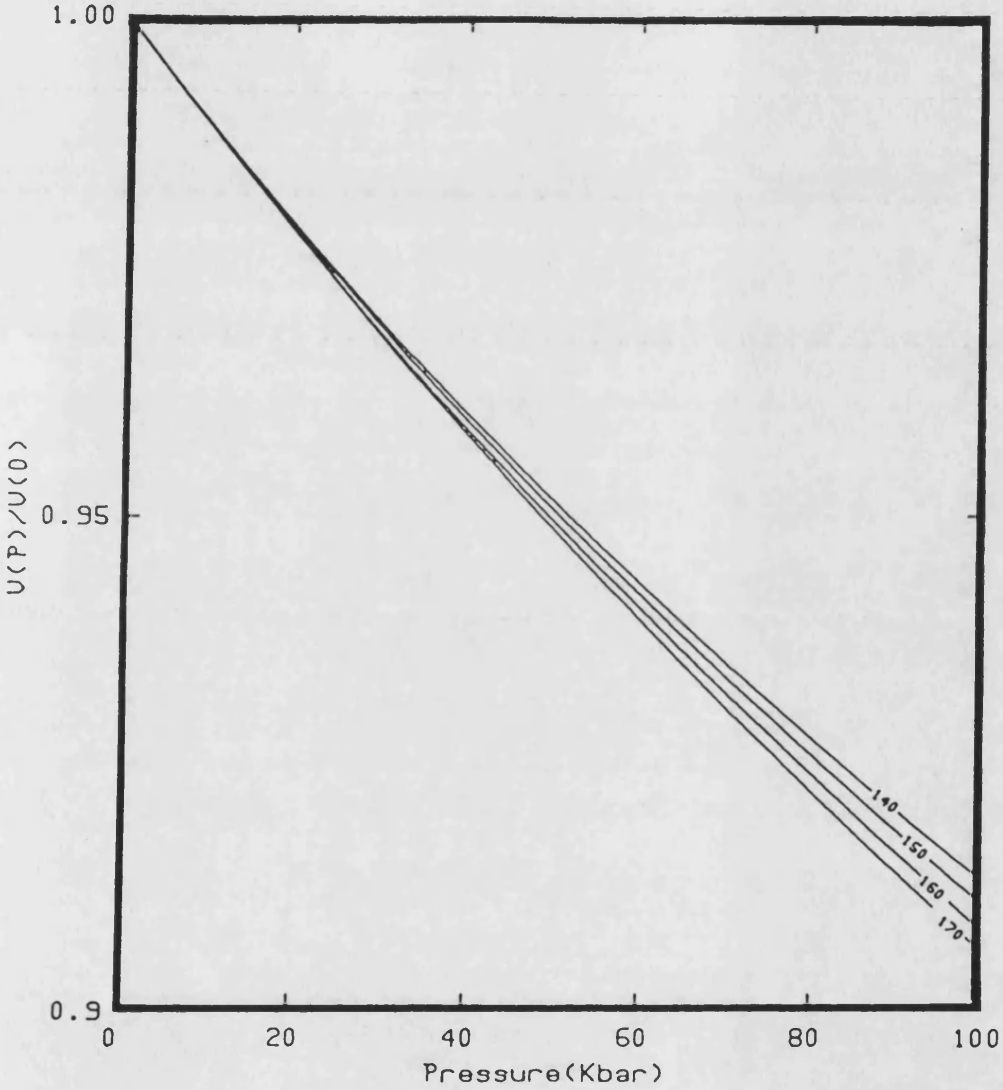

The compression V(P)/V(0) of Mn(73)Ni(27) single crystal in the paramagnetic phase based on the Murnaghan equation-of-state.

Fig 6.25a

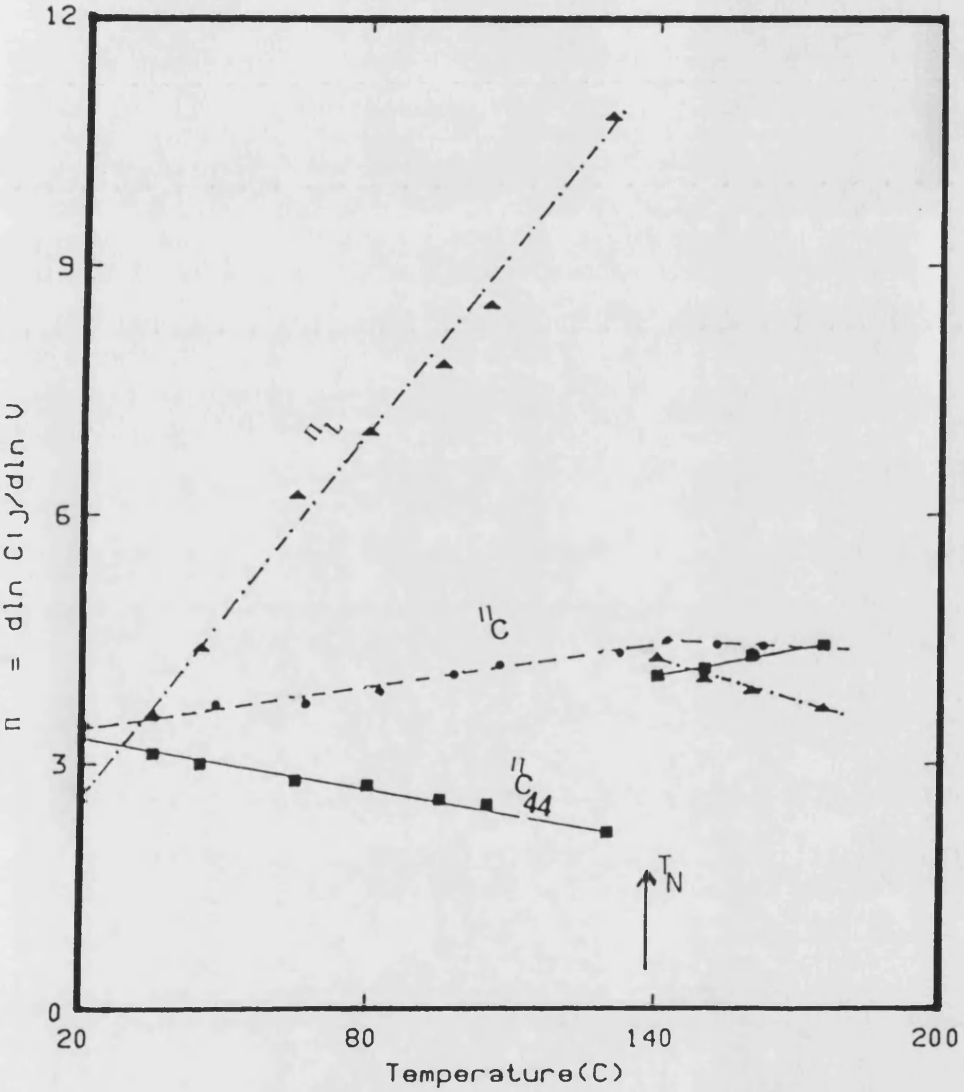

Temperature dependence of logarithmic volume derivatives of the second order elastic stiffness for longitudinal and shear modes propagate in the [110] direction of Mn(73)Ni(27) single crystal.

Fig 6.26a

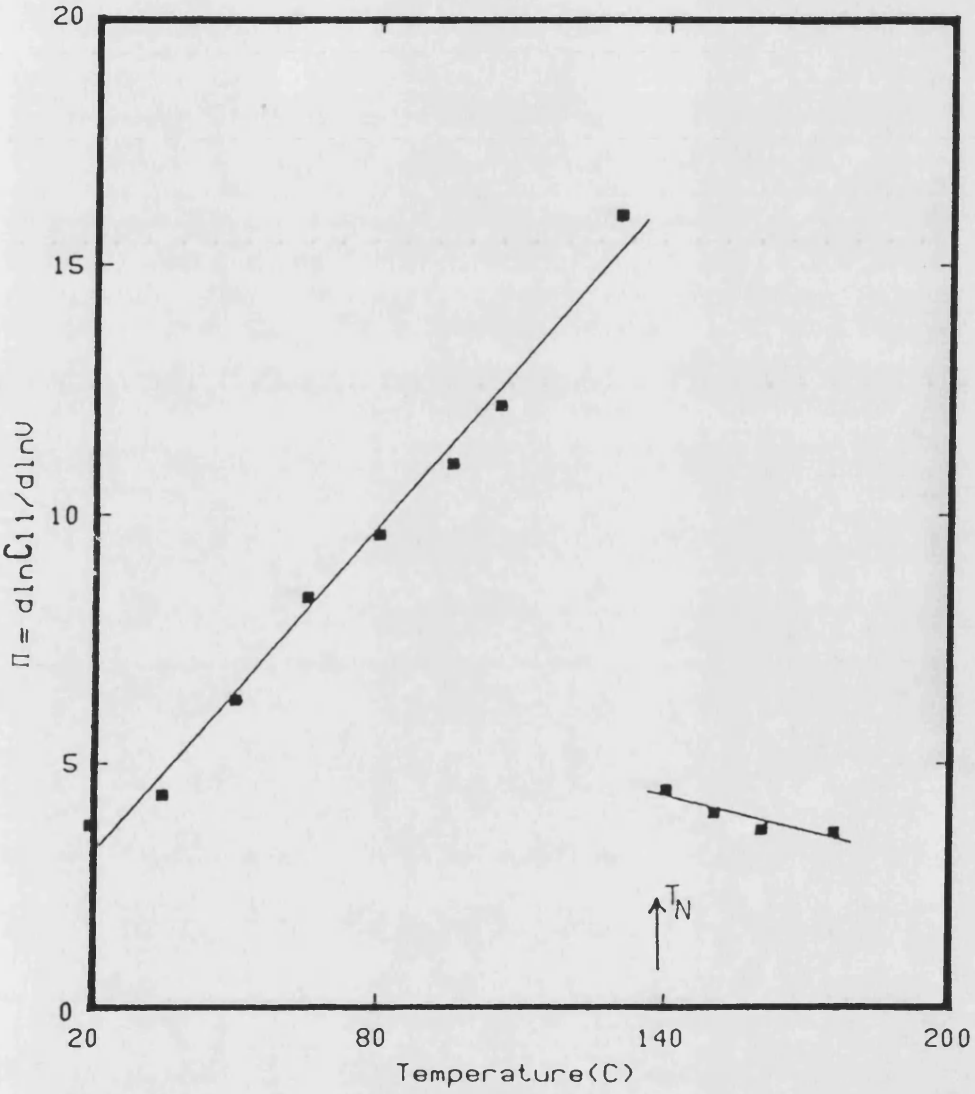

Temperature dependence of logarithmic volume derivatives of C_{11} of Mn(73)Ni(27) single crystal.

Fig 6.27a

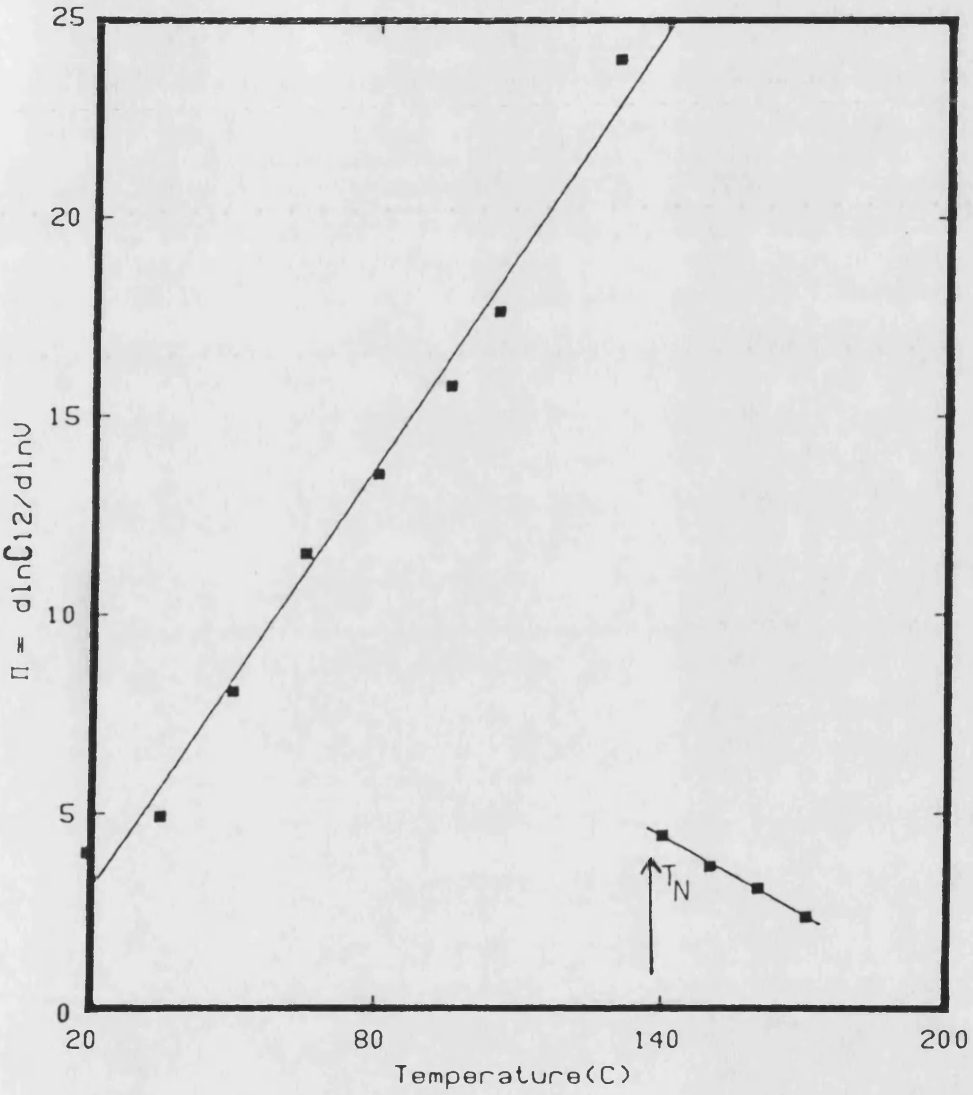

Temperature dependence of logarithmic volume derivatives of C_{12} of Mn(73)Ni(27) single crystal.

Fig 6.28a

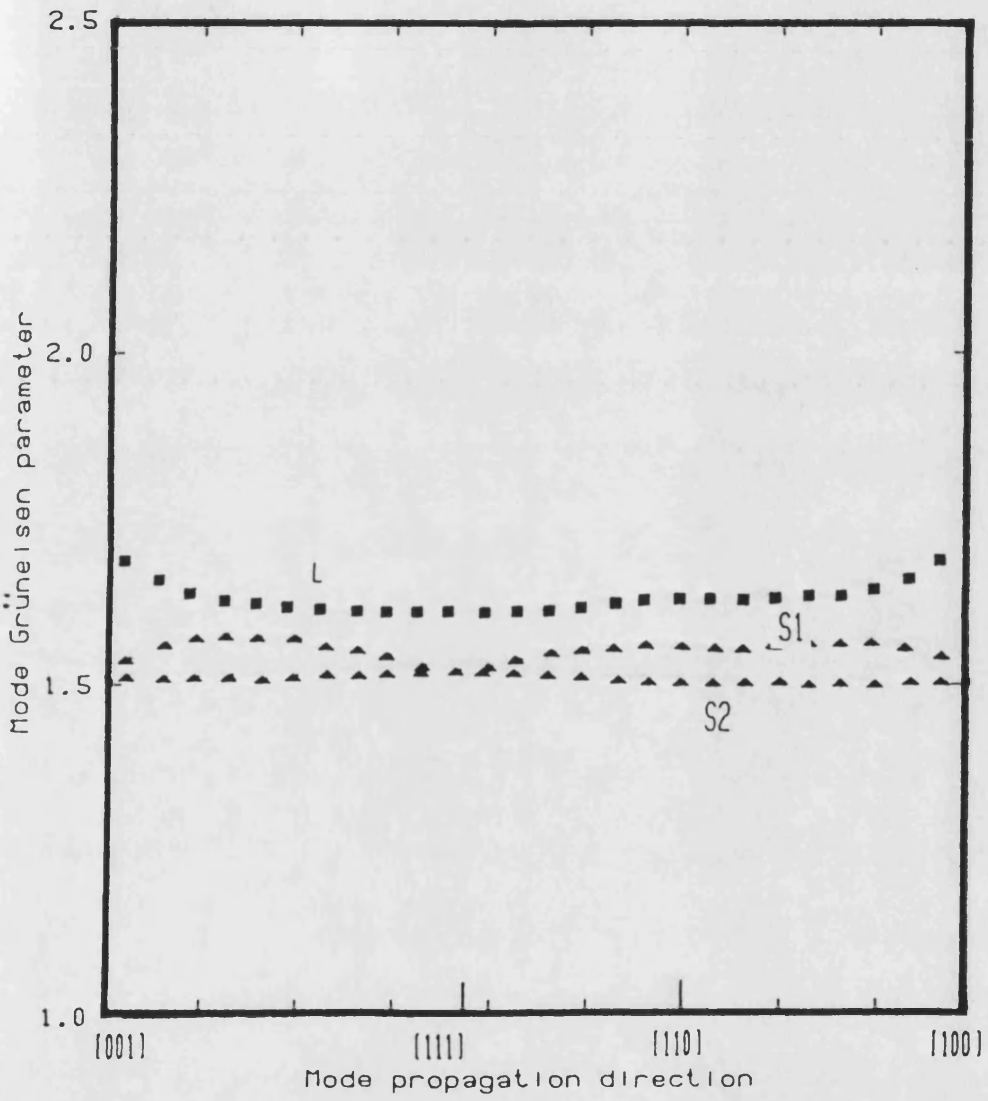

Directional dependence of long wavelength acoustic mode Grüneisen parameters of the Mn(73)Ni(27) single crystal at 20C .

Fig 6.29a

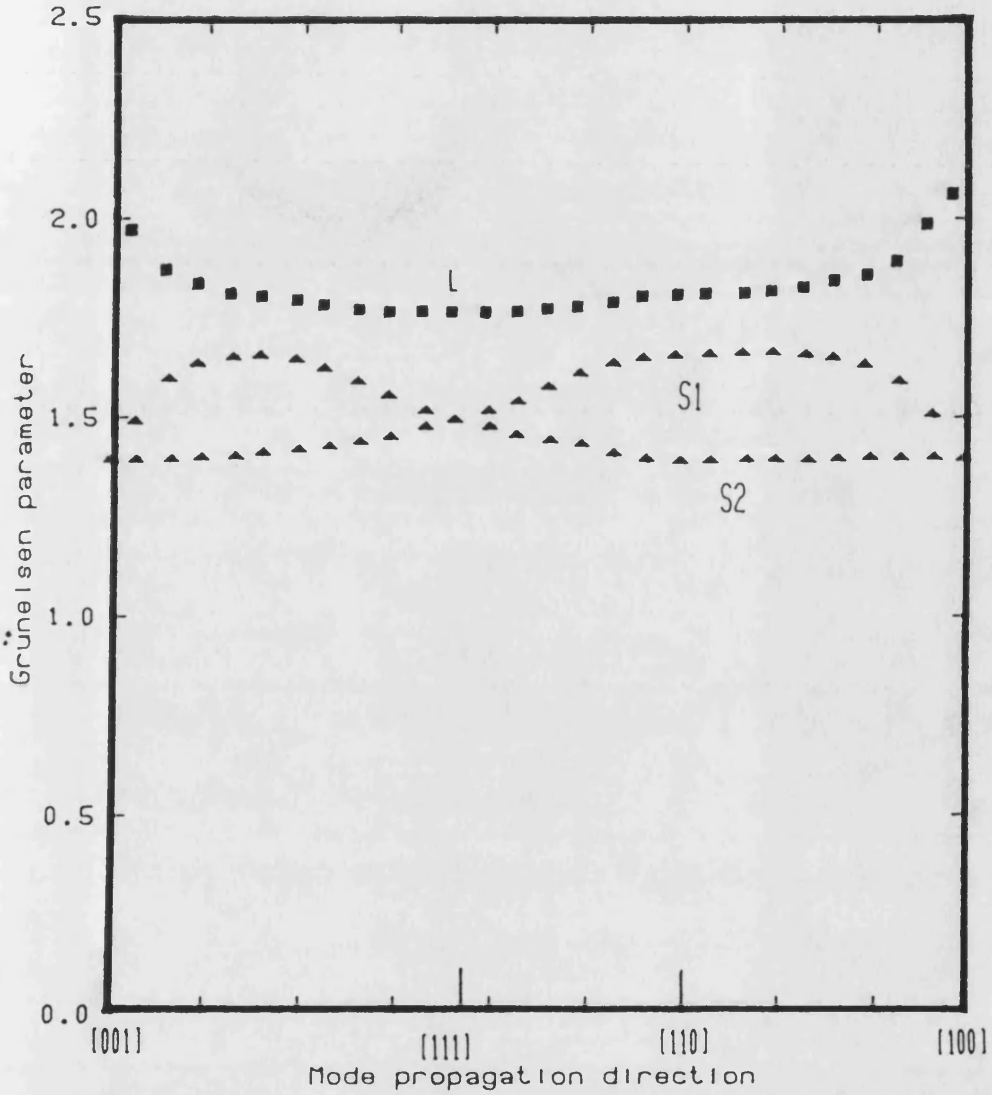

Directional dependence of long wavelength acoustic mode Grünelsen parameters of the Mn(73)Ni(27) single crystal at 35C .

Fig 6.30a

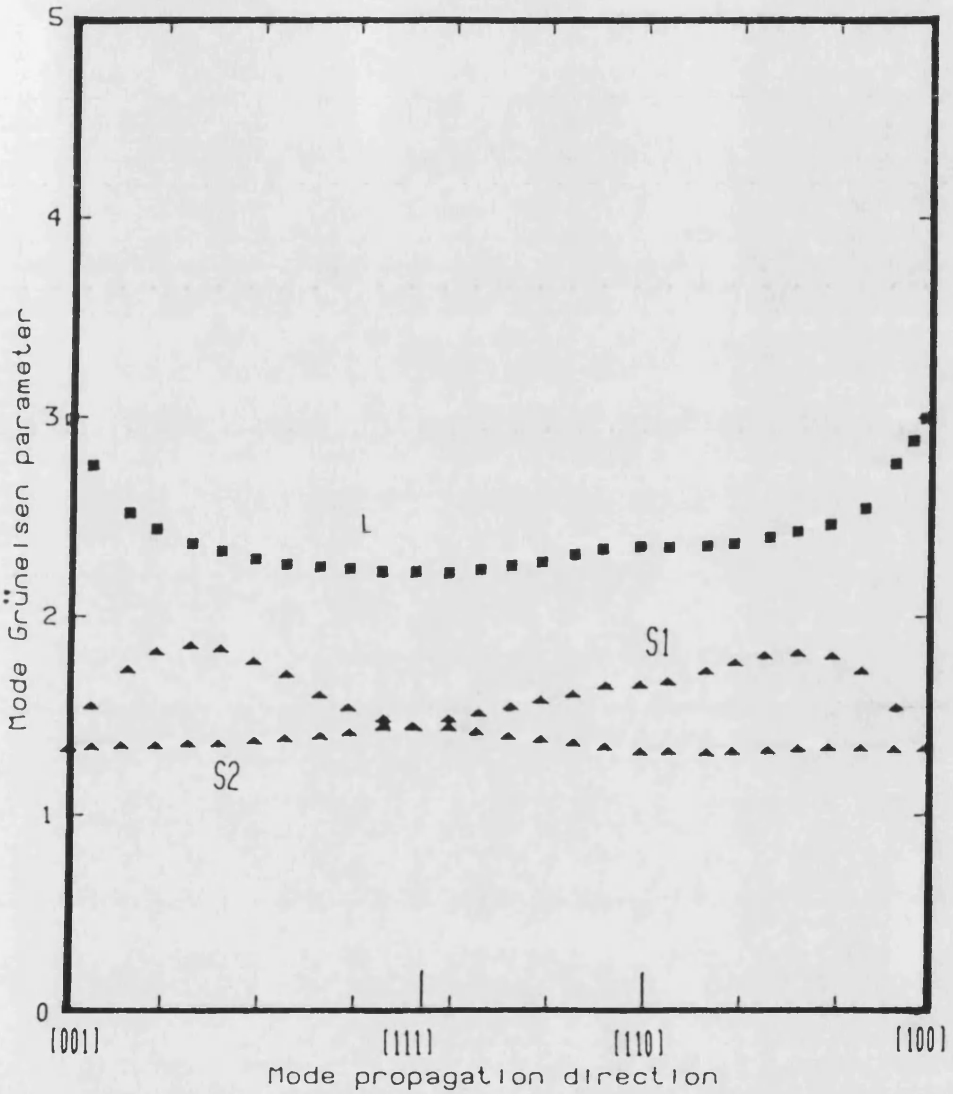

Directional dependence of long wavelength acoustic mode Grüneisen parameters of the Mn(73)Ni(27) single crystal at 50C .

Fig 6.31a

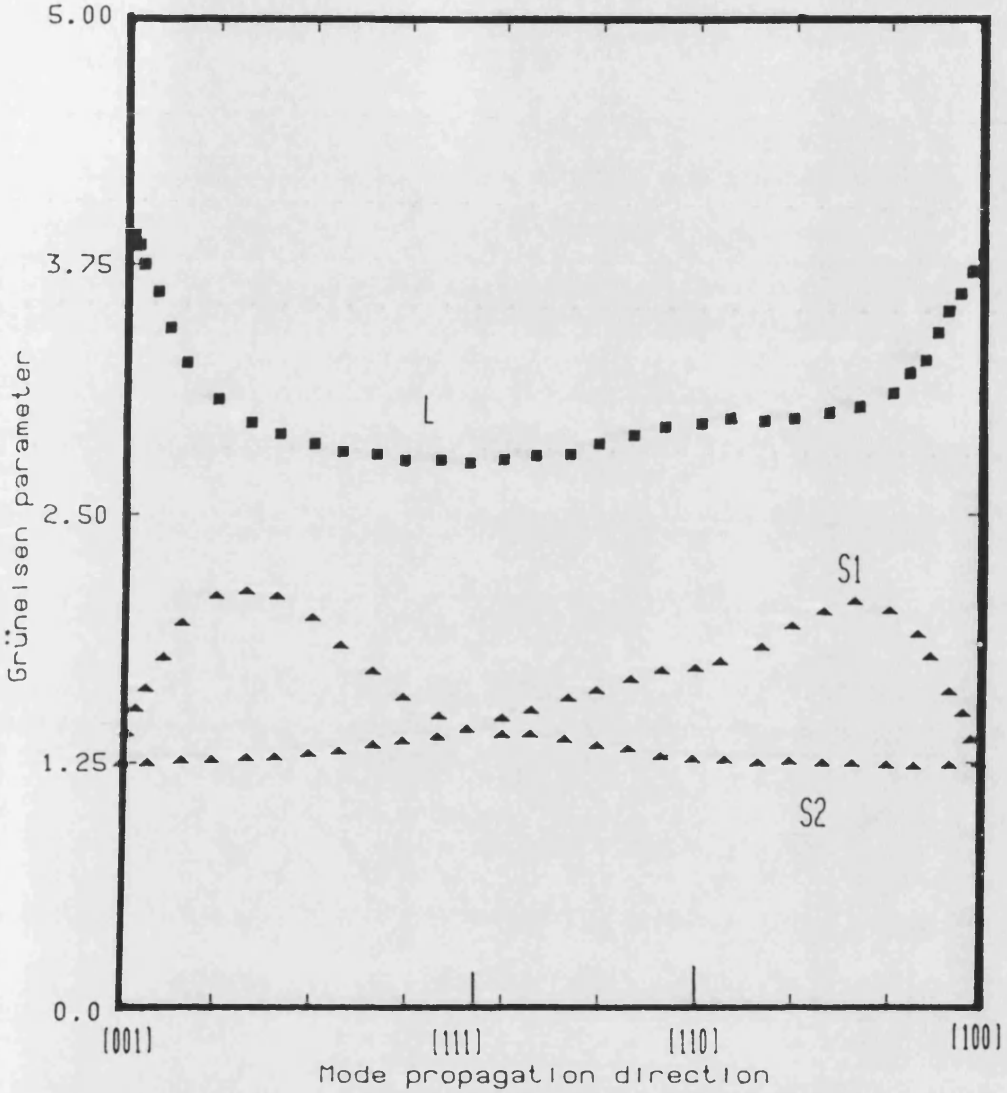

Directional dependence of long wavelength acoustic mode Grüneisen parameters of the Mn(73)Ni(27) single crystal at 65C .

Fig 6.32a

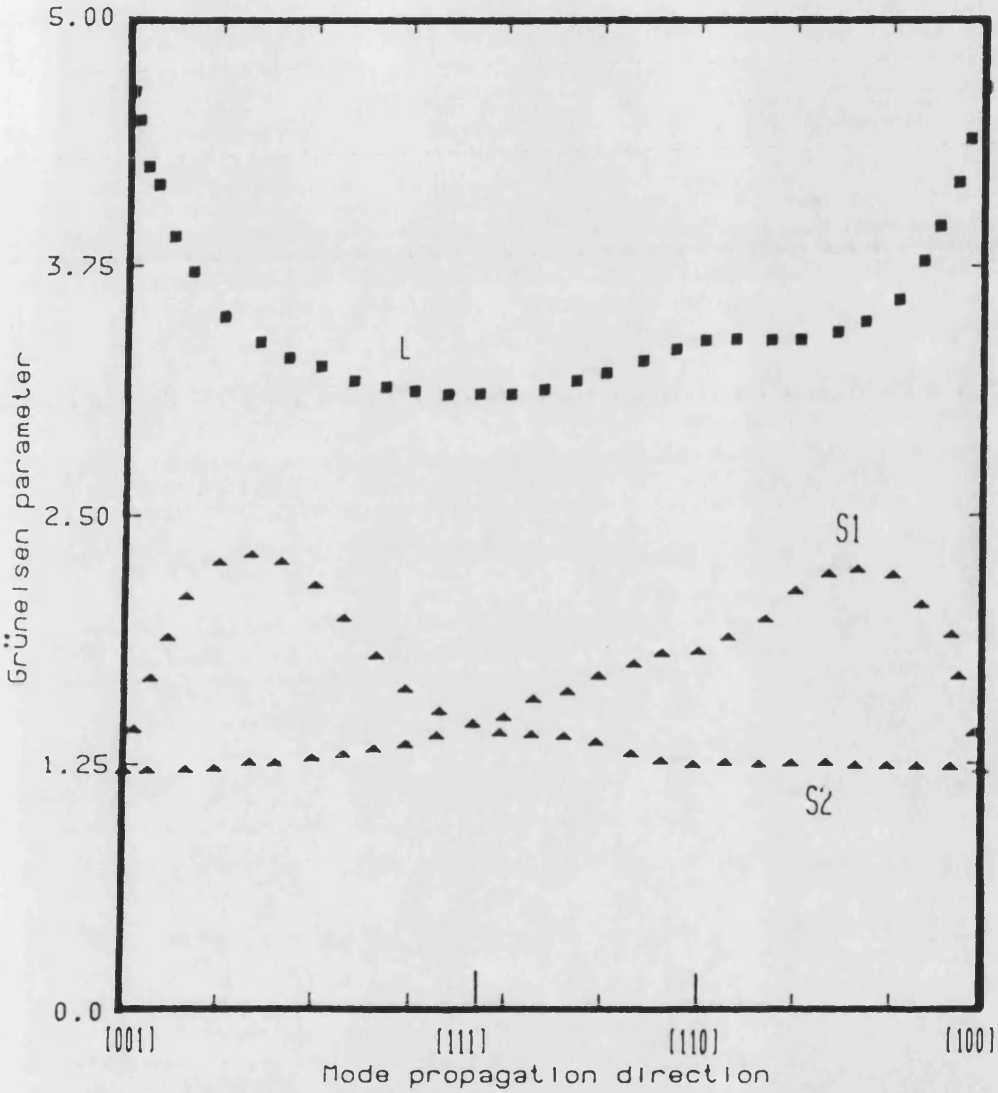

Directional dependence of long wavelength acoustic mode Grünelsen parameters of the Mn(73)Ni(27) single crystal at 75C .

Fig 6.33a

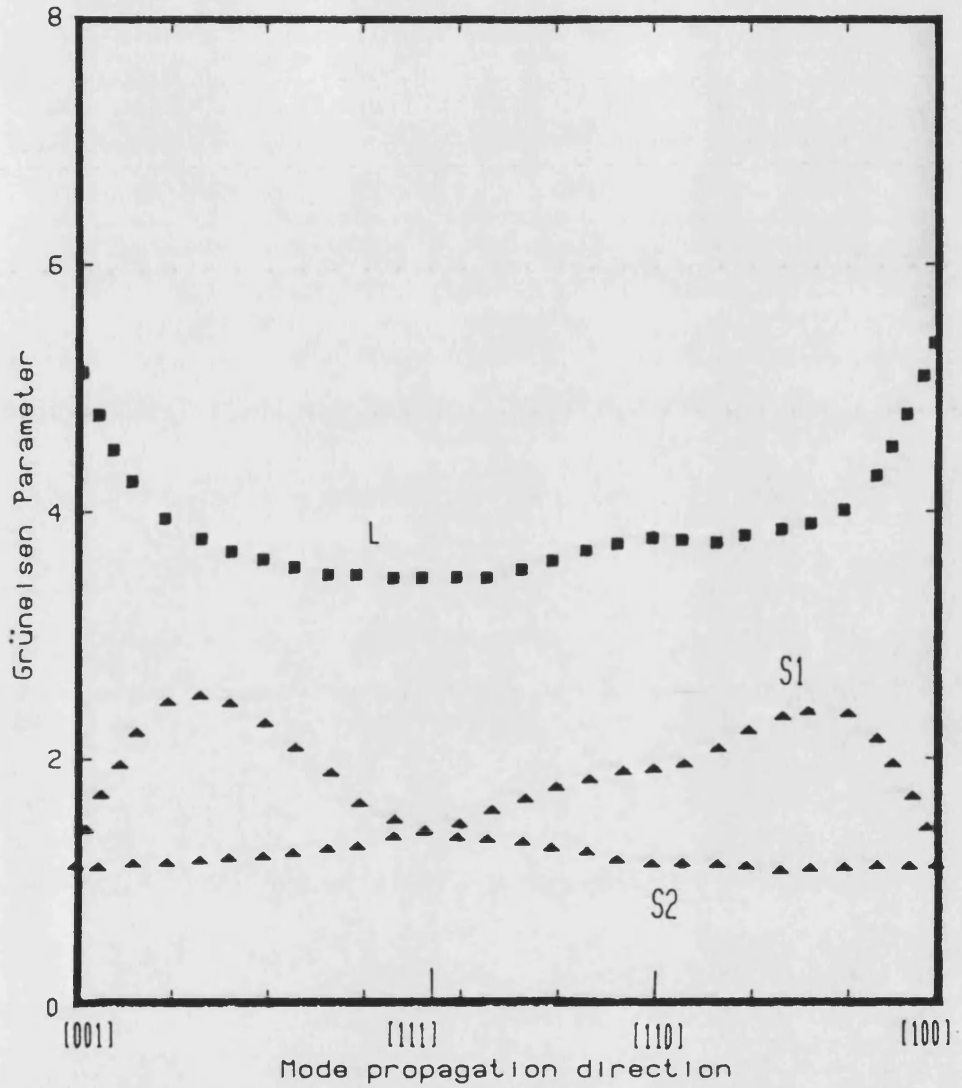

Directional dependence of long wavelength acoustic mode Grüneisen parameters of the Mn(73)Ni(27) single crystal at 95C .

Fig 6.34a

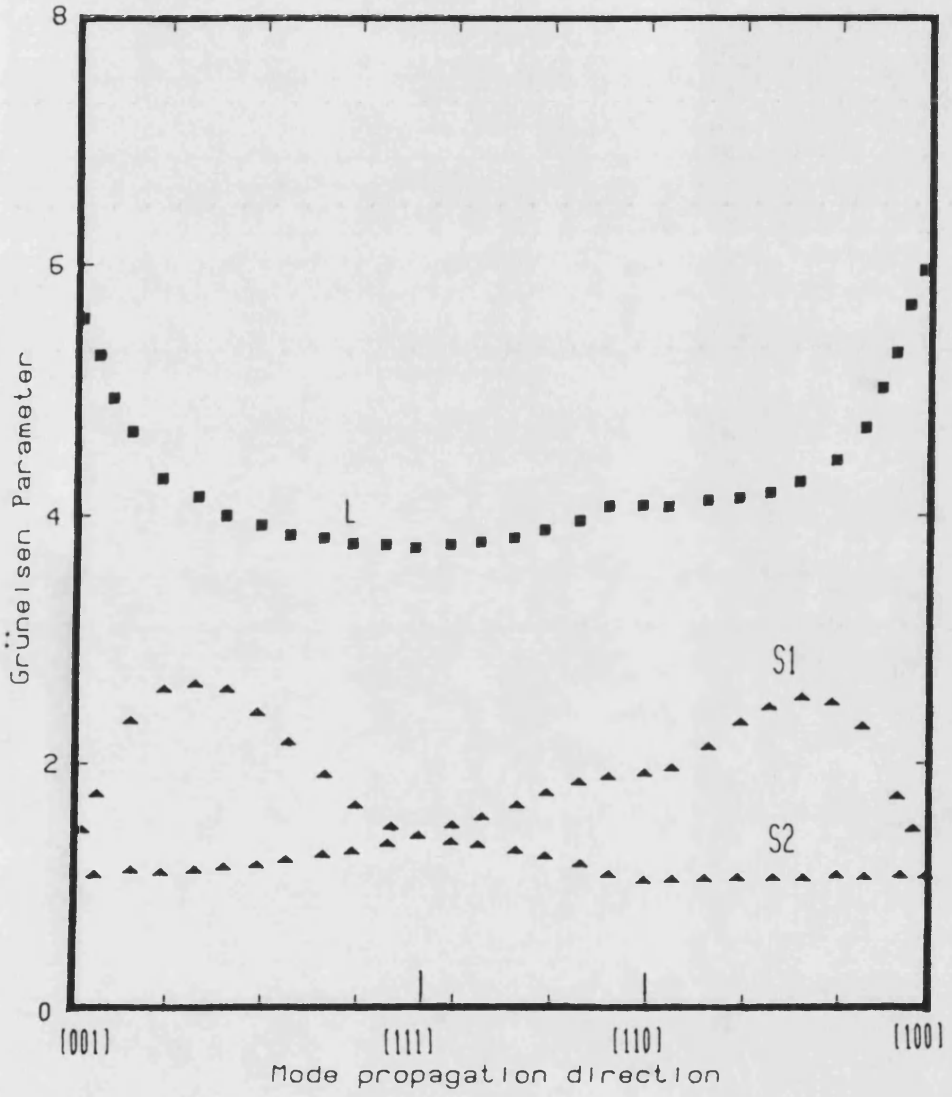

Directional dependence of long wavelength acoustic mode Grüneisen parameters of the Mn(73)Ni(27) single crystal at 105C.

Fig 6.35a

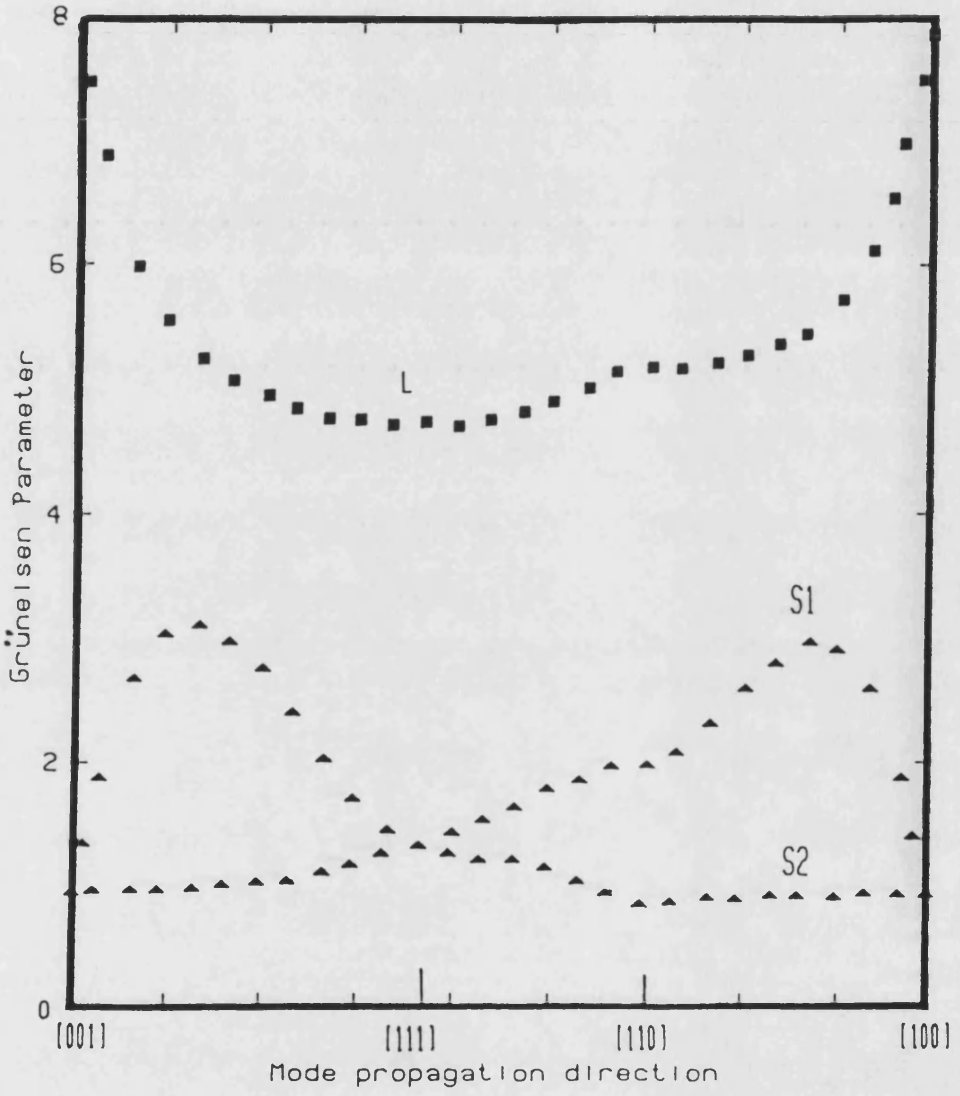

Directional dependence of long wavelength acoustic mode Grünelsen parameters of the Mn(73)Ni(27) single crystal at 130C.

Fig 6.36a

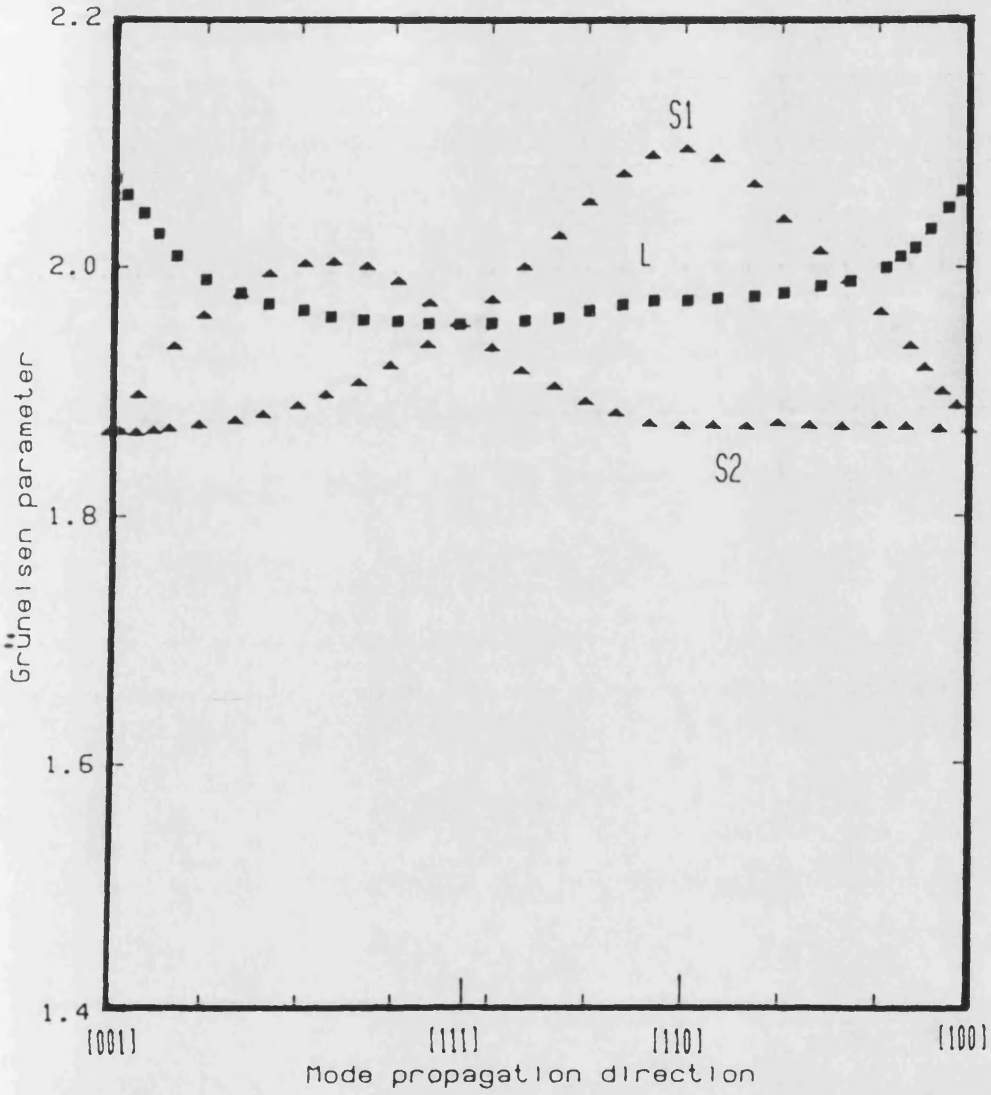

Directional dependence of long wavelength acoustic mode Grüneisen parameters of the Mn(73)Ni(27) single crystal at 140C .

Fig 6.37a

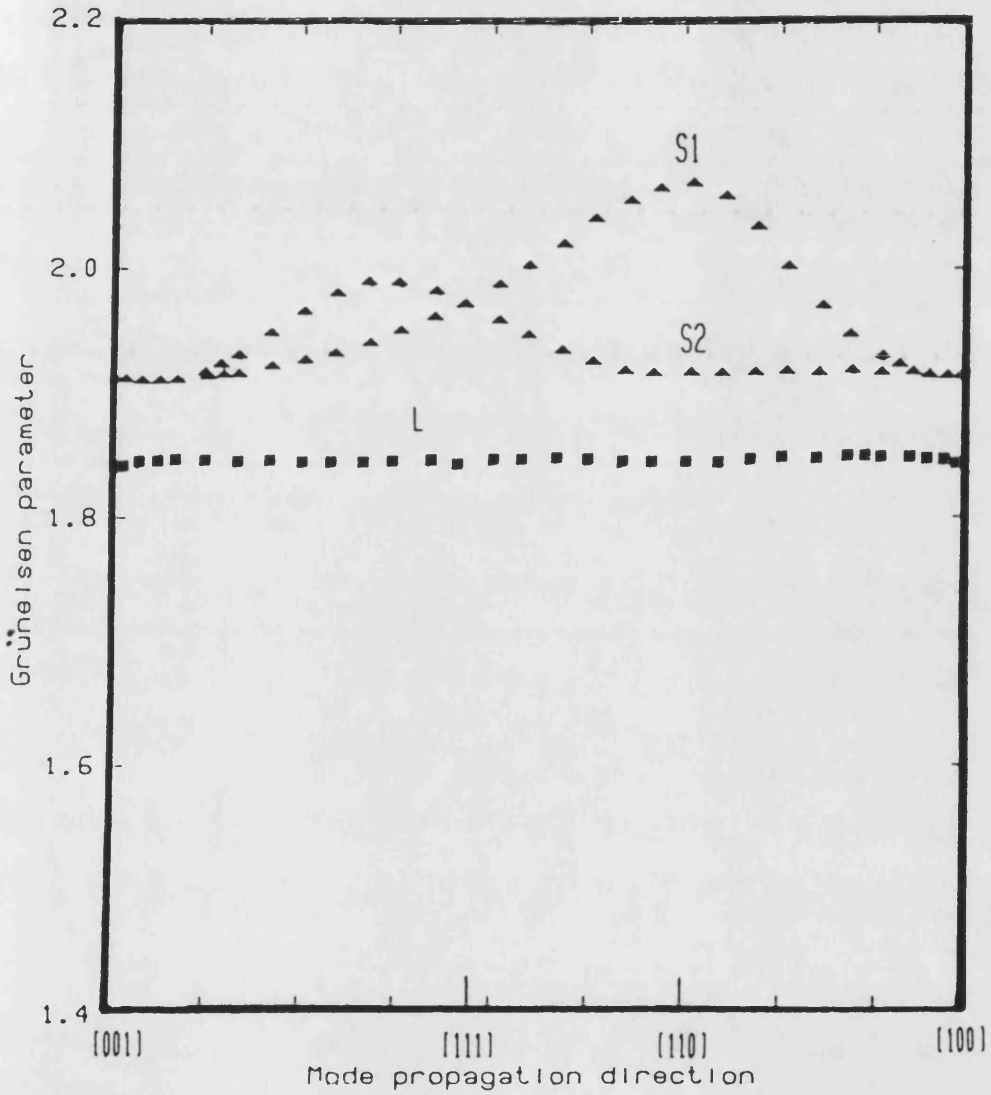

Directional dependence of long wavelength acoustic mode Grünelsen parameters of the Mn(73)Ni(27) single crystal at 150C.

Fig 6.38a

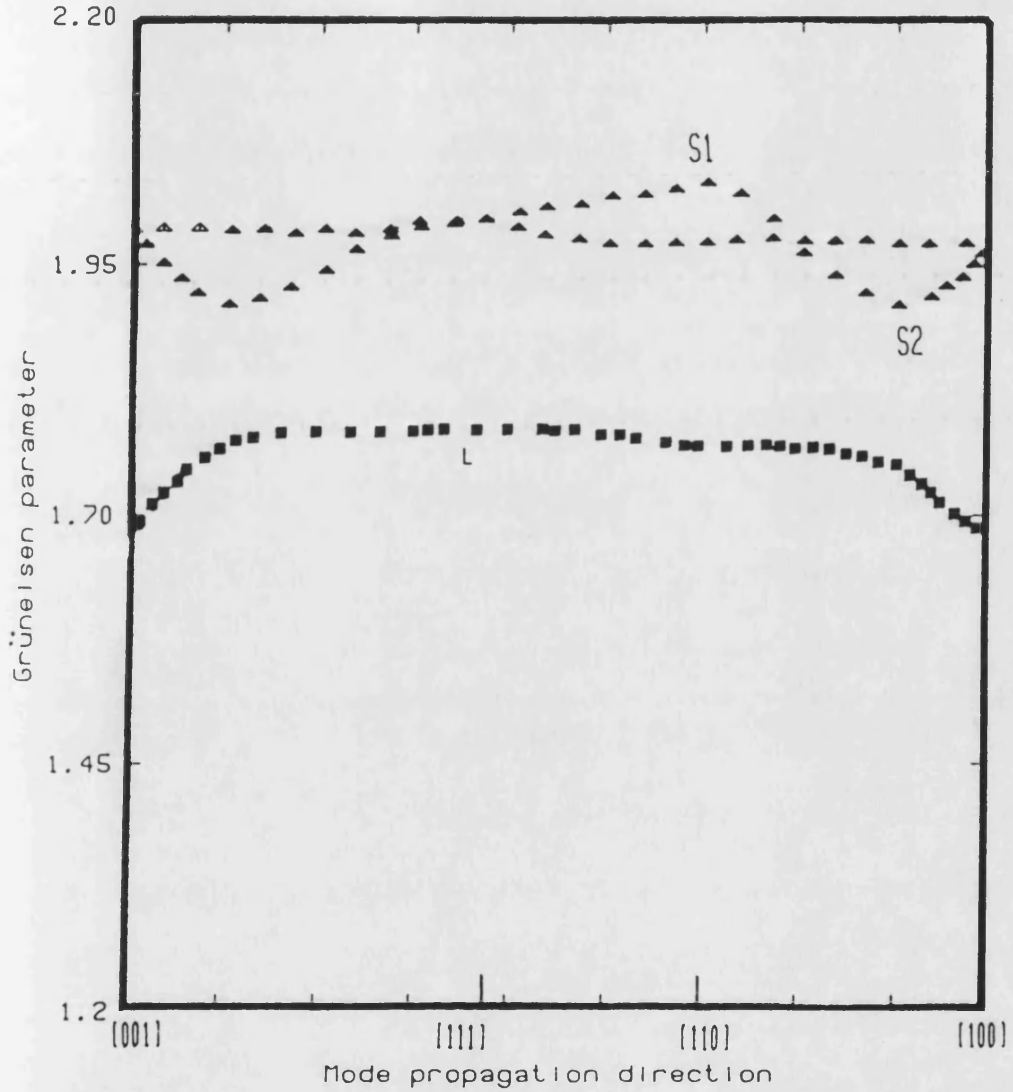

Directional dependences of long wavelength acoustic mode Grünelsen parameters of Mn(73)Ni(27) single crystal at 160C

Fig 6.39a

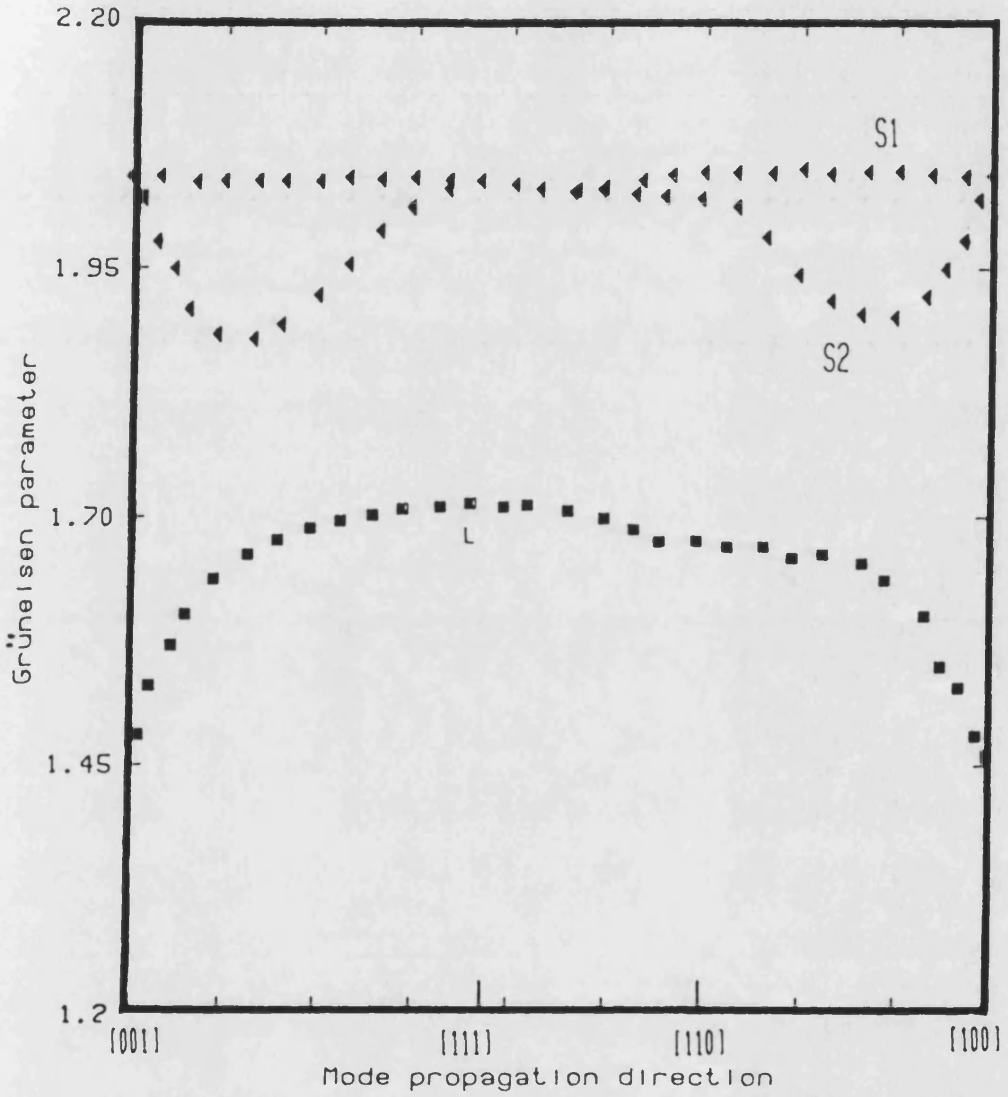

Directional dependences of long wavelength acoustic mode Grünelsen parameters of Mn(73)Ni(27) single crystal at 170C

Fig 6.40a

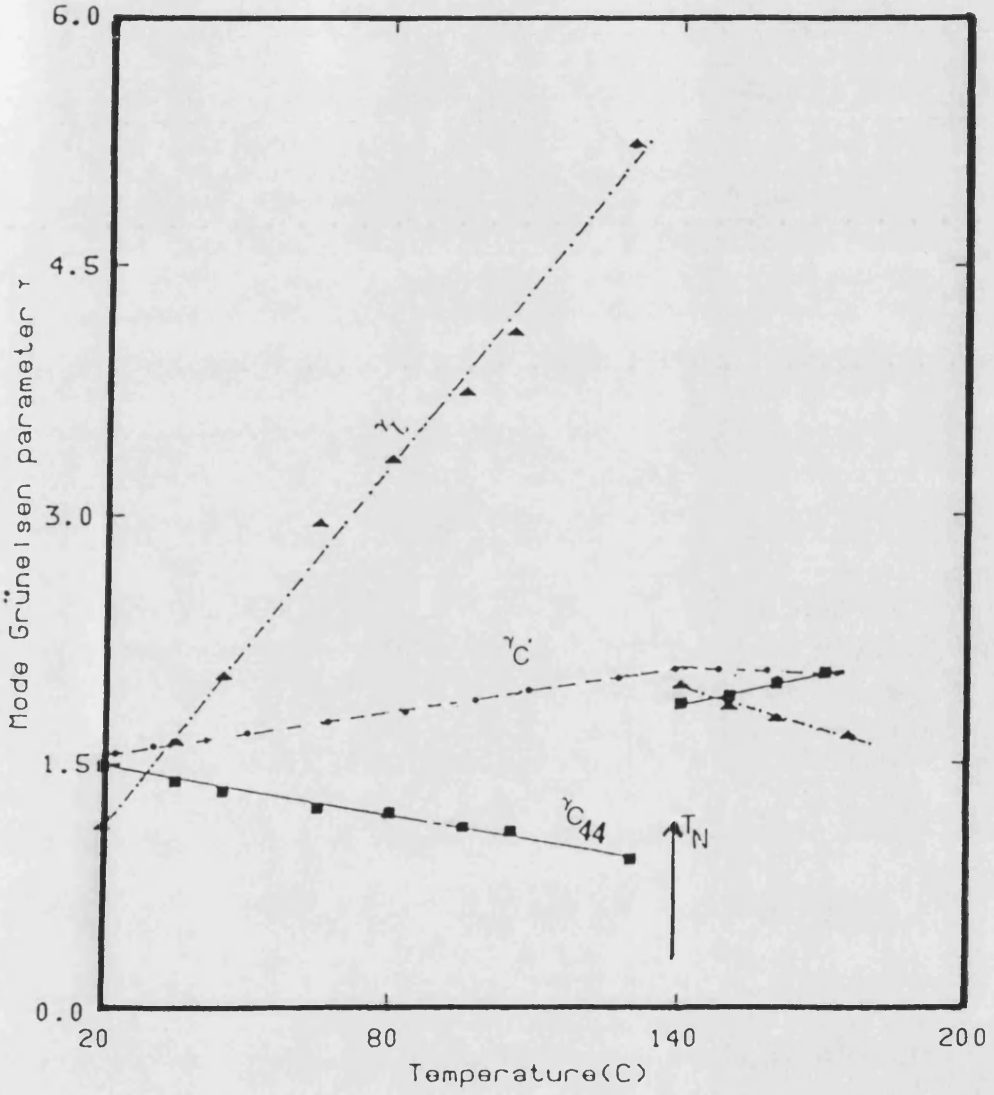

Temperature dependence of acoustic mode Grüneisen parameters in the [110] direction of the Mn(73)Ni(27) single crystal.

Fig 6.41a

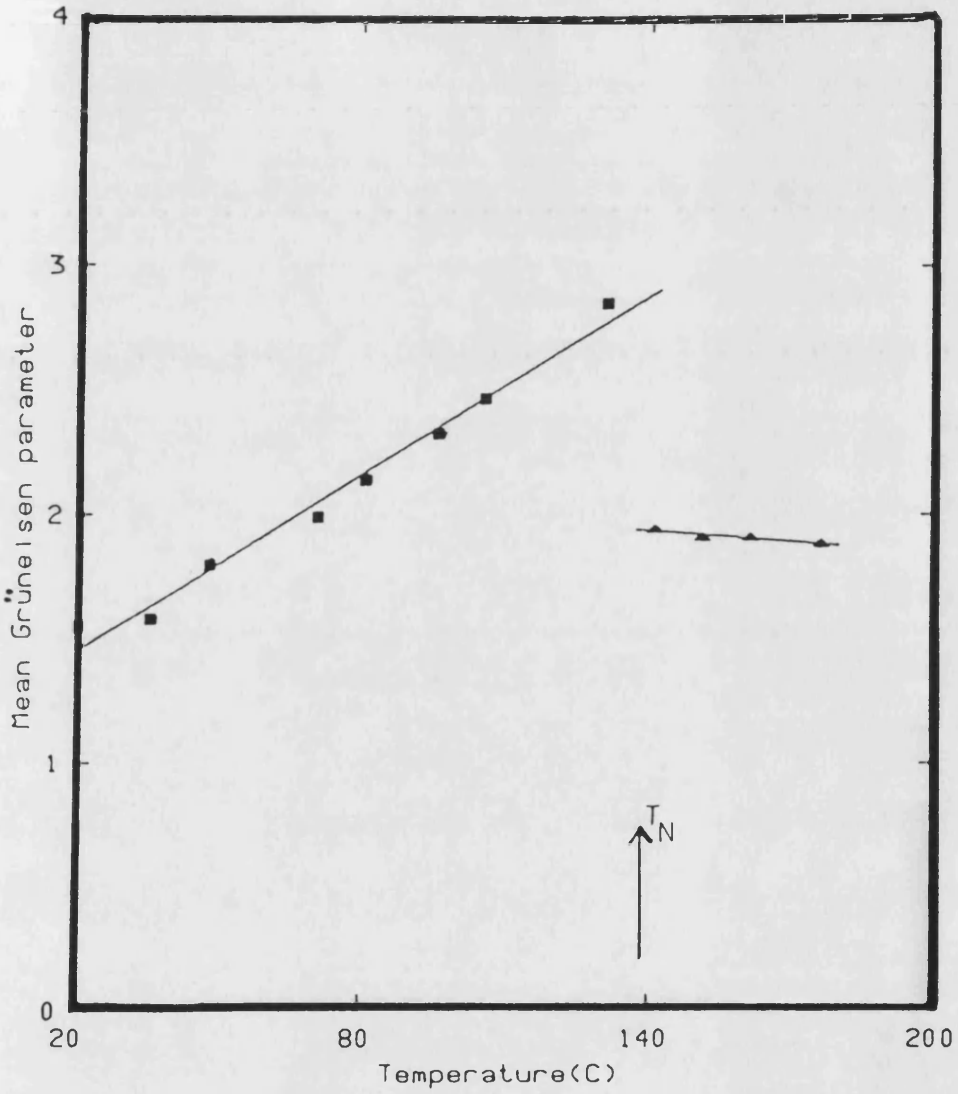

Temperature dependence of acoustic mode mean Grüneisen parameter of Mn(73)Ni(27) single crystal in anti-ferromagnetic and paramagnetic phases.

Fig 6.42a

SECTION B. EXPERIMENTAL RESULTS OBTAINED ON TWO TERNARY ALLOYS Mn-Ni-C ($Mn_{85}Ni_9C_6$-SAMPLE C2 AND $Mn_{85}Ni_9C_6$-SAMPLE F).

Table 6.1b. The basic parameter and crystal orientations of ternary $Mn_{85}Ni_9C_6$ alloy single crystals on which ultrasonic velocity measurements have been made

	Thickness (mm)	density (kgm^{-3})	Neel Temp.(C)	Associated SOEC	Mode(N) Direction	Polarisation Vector(U)
$Mn_{85}Ni_9C_6$ sample C2	3.78	6970	320	C_L	[110]	[110]
				C'	[110]	[110]
				C_{44}	[110]	[001]
$Mn_{85}Ni_9C_6$ sample F	3.22	7055	274	C_{11}	[001]	[001]
				C_{44}	[001]	in (100) plane
	7.47			C_L	[110]	[110]
				C'	[110]	[110]

Table 6.2b. The room temperature second order elastic stiffness constants of ternary alloy $Mn_{85}Ni_9C_6$ single crystals.

N	U	C_{IJ}	f(khz)	Observed velocity (ms^{-1})	Corrected velocity (ms^{-1})	ρV^2 ($10^{10}Nm^{-2}$)
$Mn_{85}Ni_9C_6$ (sample C2)						
[110]	[110]	C_L	675	5103	5150	18.4
[110]	[110]	C'	201	1520	1528	1.7
[110]	[001]	C_{44}	515	3893	3927	10.6
$Mn_{85}Ni_9C_6$ (sample F)						
[001]	[001]	C_{11}	549	3537	3585	8.8
[001]in plane	(001)	C_{44}	595	3833	3870	10.4
[110]	[110]	C_L	342	5109	5173	18.4
[110]	[110]	C'	71	1060	1065	0.8

Table 6.3b. Temperature dependence of the second order elastic stiffness constants and elastic compliances of ternary alloy $Mn_{85}Ni_9C_6$ single crystal (sample C2). C' is $(C_{11}-C_{12})/2$

Temp. (°C)	C_{11}	C_{12}	C_{44}	C'	S_{11}	S_{12}	S_{44}
		($10^{10}Nm^{-2}$)			($10^{-11}m^2N^{-1}$)		
20	8.70	6.03	10.57	1.34	2.74	-1.13	0.95
35	8.68	5.96	10.51	1.36	2.61	-1.06	0.95
50	8.64	5.92	10.49	1.36	2.61	-1.06	0.95
75	8.62	5.90	10.34	1.36	2.61	-1.06	0.97
90	8.60	5.87	10.32	1.37	2.61	-1.06	0.97
115	8.59	5.85	10.24	1.37	2.59	-1.05	0.98
125	8.58	5.80	10.21	1.39	2.59	-1.04	0.98
140	8.57	5.78	10.05	1.40	2.55	-1.03	0.99
165	8.55	5.68	9.98	1.44	2.53	-1.01	1.00
280	8.47	5.32	9.40	1.56	2.29	-0.88	1.06
300	8.25	5.10	9.30	1.58	2.29	-0.88	1.07
325	8.07	4.98	9.24	1.55	2.35	-0.89	1.08
340	7.95	4.90	9.03	1.53	2.37	-0.91	1.11

Table 6.4b. Temperature dependence of the second order elastic stiffness constants and elastic compliances of binary alloy $Mn_{85}Ni_9C_6$ single crystal (sample F).
C' is $(C_{11}-C_{12})/2$

Temp. (°C)	C_{11}	C_{12}	C_{44}	C'	S_{11}	S_{12}	S_{44}
		(10^{10} Nm-2)			($10^{-11}m^2N^{-1}$)		
20	8.81	7.22	10.40	0.80	4.34	-1.96	0.96
60	8.42	6.76	9.90	0.83	4.16	-1.85	1.01
80	8.12	6.50	9.60	0.81	4.29	-1.9	1.04
125	7.53	5.80	9.22	0.87	4.02	-1.8	1.08
145	7.28	5.60	9.01	0.84	4.16	-1.81	1.10
155	7.12	5.41	8.88	0.88	4.09	-1.76	1.12
170	7.67	5.32	8.72	1.18	3.02	-1.23	1.13
190	7.09	5.33	8.58	0.88	3.98	-1.71	1.17
255	7.32	5.50	7.95	0.91	3.84	-1.64	1.30
275	7.30	5.41	7.80	0.95	3.78	-1.61	1.28
295	7.21	5.33	7.79	0.94	3.75	-1.60	1.28
310	7.11	5.20	7.06	0.96	3.80	-2.20	1.32

Table 6.5b. Temperature dependence of bulk modulus and compressibilities of ternary alloy $Mn_{8.5}Ni_9C_6$ single crystal (sample C2).

Temp. (°C)	Anistropic ratio	Bulk Modulus (10^{10} Nm^{-2})	Volume compress. ($10^{-10}m^2N^{-1}$)	Linear compress.
20	0.13	6.92	0.15	0.048
35	0.13	6.86	0.15	0.049
50	0.13	6.83	0.15	0.049
75	0.13	6.78	0.15	0.049
90	0.13	6.76	0.15	0.049
115	0.13	6.75	0.15	0.048
125	0.13	6.73	0.15	0.049
140	0.14	6.71	0.15	0.050
165	0.14	6.64	0.15	0.050
280	1.67	6.37	0.16	0.052
300	1.69	6.12	0.16	0.054
324	1.67	6.01	0.17	0.055
340	1.69	5.91	0.17	0.056

Table 6.6b. Temperature dependence of bulk modulus and compressibilities of ternary alloy $Mn_{85}Ni_9C_6$ single crystal (sample F).

Temp. (°C)	Anistropic ratio	Bulk Modulus (10^{10} Nm^{-2})	Volume compress. ($10^{-10}m^2N^{-1}$)	Linear compress.
20	0.076	7.75	0.12	0.043
60	0.084	7.31	0.137	0.046
80	0.084	7.04	0.142	0.047
125	0.094	6.38	0.157	0.052
145	0.093	6.16	0.162	0.054
155	0.096	5.98	0.167	0.056
170	0.135	6.10	0.164	0.055
190	0.103	5.92	0.169	0.056
255	0.114	6.11	0.164	0.055
275	0.121	6.041	0.166	0.055
293	0.121	5.96	0.168	0.056
310	0.135	5.84	0.171	0.056

Table 6.7b The second order elastic stiffness constants and bulk modulus in the antiferromagnetic and the paramagnetic* phases at 20° C of ternary alloy $Mn_{85}Ni_9C_6$ single crystal (sample C2).

	C_L	C'	C_{44}	C_{11}	C_{12}	Bulk Modulus
		(10^{10} Nm^{-2})				($10^{10}Nm^{-2}$)
Magnetically ordered	18.4	1.7	10.6	8.70	6.03	7.23
Paramagnetic	18.0	2.21	11.0	8.57	5.48	6.85

* the back extrapolation of the paramagnetic data.

Table 6.8b The second order elastic stiffness constants and bulk modulus in the antiferromagnetic and the paramagnetic* phases at 20° C of ternary alloy $Mn_{85}Ni_9C_6$ single crystal (sample F).

	C_L	C'	C_{44}	C_{11}	C_{12}	Bulk Modulus
		($10^{10}Nm^{-2}$)				($10^{10}Nm^{-2}$)
Magnetically ordered	18.4	0.80	10.4	8.81	7.22	7.75
Paramagnetic	18.3	1.03	10.8	8.49	6.57	7.37

* The back extrapolation of the paramagnetic data.

Table 6.9b. Temperature derivatives of the second order elastic stiffness constants in the antiferromagnetic and the paramagnetic states of ternary alloys $Mn_{85}Ni_9C_6$.

	Antiferromagnetic ($x10^7 Nm^{-2}K^{-1}$)	Paramagnetic ($x10^7 Nm^{-2}K^{-1}$)
$Mn_{85}Ni_9C_6$ (sample C2)		
$\partial C_L/\partial T$	-5.4	-4.82
$\partial C'/\partial T$	+1.12	-1.40
$\partial C_{44}/\partial T$	-4.85	-6.17
$\partial C_{11}/\partial T$	-2.26	-4.62
$\partial C_{12}/\partial T$	-1.60	-3.50
$\partial B/\partial T$	-2.74	-3.08
$Mn_{85}Ni_9C_6$ (sample F)		
$\partial C_L/\partial T$	-5.36	-5.43
$\partial C'/\partial T$	+0.60	-0.35
$\partial C_{44}/\partial T$	-11.3	-9.89
$\partial C_{11}/\partial T$	-7.50	-6.10
$\partial C_{12}/\partial T$	-8.29	-5.12
$\partial B/\partial T$	-7.30	-5.60

Table 6.10b. The Young's modulus and their temperature dependences in both the antiferromagnetic and the paramagnetic states of $Mn_{85}Ni_9C_6$ (sample C2)

	[111] direction	[110] direction	[001] direction
Young's Mod. $E(10^{10}\ Nm^{-2})$			
E_{anti}	20.7	11.1	4.48
E_{para}	20.9	11.8	5.41
$\Delta E_m/E$	-0.8%	-6%	-20%
$(\partial E/\partial T)_{anti}$ $(10^7 Nm^{-2}K^{-1})$	-8.88	-2.04	-1.75
$(\partial E/\partial T)_{para}$ $(10^7 Nm^{-2}K^{-1})$	-9.29	-5.34	+2.3
$(1/E)(\partial E/\partial T)_{anti}$ $(10^{-3}K^{-1})$	-0.43	-0.18	-0.39
$(1/E)(\partial E/\partial T)_{para}$ $(10^{-3}K^{-1})$	-0.44	-0.45	+0.42

Table 6.11b. The Young's modulus and their temperature dependences in both the antiferromagnetic and the paramagnetic states of $Mn_{85}Ni_9C_6$ (sample F)

	[111] direction	[110] direction	[001] direction
Young's Mod. E(10^{10} Nm^{-2})			
E_{anti}	21.3	6.98	2.26
E_{para}	22.3	7.61	3.14
$\Delta E_m/E$	-2.2%	-8.6%	-37%
$(\partial E/\partial T)_{anti}$ ($10^7 Nm^{-2}K^{-1}$)	-22.2	-0.19	+1.3
$(\partial E/\partial T)_{para}$ ($10^7 Nm^{-2}K^{-1}$)	-22.1	-1.86	-1.8
$(1/E)(\partial E/\partial T)_{anti}$ ($10^{-3}K^{-1}$)	-1.03	-0.26	+0.58
$(1/E)(\partial E/\partial T)_{para}$ ($10^{-3}K^{-1}$)	-0.99	-0.02	-0.57

Table 6.12b. Magnetic contribution to the second order elastic stiffness constants and bulk modulus at 20°C of ternary alloys Mn-Ni-C.

	$Mn_{85}Ni_9C_6$ (sample C2)	$Mn_{85}Ni_9C_6$ (sample F)
$\Delta C_L / C_L$	+2.2%	+3.0%
$\Delta C'/C'$	-30%	-28%
$\Delta C_{44}/C_{44}$	-3.5%	-4.1%
$\Delta C_{11}/C_{11}$	+1.5%	+3.6%
$\Delta C_{12}/C_{12}$	+9.1%	+9.0%
$\Delta B/B$	+5.2%	+4.9%

Table 6.13b. Debye temperatures of $Mn_{85}Ni_9C_6$ (sample C2):

1) At several experimental temperatures:

Temp.(C)	20	35	90	125	165	280	300	327	340
θ_D (K)	337	338	337	337	337	340	338	336	333

11) At absolute zero (K)	θ_D
Magnetically ordered	335
(Antiferromagnetic)	
Paramagnetic	381

Table 6.14b. Debye temperatures of $Mn_{85}Ni_9C_6$ (sample F):

1) At several experimental temperatures:

Temp.(C)	20	60	125	155	170	190	255	275	295	310
θ_D(K)	300	298	293	289	289	285	287	288	287	282

11) At absolute zero (K)	θ_D
Magnetically ordered	319
(Antiferromagnetic)	
Paramagnetic	379

Table 6.15b. Temperature dependence of pressure derivatives of the SOEC of $Mn_{85}Ni_9C_6$ (sample C2). C' is $(C_{11}-C_{12})/2$

Temp. (°C)	$\partial C_{11}/\partial P$	$\partial C_{12}/\partial P$	$\partial C_{44}/\partial P$	$\partial C'/\partial P$	$\partial B/\partial P$	B_{11}	B_{12}	B_{44}
20	8.07	4.89	5.79	1.59	5.95	9.60	4.13	7.29
35	8.74	5.61	5.54	1.57	6.65	10.3	4.84	7.04
50	9.51	6.25	5.07	1.63	7.34	11.0	5.49	6.56
75	10.3	6.42	4.83	1.95	7.71	11.8	5.65	6.32
90	10.8	6.28	4.49	2.26	7.78	12.3	5.51	5.98
115	10.2	5.62	3.57	2.28	7.14	11.7	4.85	5.06
125	9.28	4.64	3.2	2.30	6.19	10.8	3.87	4.69
140	6.72	1.65	4.67	2.53	3.34	8.26	0.88	6.16
165	13.0	7.64	4.64	2.67	9.42	14.5	6.86	6.13

Table 6.16b. Temperature dependence of the TOEC combinations and the mean Grüneisen parameters of $Mn_{8.5}Ni_9C_6$ single crystal (sample C2).

Temp. (°C)	$C_{111}+2C_{112}$	$C_{144}+2C_{166}$ ($10^9 Nm^{-2}$)	$C_{123}+2C_{112}$	γ_{mean}
20	-2035	-1545	-876	1.89
35	-2179	-1493	-1028	1.89
50	-2336	-1389	-1161	1.86
75	-2510	-1340	-1198	1.95
90	-2611	-1266	-1167	1.97
115	-2434	-1050	-1006	1.71
125	-2223	-964	-795	1.56
140	-1692	-1262	-180	1.70
165	-2963	-1251	-1400	2.18

Table 6.17b. Mode Grüneisen parameter for the $Mn_{8.5}Ni_9C_6$ single crystal (sample C2).

Temperature	20	35	50	75	90	115	125	140	165
γ_{CL}	2.17	2.26	2.30	2.38	2.34	2.01	1.74	1.52	2.70
γ_{C44}	1.78	1.71	1.55	1.49	1.38	1.03	0.89	1.43	1.41
$\gamma_{C'}$	1.66	1.63	1.68	2.04	2.40	2.35	2.37	2.58	2.67

$\gamma^{th} = 1.48$

Table 6.18b. The elastic stiffness and their hydrostatic presure derivatives of ternary alloys $Mn_{85}Ni_9C_6$ (sample C2) and $Mn_{85}Ni_9C_6$ (sample F) at 20°C.
Unit of C_{IJ} and C_{IJK}: GPa

	$Mn_{85}Ni_9C_6$-C2	$Mn_{85}Ni_9C_6$-F
C^S_{11}	87	88
C^S_{12}	60	72
C^S_{44}	106	104
C'	13	8.0
B	69	78
$\partial C_{11}/\partial p$	8.1	8.4
$\partial C_{12}/\partial p$	4.9	7.6
$\partial C_{44}/\partial p$	5.8	3.4
$\partial C'/\partial p$	1.6	1.7
$\partial B/\partial p$	6.0	7.5
$C_{111}+2C_{112}$	-2035	-2035
$C_{144}+2C_{166}$	-1545	-908
$C_{123}+2C_{112}$	-877	-1011

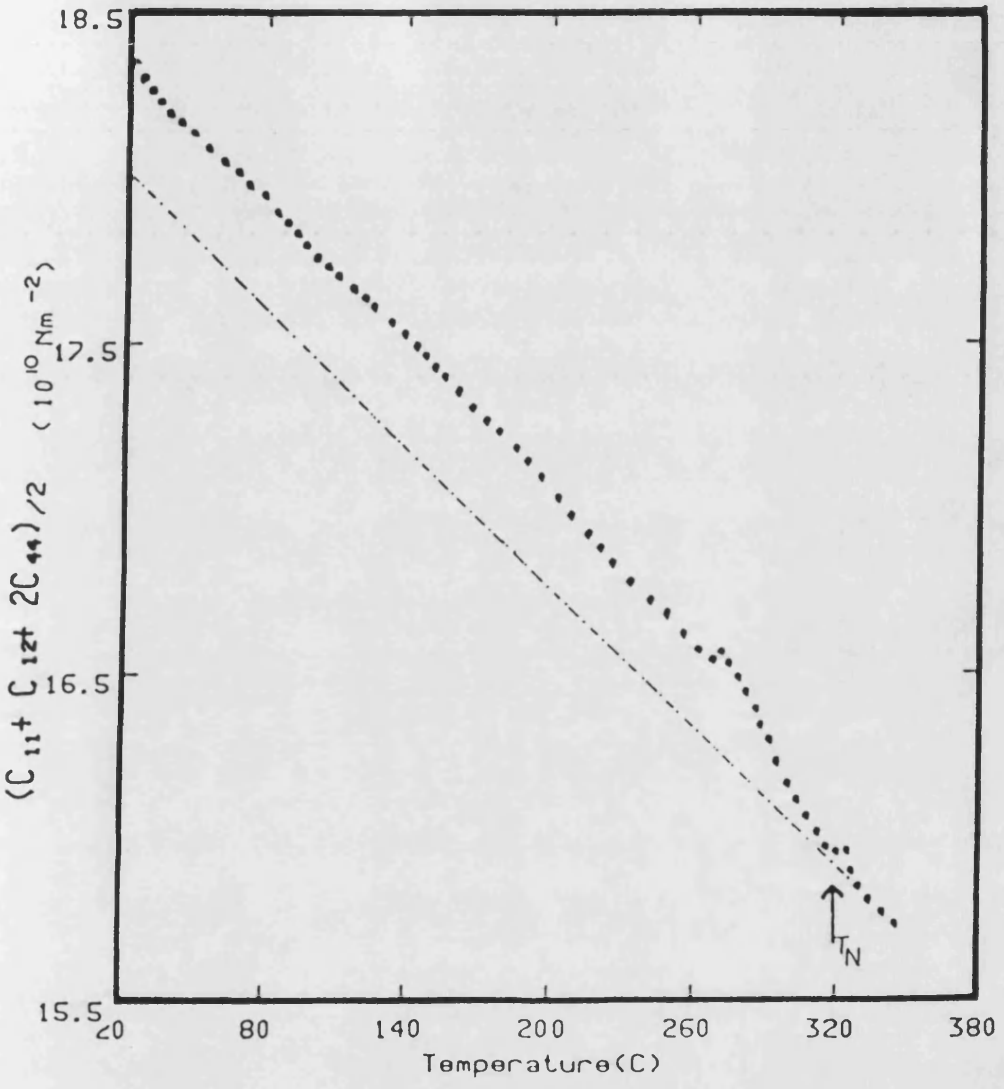

Temperature dependence of the second order elastic stiffness constant of Mn(85)Ni(9)C(6) single crystal (sample C2) for a longitudinal acoustic wave propagates in the [110] direction

Fig 6.1b

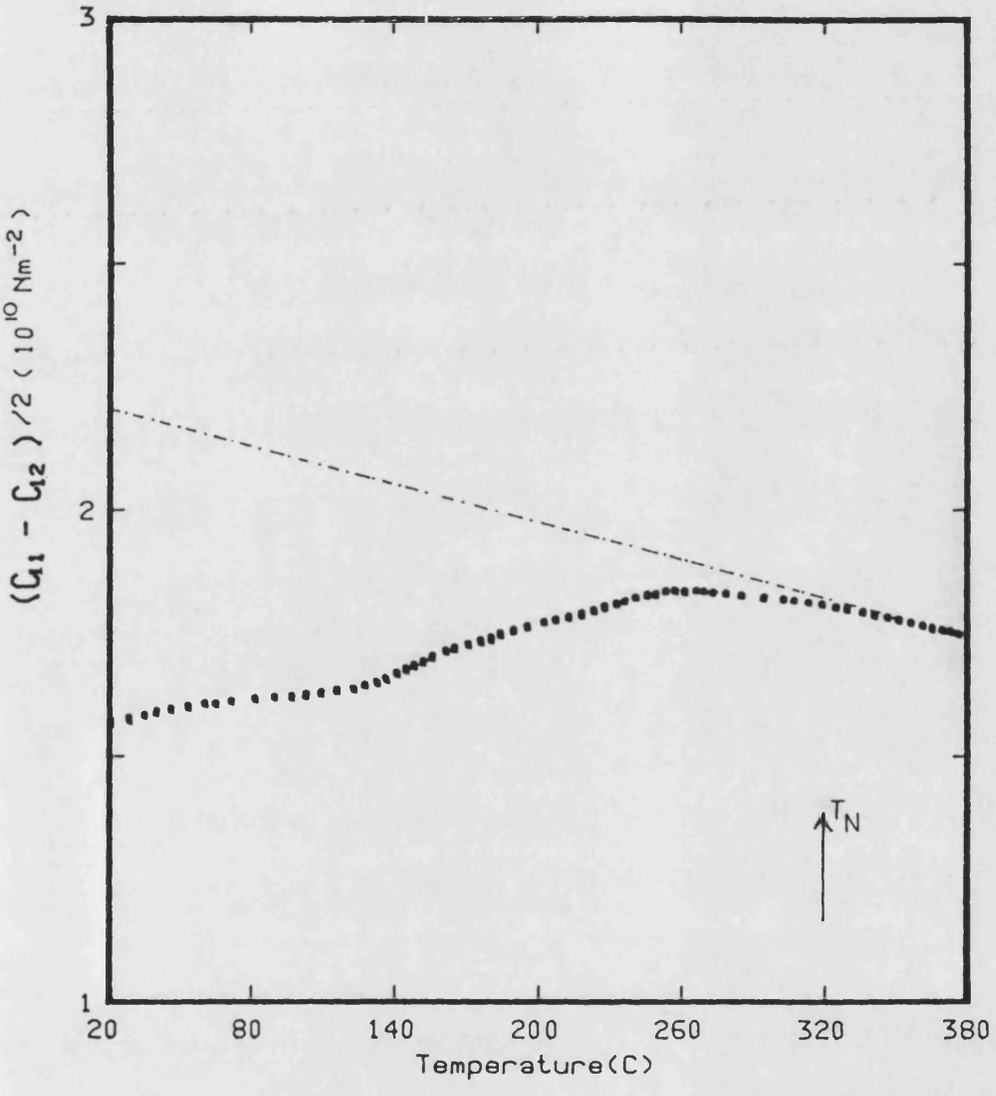

Temperature dependence of the second order elastic stiffness of Mn(85)Ni(9)C(6) single crystal (sample C2) for a shear acoustic wave propagates in the [110] direction.

Fig 6.2b

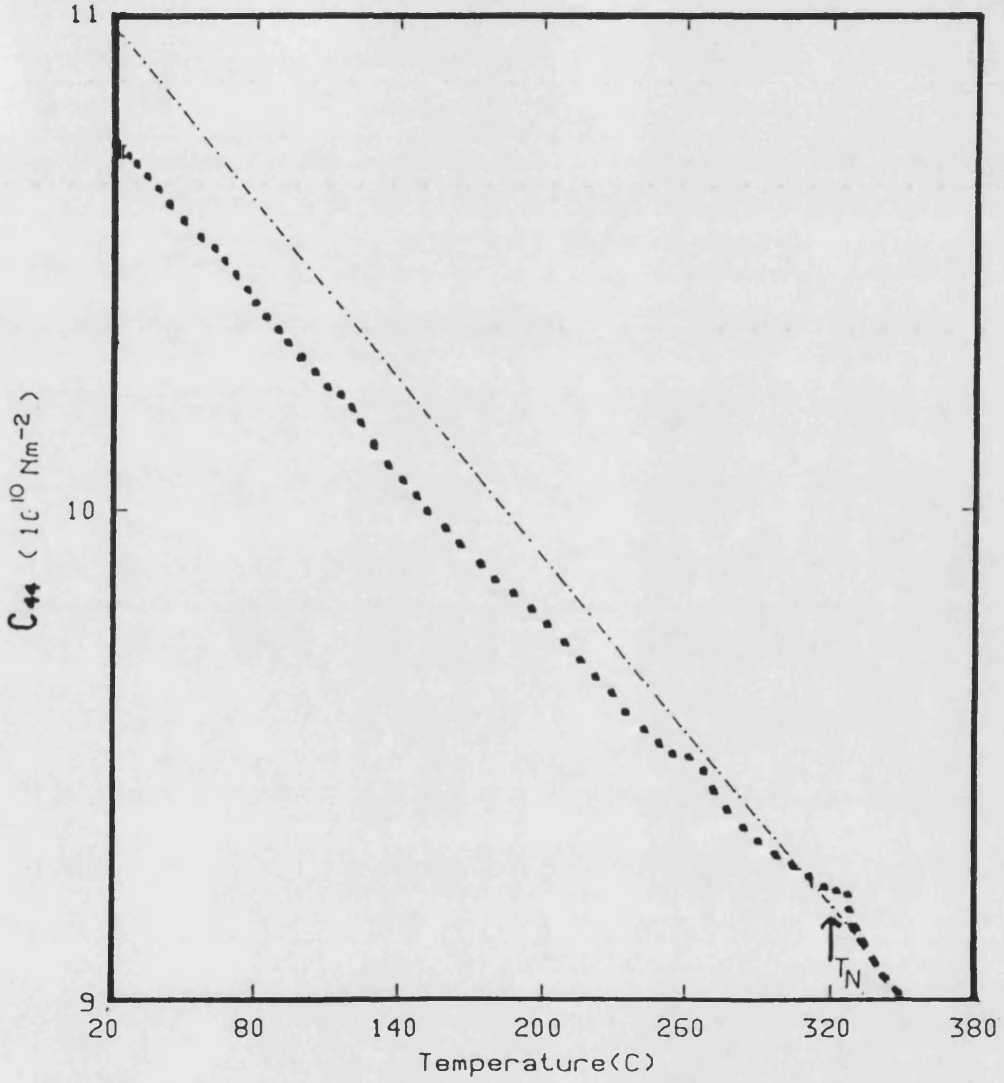

Temperature dependence of the second order elastic stiffness constant of Mn(85)Ni(9)C(6) single crystal (sample C2) for a shear acoustic wave propagates in the [110] direction

Fig 6.3b (1)

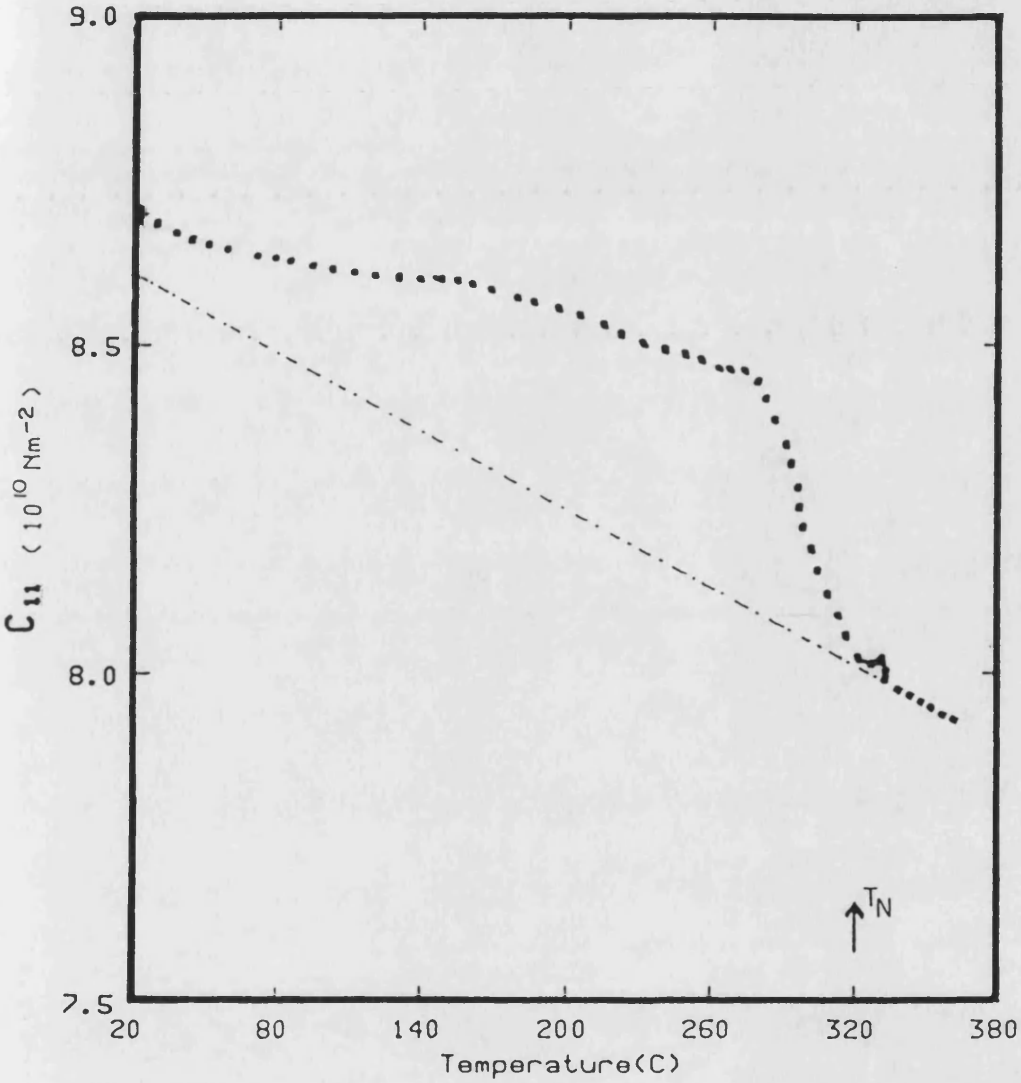

Temperature dependence of the second order elastic stiffness constant (C_{11}) of Mn(85)Ni(9)C(6) single crystal (sample C2)

Fig 6.4b (1)

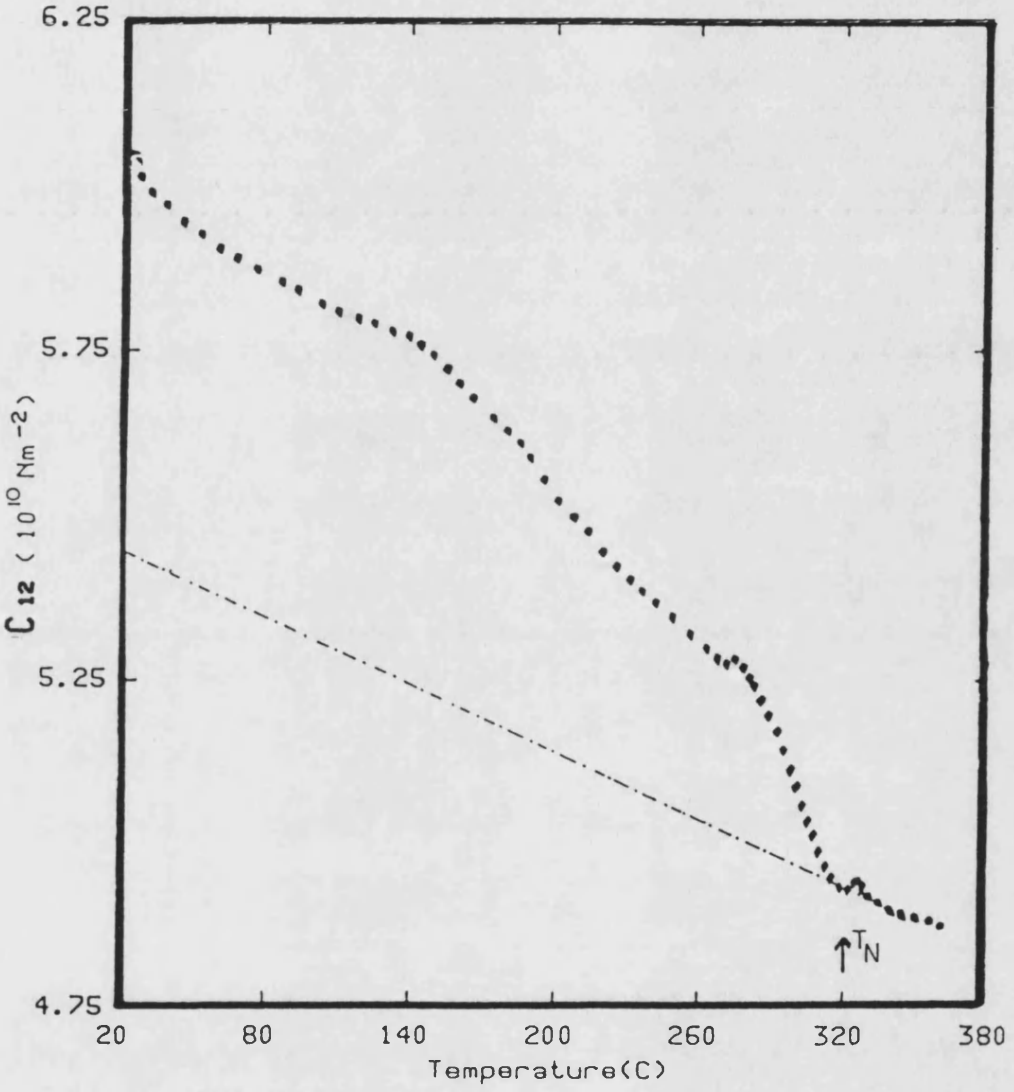

Temperature dependence of the second order elastic stiffness constant (C_{12}) of Mn(85)Ni(9)C(6) single crystal (sample C2).

Fig 6.5b

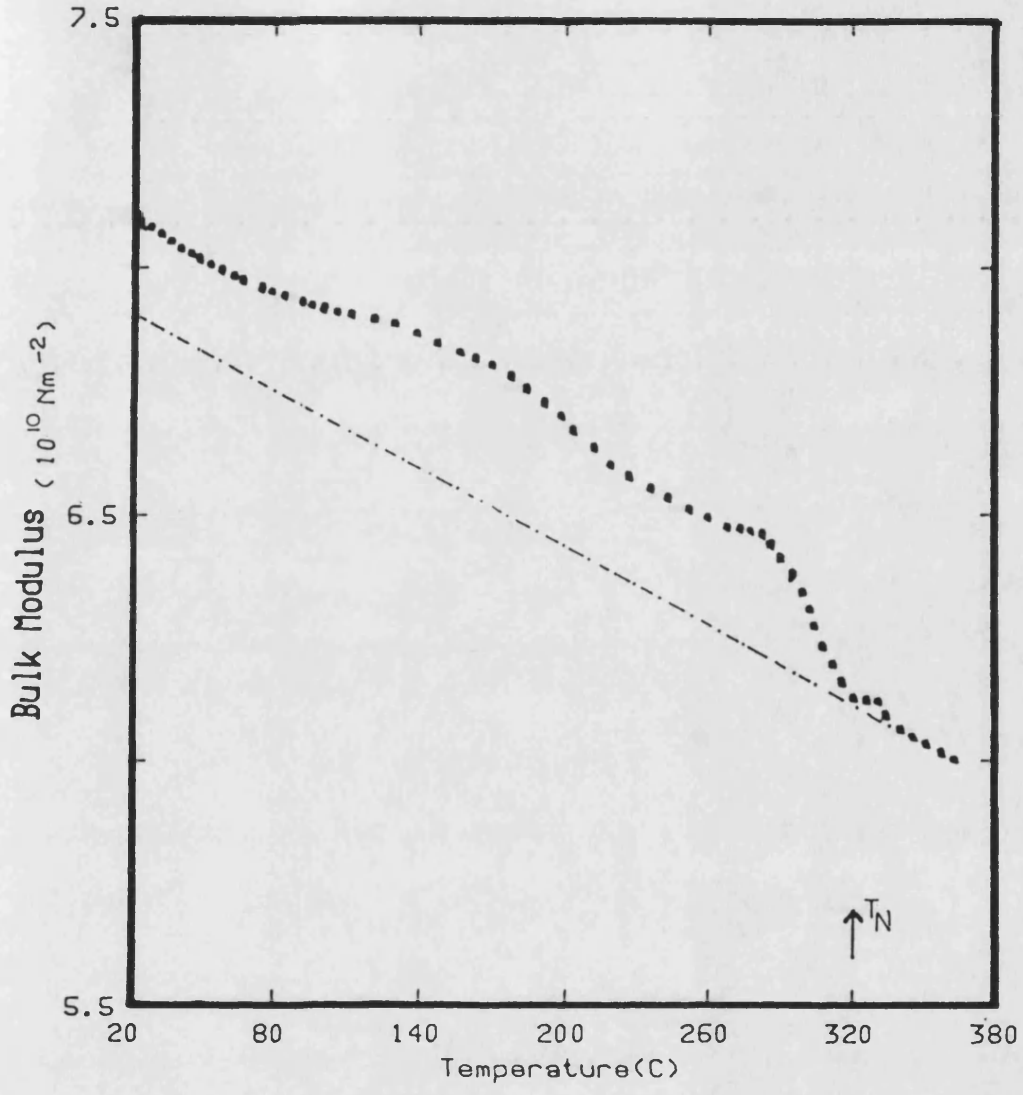

Temperature dependence of bulk modulus of Mn(85)Ni(9)C(6) single crystal (sample C2).

Fig 6.6b

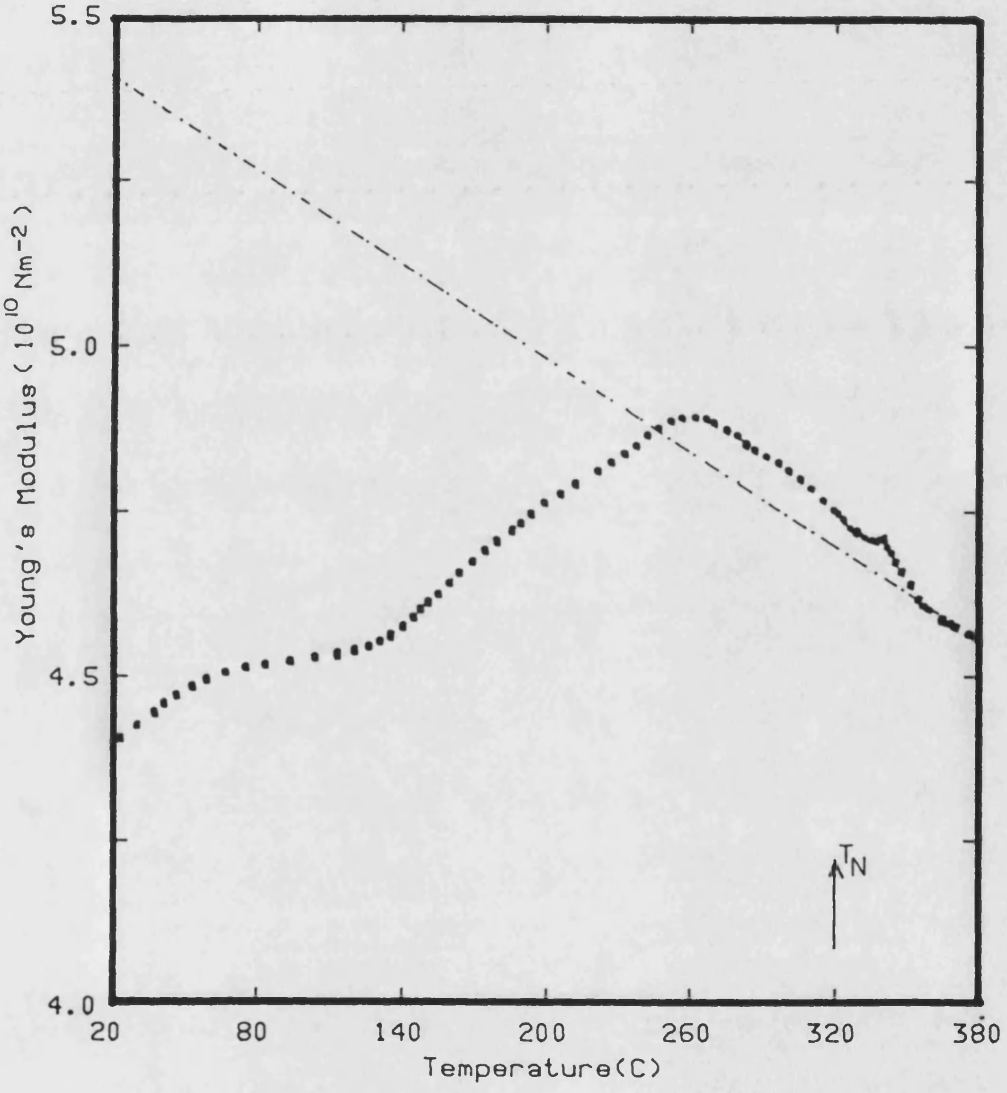

Temperature dependence of Young's modulus in the [001] direction of Mn(85)Ni(9)C(6) single crystal (sample C2).

Fig 6.7b

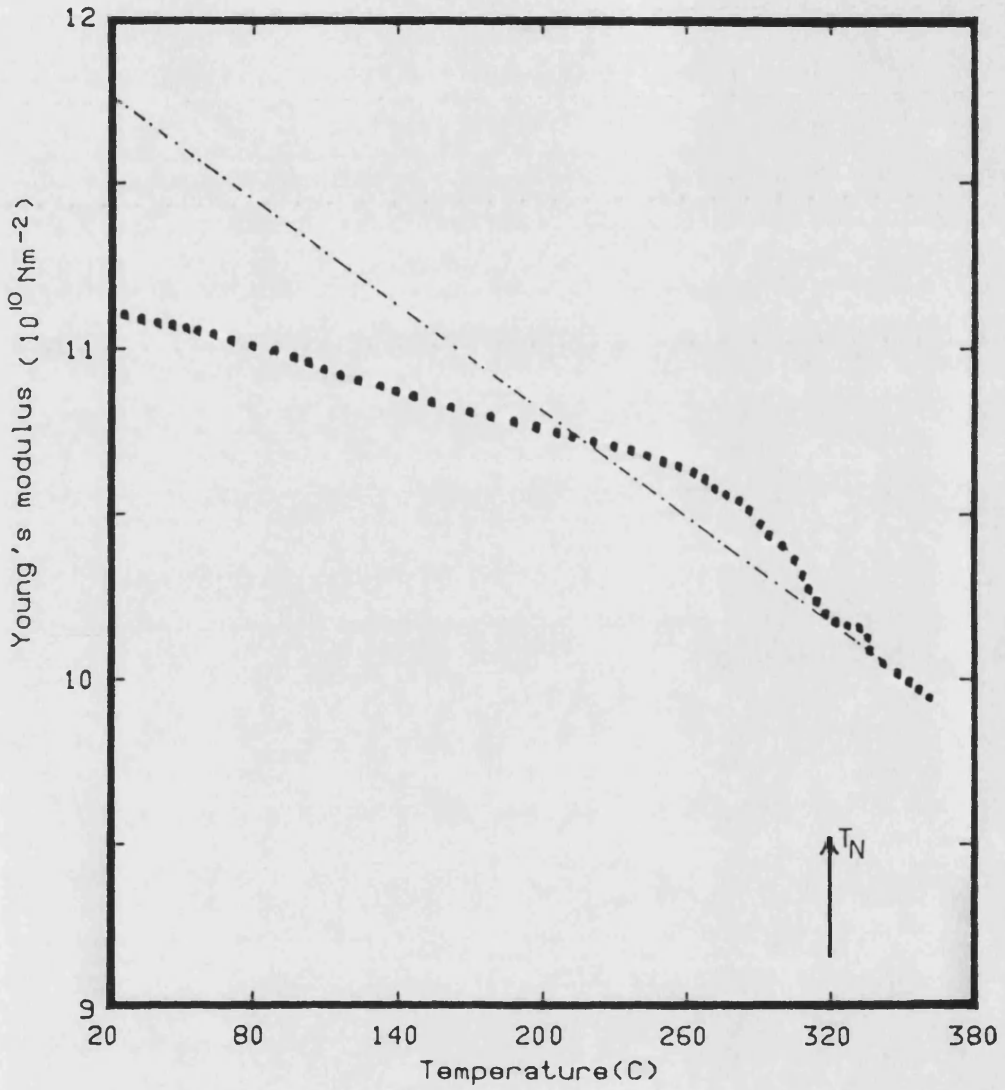

Temperature dependence of Young's modulus in the [110] direction of Mn(85)Ni(9)C(6) single crystal (sample C2).

Fig 6.8b

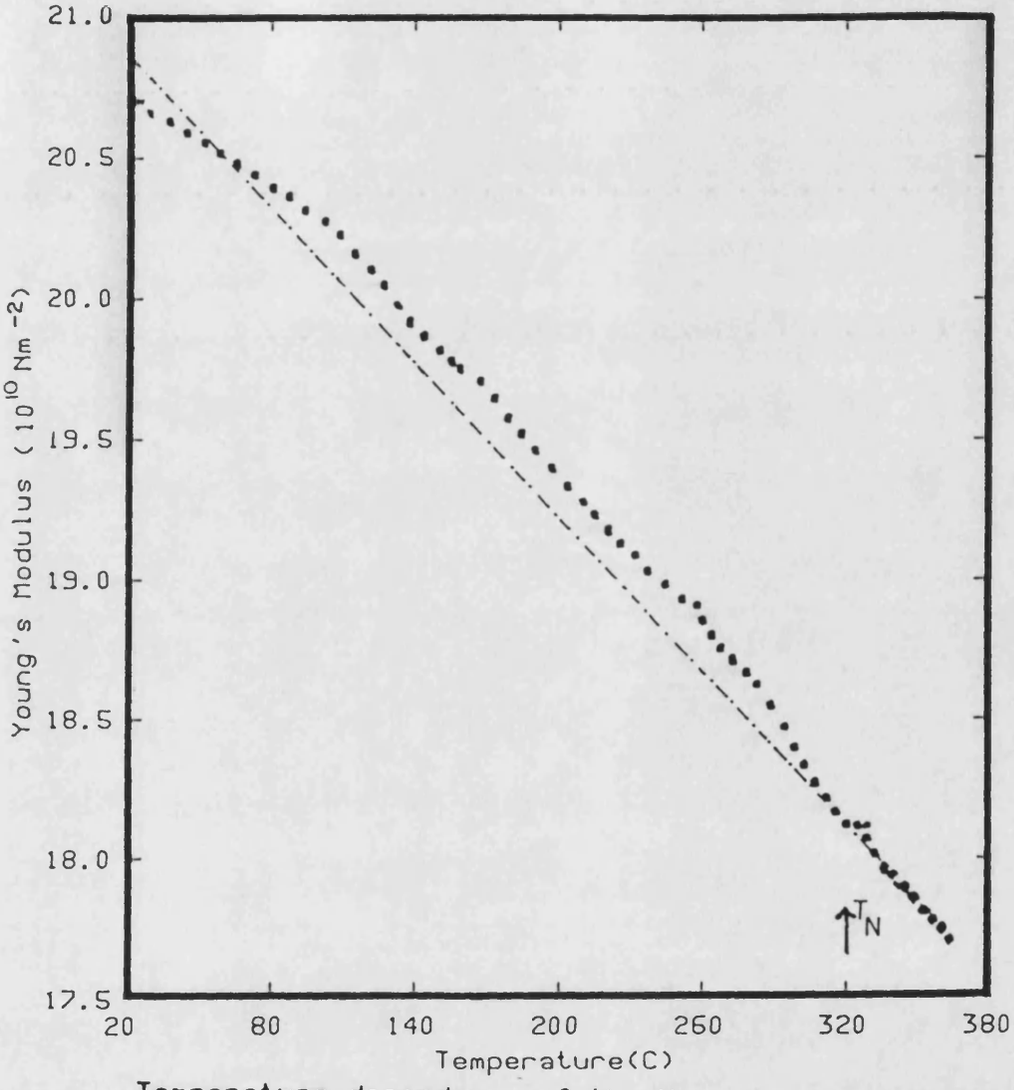

Temperature dependence of the Young's modulus E in the [111] direction of the Mn(85)Ni(9)C(6) single crystal (sample C2)

Fig 6.9b

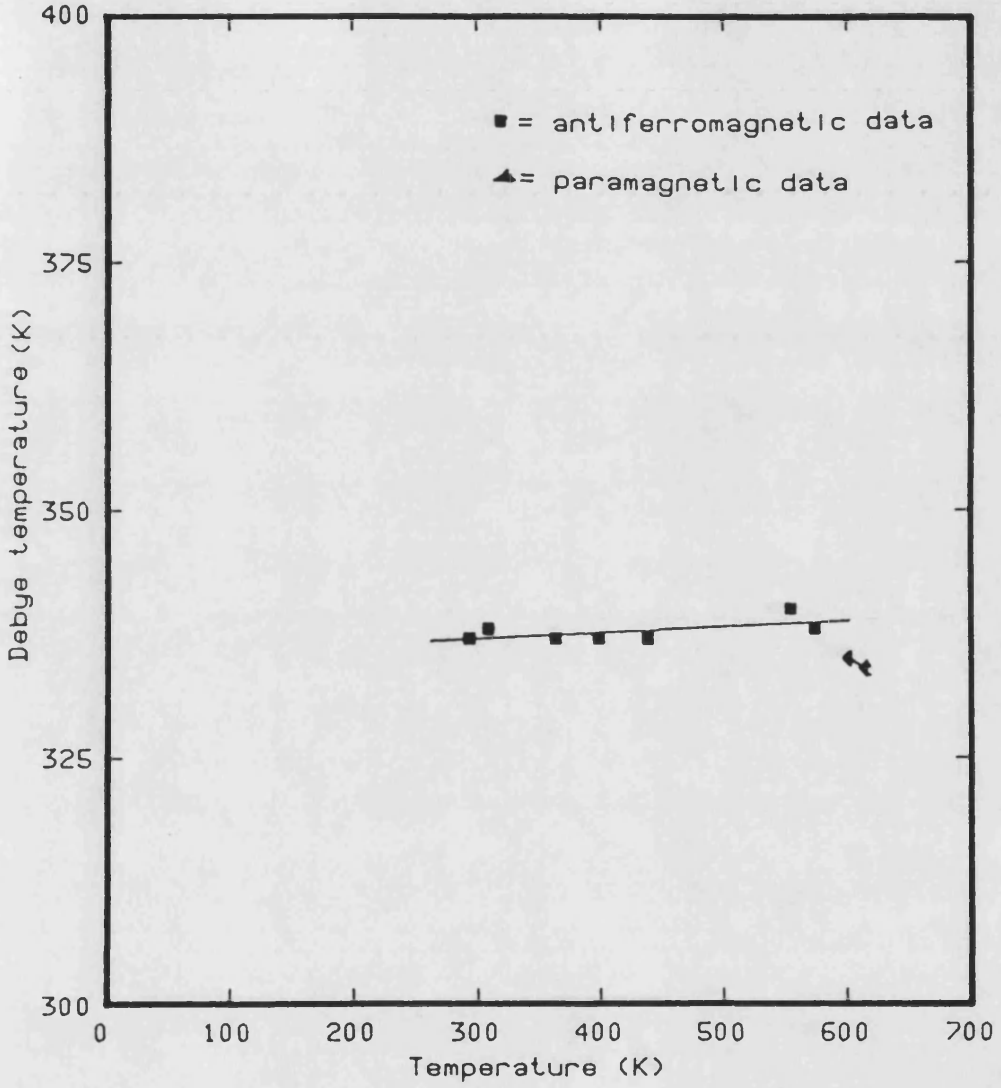

Determination of Debye temperature of Mn(85)Ni(9)C(6) single crystal (sample C2)at 0K by extrapolating the experimental data.

Fig 6.10b

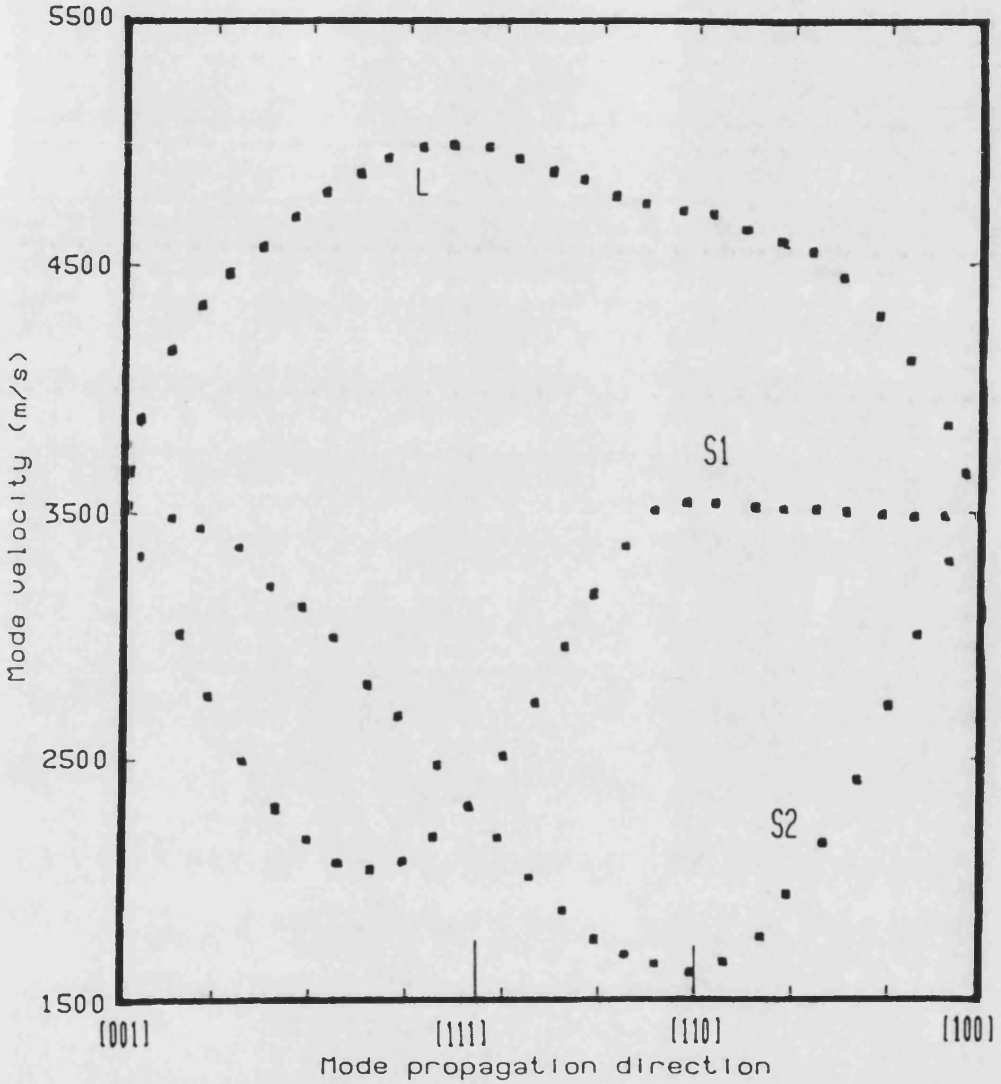

Directional dependence of long wavelength acoustic mode velocities of the Mn(85)Ni(9)C(6) single crystal (sample C2) at 20C

Fig 6.11b

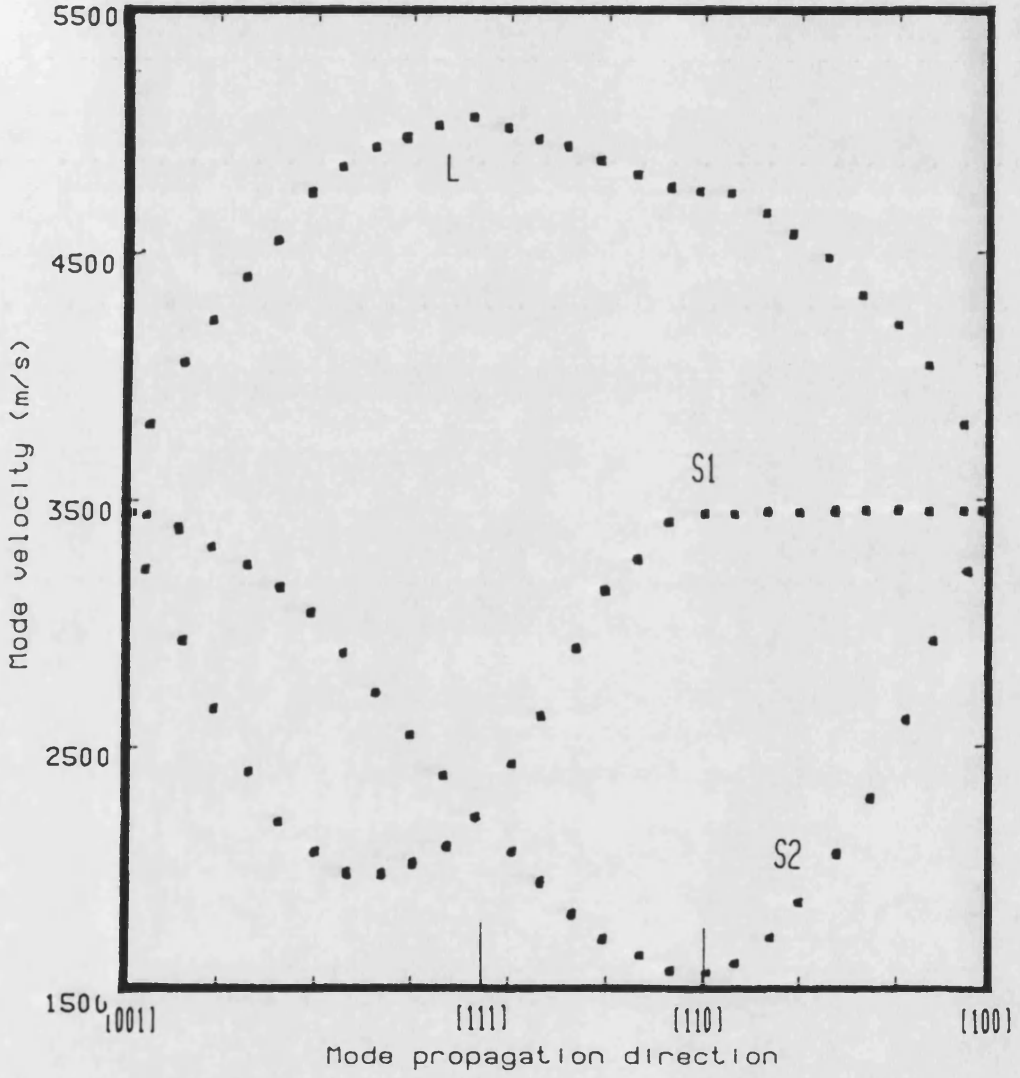

Directional dependence of long wavelength acoustic mode velocities of the Mn(85)Ni(9)C(6) single crystal (sample C2) at 75C

Fig 6.12b

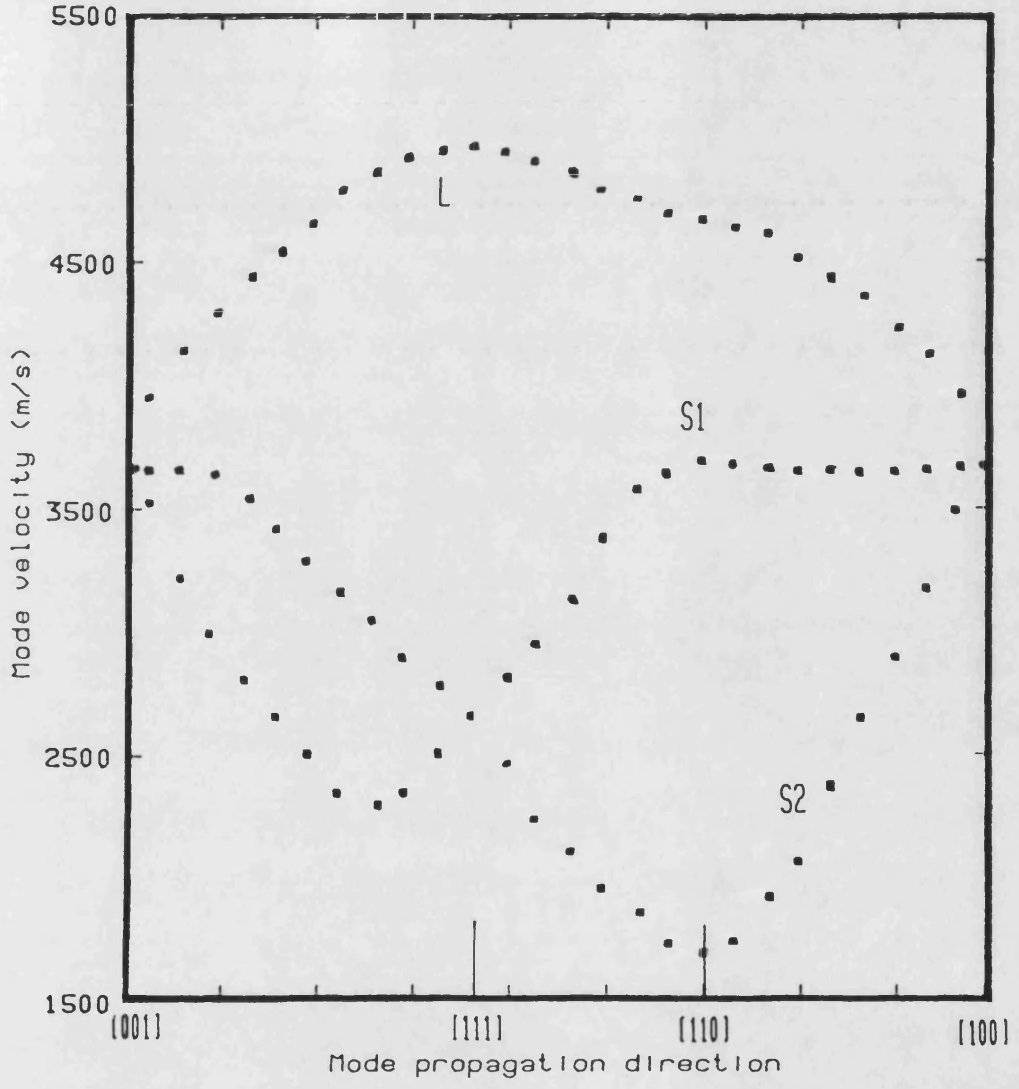

Directional dependence of long wavelength acoustic mode velocities of the Mn(85)Ni(9)C(6) single crystal (sample C2) at 125C

Fig 6.13b

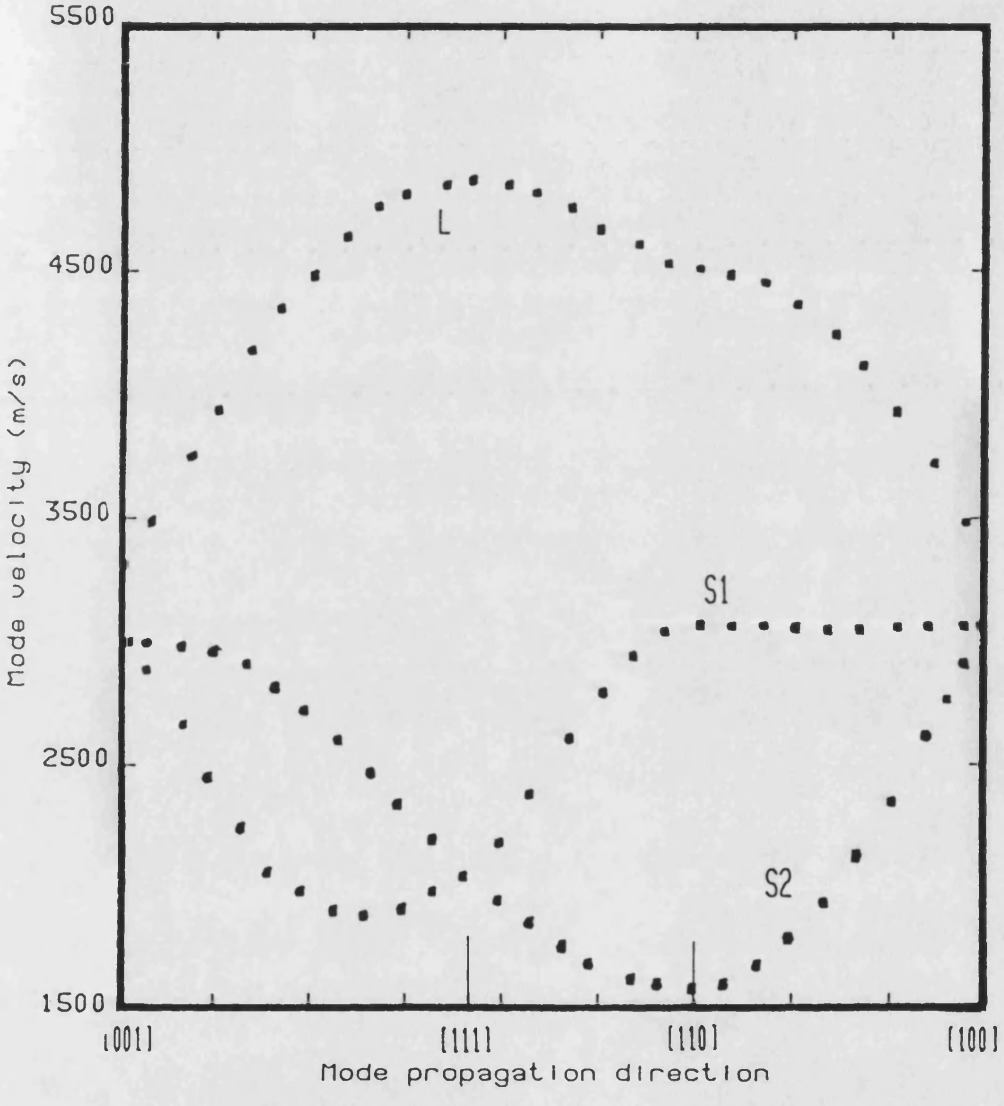

Directional dependence of long wavelength acoustic mode velocities of the Mn(85)Ni(9)C(6) single crystal (sample C2) at 140C

Fig 6.14b

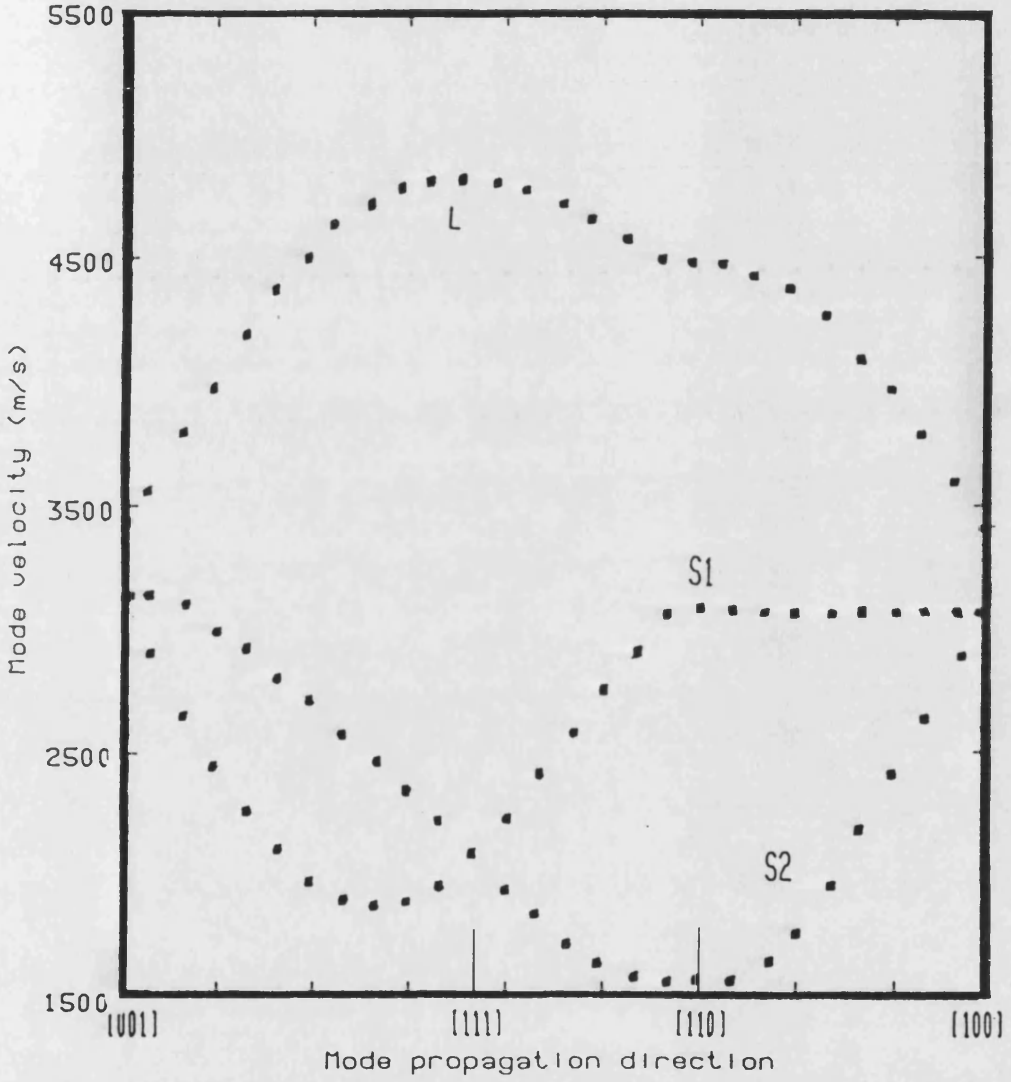

Directional dependence of long wavelength acoustic mode velocities of the Mn(85)Ni(9)C(6) single crystal (sample C2) at 165C C.

Fig 6.15b

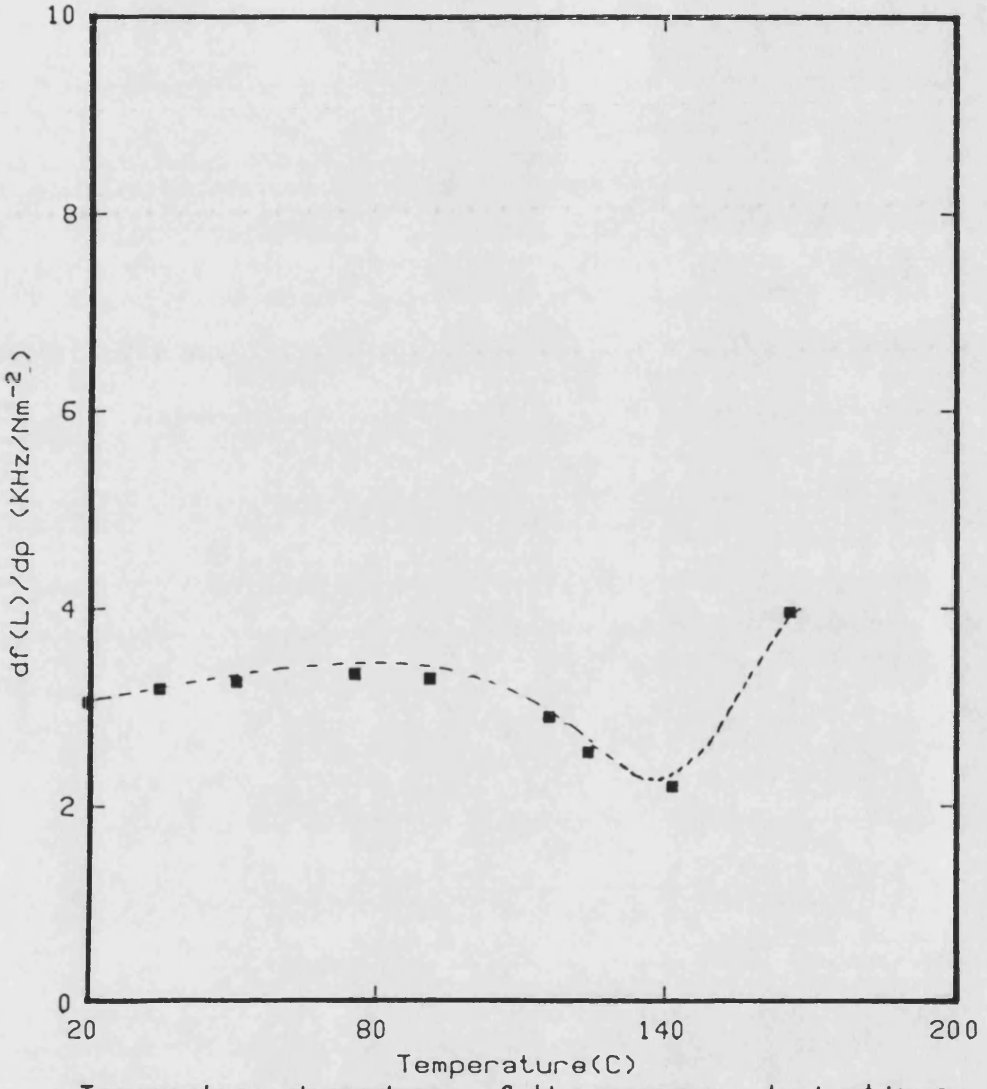

Temperature dependence of the pressure derivatives of long wavelength acoustic mode frequency propagates in the [110] direction and polarises in the [110] direction of Mn(85)Ni(9)C(6) (sample C2) single crystal.
(The curve is drawn solely as visual guide.)

Fig 6.16b

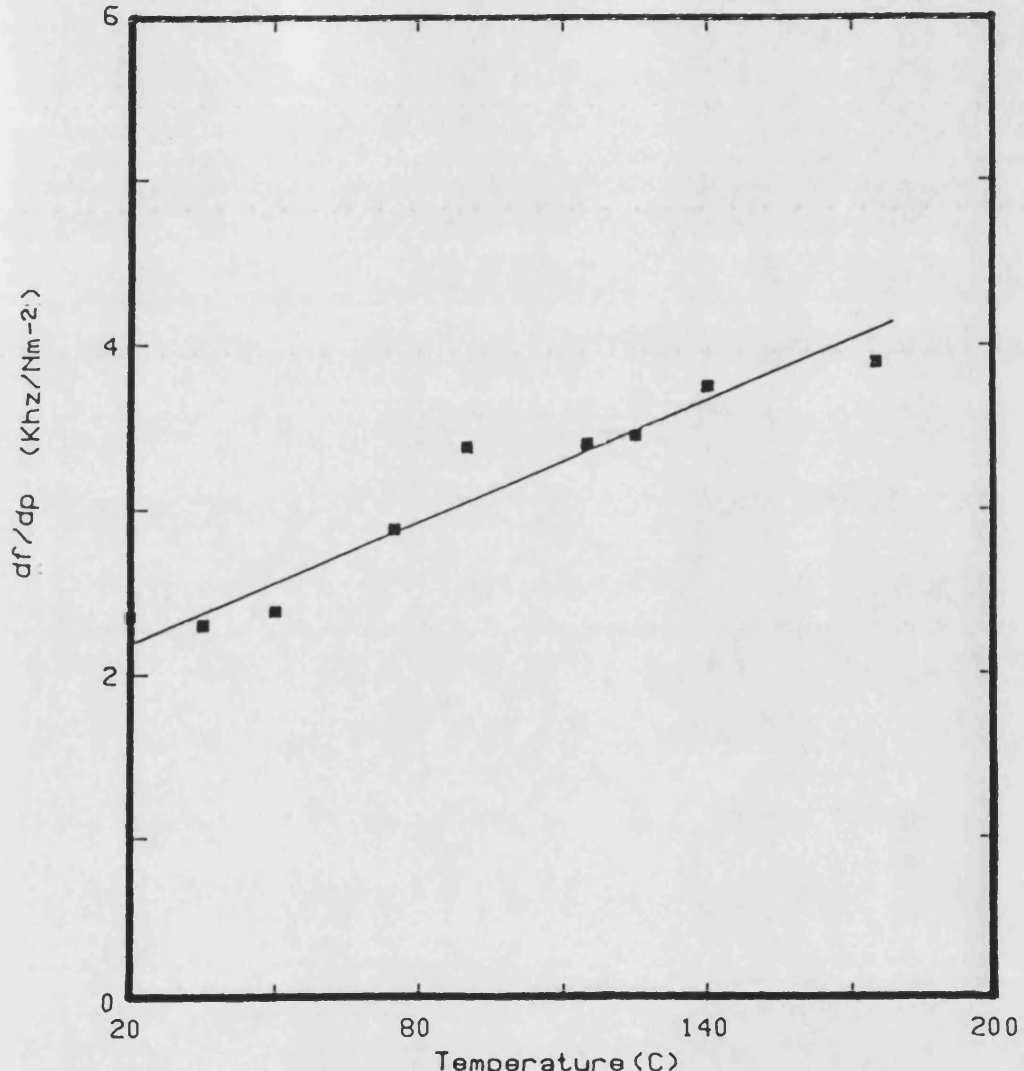

Temperature dependence of the pressure derivatives of long wavelength acoustic mode frequency propagates in the [110] direection and polarises in the [110] direction of Mn(85)Ni(9)C(6) (sample C2) single crystal.
(The curve is drawn solely as visual guide.)

Fig 6.17b

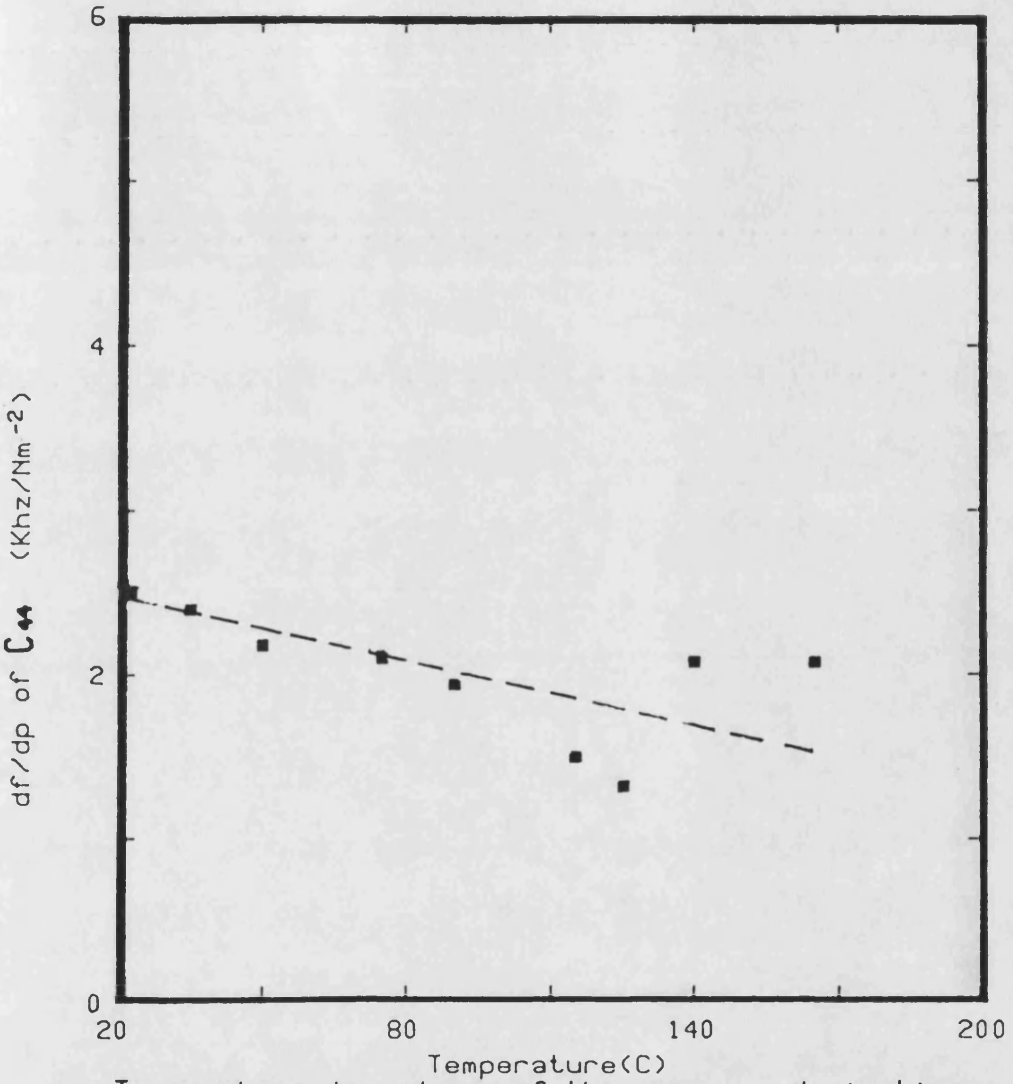

Temperature dependence of the pressure derivatives of long wavelength acoustic mode frequency propagates in the [110] direction and polarises in the [001] direction of Mn(85)Ni(9)C(6) (sample C2) single crystal.
(The curve is drawn solely as visual guide.)

Fig 6.18b

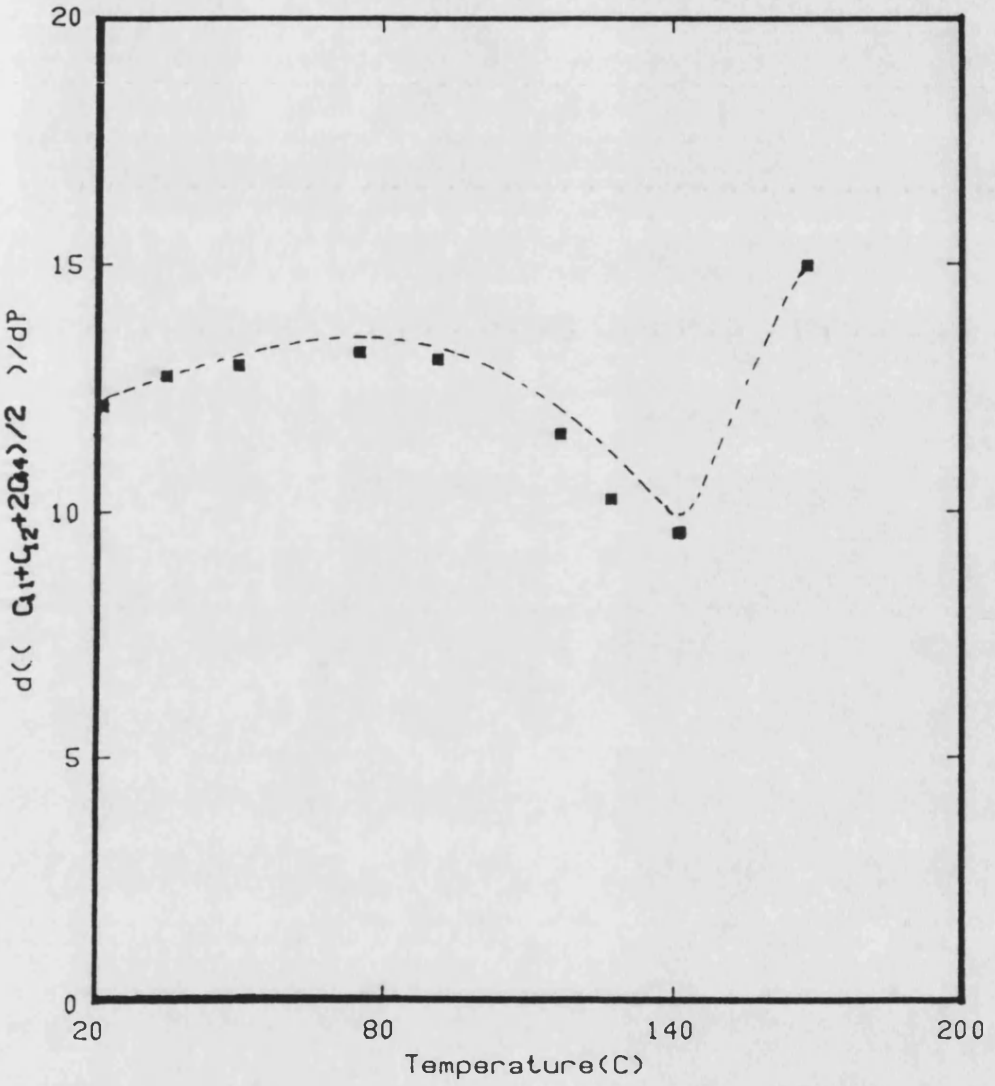

Temperature dependence of hydrostatic pressure derivatives of the second order elastic stiffness $(C_{11}+C_{12}+2C_{44})/2$ of Mn(85)Ni(9)C(6) single crystal (sample C2).

(The curve is drawn solely as visual guide.)

Fig 6.19b

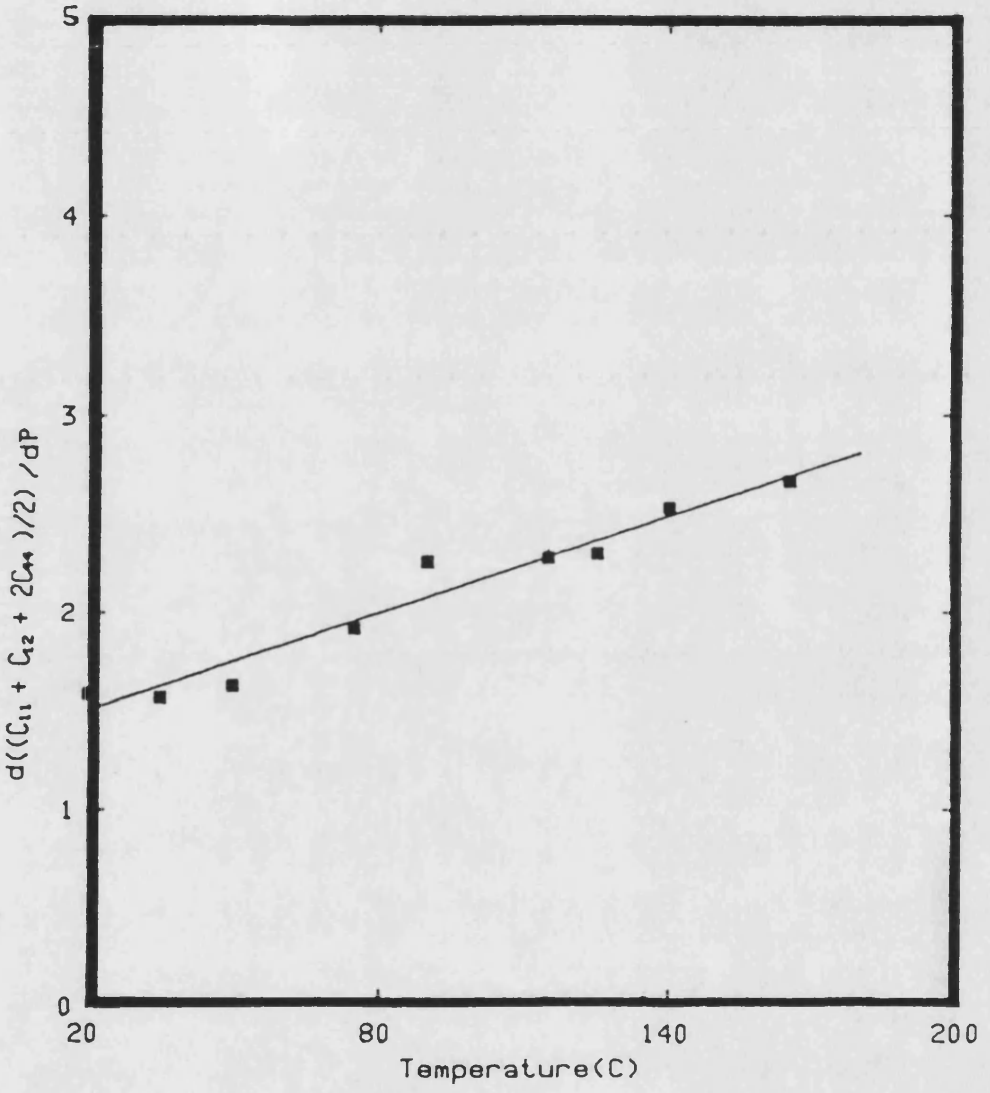

Temperature dependence of hydrostatic pressure derivative of the second order elastic stiffness constants of Mn(85)Ni(9)C(6) single crystal (sample C2)

Fig 6.20b

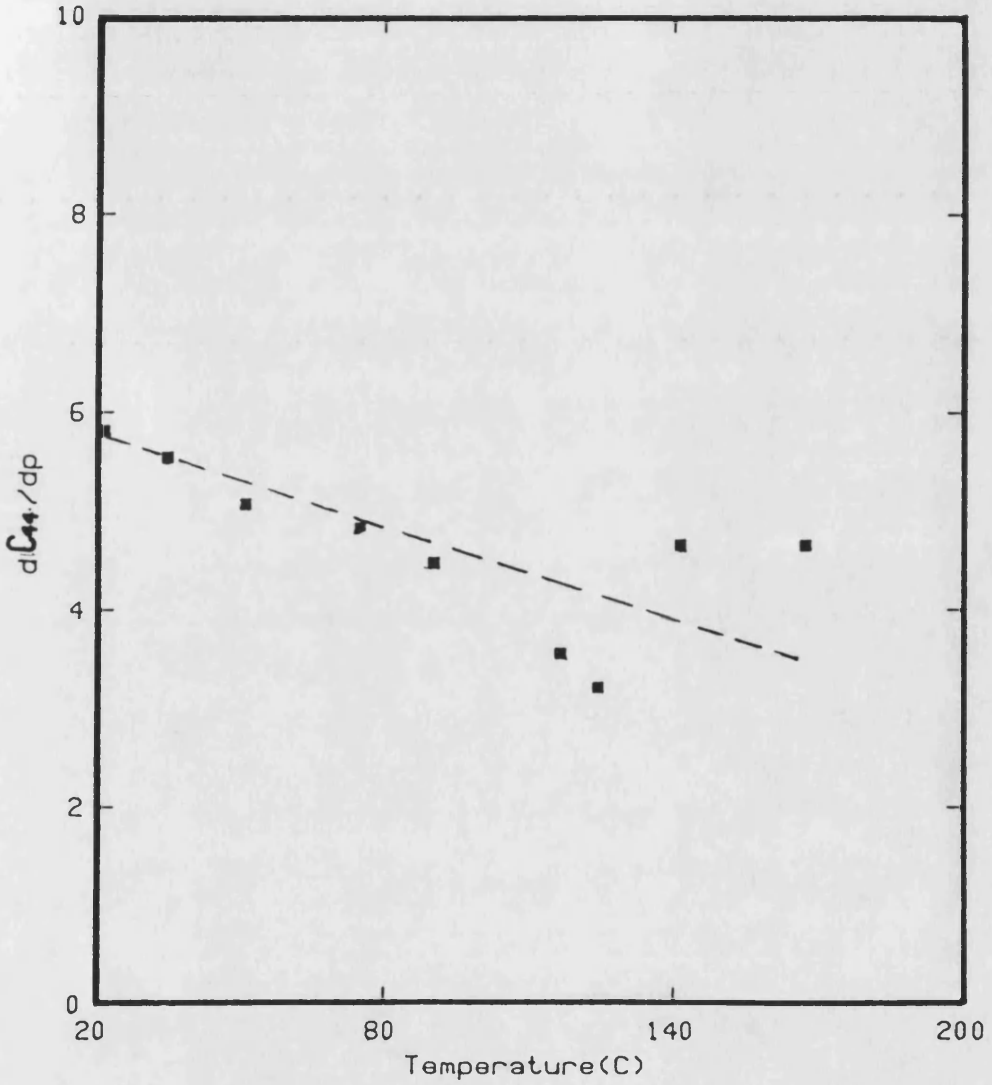

Temperature dependence of hydrostatic pressure derivatives of the second order elastic stiffness (C44) of Mn(85)Ni(9)C6) single crystal (sample C2)

(The curve is drawn solely as visual guide.)

Fig 6.21b

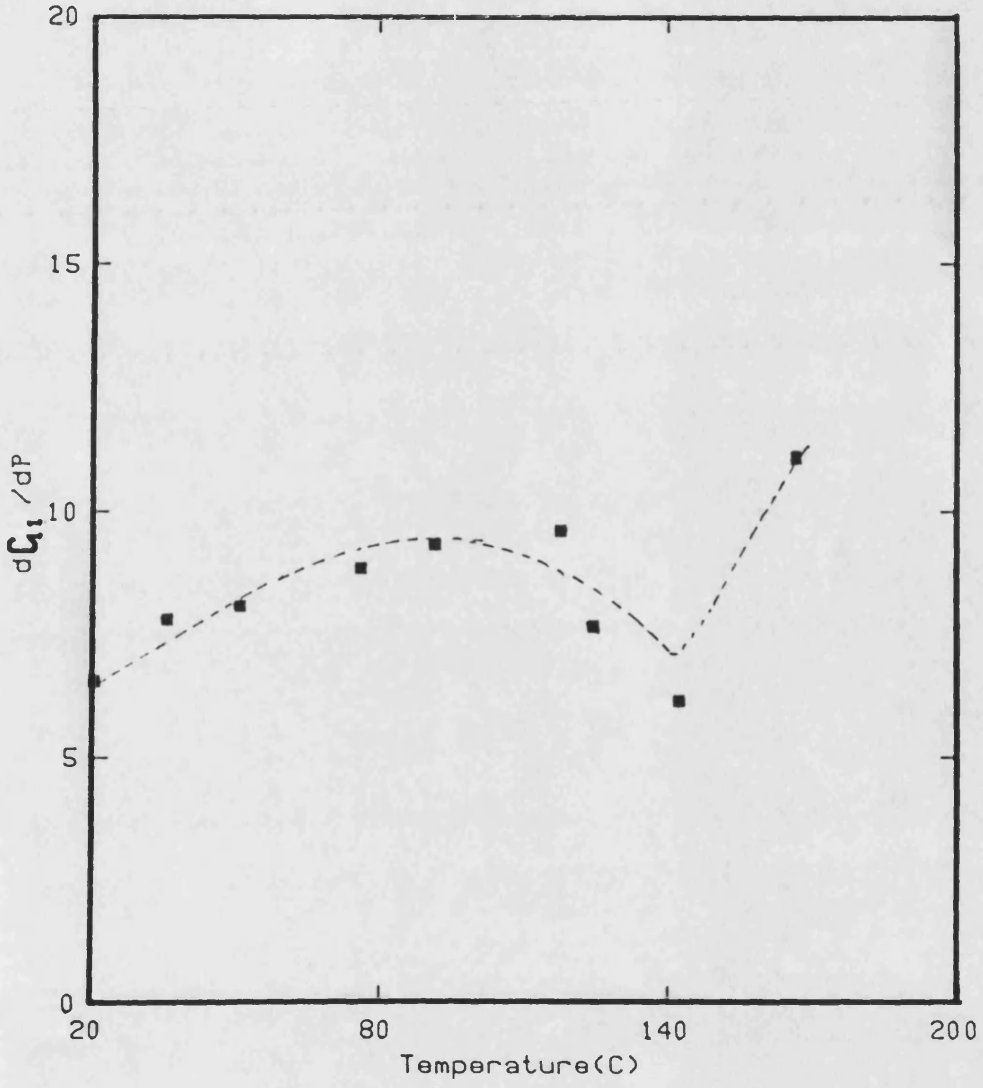

Temperature dependence of hydrostatic pressure derivatives of the second order elastic stiffness C11 of Mn(85)Ni(9)C(6) single crystal (sample C2).

(The curve is drawn solely as visual guide.)

Fig 6.22b

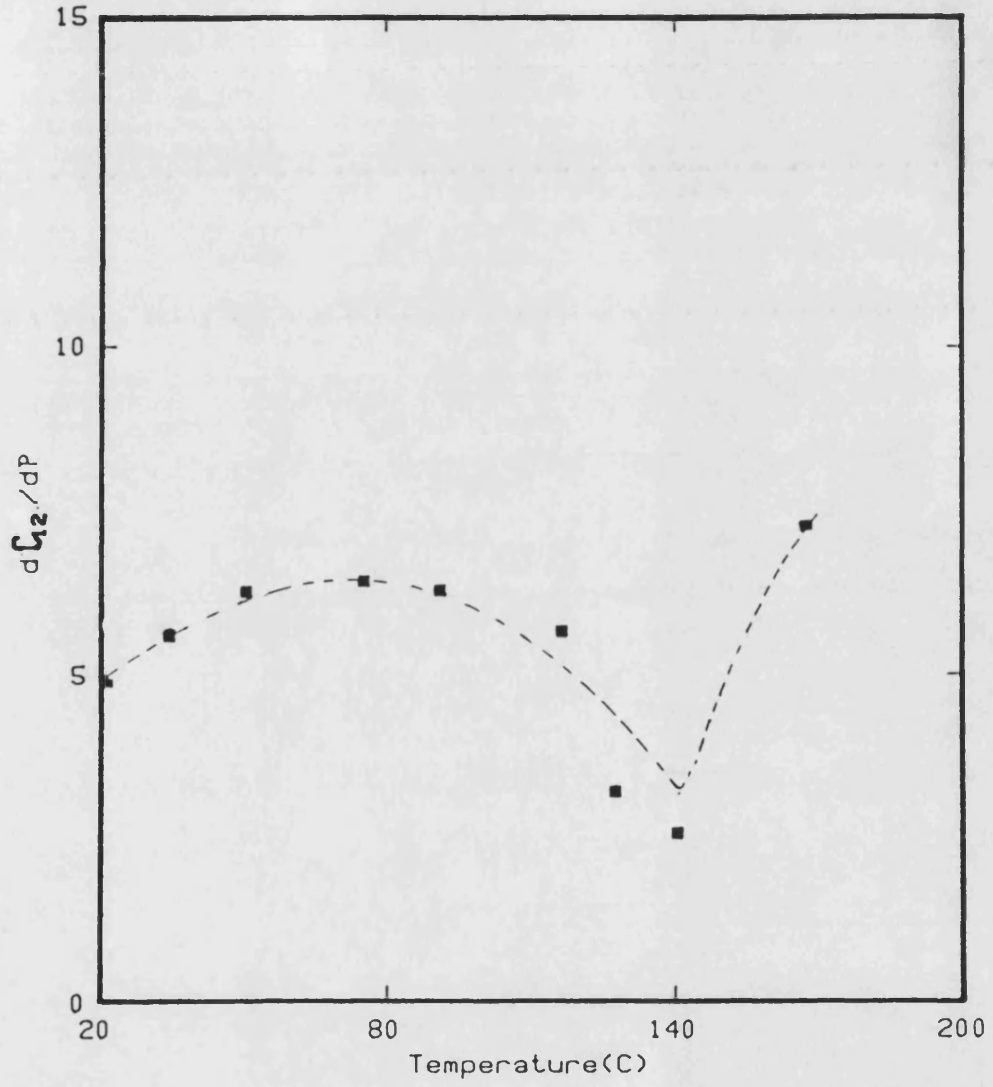

Temperature dependence of hydrostatic pressure derivatives of the second order elastic stiffness (C12) of Mn(85)Ni(9)C(6) single crystal (sample C2)

(The curve is drawn solely as visual guide.)

Fig 6.23b

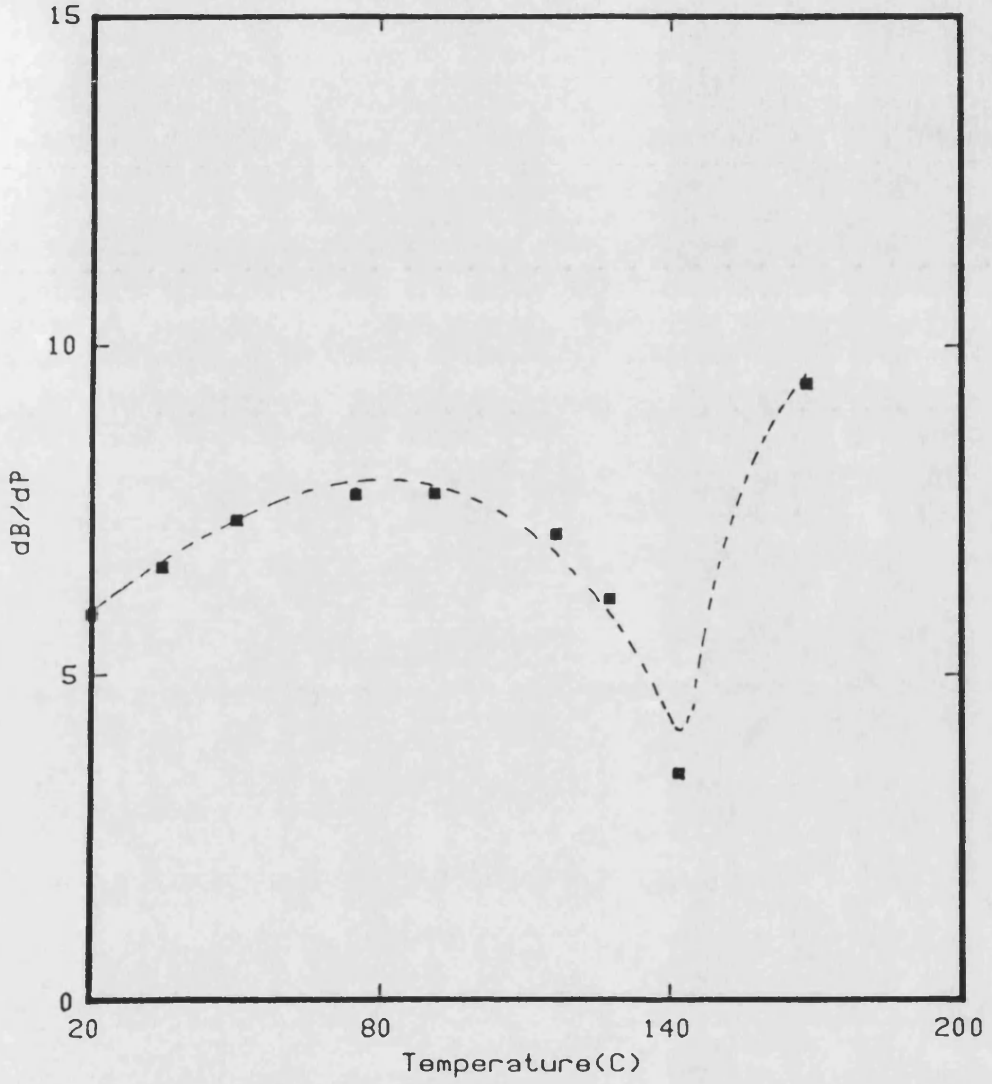

Temperature dependence of the pressure derivative of bulk modulus of Mn(85)Ni(9)C(6) single crystal (sample C2).

(The curve is drawn solely as visual guide.)

Fig 6.24b

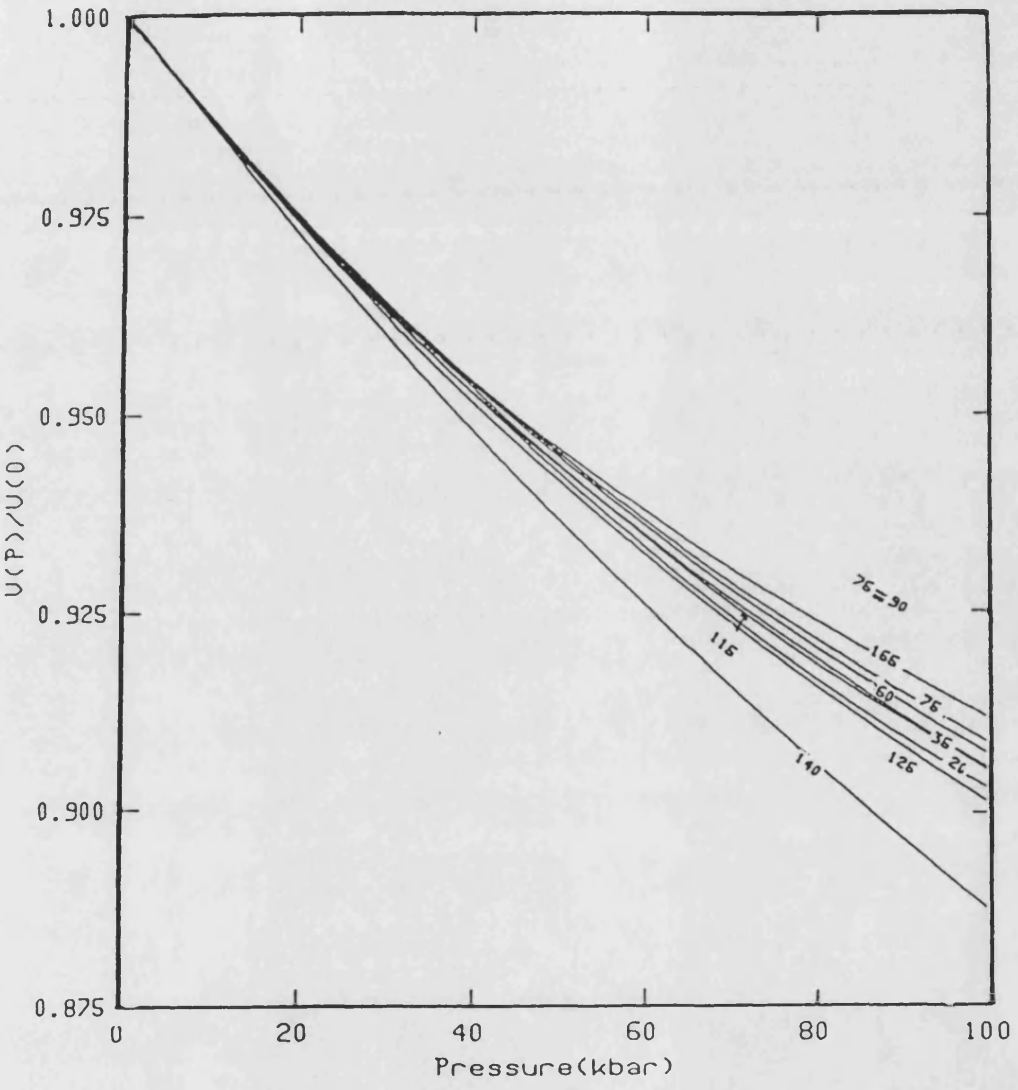

The compression V(P)/V(0) of Mn(85)Ni(9)C(6) single crystal (sample C2) in the antiferromagnetic phase based on the Murnaghan equation-of-state.

Fig 6.25b

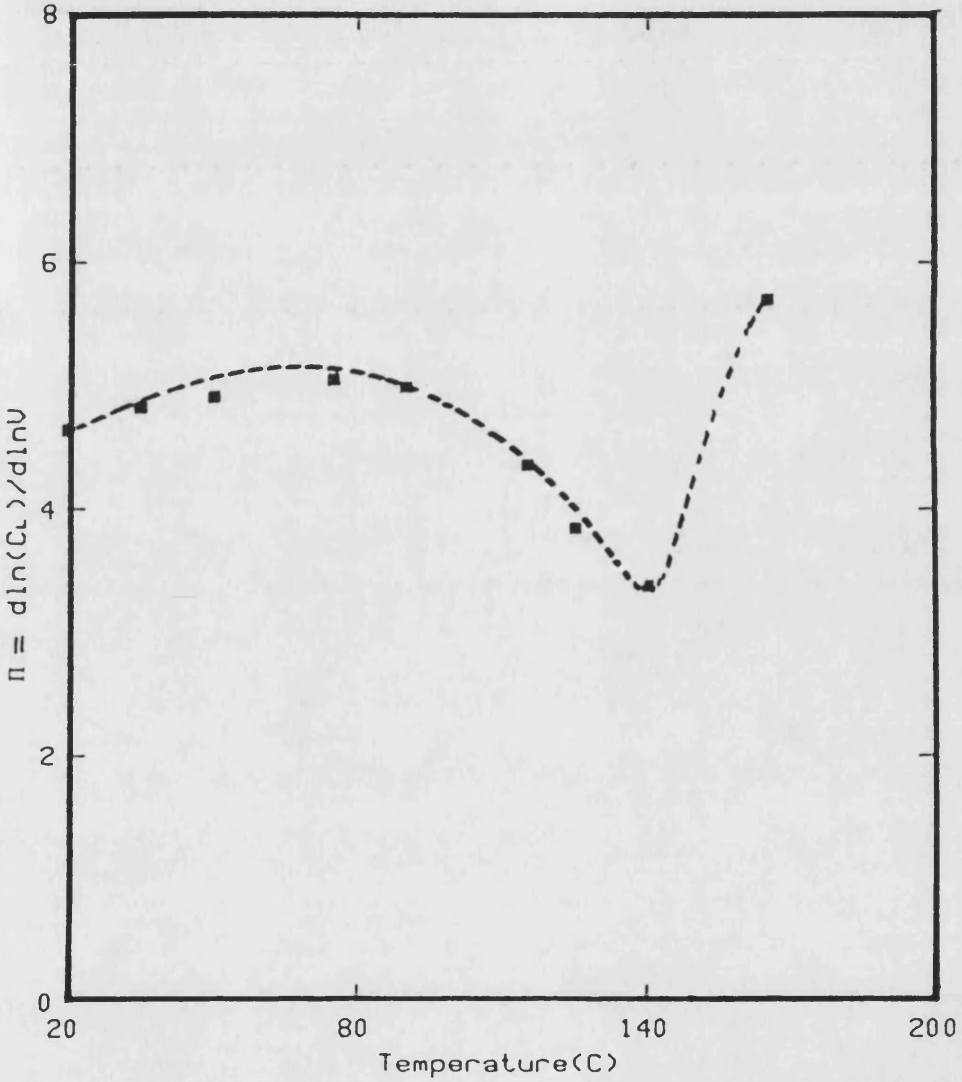

Temperature dependence of logarithmic volume derivatives of $(C_{11}+C_{12}+2C_{44})/2$ of Mn(85)Ni(9)C(6) single crystal (sample C2).
(The curve is drawn solely as visual guide)

Fig 6.26b

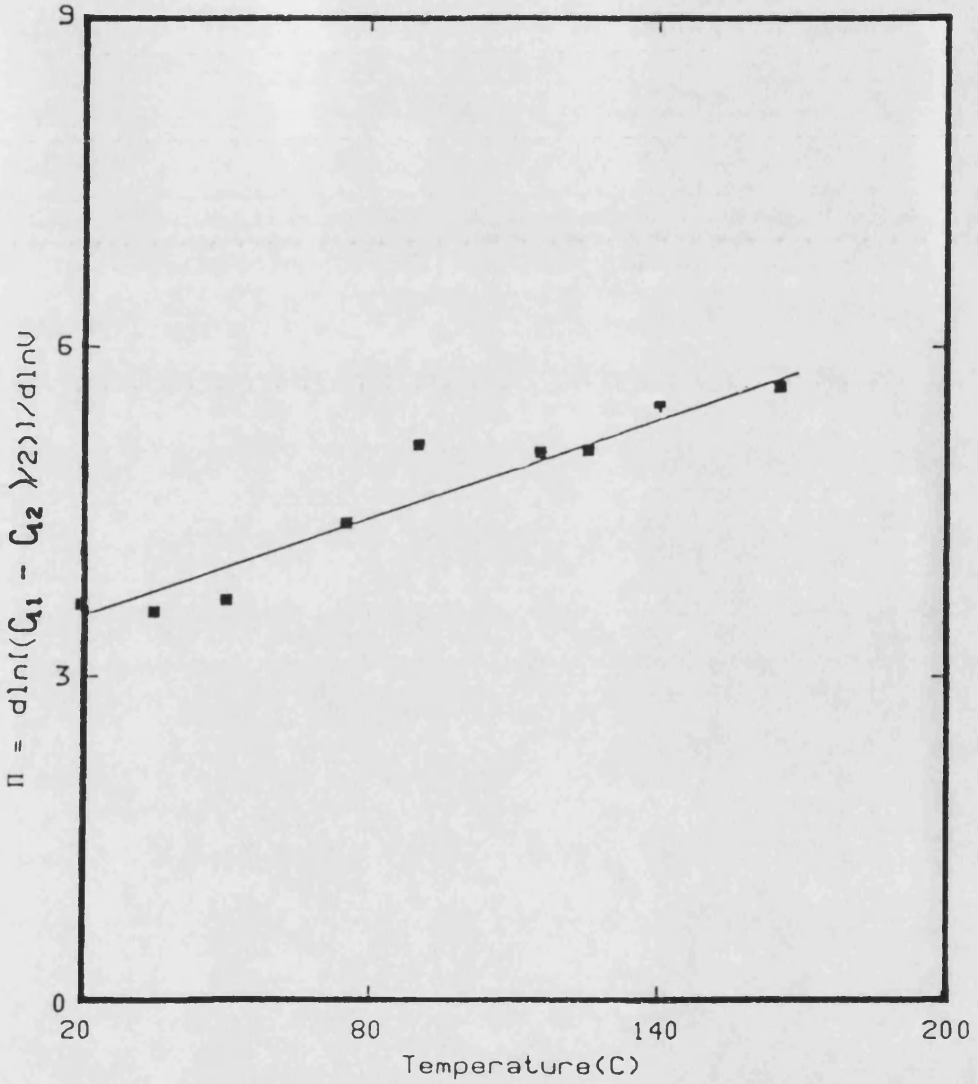

Temperature dependence of logarithmic volume derivatives of (C11-C12)/2 of Mn(85)Ni(9)C(6) single crystal (sample C2).
(The curve is drawn solely as visual guide.)

Fig 6.27b

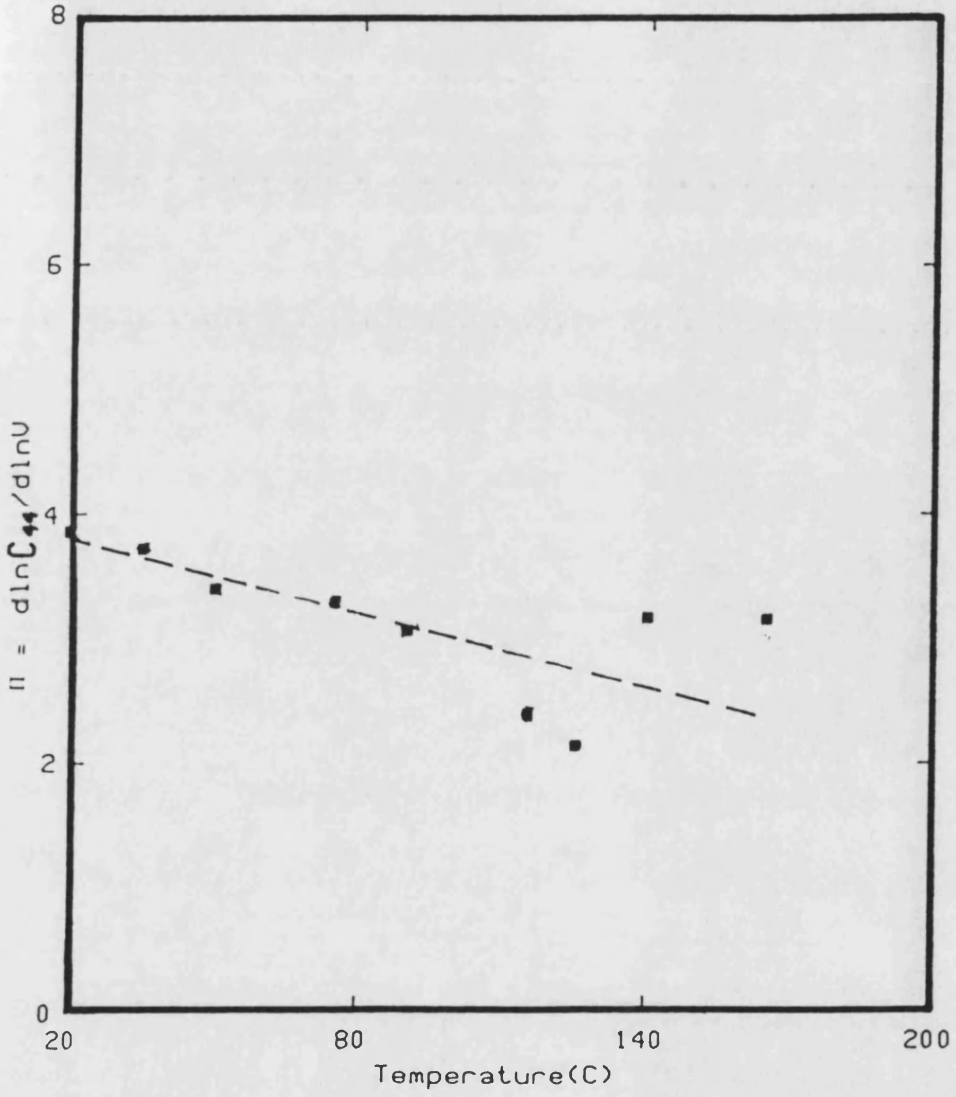

Temperature dependence of logarithmic volume derivative of elastic stiffness constant C44 of MN(85)NI(9)C(6) single crystal (sample C2).

(The curve is drawn solely as visual guide.)

Fig 6.28b

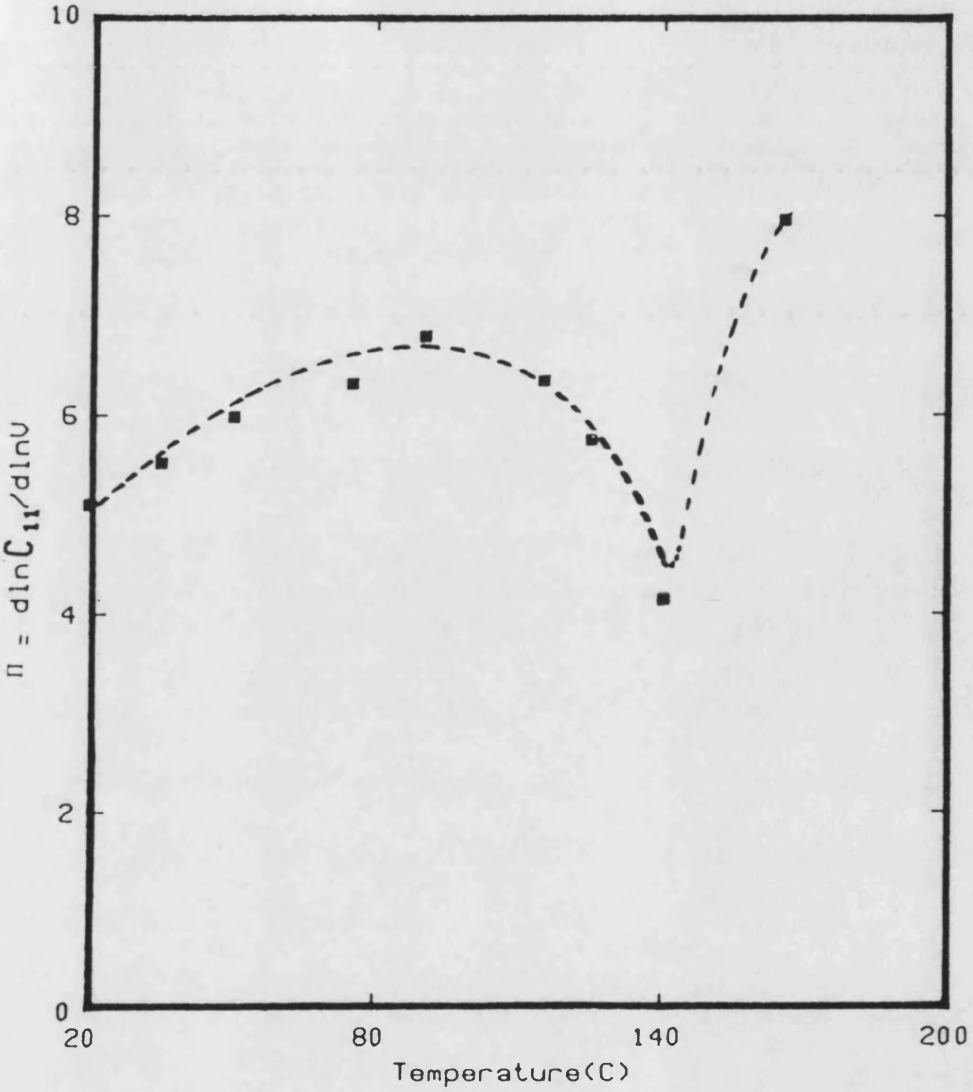

Temperature dependence of logarithmic volume derivatives of C11 of Mn(85)Ni(9)C(6) single crystal (sample C2).
(The curve is drawn solely as visual guide.)

Fig 6.29b

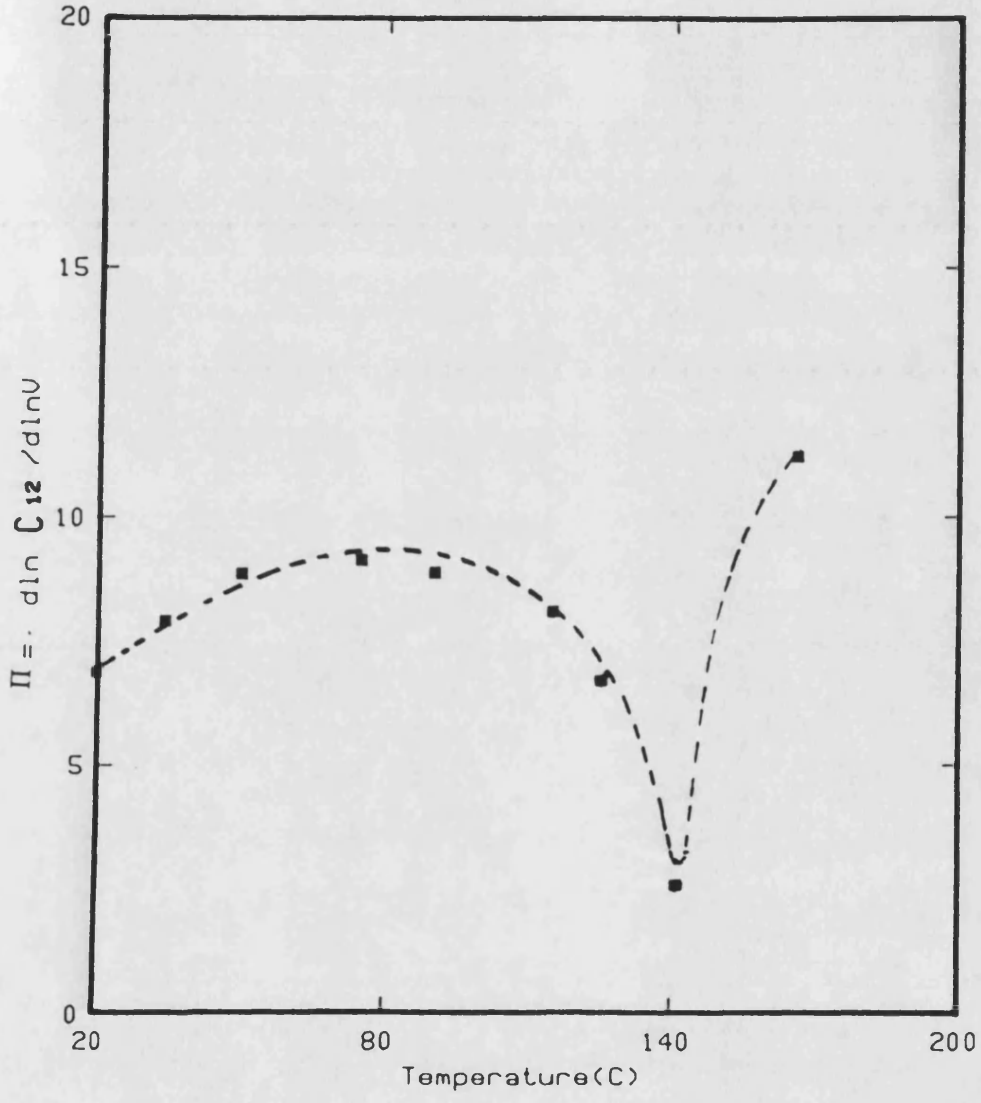

Temperature dependence of logarithmic volume detrivative of the second order elastic stiffness constant C12 of Mn(85)Ni(9)C(6) single crystal (sample C2).
(The curve is drawn solely as visual guide)

Fig 6.30b

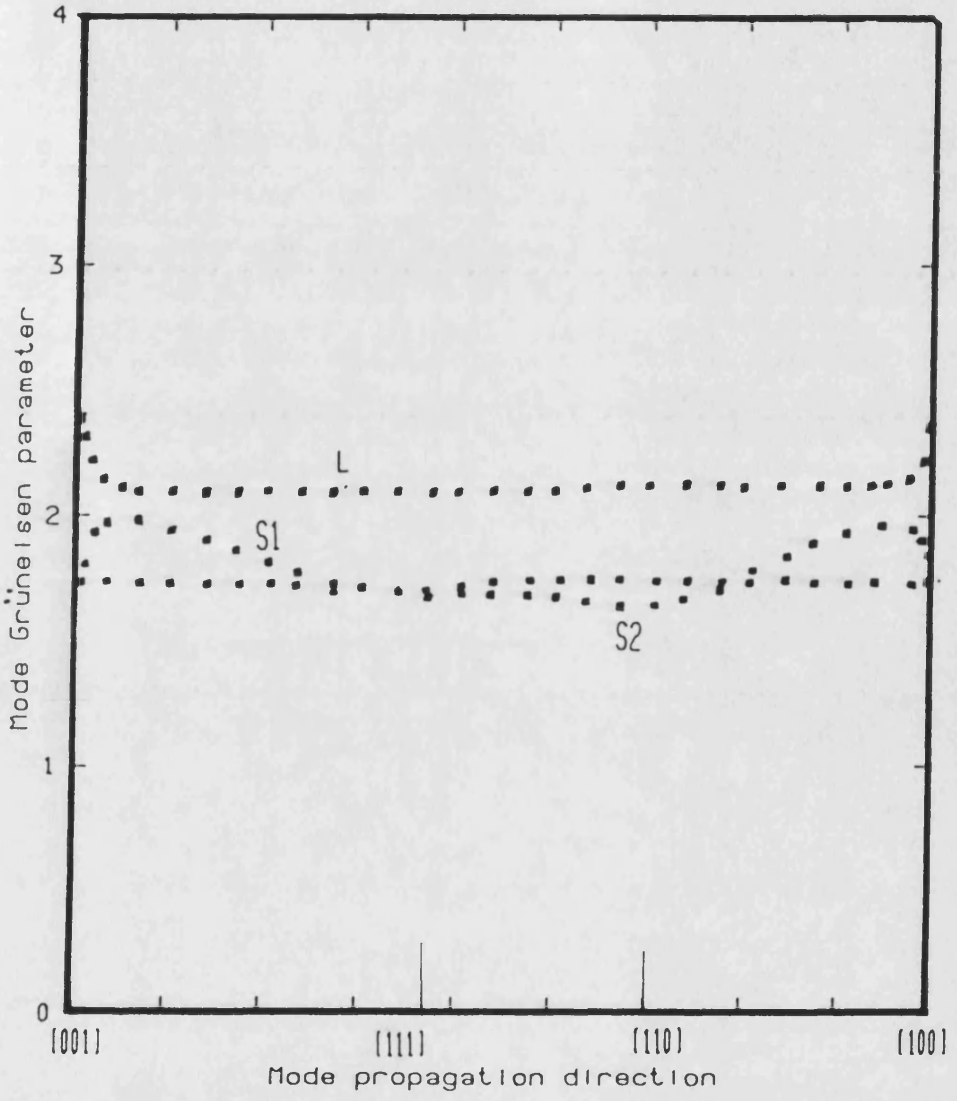

Directional dependence of long wavelength acoustic mode Grüneisen parameters of the Mn(85)Ni(9)C(6) single crystal (sample C2) at 20C

Fig 6.31b

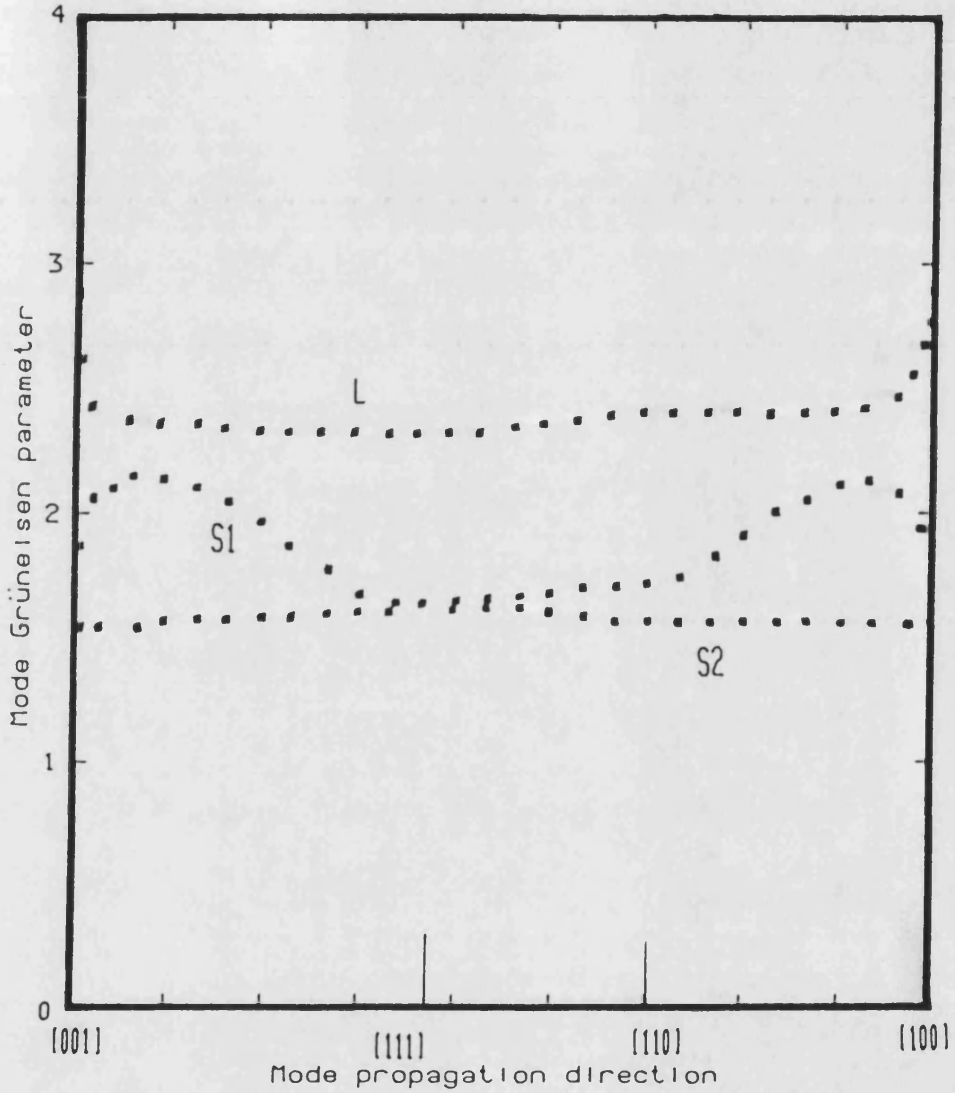

Directional dependence of long wavelength acoustic mode Grüneisen parameters of the Mn(85)Ni(9)C(6) single crystal (sample C2) at 50C

Fig 6.32b

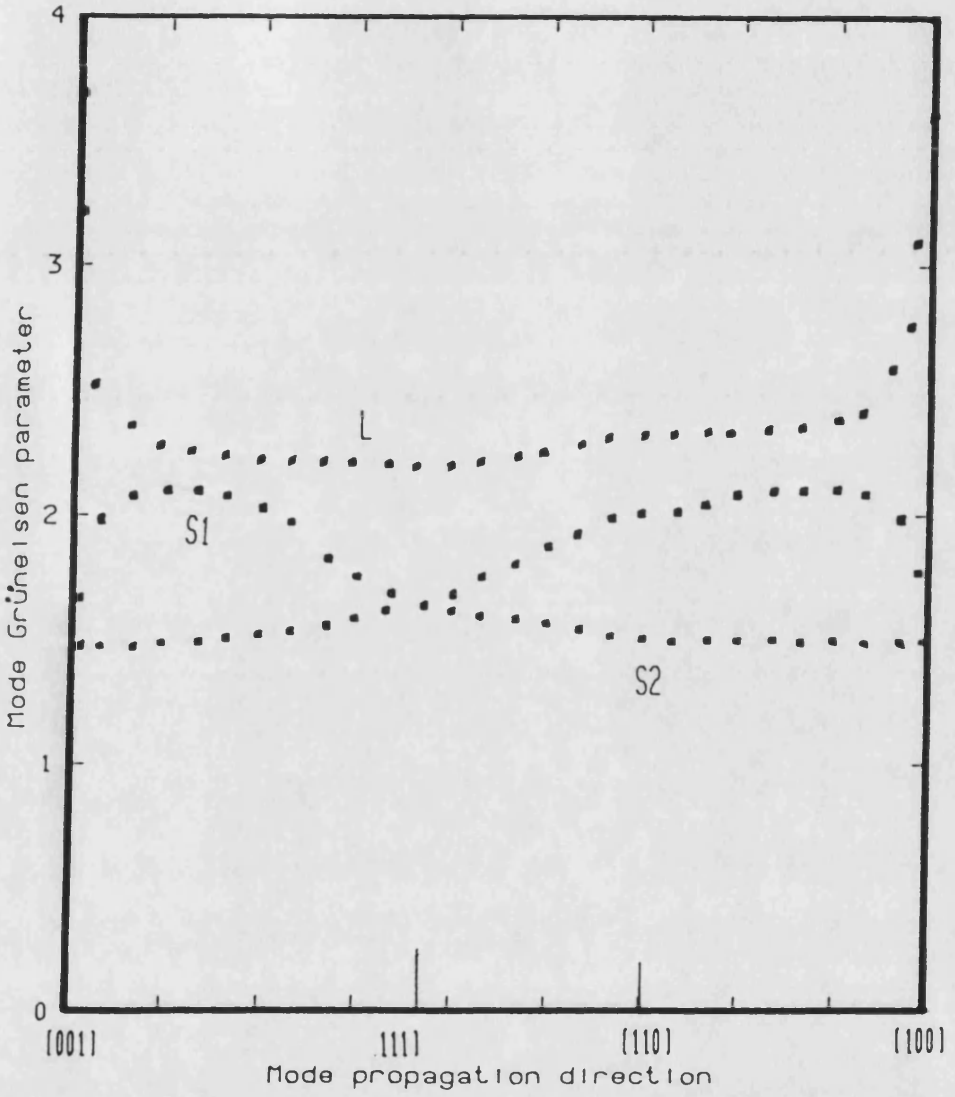

Directional dependence of long wavelength acoustic mode Grüneisen parameters of the Mn(85)Ni(9)C(6) single crystal (sample C2) at 75C

Fig 6.33b

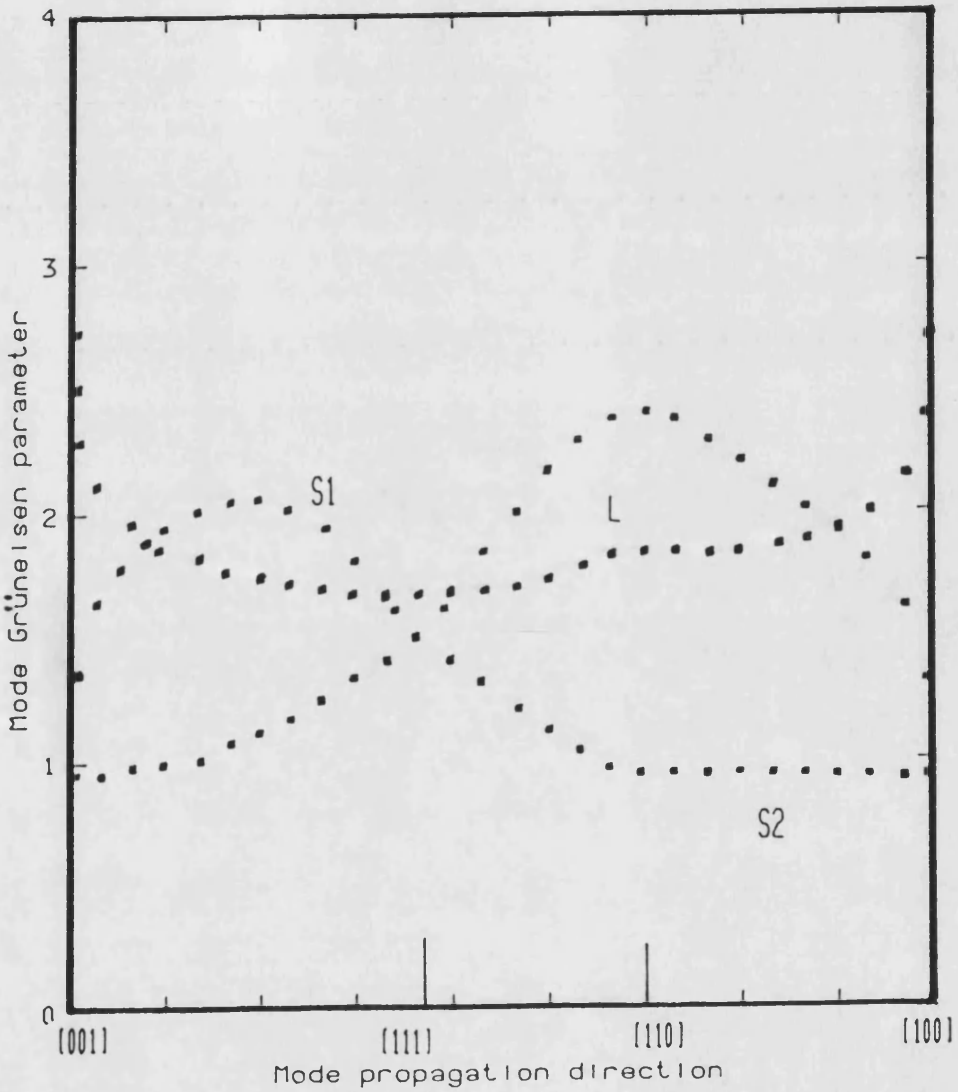

Directional dependence of long wavelength acoustic mode Grüneisen parameters of the Mn(85)Ni(9)C(6) single crystal (sample C2) at 125C

Fig 6.34b

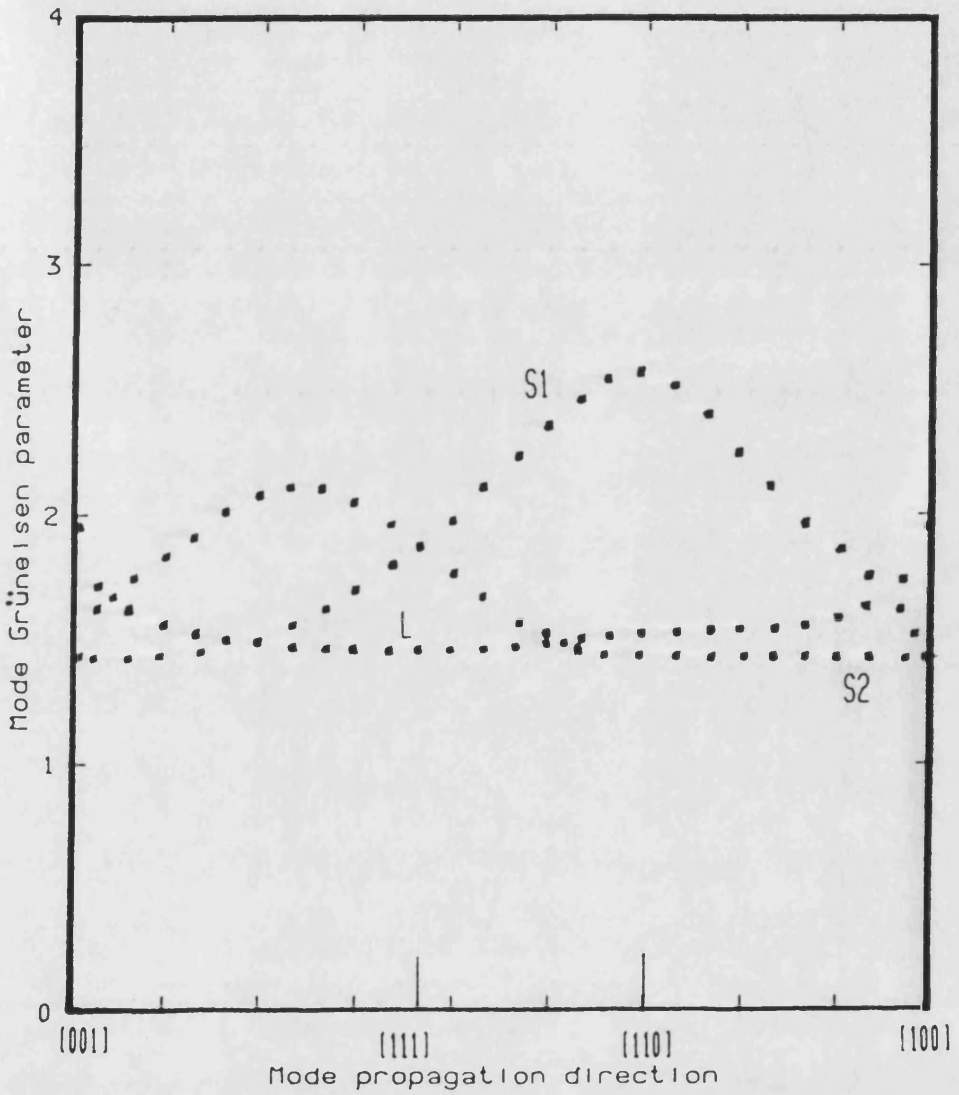

Directional dependence of long wavelength acoustic mode Grüneisen parameters of the Mn(85)Ni(9)C(6) single crystal (sample C2) at 140C

Fig 6.35b

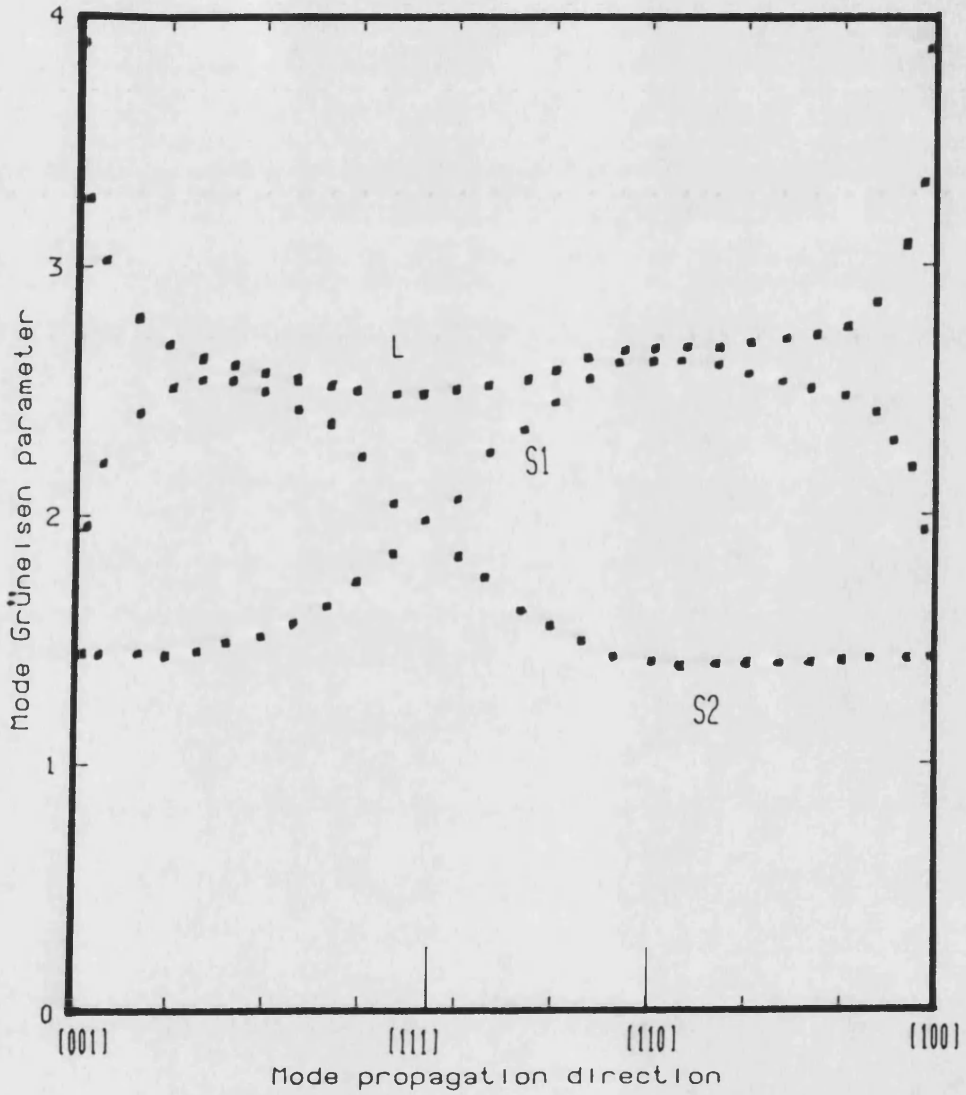

Directional dependence of long wavelength acoustic mode Grüneisen parameters of the Mn(85)Ni(9)C(6) single crystal (sample C2) at 165C

Fig 6.36b

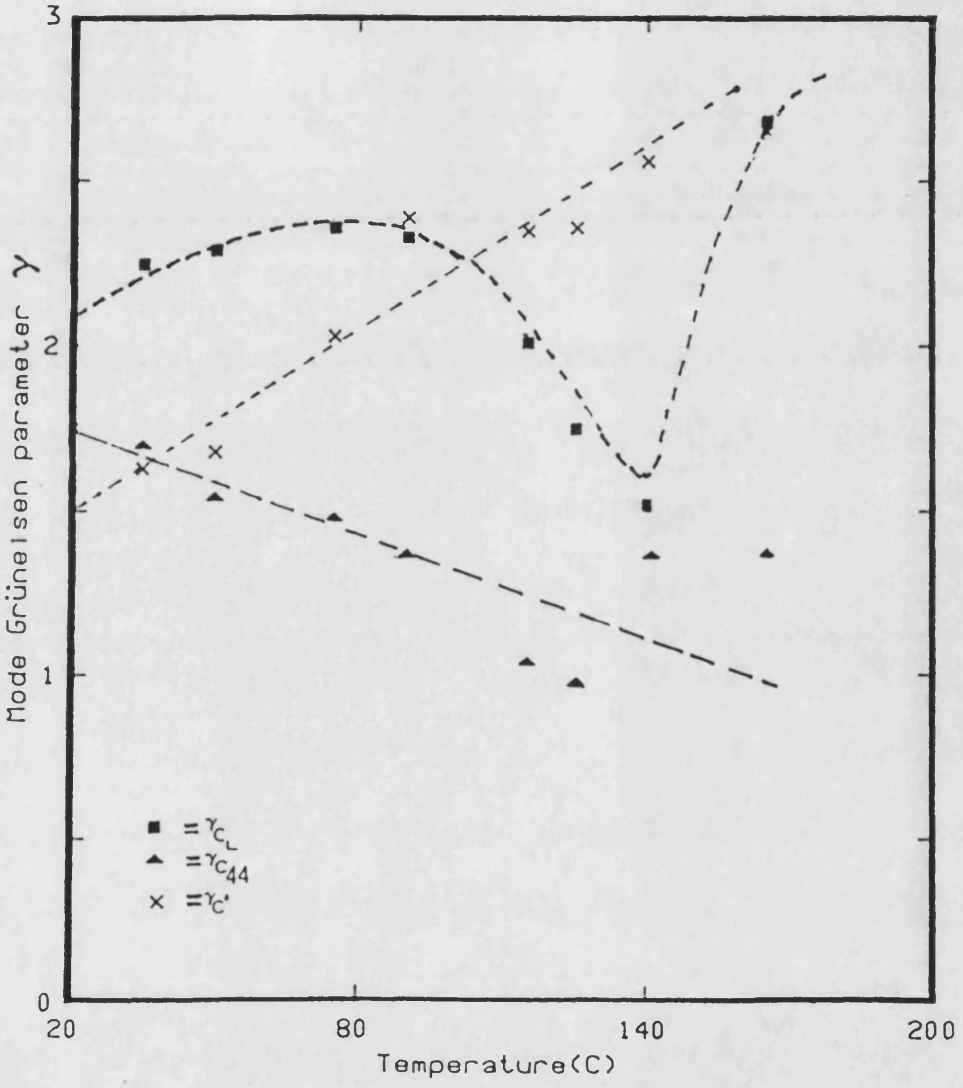

Temperature dependences of the acoustic mode Grüneisen parameter in the [110] direction of the Mn(85)Ni(9)C(6) single crystal (sample C2)

(The curve is drawn solely as visual guide)

Fig 6.37b

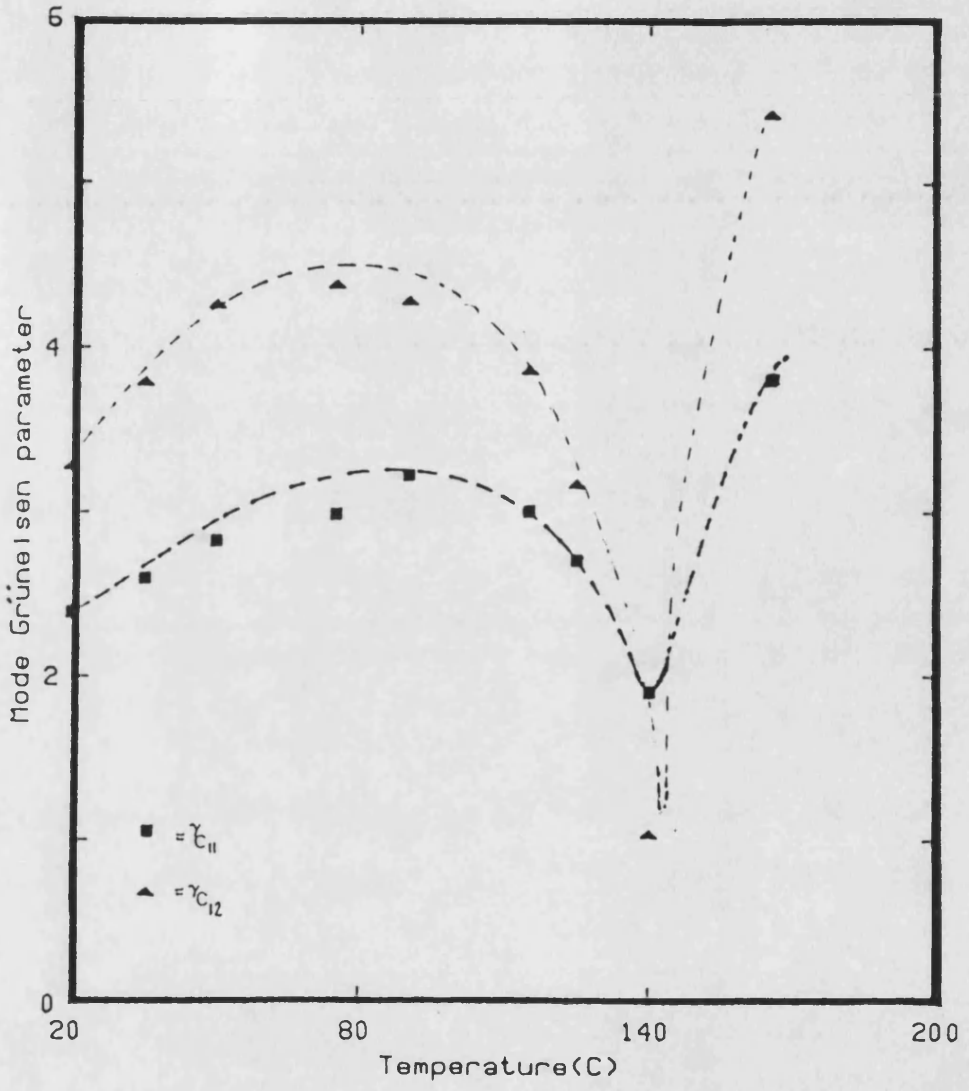

Temperature dependences of the acoustic mode Grüneisen parameter of the Mn(85)Ni(9)C(6) single crystal (sample C2)

(The curve is drawn solely as visual guide)

Fig 6.38b

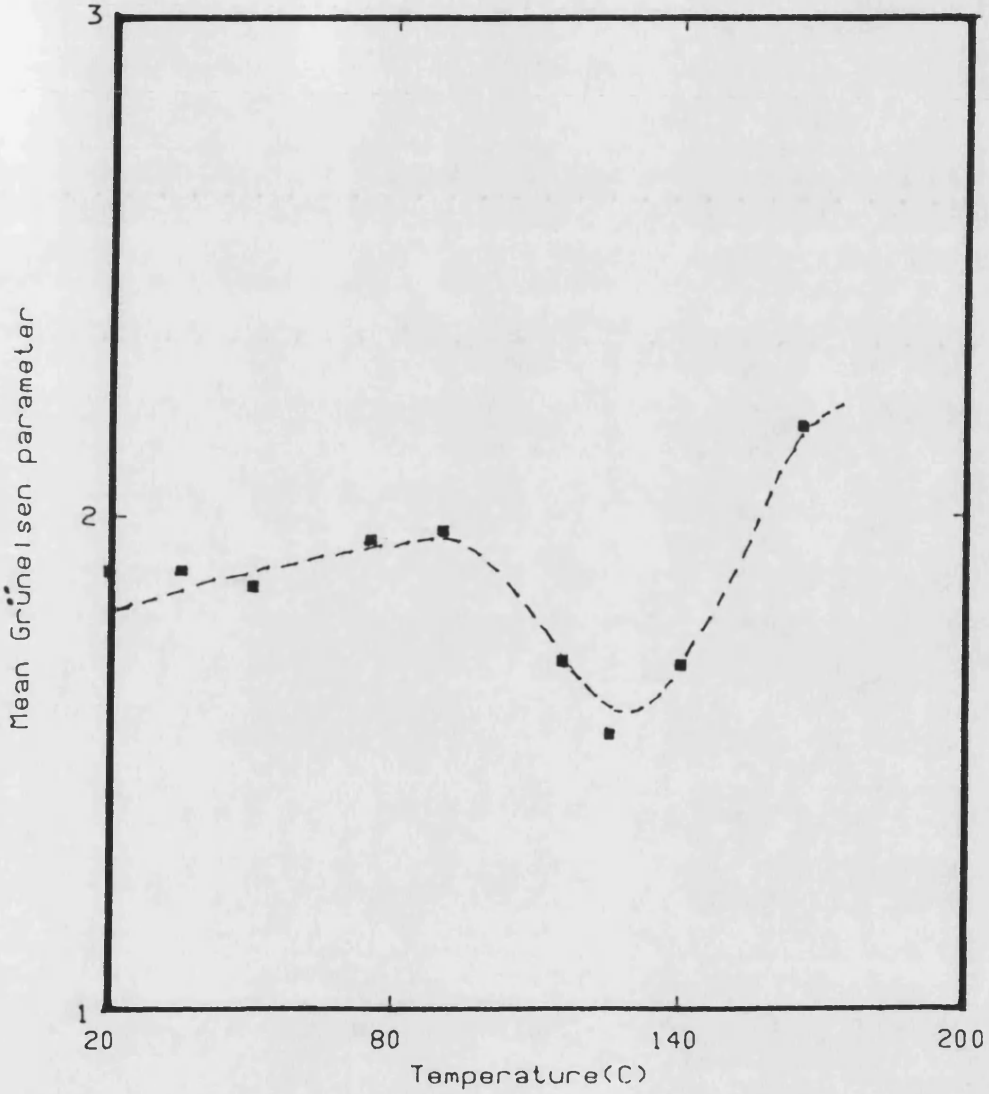

Temperature dependence of acoustic mode mean Grüneisen parameter of the Mn(85)Ni(9)C(6) single crystal (sample C2) in the antiferromagnetic state.

(The curve is drawn solely as visual guide.)

Fig 6.39b

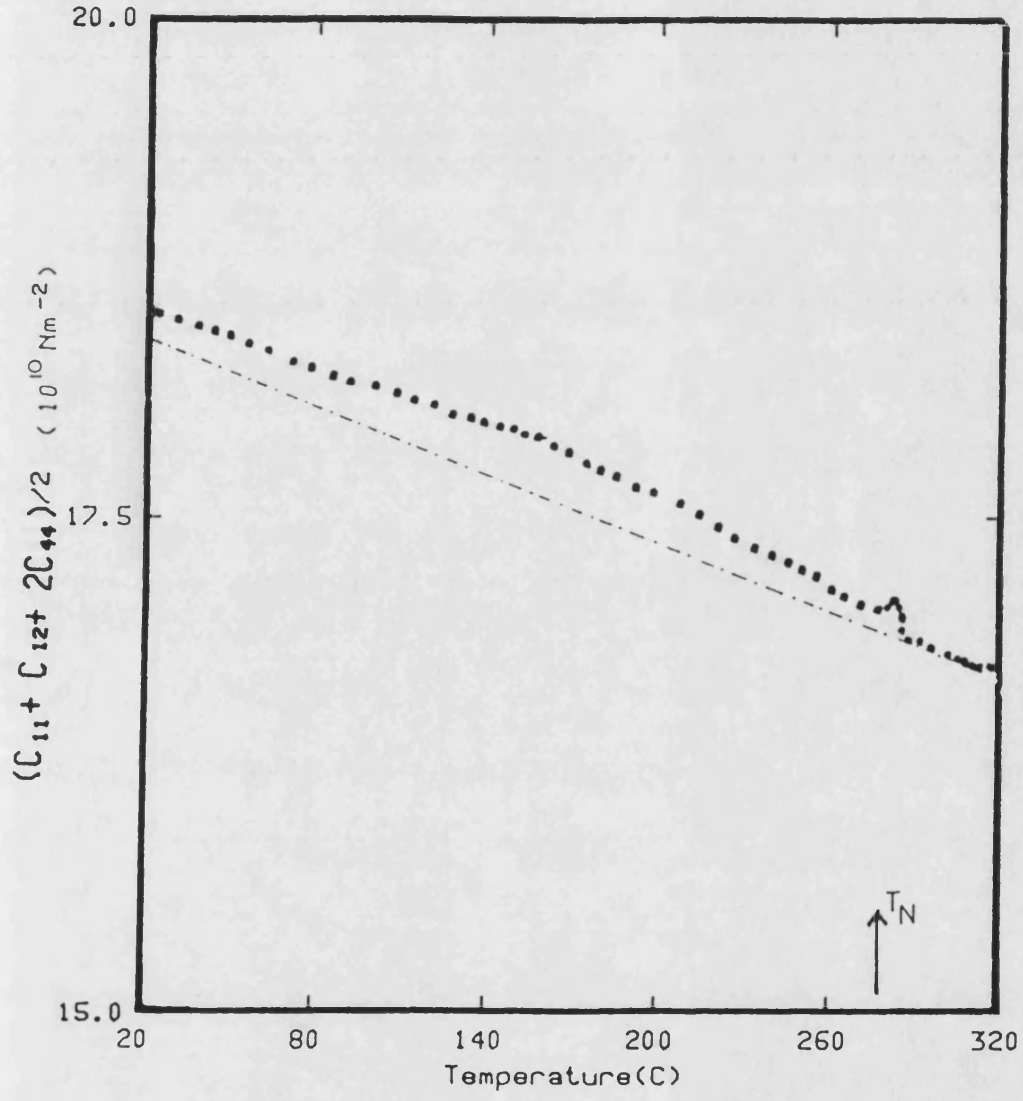

Temperature dependence of the second order elastic stiffness constant of Mn(85)Ni(9)C(6) single crystal (sample F) for a longitudinal acoustic wave propagates in the [110] direction

Fig.6.1c

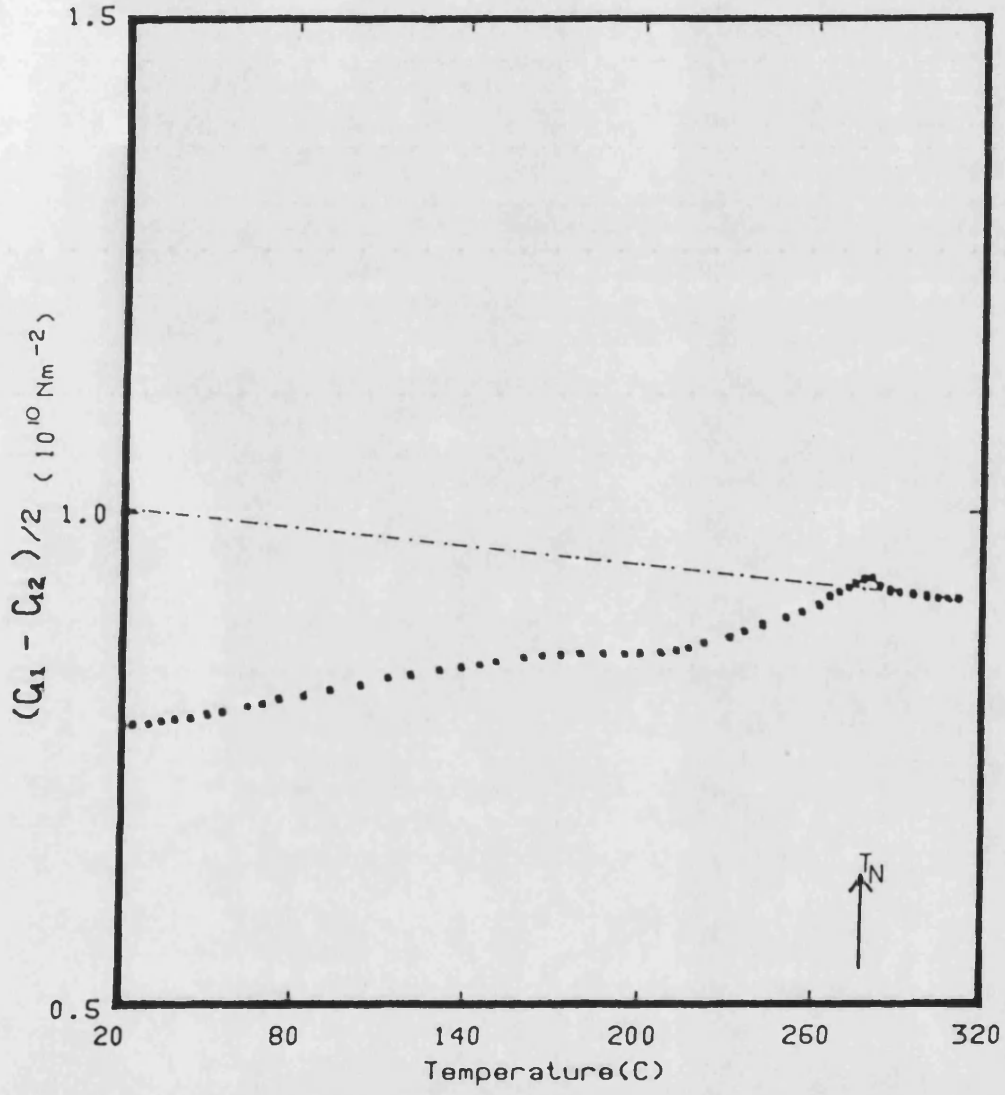

Temperature dependence of the second order elastic stiffness constant of Mn(85)Ni(9)C(6) single crystal (sample F) for a **shear** acoustic wave propagates in the [110] direction

Fig.6.2c

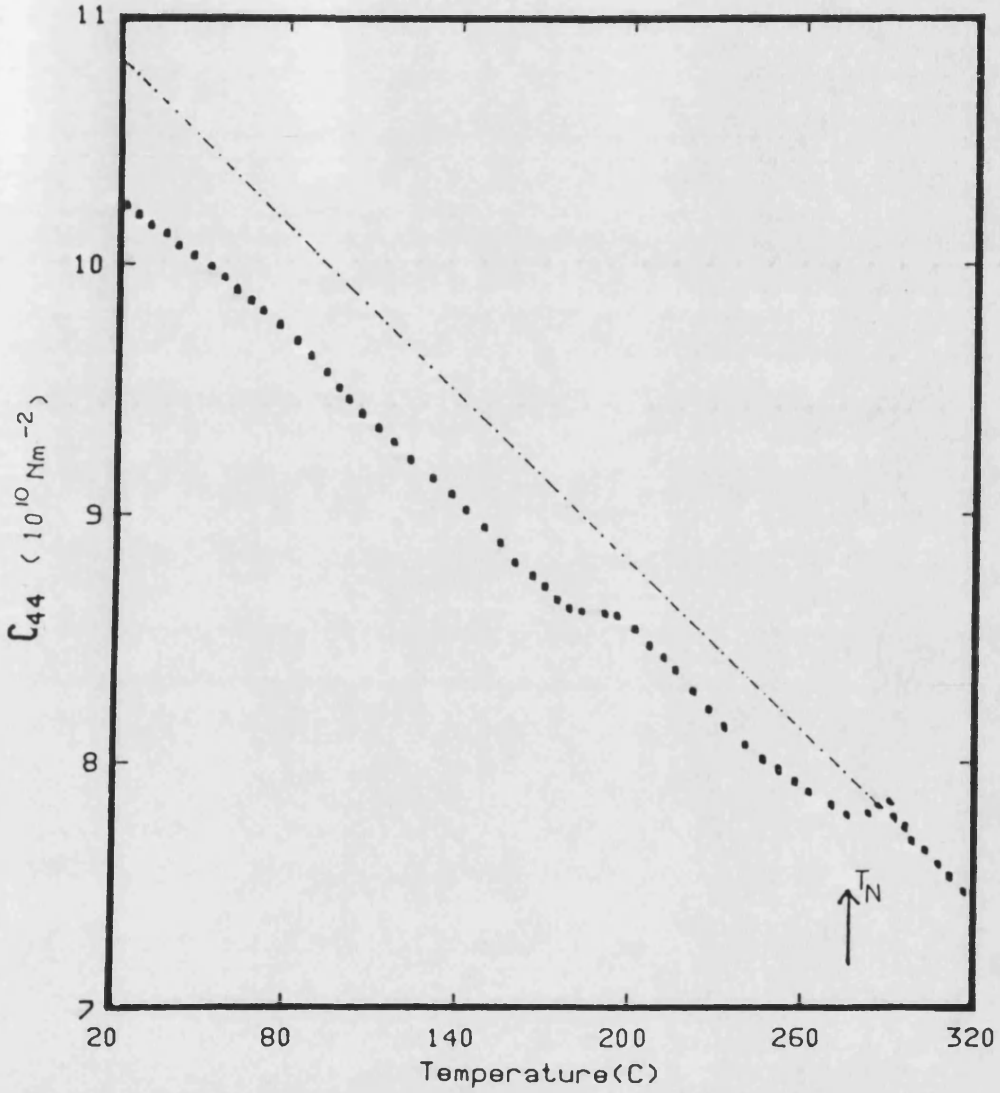

Temperature dependence of the second order elastic stiffness constant of Mn(85)Ni(9)C(6) single crystal (sample F) for a shear acoustic wave propagates in the [110] direction

Fig.6.3c

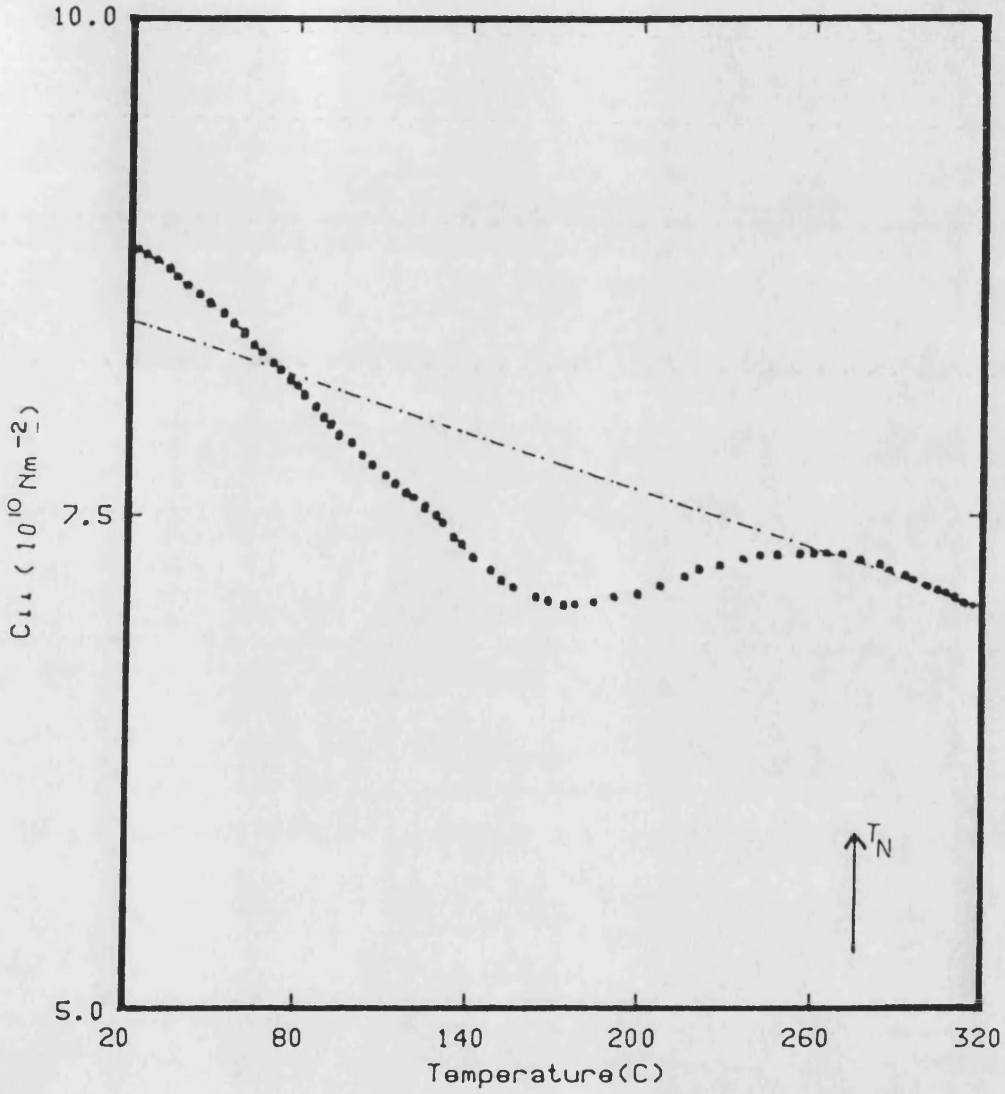

Temperature dependence of the second order elastic stiffness constant (C_{11}) of Mn(85)Ni(9)C(6) single crystal (sample F)

Fig.6.4c

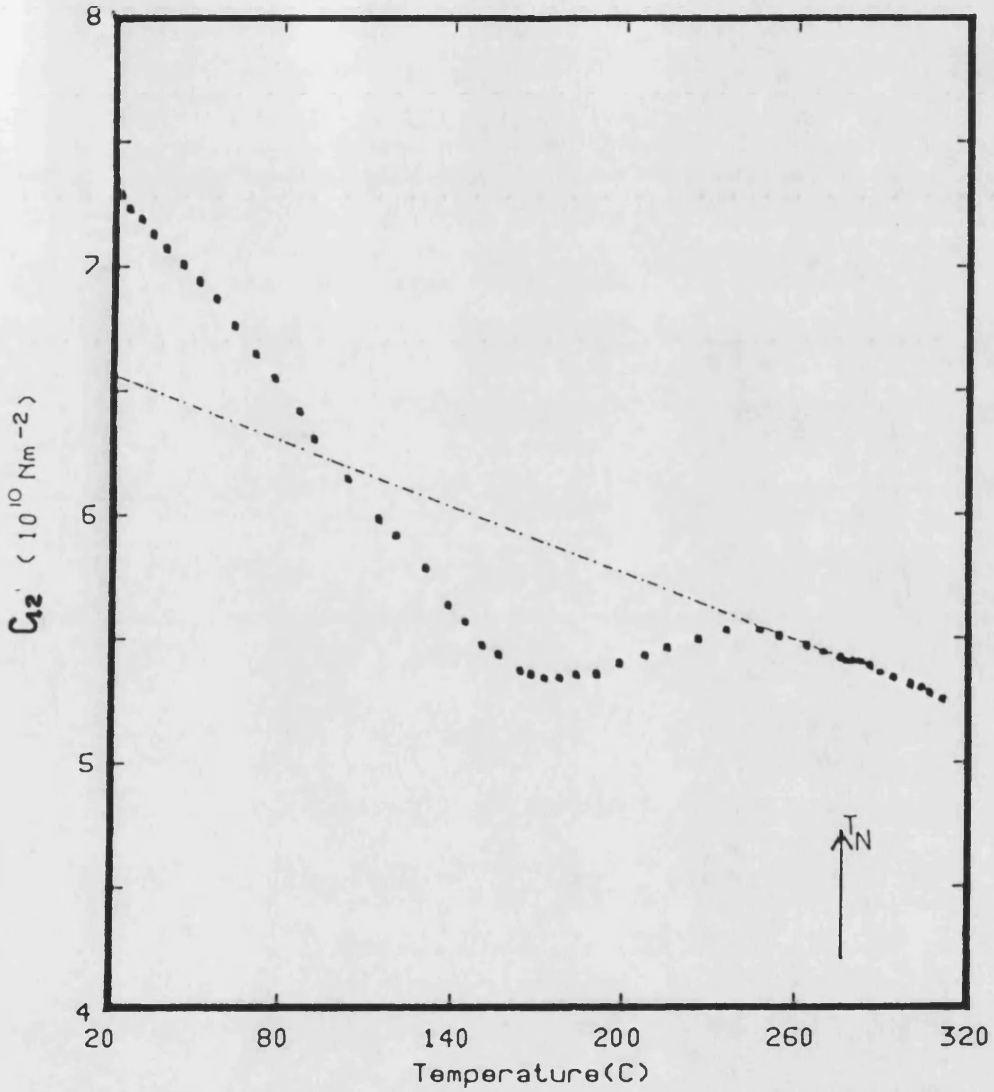

Temperature dependence of elastic stiffness constant C_{12} of Mn(85)Ni(9)C(6) single crystal (sample F)

Fig.6.5c

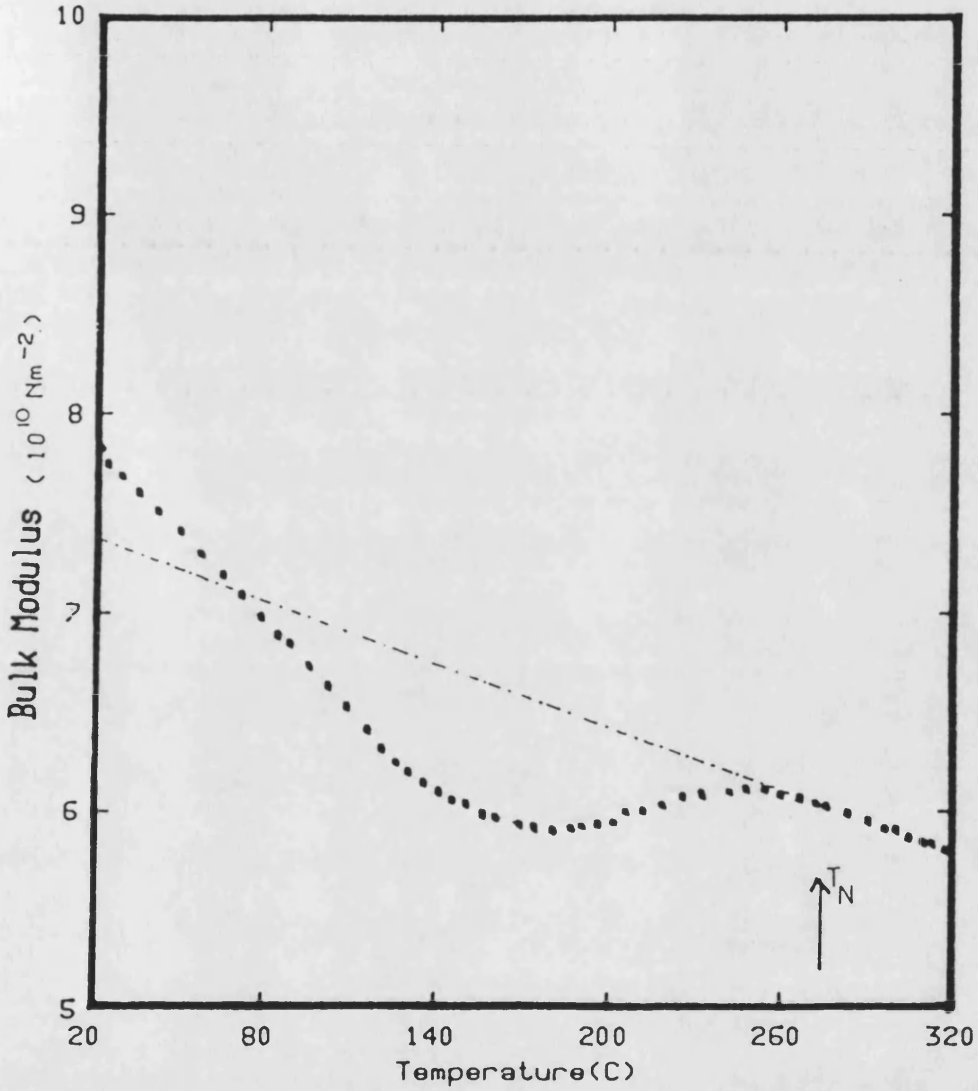

Temperature dependence of bulk modulus of Mn(85)Ni(9)C(6) single crystal (sample F)

Fig.6.6c

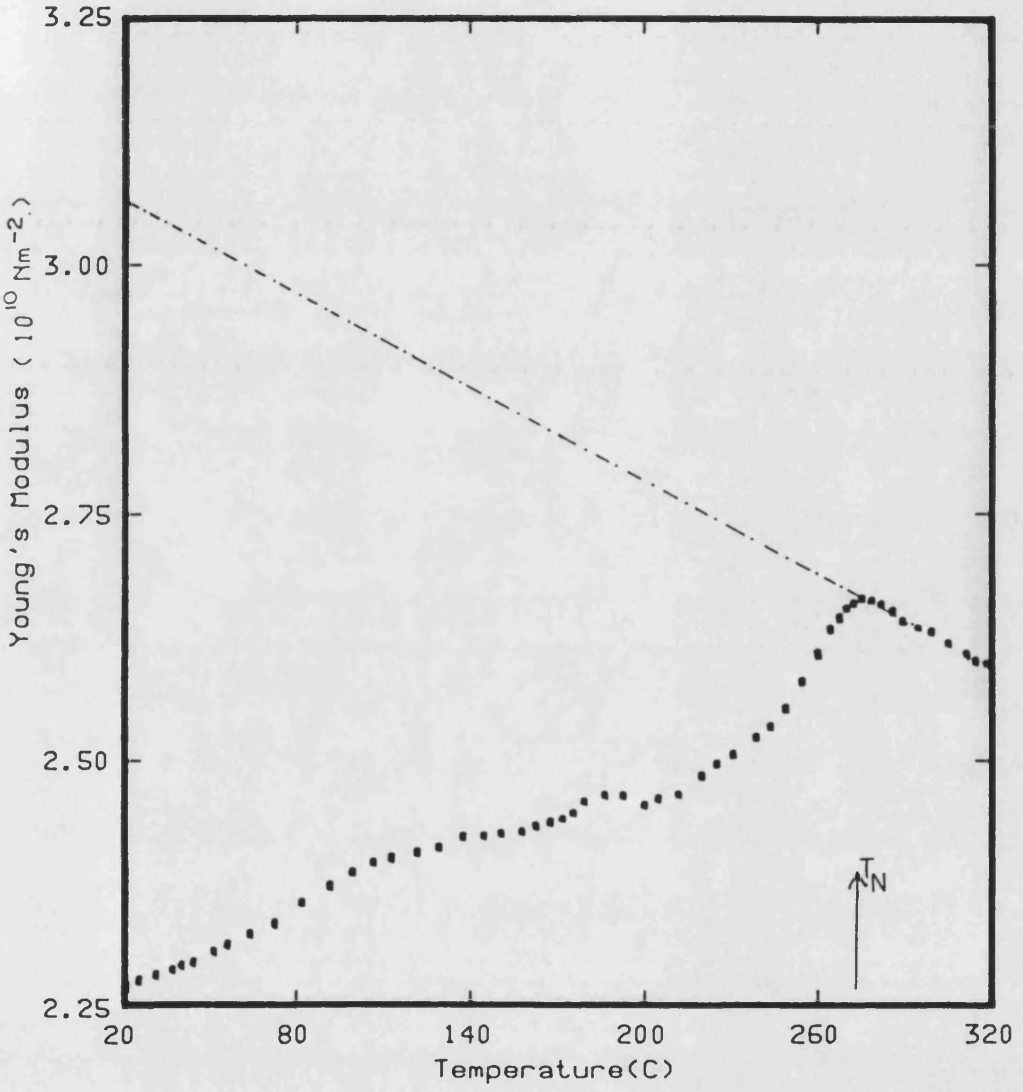

Temperature dependence of Young's modulus in the [001] direction of Mn(85)Ni(9)C(6) sample F single crystal.

Fig.6.7c

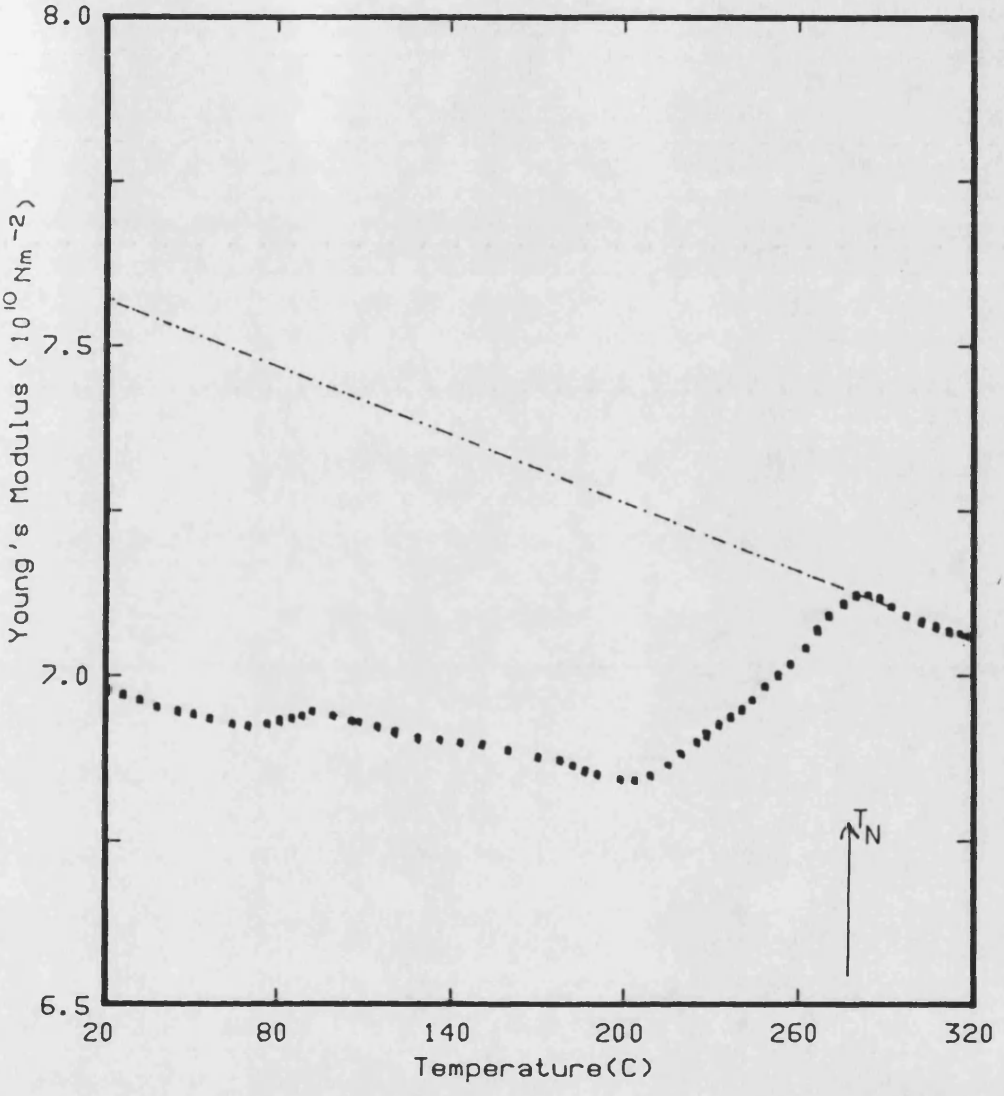

Temperature dependence of Young' modulus in the [110] direction of Mn(85)Ni(9)C(6) sample F single crystal.

Fig.6.8c

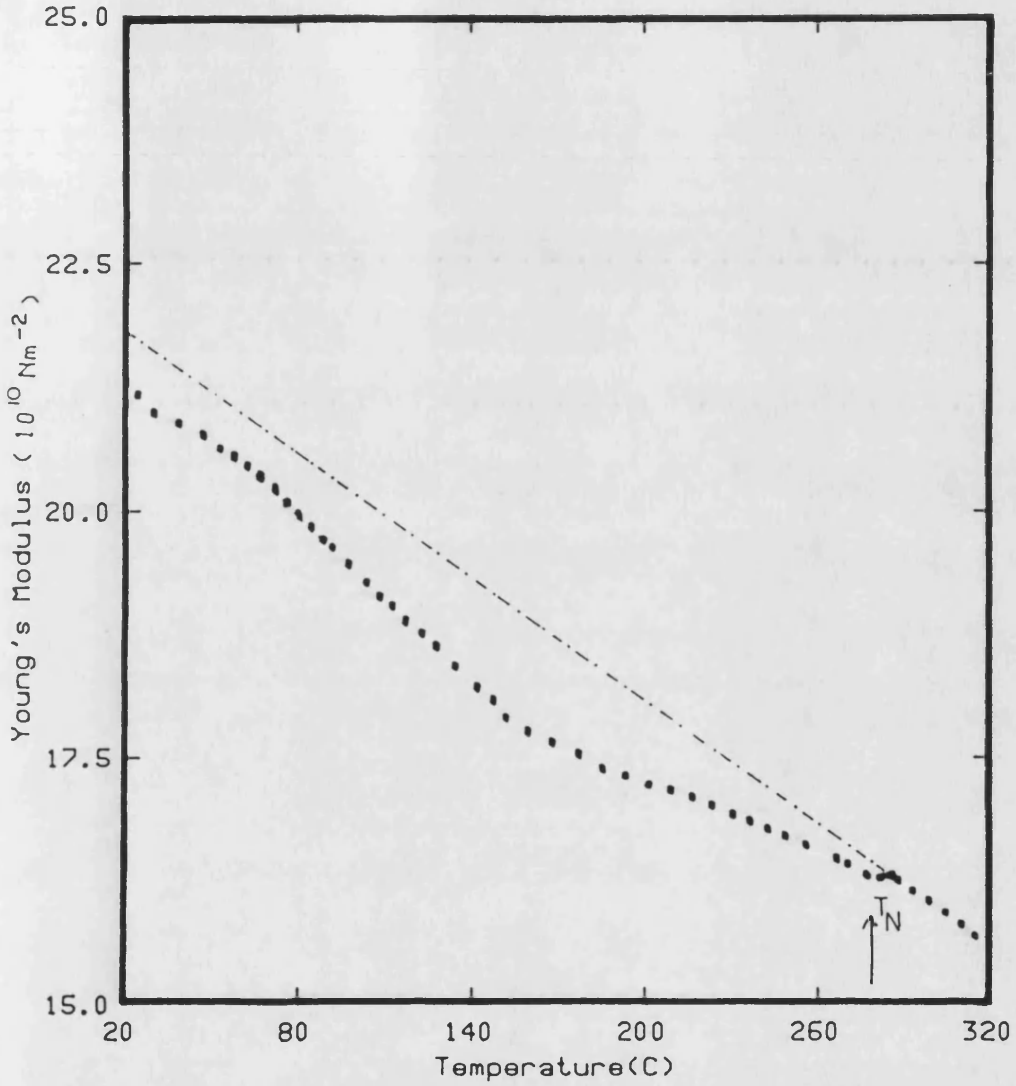

Temperature dependence of Young's modulus in the [111] direction of Mn(85)Ni(9)C(6) sample F single crystal.

Fig.6.9c

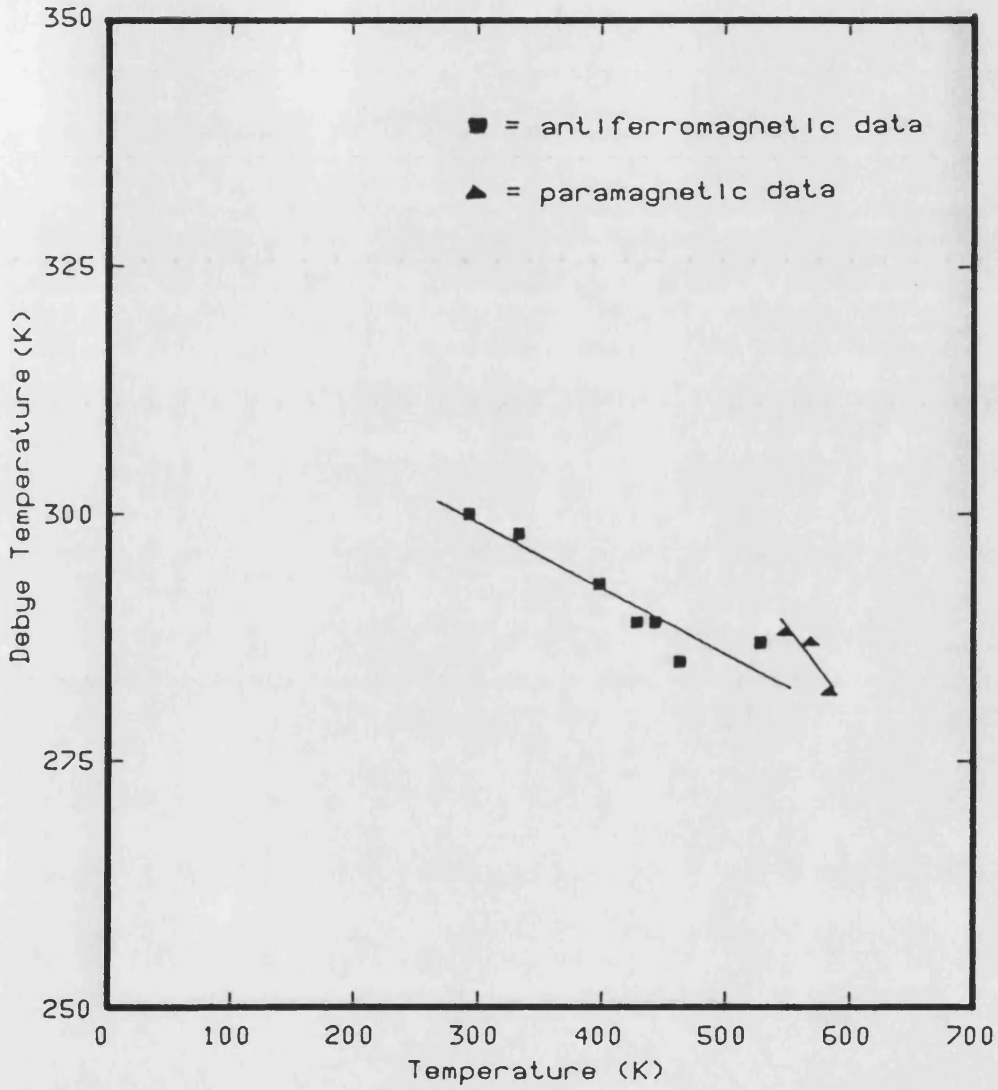

Determination of Debye temperature of Mn(85)Ni(9)C(6) single crystal (sample F) at 0K by extrapolating the experimental data.

Fig.6.9c1

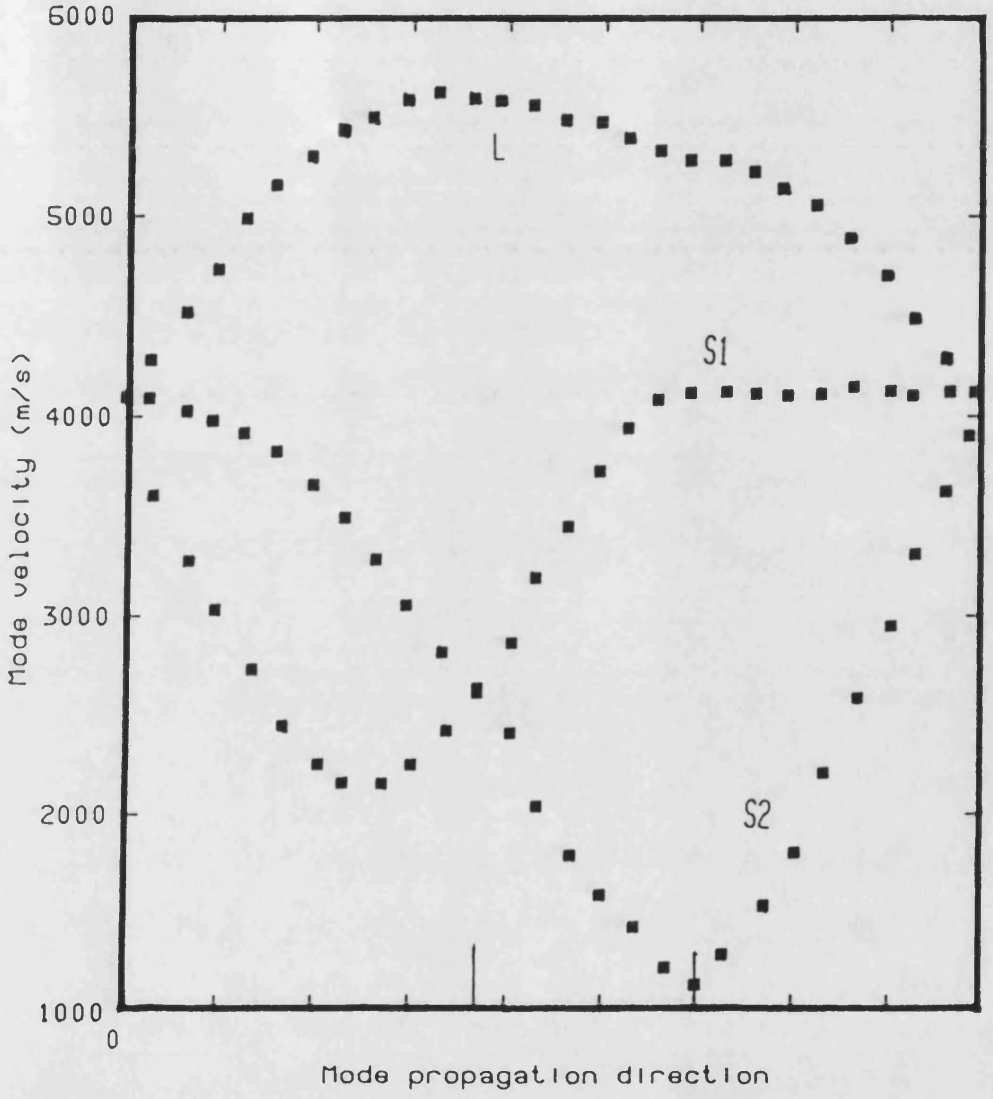

Directional dependence of long wavelength acoustic mode velocities of the Mn(85)Ni(9)C(6) single crystal (sample F) at 20C

Fig.6.10c

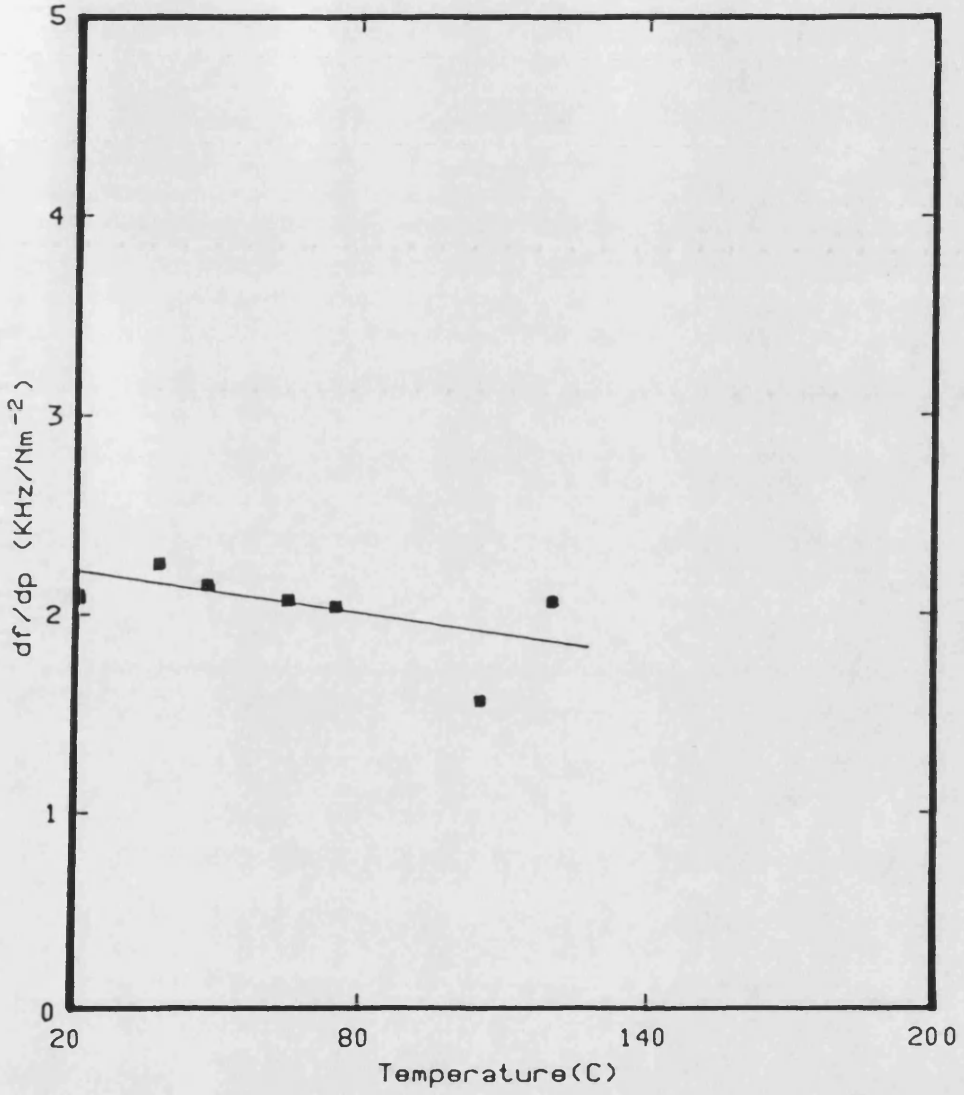

Temperature dependence of pressure derivative of overlapping frequency associated with C_{44} of Mn(85)Ni(9)C(6) (sample F).

The curve is drawn solely as visual guide.

Fig 6.12c

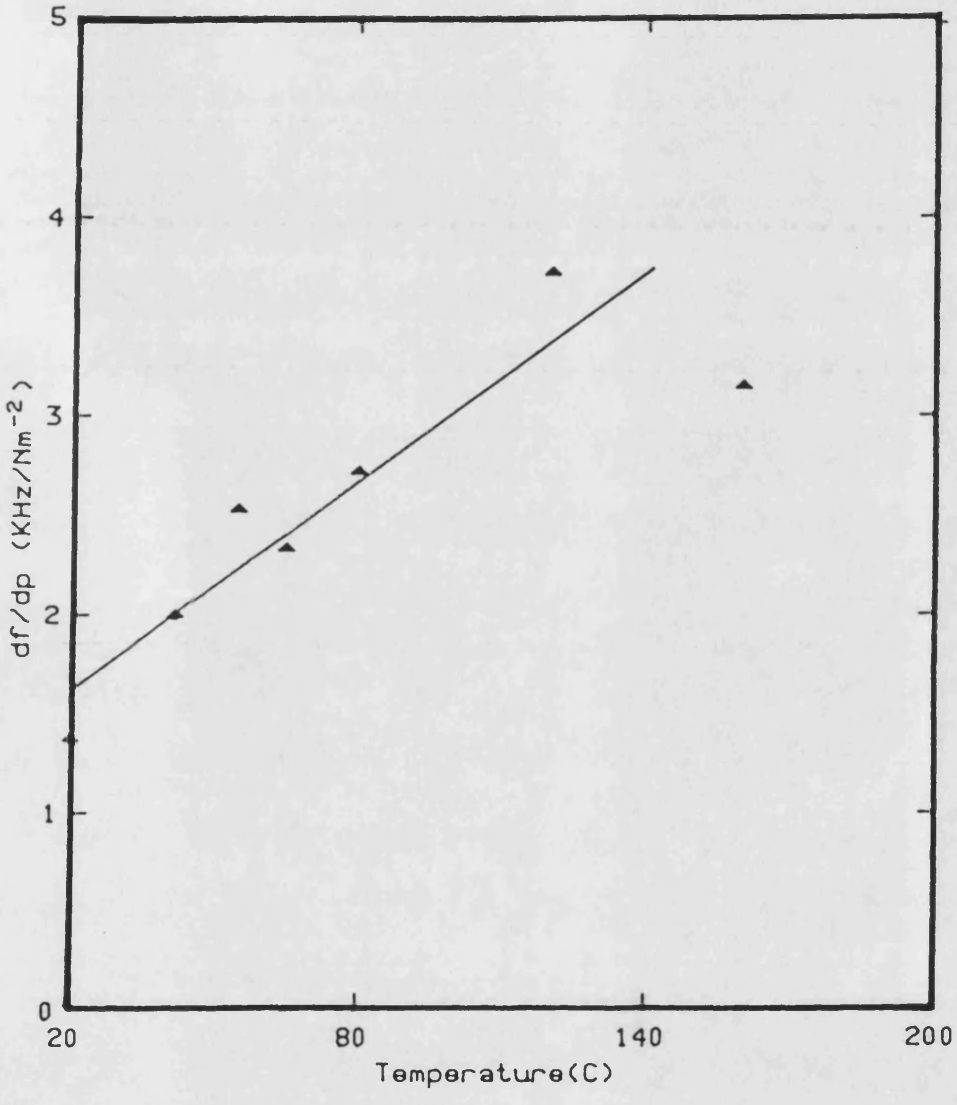

Temperature dependence of pressure derivative of overlapping frequency associated with C_{11} of Mn(85)Ni(9)C(6) (sample F).

The curve is drawn solely as visual guide.

Fig.6.11c

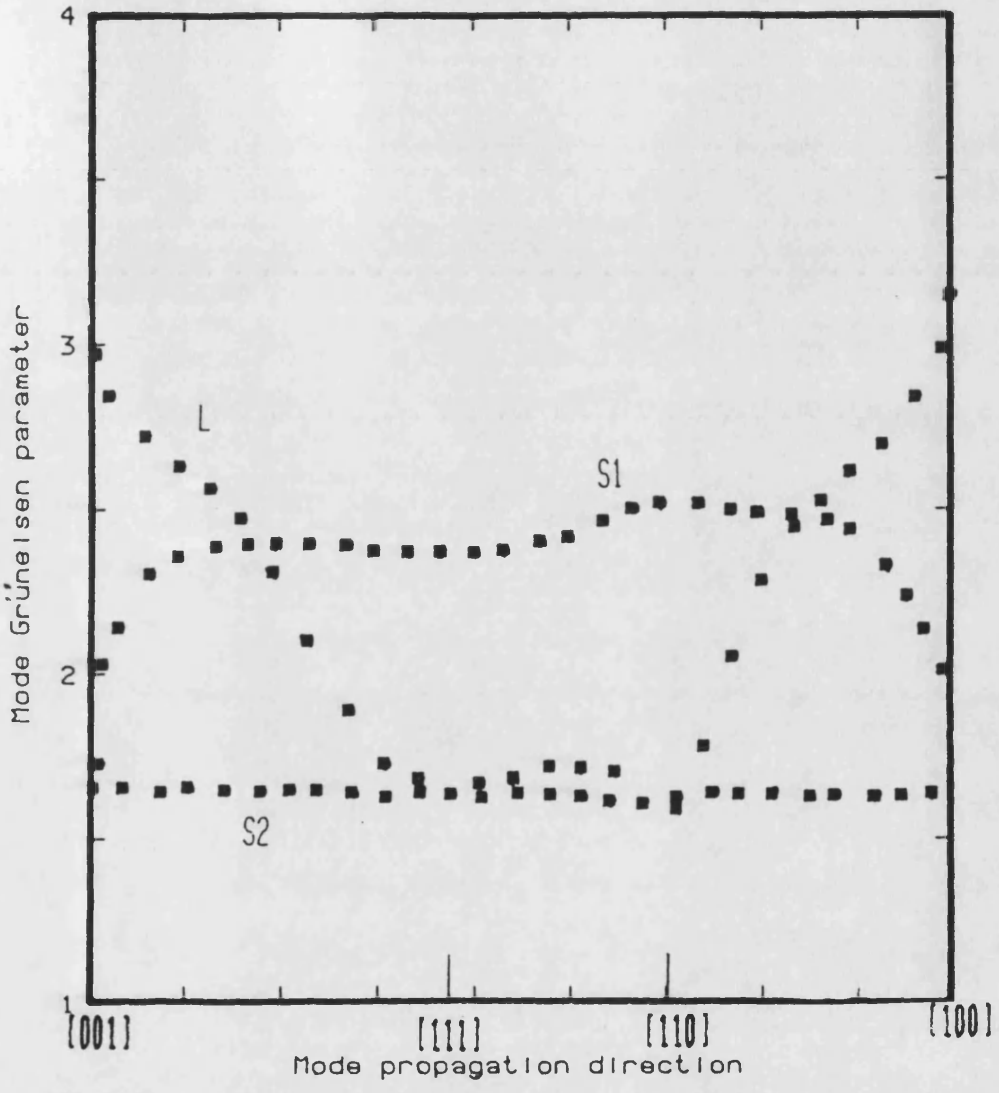

Directional dependence of long wavelength acoustic mode Grüneisen parameters of the Mn(85)Ni(9)C(6) single crystal (sample F) at 20C

Fig 6.13c

CHAPTER 7

DISCUSSION OF EXPERIMENTAL RESULTS OBTAINED ON γ-Mn-Ni ALLOYS

7.1 Introduction

In this chapter the experimental results which have been described in chapter 6 will be discussed under the following headings:

i) The second order elastic stiffness constants of $Mn_{73}Ni_{27}$ and $Mn_{84}Ni_{16}$ obtained as a function of temperature up to and through the Nēel temperatures.

ii) The hydrostatic pressure derivatives of the second order elastic stiffness constants of $Mn_{73}Ni_{27}$ up to and through the Nēel temperature.

iii) These results are then used to determine the acoustic mode Grüneisen parameters of $Mn_{73}Ni_{27}$ on both the antiferromagnetic and the paramagnetic states.

iv) The elastic stiffness constants as a function of temperature of the ternary manganese nickel carbon alloys $Mn_{85}Ni_9C_6$ (sample C2) and $Mn_{85}Ni_9C_6$ (sample F) up to and through the Nēel temperatures.

v) The hydrostatic pressure derivatives of the SOEC of the two $Mn_{85}Ni_9C_6$ alloys.

vi) The Grüneisen parameter of $Mn_{85}Ni_9C_6$ (sample C2) in the antiferromagnetic state.

7.2 The Second Order Elastic Stiffness Constants as a Function of Temperature of $Mn_{73}Ni_{27}$ and $Mn_{84}Ni_{16}$ up to and through the Nēel Temperatures.

A binary γ-Mn-Ni alloy with a composition $Mn_{73}Ni_{27}$ was chosen to make a complete study of the elastic constants as a function of temperature up to and through the Nēel point T_N primarily because this particular crystal has a low Nēel temperature($\sim$410K) compared with those of alloys which are richer in manganese. Hence it was possible to measure the hydrostatic pressure effects on the elastic constants in the paramagnetic state above T_N. An important consideration is that this alloy composition is definitively in the range in which the crystal is f.c.c. both above and below T_N and at room temperature (Fig.2.2). It is important to make this first study of the magnetic effects on elastic behaviour on a crystal in which there is no martensitic transition to influence the physical properties in a different way. This provides the platform for understanding the behaviour of alloys which are richer in manganese and whose crystallography is more complex.

The elastic constants C_L (=$(C_{11}+C_{12}+2C_{44})/2$), C'(=$(C_{11}-C_{12})/2$) and C_{44} have been obtained from the measurements of transit times of ultrasonic waves corresponding to these modes. These data enable the individual elastic stiffness tensor components C_{11}, C_{12} and C_{44} to be determined. The elastic constants C_L, C_{44}, $(C_{11} - C_{12})/2$, C_{11} and C_{12} of $Mn_{73}Ni_{27}$ are shown as a function of temperature in Fig.6.1a to 6.5a. This is the first complete set of elastic constants of a Mn-Ni alloy measured up to and through the Nēel point. However, there have been earlier related studies (see section 2.6) of the elastic behaviour of Mn-Ni alloys. Hicks, Pepper and Smith (1968) observed that Young's modulus for a Mn-18.7at.%Ni alloy decreased considerably when a polycrystalline sample was cooled through T_N. Both the Young's modulus and shear moduli, measured by Honda, Tanji and Nakagawa (1976) on polycrystalline γ-Mn alloys over the composition range 12 to 40at.%Ni, show a step-like increase as the temperature was taken up through T_N. Young's modulus by itself is difficult to interpret in terms of an atomic interaction model. Hausch and Torok (1977) reported the elastic constants $(C_{11}+C_{12}+2C_{44})/2$ and C_{44} in $Mn_{85}Ni_{15}$ single crystal as a function of temperature but were unable to measure $(C_{11}-C_{12})/2$ because the $[1\bar{1}0]$ polarised shear mode could not be propagated in the [110] direction. Their results for C_L show a small dip near T_N and a magnetically

induced stiffness compared with that of the paramagnetic state. For our $Mn_{73}Ni_{27}$ crystal, C_L shows features (Fig.6.1a) which are similar to those found by Hausch and Torok (1977) for C_L in $Mn_{85}Ni_{15}$. There is a sharp step-like decrease in C_{11}; this modulus then rises again to give a pronounced kink at T_N(= 140°C) (Fig.6.4a). If the data obtained in the paramagnetic phase are extrapolated well below T_N, it can be seen that at room temperature (ie.20°C), C_{11} is larger when the crystal is in the antiferromagnetic than in the paramagnetic state: at 20°C $\Delta C_{11}/C_{11}$ is about +3.6% (Table 6.11a). The temperature dependence of C_{11} is much greater when the crystal is in the antiferromagnetic state than when it is in the paramagnetic state (Fig.6.4a and Table 6.8a): $(\partial C_{11}/\partial T)_{anti} = -0.55 \times 10^8\ Nm^{-2}K^{-1}$, $(1/C_{11})(\partial C_{11}/\partial T)_{anti} = -4.23 \times 10^{-4}\ K^{-1}$, $(\partial C_{11}/\partial T)_{para} = -0.20 \times 10^8\ Nm^{-2}K^{-1}$ $(1/C_{11})(\partial C_{11}/\partial T)_{para} = -1.6 \times 10^{-4}K^{-1}$. C_{44} is smaller but C_{12} is also larger in the antiferromagnetic than in the paramagnetic state. $\Delta C_{44}/C_{44} \backsim -4.2\%$, $\Delta C_{12}/C_{12} \backsim 4.6\%$ at 20°C. The softening of C_{44} in the antiferromagnetic state for this $Mn_{73}Ni_{27}$ crystal is quite close to that found by Hausch and Torok (1977) for their $Mn_{85}Ni_{15}$ crystal ($\Delta C_{44}/C_{44}=-4.8\%$) which should have become fct c/a <1 at a temperature not far below T_N. For $Mn_{73}Ni_{27}$, C_{44} shows only a very small upward kink at T_N (Fig.6.3a), but C_{12} shows a pronounced peak (Fig.6.5a). The shear elastic constant C' [=(C_{11} -C_{12})/2] goes through a pronounced downward step at T_N

(Fig.6.2a). The $\Delta C'/C'$ measured at room temperature, shows that the magnetic contribution softens this shear constant C'($\Delta C'/C'=-3.9\%$) (Table 6.11a). With the exception of C' and C_{44} the elastic constants are greater in the antiferromagnetic than in the paramagnetic state: the magnetic interaction stiffens most of the elastic modes.

A distinctive and well-established elastic effect of the polycrystalline alloys as they are taken through T_N is the step-like behaviour of Young's modulus (Hicks, Pepper and Hausch 1986, Honda, Tanji and Nakagawa 1976, Hausch and Torok 1977). For a single crystal Young's modulus is an anisotropic property, and is plotted here as as a function of temperature for stress applied along the fourfold, threefold and twofold axes of rotation respectively (Fig 6.7a to 6.9a). It can be seen that the step-like behaviour is a characteristic feature of the single crystalline a well as polycrystalline alloys. The step at T_N is more pronounced for this property along the [001] and [110] axes while being barely discernible along the [111] axis. The Young's modulus of $Mn_{73}Ni_{27}$ is large along the [111] direction and shows the smallest value along the [001] direction (Table 6.10a). However the difference in Young's modulus between the antiferromagnetic and the paramagnetic states $\Delta E/E$ is the largest along the [001] direction (-5.6%). Except for the [110] direction where the temperature dependence of

Young's modulus is larger in the paramagnetic state, the other directions of Young's modulus show an almost similar temperature dependence for both the antiferromagnetic and the paramagnetic states.

To visualize the effect on temperature on the velocities of ultrasonic modes propagated in different directions in a crystal, the mode velocities obtained by solution of the Christoffel equations (equation 3.36) are plotted at 20°C, 130°C (in the antiferromagnetic phase) and at 150°C, and at 170°C (in the paramagnetic phase) (Fig.6.11a to 6.14a).

The effect of temperature on the adiabatic bulk modulus B^S for this $Mn_{73}Ni_{27}$ single crystal is shown in Fig.6.6a. Previously Honda, Tanji and Nakagawa (1976) have reported compressibility measurements as a function of temperature on polycrystalline Mn-Ni alloys (see section 2.6). Those workers did not obtain the compressibility in the vicinity of T_N, whereas in the present work we have been able to do so. The bulk modulus B^S of the single crystal has a peak at T_N (so the compressibility dips) (Fig.6.6a). The slope of the temperature dependence of the bulk modulus ($\partial B/\partial T$) with temperature is listed in Table 6.9a. The results show that in the antiferromagnetic phase, the bulk modulus of the single crystal $Mn_{73}Ni_{27}$ (= $-3.93\times10^{7}Nm^{-2}K^{-1}$) is less temperature dependent than that of the polycrystalline 25.1 at.%Ni alloy (= $-5.10\times10^{7}Nm^{-2}$) (refer to Table 6.9a).

An assessment of the magnetic contribution to the

bulk modulus has been made by a linear extrapolation down to room temperature of the data (B_P) obtained in the paramagnetic phase (Fig.6.6a). Substraction of the value of B_P at 20°C from the measured value B_m in the antiferromagnetic state at 20° gives ΔB_m (= B_m- B_P). The value determined for ($\Delta B_m)_{20C}$ (= +3.6%) for the $Mn_{73}Ni_{27}$ single crystal is compared in Table 6.9a with those for polycrystalline Mn-Ni alloys obtained from the compressibilities given by Honda, Tanji and Nagasawa (1976) using the same extrapolation procedure. The polycrystalline 25.1at.%Ni alloy has a closely similar $(\Delta B_m)_{20C}$ to that of single crystal $Mn_{73}Ni_{27}$. In all alloys the magnetic contribution to the bulk modulus ΔB_m is positive. In these polycrystalline Mn-Ni alloys, as the nickel concentration is increased, ΔB_m increases linearly (Fig.6.6a1) with the following equation:

$$(\Delta B_m/B) = -0.72C_N + 22 \qquad (7.1)$$

where $\Delta B_m/B$ is the magnetic contribution to the bulk modulus and C_N is nickel concentration in the units of at.%. This implies that the magnetic contributions to the bulk modulus of polycrystalline Mn-Ni alloys increase as the nickel concentration is decreased. The results also suggest that the magnetic contribution to the bulk modulus $\Delta B_m/B$ of pure γ-manganese in this antiferromagnetic state would be about +22%. There does not seem to be a theoretical prediction of the sign of

the magnetic contribution to the bulk modulus in the antiferromagnetic materials. However, in the case of ferromagnetism the itinerant electron model of Hausch (1977) indicates that the bulk modulus in the magnetic state should be greater than that in the non-magnetic state. The results obtained here for the difference in bulk modulus between the antiferromagnetic and the paramagnetic states of Mn-Ni alloys agree with this trend. In general the increased bulk modulus in the antiferromagnetic phase shows that the interatomic forces are strengthened by the antiferromagnetic ordering. Alers, Neighbours and Sato (1960) have suggested the following formula to separate the ferromagnetic contribution from the non-magnetic contribution to the bulk modulus of a f.c.c.structure material:

$$B = B_o - (2N/3)(I/I_o)^2 r_o^2 \, (d^2J/dr^2) \qquad (7.2)$$

where J is the exchange interaction energy, I/I_o is the relative magnetization, r_o is interatomic distance and N is the number of atoms per unit volume. The term B_o represents the value that the bulk modulus would have if ferromagnetism did not occur. The second term is the intrinsic magnetic contribution to the bulk modulus and exhibits a dependence upon the magnitude of the spontaneous magnetization. From this model, Alers, Neighbours and Sato (1960) obtained for pure nickel the

second term of equation (7.2) as $+12\times10^{9}$dyne/cm^2 so that a negative contribution is obtained for that ferromagnetic material. However these workers observed experimentally a small positive magnetic contribution to the bulk modulus (ΔB_m) in pure nickel as it is taken down from the paramagnetic to the ferromagnetic states (Alers, Neighbours and Sato 1960). Hence even in the ferromagnetic case there is a contradiction between the experimental result and the predicted sign of the magnetic contribution to the bulk modulus. For the Mn-Ni antiferromagnetic alloys the positive sign of $\Delta B_m/B$ shows that there is a magnetic stiffening of the bulk modulus. A positive value of ΔB_m has also been observed in some ferromagnetic invar alloys: Fe-28.2at.%Pt single crystal gives $\Delta B_m/B$ approximately +13% at OK (Hausch 1977). A ferromagnetic Fe-Cr-Ni-Mn polycrystal showed a zero slope above Tc while having normal behaviour (positive slope) below the transition temperature (335K): when the line from paramagnetic data is extrapolated downwards to about 70K the paramagnetic bulk modulus falls below the ferromagnetic bulk modulus (Ledbetter 1983).

A binary alloy of Mn-Ni [001] crystal with a lower nickel concentration ($Mn_{84}Ni_{16}$) has also been investigated here. C_{11} and C_{44} have been measured up to and through the Nēel temperature (170°C) and the results are shown in Table 6.4a, Fig.6.3a1 and 6.4a1. These results show that C_{11} and C_{44} follow a similar trend to

those for $Mn_{73}Ni_{27}$; namely C_{11} is stiffened while C_{44} is softened. $\partial C_{11}/\partial T$ of $Mn_{84}Ni_{16}$ (=-4.9) is smaller than that of $Mn_{73}Ni_{27}$ (-5.55) whilst $\partial C_{44}/\partial T$ is larger than that of the $Mn_{73}Ni_{27}$ (Table 6.8a).

7.3 Hydrostatic Pressure Derivatives of the Second Order Elastic Stiffnesses Constants of the $Mn_{73}Ni_{27}$ alloy.

The hydrostatic pressure dependences of the elastic stiffness constants of all the three modes of propagation in the [110] direction of $Mn_{73}Ni_{27}$ have been measured at several different temperatures. The results have been shown in Table 6.13a. Those are the first data for the effect of pressure on the elastic behaviour of the binary alloy Mn-Ni alloys, and as they refer to both the antiferromagnetic and the paramagnetic phases are singularly instructive, ultrasonic velocity measurements under pressure in both phases of an antiferromagnetic material being absent from the literature. The pressure derivatives ($\partial C_{ij}/\partial P$) of $Mn_{73}Ni_{27}$ are sensitive to temperature as can be seen from the temperature dependences of the pressure derivatives of the second order elastic stiffness constants of $Mn_{73}Ni_{27}$ plotted in Fig 6.18a to Fig 6.22a. To understand the effect of pressure on the interatomic forces one approach is to look at this behaviour of $\partial C_{ij}/\partial P$ of $Mn_{73}Ni_{27}$. At every temperature in which this pressure experiment has been carried out, all the three pressure derivatives of the elastic constants have been found to have positive values. This shows normal behaviour of this crystal under applied pressure; that is, the elastic stiffness constants increase with pressure. This increase in elastic constants gives an indication of the change in

interatomic forces as a result of reducing the atomic spacing in this alloy. At every experimental temperature, C_{11} shows the largest pressure dependence of elastic constants (Table 6.13a). The significance of this can be seen by considering the relation between $\partial C_{11}/\partial P$ with the third order elastic stiffness constants (TOEC):

$$\left(\frac{\partial C_{11}}{\partial P}\right)_{P=0} = -\frac{(2C_{11}+2C_{12}+C_{111}+2C_{112})}{(C_{11}+2C_{12})} \qquad (7.3)$$

Usually C_{111} is the largest TOEC for a cubic crystal because it is the one dominated by repulsive forces between the nearest neighbour atoms. C_{111} is the largest TOEC for the $Mn_{80.5}Ni_{19.5}$ at 20°C (Table 6.18a) (Saunders 1985): C_{111} is -2100 GPa while C_{112} is +640 GPa, so the contribution to (C_{111} + $2C_{112}$) is dominated largely by C_{111}. A similar dominance of C_{111} for the $Mn_{73}Ni_{27}$ alloy is suggested by inspection of the TOEC combinations measured at several temperatures (Table 6.14a). Thus the large increase in elastic constant C_{11} when pressure is increased implies that the interatomic repulsive forces $Mn_{73}Ni_{27}$, which increase as the atoms are brought closer together, dominate $\partial C_{11}/\partial P$.

As the temperature of the $Mn_{73}Ni_{27}$ alloy is taken towards the Nēel temperature, $\partial C_{11}/\partial P$ increases rapidly and reaches a maximum in the vicinity of T_N (Fig 6.21a). On passing through the Nēel temperature, $\partial C_{11}/\partial P$ undergoes a marked change which must be associated with the magnetic phase change from the antiferromagnetic to

the paramagnetic state. $\partial C_{11}/\partial P$ decreases linearly towards higher temperature as the temperature is raised further in the paramagnetic state. In the antiferromagnetic state the increase of ($\partial C_{11}/\partial P$) as T_N is approached corresponds to a marked increase in the TOEC combination (C_{111} + $2C_{112}$) (Table 6.14a.) and therefore indicates that C_{111} increases as T_N is neared. In turn this suggests that there is an increase in the interatomic repulsive forces in the vicinity of the Nêel temperature. The only work on the pressure dependence of second order elastic constants in any other magnetic material on both sides of transition temperature is that reported by Renaud and Steinemann (1984) who measured the hydrostatic pressure derivatives of the ferromagnetic FeNi alloys in both the ferromagnetic and the paramagnetic phases. They did not measure $\partial C_{11}/\partial P$ directly. The values measured for the pressure derivative of the modulus corresponding to longitudinal wave propagation down the [110] direction, $\partial C_L/\partial P$ of these alloys (Fe-31.5at.%Ni, Fe-32at.%Ni and Fe-36at.%Ni) (Renaud and Steinemann 1984) go through a peak at the Curie point T_C. $\partial C_L/\partial P$ shows a similar trend with temperature to that found here for the antiferromagnetic alloy $Mn_{73}Ni_{27}$ (Fig 6.18a). The results of Renaud and Steinemann (1984) show that $\partial C_L/\partial P$ decreases with temperature in the paramagnetic state of iron-nickel alloys as it does in the paramagnetic state in the $Mn_{73}Ni_{27}$ (Fig 6.18a).

The data given in Table 6.13a shows that $\partial C'/\partial P$ is the smallest hydrostatic pressure derivative of the SOEC. This is true up to and into the paramagnetic state of $Mn_{73}Ni_{27}$. Many f.c.c. materials, particularly transition metals, show a similar trend of the SOEC under hydrostatic pressure: namely that $\partial C'/\partial P$ is the smallest pressure derivative: for example, for pure nickel [$\partial C_{11}/\partial P$=5.93, $\partial C_{44}/\partial P$=2.44 and $\partial C'/\partial P$=1.19 (Salama and Alers 1968)] and for the pure palladium [$\partial C_{11}/\partial P$=6.05, $\partial C_{44}/\partial P$ =1.86 and $\partial C'/\partial P$=0.86 (Weinmann and Steinemann 1974)], and pure copper [$\partial C_{11}/\partial P$=5.86, $\partial C_{44}/\partial P$=5.15 and $\partial C'/\partial P$=0.24 (Daniels and Smith 1958)] (refer also Fig 6.13a1). For these transition metals, as well as $Mn_{73}Ni_{27}$, the shear pressure derivatives $\partial C_{44}/\partial P$ and $\partial C'/\partial P$ each are smaller than $\partial C_{11}/\partial P$. To understand this physical interpretations of C_{44} and C' are needed. Take for example $\partial C_{44}/\partial P$; the shear involved in C_{44} is $\varepsilon_{yz}(=\partial v/\partial z+\partial w/\partial z)$, where v is a displacement in the fourfold y direction and w is one in the z-direction, and corresponds to sliding of planes of constant z over each other in the y-direction: there is no change in nearest-neighbour distance to first order in strain and no nearest-neighbour repulsive contribution to C_{44}. The pressure derivatives of the two shears, $(\partial C_{44}/\partial P')_{P=0}$ and $(\partial C_{12}/\partial P)_{P=0}$ are given by

$$\left(\frac{\partial C_{44}}{\partial P}\right)_{P=0} = -\frac{(C_{11}+2C_{12}+C_{44}+C_{144}+2C_{166})}{(C_{11}+2C_{12})} \qquad (7.4)$$

and

$$\left(\frac{\partial C_{12}}{\partial P}\right)_{P=0} = -\frac{(C_{123}+2C_{112}-C_{11}-C_{12})}{(C_{11}+2C_{12})} \qquad (7.5)$$

Nearest-neighbour repulsive forces do not contribute to either of these pressure derivatives for cubic crystals (Miller, Saunders and Yogurtcu '1981), so that $(\partial C_{44}/\partial P)_{P=0}$ and $(\partial C_{12}/\partial P)_{P=0}$ tend to be small, as they are for the $Mn_{73}Ni_{27}$ alloy (Table 6.14a). The temperature dependences of $\partial C_{44}/\partial P$ and $\partial C_{12}/\partial P$ are shown in Fig 6.20a and Fig 6.22a respectively. For the ferromagnetic FeNi alloys (Fe-31.5at.%Ni, Fe-32at.%Ni and Fe-36at.%Ni) the curve for $\partial C_{44}/\partial P$ falls below the curves for $\partial C_L/\partial P$ (Fig.1 of Renaud and Steinemann 1984) which is similar to the results obtained here for the $Mn_{73}Ni_{27}$ alloy (Fig 6.18a to Fig 6.20a).

A large $\partial C_{11}/\partial P$ represents a pronounced pressure-induced stiffening against compression and thus corresponds to an enhanced magnitude of $\partial B/\partial P$ which is also large in this alloy (Fig 6.23a). The behaviour of the spontaneous magnetization in an antiferromagnetic material is shown in Fig 2.3b of section 2.3. The spontaneous magnetization decreases towards zero at T_N in both the antiparallel and parallel lattices. The considerable increase of $\partial C_{11}/\partial P$ with temperature can be associated with an increase in the interatomic repulsive forces as the temperature is increased up to the Nēel point. To separate the magnetic and the nonmagnetic elastic constants in their ferromagnetic Fe-Ni alloys,

Renaud and Steinemann (1984) wrote the free energy (F) as F(= F(la) + F(ma)); thus the elastic stiffness constants can then in turn can be separated into magnetic and nonmagnetic contributions:

$$C = C_{la} + C_{ma} \qquad (7.6)$$

where C_{la} is the elastic stiffness constant due to the lattice alone and C_{ma} is the magnetic contribution to the elastic stiffness constants when an alloy is in the magnetic state. Since equation 7.6 is a linear relation between the elastic stiffness constants, the same situation can also be applied to the hydrostatic pressure derivatives of the elastic stiffness constants, hence

$$\partial C_{11}/\partial P = \partial(C_{11})_{la}/\partial P + \partial(C_{11})_{ma}/\partial P \qquad (7.7)$$

Thus in the paramagnetic phase, where there is no contribution from the intrinsic magnetic moments, the elastic constants and their pressure derivatives should only include the lattice contribution. As a result there is a marked reduction in $\partial C_{11}/\partial P$ at the transition temperature. This reduction can be seen in Fig.6.21a as a data in the paramagnetic state fall far below those in the antiferromagnetic state. In the paramagnetic state $\partial C_{11}/\partial P$ decreases further with increasing temperature.

To evaluate the compression at higher pressure,

the Murnaghan (1944) equation-of-state has been employed (equation 3.53). The compressibility of $Mn_{73}Ni_{27}$ has been calculated up to about 100KBar pressure in both the antiferromagnetic and the paramagnetic states. To convert the bulk modulus from adiabatic to isothermal values, (equation 3.54) the thermal Gruneisen parameter has been used, which has a value of +0.97 (Table 6.15a). In the absence of thermal expansion data for our crystals the values of the coefficient of thermal expansion and its temperature derivative up to temperature of 400°C given by (Hausch 1977) have been used. Fig 6.24a and Fig 6.25a show the compression at several selected temperatures of $Mn_{73}Ni_{27}$ in the antiferromagnetic and the paramagnetic states respectively. At room temperature $Mn_{73}Ni_{27}$ has a smaller compression than the transition metal cobalt (Yogurtcu, Saunders and Riede 1985) but is larger than UN (Chapter 5). Uranium nitride is an ionic compound having a rocksalt structure, thus interatomic bonding is strong and hence it has quite a small compression. For a Mn-Ni alloy, the small compression can be associated with strong bonding in this transition metal alloy due to the d-electron contribution to the interatomic bonding. The effect of the magnetic contribution can be seen by comparing Fig 6.24a and Fig 6.25a; the compression is smaller in the antiferromagnetic state than in the paramagnetic state.

7.4 Grüneisen Parameters of the Binary Alloy $Mn_{73}Ni_{27}$ Single Crystal

The acoustic mode Grüneisen parameters in directions in the symmetry planes normal to the twofold and fourfold directions have been computed as a function of propagation direction using equation 3.63. The results are plotted in Figs.6.29a to 6.40a in both the antiferromagnetic and the paramagnetic states. The mean long wavelength acoustic mode Grüneisen parameters γ_{mean} are given in Table 6.14a. The $\gamma(p,N)$ for $Mn_{73}Ni_{27}$ for all the three modes of propagations are greater than unity. $\gamma(p,N)$ for the longitudinal mode of propagation in the [001] direction ranges from +1.7 to +8 in the antiferromagnetic state and ranges from +1.45 to +2.1 in the paramagnetic state. The two shear modes are also positive and larger than unity (ranging from +1.0 to + 1.96) Application of hydrostatic pressure causes an increase in mode frequency (or energy) in the normal way expected for a crystal: all acoustic modes in the long wavelength limit stiffen under pressure. These positive values of these $\gamma(p,N)$ in excess of unity show that there is no pressure induced acoustic mode softening even in the vicinity of transition temperature T_N. The data presented in these figures 6.29 to 6.36 show the temperature dependences of $\gamma(p,N)$, as temperature is taken towards T_N: $\gamma(p,N)$ increases. These Grüneisen parameters quantify the first order anharmonicity of the acoustic modes at the Brillouin zone centre. The marked

anisotropy of these $\gamma_{(p,N)}$ can be understood in terms of the types of acoustic mode which can propagate in the f.c.c. structure and their relationship to the interatomic forces especially the nearest neighbour repulsive forces. Consider for example the $\gamma_{(p,N)}$ of modes propagating along a four-fold <001> direction. At room temperature the longitudinal mode $\gamma_{(p,N)}$ has a larger value (+1.7) than those of the degenerate shear modes (Fig.6.29a). This can be thought of in terms of the third order elastic constant contribution ($C_{111} + 2C_{112} = C_1 = -18.71 \times 10^{11}$ Nm^{-2})(Table 6.14a) which is large and negative (refer to equation 3.63). Hence $C_1K_1 = -18.71 \times 10^{11}$Nm^{-2} ($K_1$ being for the longitudinal mode) is much greater than w ($C_{11}K_1 = 1.294 \times 10^{11}$ Nm^{-2}), and this term C_1K_1 mainly determines $\gamma_{(p,N)}$ (refer equation 3.63 and Table 6.14a). Now ($C_{111} + 2C_{112}$) is in turn largely determined by C_{111}: the nearest neighbour repulsion is responsible for the substantial value of $\gamma_{(p,N)}$ for the longitudinal q[001] acoustic mode. In contrast C_{111} is not involved in the Grüneisen gamma for shear acoustic waves propagated along an <001> direction - for these modes the nearest neighbour forces do not come into play and hence the corresponding pressure derivative $\partial C_{44}/\partial P$ is smaller than $\partial C_{11}/\partial P$ (Table 6.13a). In general application of the principle that when C_{111} is involved then the nearest neighbour repulsion will be important in determining the vibrational anharmonicity accounts for the marked anisotropy of the acoustic mode Grüneisen parameter of Mn-Ni alloys.

The Debye temperatures (θ_D) calculated using equation (3.44) are given in Table 6.12a. The value of θ_D obtained at room temperature is about 383K. The calculation was performed by numerical integration, taking advantage of the cubic symmetry by only integrating over one half of an octant using a total 135 directions. Through back extrapolation of the Debye temperature curve in the antiferromagnetic state to zero K, the value obtained for θ_D at zero K is about 395K.

At high temperature ($T>\theta_D$) phonons exist in states in the acoustic branches throughout the Brillouin zone. Above θ_D all phonon modes are excited. γ^{th} can be obtained using equation (3.60). The room temperature specific heat (35J/mole K) and coefficient of thermal expansion ($16\times10^{-6}K^{-1}$) are taken from data given by Hausch (1977) and Ushishiba (1971) respectively. Using these gives γ^{th} for $Mn_{73}Ni_{27}$ alloy as +0.97.

The thermodynamic properties of a crystal at low temperature (including the thermal expansion) should be determined by the dominance of the phonon population in the low lying transverse branch. To calculate $\bar{\gamma}_0^{el}$, $\gamma(p,N)$ and $v(p,N)$ were obtained from the SOEC extrapolation to 0K using the pressure derivatives of the SOEC listed in Table 6.13a. The room temperature pressure derivatives of the SOEC were used, even though the SOEC themselves were extrapolated to absolute zero. $\bar{\gamma}_0^{el}$ (Table 6.15a) is dominated by the behaviour of the low energy shear acoustic modes. The positive sign of low-temperature $\bar{\gamma}_0^{el}$ is also an indication that the

thermal expansion of $Mn_{73}Ni_{27}$ is positive. The high temperature $\bar{\gamma}_{\infty}^{el}$ was calculated using equation (3.65) and is given in Table 6.15a together with those of γ^{th} and $\bar{\gamma}_{q}^{el}$. In the high temperature limit, the thermal Grüneisen gamma of Mn-Ni is larger than at low temperatures, acoustic phonons closer to the zone boundary must be involved in the thermal properties. At room temperature most of the modes have a positive Grüneisen parameter of the order of unity associated with them in order to produce the observed anharmonic effects. From Table 6.15a γ^{th} is larger than $\bar{\gamma}_{\infty}^{el}$, which indicates that the mean of the Grüneisen parameter for all acoustic modes away from the Brillouin zone centre taken together are larger than that for the zone-centre acoustic modes.

Fig. 6.41a shows the variation of mode Grüneisen parameters $\gamma(p,N)$ of the longitudinal and shear modes propagated in the [110] direction in $Mn_{73}Ni_{27}$. These gamma have been obtained using (Renaud and Steinemann 1985)

$$\gamma_{IJ} = -(1/6) - (d\ln C_{IJ}/d\ln V) \qquad (7.8)$$

where $d\ln C_{IJ}/d\ln V = (-B/C_{IJ})(dC_{IJ}/dP)$. γ_{1a} ($\gamma(p,N)$ due to lattice) and γ_{ma} (magnetic contribution to the $\gamma(p,N)$) of three modes at 20°C are then obtained by an extrapolation procedure of the $\gamma(p,N)$ data in the paramagnetic state to the room temperature. The results

are given in Table 6.16a. Table 6.16a shows that the Grüneisen parameters $\gamma(p,N)$ of the longitudinal mode and the slow shear mode $((C_{11}-C_{12})/2)$ which propagate along [110] direction at 20°C are larger in the paramagnetic state than those in the antiferromagnetic state at the same temperature. The implication of this method of finding $\gamma_A - \gamma_P$ is that the γ_{ma} for these two modes have negative values. In contrast for C_{44}, $\gamma(p,N)$ is smaller in the paramagnetic state than in the antiferromagnetic state. A large negative γ_{ma} of the two shear modes (C' and C_{44}) can be seen in the work of Renauld and Steinemann (1984) of the Fe-32at.%Ni alloy. In fact the large negative values of γ_{ma} observed by these workers were determined using equation 3.61 but they took C_i incorrectly as an elastic constant instead of specific heat of the i^{th} mode. For this reason the values of γ_{ma} obtained for their sample (Fe-32at.%Ni) using our extrapolation method (Table 6.16a) show a marked difference from γ_{ma} given in table 1 of Renauld and Steinemann (1984). It is interesting to note that our method shows the γ_{ma} of $Mn_{73}Ni_{27}$ and that of Fe-32at.%Ni have some similarity (Table 6.16a). Renauld and Steinemann (1984) came to the conclusion that the negative value of γ_{ma} come about as a result of the fact that the magnetic contribution to the elastic stiffness C_L is negative. In a similar way it seems that in $Mn_{73}Ni_{27}$, the negative γ_{ma} is evidence that the magnetic

contribution to the mode Grüneisen parameter associated with C_L and $(C_{11}-C_{12})/2$ is negative but positive for C_{44}.

7.5 Temperature Dependences of the Elastic Stiffness Constants of Ternary Alloys of Composition $Mn_{85}Ni_9C_6$.

Two ternary alloys Mn-Ni-C of the same composition have been examined in this work. These are the $Mn_{85}Ni_9C_6$ sample C2 ($T_N \backsim 320°C$) and sample F ($T_N \backsim 273°C$) respectively. The difference in the Nēel temperature for samples having the same nominal composition illustrates the difficulty of making homogeneous specimen of these ternary alloys. The three modes which have been propagated along the [110] direction of sample C2 enable the determination of the set of three independent elastic stiffness constants of this material. Sample F has been studied previously extensively at higher temperatures using neutron scattering techniques (Lowde et al. 1981). This sample F has been prepared in the form of flat plate with the fourfold and twofold axes directed normal to the plate surfaces. A complete set of temperature dependences of both the second order elastic stiffness constants of these ternary alloys samples up to and through their Nēel temperatures have been determined. The temperature dependences of the longitudinal mode and the two shear modes, one polarised [001] and the other [$1\bar{1}0$] directions are shown in the form of elastic constants ($C_{ij} = \rho V^2$) in Figs.6.1b to 6.5b and Figs.6.1c to 6.5c for sample C2 and sample F respectively. In looking at this ultrasonic data, and attempting to estimate the degree to which they

indicate special effects due to the presence of carbon in the alloys, it may be well to recall the characteristics of simple materials. If only central forces are present in a f.c.c. crystal, C_{12} equals C_{44}; and if the forces extend only between nearest neighbour atoms then furthermore $C_{11} = 2C_{12} = 2C_{44}$. With a longer range of forces, C_{11}/C_{44} can take a range of value, but C_{11} can not go below C_{44} unless interatomic forces are non-central. If the restoring forces are harmonic, the elastic constants will be independent of temperature; in practice, with a normal degree of anharmonicity there is a moderate decrease of the elastic constants as the temperature is increased _ in the case of nickel, the largest downward slope is that of C_{44} - about 3% per 100K (Alers et al. 1960). As for iron-nickel alloys, whose behaviour in some respects resembles that of our manganese-nickel ones, the result of introducing substantial quantities of iron into nickel is to lower all the three elastic stiffness constants; C_{12} and C_{44} slightly, C_{11} by a factor that eventually attains about 1.7, although at room temperature when the amount of iron is increased, C_{11} is still about $1.3C_{44}$ when the martensitic transformation supervenes (Hausch and Warlimont 1973).

Consider first $Mn_{85}Ni_9C_6$ sample C2, the elastic constants of which are displayed in Figs.6.1b to 6.5b. The temperature dependences of $(C_{11}+C_{12}+2C_{44})/2$ and C_{44} are qualitatively normal, as far as the derivatives are

concerned. C_{11} (= 8.7) is smaller than C_{44}(10.6), while C_{12} is about 6 in units of $10^{10}Nm^{-2}$ (Table 6.3b). This anomaly ($C_{11} < C_{44}$) is observed throughout this range of temperature (20°C to 380°C). This highly exceptional effect produces a situation where, in this temperature region when $C_{11} < C_{44}$, a longitudinal sound wave travelling in a direction near [100] is actually slower than transverse sound. Going together with this, Fig.6.2b shows that the transverse mode propagated along [110] and polarised $[1\bar{1}0]$ undergoes acoustic phonon softening but the slope changes sign at approximately 70° below T_N. This softening of $C'(=(C_{11}- C_{12})/2)$ in this alloy is related to the phase transformation from a cubic to a tetragonal structure which occurs at much lower temperature (ω174K) (Lowde et al.1981). For the structural transformation from a cubic lattice to a tetragonal one there is a cubic invariant in the order parameter so that this type of structural transformation should be first order. Such a transition occurs via softening of the [110] acoustic phonon which has the vibrational polarization direction $[1\bar{1}0]$. The corresponding elastic stiffness constant is C', and in a nearly-second-order transition C' would go critically soft.

Figs.6.1c to 6.5c show the temperature dependences of the SOEC for $Mn_{85}Ni_9C_6$ sample F. Mode softening of C' of sample F has been observed: C' increases with temperature from room temperature up to

the Nēel temperature (Fig.6.2c). The temperature dependence of C_{44} (Fig.6.3c) is qualitatively the same as that of sample C2 in Fig.6.3b; it decreases with temperature. With increasing temperature C_{11} at 145°C changes sign to a positive slope as shown by a dip in Fig.6.4c. One possible interpretation of this dip is that there is a lattice instability just before the magnetic phase transition from the antiferromagnetic to the paramagnetic phase. There is a change in slope found here (Fig.6.4c) in the vicinity of T_N which occur at the magnetic phase transition from the antiferromagnetic to the paramagetic state. C_{12} of sample F exhibits a similar behaviour qualitatively to C_{11} throughout the experimental range of temperatures (Fig.6.5c). Extrapolation of the three elastic stiffness constants back from the paramagnetic region to room temperature shows that C_{44} is softened but C_{11} and C_{12} are stiffened by the magnetic contributions in this alloy.

The Young's Moduli for the fourfold, threefold and twofold axes of rotation are plotted as a function of temperature in Figs.6.7b to 6.9b and Figs.6.7c to 6.9c of both samples C2 and F respectively. For the [111] direction Young's modulus of both samples do not differ greatly between the paramagnetic and the antiferromagnetic phases. However large differences between the paramagnetic and the antiferromagnetic phases are found for this property along the [001] and [110] axes. Along the [001] direction the Young's Modulus is

much smaller in the antiferromagnetic phase than in the paramagnetic phase for both samples in a temperature range between 20°C to T_N (Fig.6.7b and Fig.6.7c).

To visualize the effect of temperature on the velocities of ultrasonic modes propagated in different directions in these crystals, the mode velocities calculated using the Christoffel equations are plotted at several different temperatures in the antiferromagnetic phase of sample C2 (Figs.6.11b to 6.15b) and at 20°C for sample F (Fig.6.10c). The cross sections of the velocity surface do not show any pronounced changes with temperature.

From the linear extrapolation of the bulk modulus data in the paramagnetic phase down to room temperature it can be seen that there is a positive magnetic contribution to the bulk modulus (Figs.6.6b and 6.6c for samples C2 and F respectively).

7.6 Hydrostatic Pressure Derivatives of the Elastic Stiffness Moduli of Ternary Alloys $Mn_{85}Ni_9C_6$

The set of data on the hydrostatic pressure derivatives of the second order elastic stiffness constants of the ternary alloy $Mn_{85}Ni_9C_6$ sample C2 at several different temperatures have been shown in Table 6.15b. These are the first measurements of the hydrostatic pressure dependences on the elastic stiffness constants of a ternary alloy Mn-Ni-C single crystal and have been measured at several different temperatures.

These hydrostatic pressure derivatives $(\partial C_{ij}/\partial P)_{P=0}$ provide useful physical insight into the interatomic repulsive forces in this material. Consider first $(\partial C_{11}/\partial P)_{P=0}$: as for the binary Mn-Ni alloys, this is the largest pressure derivative of elastic stiffness constants (Table 6.15b). Using equation 7.3, $\partial C_{11}/\partial P$ can be written in terms of the second and the third order elastic stiffness constants; the third order elastic stiffness constant combination ($C_{111} + 2C_{112}$) is given in Table 6.16b. This result suggests that C_{111} is the largest third order elastic stiffness; this parameter C_{111} is dominated by nearest neighbour repulsive forces. Therefore ($C_{111}+2C_{112}$) and in turn $(\partial C_{11}/\partial P)_{P=0}$ are dominated by C_{111} which is large and negative owing to the overriding contribution from nearest neighbour repulsive forces. C_{112} is small because it is largely determined by the next-nearest-neighbour repulsive forces.

The temperature dependences of hydrostatic pressure derivatives $\partial C_{ij}/\partial P$ of sample C2 are plotted in Fig.6.16b to 6.23b. According to Long et al.(1988), the major influence of carbon in this ternary alloy is in collapsing the phase diagram of Fig.2.2 by a factor of about 7/16 and they suggest that the behaviour of $Mn_{85}Ni_9C_6$ can be considered to be roughly comparable with that of the binary alloy $Mn_{78}Ni_{22}$. Since this nickel concentration in $Mn_{78}Ni_{22}$ is quite close to $Mn_{73}Ni_{27}$, we can expect quite a close resemblance in elastic behaviour

between ternary alloy $Mn_{85}Ni_9C_6$ and binary alloy $Mn_{73}Ni_{27}$. Some similarity of behaviour can be seen in $\partial C_{44}/\partial P$ and $\partial C'/\partial P$. Thus $\partial C'/\partial P$ increases linearly with temperature (Fig.6.20b) while $\partial C_{44}/\partial P$ decreases linearly with temperature (Fig.6.21b) (refer to Fig.6.19a and 6.20a of $Mn_{73}Ni_{27}$ for comparison). The introduction of carbon into the $Mn_{85}Ni_9C_6$ interstitially does not seem to produce a significant effect on the pressure derivatives of the shear elastic stiffness constants. However, the dip in the longitudinal mode pressure derivative $\partial C_{11}/\partial P$ at 140°C is possibly due to effects of carbon on the nearest neighbour repulsive force, in this case to decrease the interatomic repulsive force as the temperature is taken towards 140°C. With further increase in temperature above 140°C, $\partial C_{11}/\partial P$ increases and shows a similar behaviour to that of the binary alloy $Mn_{73}Ni_{27}$ (Fig.6.22b). Since no nearest neighbour interatomic repulsive forces are involved in the pressure derivatives of shear elastic constants, the temperature dependences of $\partial C'/\partial P$ and $\partial C_{44}/\partial P$ tend to be small for the ternary alloys Mn-Ni-C sample C2. This behaviour has been observed in $Mn_{85}Ni_9C_6$ from the data given in Table 6.15b.

7.7 Compression in $Mn_{85}Ni_9C_6$ Sample C2

Fig.6.25b shows the compression at several temperatures of sample C2 of $Mn_{85}Ni_9C_6$ alloy obtained up to about 165°C in the antiferromagnetic state. A decrease in compressibility with increasing temperature is

observed between room temperature to about 75°C. This behaviour has also been observed in the binary alloy $Mn_{73}Ni_{27}$ single crystal (Fig.6.24a). In the ternary alloy there is a marked increase of compressibility above 75°C which continues up to 140°C. Higher in temperature (about 165°C) the compressibility returns to the normal behaviour of showing a decrease with temperature. The reduction of compressibility particularly at 140°C may be related to the structural transformation which occurs at approximately 410°K (≃140°C) according to Fig.2.2. for an alloy containing 85at.% Mn.

7.8 Grüneisen parameters of Ternary Alloy $Mn_{85}Ni_9C_6$ (sample C2)

The values of $\gamma(p,N)$ have been computed as a function of mode propagation directions. The acoustic mode Grüneisen parameters in directions in the symmetry plane normal to the twofold and fourfold directions are plotted in Figs.6.31b to 6.36b. At 20°C these mode Grüneisen parameters show a similar behaviour to those of the $Mn_{73}Ni_{27}$ alloy particularly in the [001] direction. γ_L (gamma longitudinal) is the largest parameter (Fig.6.31b) probably as a result of nearest neighbour repulsive forces which dominate this gamma. As the temperature is increased towards approximately 75°C, γ_L increases from +2.3 at room temperature to +3.8 (Fig.6.33b) which indicates that there is an increase in interatomic repulsive forces. On further increase in

temperature there is a marked reduction in γ_L (see Fig.6.34b) and it reaches a minimum at approximately 140°C (Fig.6.35b). This reduction in γ_L is associated with the corresponding reduction in $\partial C_{11}/\partial P$. To understand this behaviour, inspection of the phase digaram Fig.2.2 is instructive. According to this figure there will be a structural transition at approximately 140°C for a crystal having a composition of 85at.%Mn. Since this structural phase transition is related to mode softening (Lowde et al.1981), the short range interatomic repulsive forces could be expected to decrease, and because they provide a direct contribution to $\partial C_{11}/\partial P$ and hence to γ_L, therefore $\partial C_{11}/\partial P$ and γ_L decrease in this temperature region. A set of mode Grüneisen parameters obtained for each mode which propagates along the [110] direction has been plotted as a function of temperature in Fig.6.37b; both γ_{C44} and $\gamma_{C'}$ show a similar behaviour to those of $Mn_{73}Ni_{27}$ alloy: γ_{C44} decreases with temperature whilst $\gamma_{C'}$ increases with temperature. γ_L along the [110] direction shows a marked reduction at 140°C. The reduction in γ_L may be due to the following factors: i) the presence of carbon atoms reduces the interatomic repulsive forces at this particular temperature, ii) lattice instability which result from the structural transition as shown in Fig.2.2. for Mn-Ni alloy having a composition of 85at.%Mn. The mean gamma Grüneisen parameter γ_{mean} for several different temperatures has also been calculated and results are

given in Table 6.16b. There is a minimum γ_{mean} at 140°C.

γ_L provides a direct contribution to γ_{mean}. Therefore the minimum γ_{mean} is related to the reduction in γ_L at 140°C as shown in Fig.6.37b.

7.9 Conclusions

A complete set of temperature dependences of the SOEC of the binary alloys $Mn_{73}Ni_{27}$ and the ternary alloys $Mn_{85}Ni_9C_6$ sample C2 and sample F have been determined. These measurements have been carried out in both the antiferrromagnetic and the paramagnetic phases. The hydrostatic pressure derivatives of the second order elastic stiffness constants have been measured for these alloys at several different temperatures. A complete set of data of $\partial C_{ij}/\partial P$ for the $Mn_{73}Ni_{27}$ has been obtained in both the antiferromagnetic and the paramagnetic phases. This is the first measurement of the hydrostatic pressure derivatives of the elastic stiffness constants on both sides of the Nēel temperature obtained in any material.

The following behaviour of the SOEC of the $Mn_{73}Ni_{27}$ alloy as the temperature is taken to and through the Nēel point has been observed ; C_L and C_{44} decrease linearly with temperature both in the antiferromagnetic and the paramagnetic states. For $(C_{11}-C_{12})/2$, there is a dip in the vicinity of T_N. From the extrapolation of the paramagnetic data of the SOEC to room temperature, it has been found that the magnetic contribution stiffens C_L but softens C_{44} and $(C_{11}-C_{12})/2$. For the ternary alloys $Mn_{85}Ni_9C_6$, mode softening has been observed through $(C_{11}-C_{12})/2$ in both alloy samples (C2 and F) as temperature is taken towards T_N. Sample F shows this mode softening from room temperature up to the Néel temperature whilst in sample C2 this soft mode disappears

at approximately 70° below T_N. These mode softenings are probably related to the structural transition that occurs at 174K for these particular ternary alloys (Lowde et al.1981). This f.c.c.-f.c.t elastic phase transition is associated with an instability of the crystal lattice (in either phase) to a soft, long wavelength, acoustic phonon (N<110> U<110>). This SOEC is a measure of the crystal lattice resistance to the strain imposed by the soft phonon; as $(C_{11}-C_{12})/2$ decreases the amplitude of this vibration would be expected to increase. In order to restore equilibrium the crystal is obliged to take a new structure.

The hydrostatic pressure dependences of all the three mode velocities of $Mn_{73}Ni_{27}$ have been measured at several different temperatures and the temperature dependences of $\partial C_L/\partial P$, $\partial C'/\partial P$ and $\partial C_{44}/\partial P$ determined. Then the individual pressure derivatives $\partial C_{11}/\partial P$, $\partial C_{44}/\partial P$ and $\partial C_{12}/\partial P$ have been obtained. There is a rapid linear increase of $\partial C_{11}/\partial P$ with temperature up to the Néel point and a marked decrease in $\partial C_{11}/\partial P$ above it. The increase in $\partial C_{11}/\partial P$ as the temperature is taken towards T_N is associated with the reduction in magnetic contribution to the interatomic repulsive forces. $\partial C'/\partial P$ increases slightly with temperature while $\partial C_{44}/\partial P$ decreases with temperature. Since there is no contribution from interatomic repulsive forces to both shears C' and C_{44}, the pressure dependence dC'/dP and $\partial C_{44}/\partial P$ are smaller than $\partial C_{11}/\partial P$ at all temperatures.

With the introduction of carbon into the Mn-Ni alloy, a change in the behaviour of the interatomic repulsive forces has been observed. Through our investigation on sample C2, $\partial C_{11}/\partial P$ initially increased with temperature and then decreased to a minimum at approximately 140°C. The existence of carbon seems to weaken the interatomic repulsive forces: this can be seen as a decrease in $\partial C_{11}/\partial P$ at 140° C. Above 140°C there is a similar trend to that observed in the $Mn_{73}Ni_{27}$ alloy over the whole temperature range (ie $\partial C'/\partial P$ and $\partial C_{44}/\partial P$ show a similar pattern as for those in the $Mn_{73}Ni_{27}$; $\partial C'/\partial P$ increases with temperature while $\partial C_{44}/\partial P$ decreases with temperature in the antiferromagnetic state).

The measurements made on the hydrostatic pressure derivatives of the SOEC on both sides of the Neel point shed further light on the elastic behaviour of the Mn-Ni binary alloy in both the antiferromagnetic and the paramagnetic phases. As the temperature is increased towards T_N, $\partial C_{11}/\partial P$ of $Mn_{73}Ni_{27}$ increases rapidly in a linear fashion. Since the magnetic contribution to the elasticity decreases with temperature, increases in $\partial C_{11}/\partial P$ result from the reduction in the magnetic contribution. The maximum values of $\partial C_{11}/\partial P$ and hence the mode Grüneisen parameter are observed near the transition temperature T_N. The hydrostatic pressure dependence gives an indication of the shift of the phonon dispersion curve at long wavelengths for the sample under pressure. In normal behaviour the phonon states increase in energy as

a result of increasing the frequency of the phonon modes and consequently $\partial w/\partial k$ will then increase. This behaviour has been observed in the $Mn_{73}Ni_{27}$ single crystal. The most noteable behaviour observed in $\partial C_{11}/\partial p$ with temperature is its rapid reduction at the transition temperature. Although the magnetic effect is diminishing as T_N is approached, its effect on the elastic constant is still significant. Once the paramagnetic state is reached C_{11} is no longer influenced by the magnetic interaction with the elastic constant, thus $\partial C_{11}/\partial P$ decreases and the value of mode Grüneisen parameter $\gamma(p,N)$ of the C_{11} is smaller. This implies that phonon states reduce in energy as the material is transformed from a magnetic to a non-magnetic state. In this new phase $\partial w/\partial k$ then decreases with increasing temperature.

In conclusion it can be seen that the interatomic repulsive forces of a binary alloy of Mn-Ni can be altered in the following ways;

i) By varying the temperature of the sample which usually decreases these forces with increasing temperature,

ii) By the application of pressure (in this case hydrostatic pressure) to the sample. For $Mn_{73}Ni_{27}$ the interatomic repulsive forces have been found to increase linearly with temperature in the antiferromagnetic state, and decrease linearly in the paramagnetic state, and

iii) By the introduction of carbon to the binary

alloy which for $Mn_{85}Ni_9C_6$, the interatomic repulsive forces are reduced at 140°C.

Publications

In order to develop the experimental methods and apparatus described in this work, experiments were performed on a variety of solid compounds and alloy. The measurements of the temperature dependences of the SOEC and their hydrostatic pressure derivatives of some crystalline solids used led to the following publications:

"Hydrostatic Pressure Dependences of Elastic Constants and Vibrational Anharmonicity of Uranium Nitride". Salleh,M.D., Macdonald,J.E. and Saunders,G.A. (1986) J. Mat Sc. 21, pp 2577-2580

"Elastic Behaviour and Vibrational Anharmonicity of the Cluster Compound $(Ag_6Sn_4P_{12})Ge_6$".
Comins,J.D., Heremans,C., Salleh,M.D., Saunders,G.A. and Honle,W. 1986. J. Mat. Sc. Lett. 5 pp 1195-1197

"Interatomic Repulsive Interaction and Vibrational Anharmonicity of $Eu_{0.8}Ba_{0.2}S$".
Salleh,M.D., Saunders,G.A. and Sullivan,R.A.L. 1987. Phil. Mag. Lett. 55, 2, pp 81-86

APPENDIX A: The Program "TRANS-CORR"

From the input of mode type, sample density and thickness, echo overlap frequency and carrier frequency, the program computes the acoustic impedance of the sample, the reflection coefficient of the sample transducer boundary, the estimated echo delay caused by multiple internal reflections within the transducer and corrects the observed echo transit time accordingly. The transducer is assumed to be of quartz.

The computation is made on the basis of the results of calculations made by Kittinger (1977) who gave the estimated echo delay as a function of the reflection coefficient, see Fig.4.15. Here the estimated echo delay (t_c) is calculated from the equation

$$(t_c) = (0.1602 \exp(1.831(r_f + 1)))/f_c$$

where (r_f)= reflection coefficient coefficient of the sample-transducer boundrary and (f_c)= carrier frequency (usually equal to the fundamental frequency of the transducer). This equation is found to represent well the results of Kittinger for $-0.6<r_f>+0.6$

The Program

Language - Microsoft Basic.

Machine - CBM PET.

Variable - q$...mode type; "l"=longitudinal, "s"=shear.
ro...sample density
l...sample thickness in cm.

f...echo overlap frequency in Khz

fc...carrier frequency in Mhz

v...uncorrected sound velocity in ms^{-1}.

z...acoustic impedence of transducer in units of $10^6 kgm^{-2}s^{-1}$.

ai...acoustic impedence of sample in units of $10^6 kgm^{-2}s_{-1}$.

rf...reflection coefficient.

tc...estimated echo delay.

vc...corrected sound velocity in ms^{-1}.

er...correction as a percentage of uncorrected velocity.

```
10 rem program to calculate corrected velocities
15 rem (c) m.d.m salleh (1985) bath university
20 print"Program to calculate wave velocities"
30 print"corrected for transducer delays."
40 print"MODE TYPE?:'l' for longitudinal"
50 print"'s' for shear."
60 get q$:if q$="" goto 60
70 print"TRANSDUCER CORRECTION."
80 if q$="l" then print"MODE TYPE:-longitudinal.":goto 100
90 print"MODE TYPE:-shear."
100 input"Density in Kg/m3";ro
110 input"Sample thickness in cm.";l
120 input"Overlap frequency in KHz";f
130 input"Carrier frequency in MHz.";fc
140 l=l*1e-2:f=f*1e3:fc=fc*1e6
150 v=2*l*f:ai=ro*v*1e-6
160 if q$="s" then z=10.3:goto 180
170 z=15.2
180 rf=(z-ai)/(z+ai):tc=(.1602*exp(1.831*(rf+1)))/fc
185 if rf>=-.6 and rf<=.6 then goto 190
186 print"WARNING: Reflection Coeff. out of range.
190 vc=2*l/((l/f)-tc):er=vc*100/v-100
200 print"Uncorrected velocity=";v;"m/s"
210 print"Acoustic impedence=";ai
220 print"Reflection coefficient=";rf
230 print"Estimated echo delay=";tc;"sec"
240 print"Corrected velocity=";vc;"m/s"
250 print"ie. a correction of";er;"%"
260 get q$:ifq$="" goto 260
265 if q$=" " goto 20
270 print"":poke59468,12:end
```

REFERENCES

Acet,M., Stamin,W., Zahres,H. Wassermann, E.F. 1987, Journal of Magnetism and Magnetic Materials, 68, 23

Alers,G.A., Neighbours,J.R., Sato,H. 1960. J. Phys. Chem. Solids, 13, 40

Altman,H.E. and Margolin,H. 1966. J.Acoust. Soc. Am., 59, 545

Anderson,P.W. 1960, In Fizika dielektrikov (ed. G.I. Skanavi), p.290, Moscow Akad. Nauk, USSR.

Anderson,O.L. 1963. J. Phys. Chem. Sol. 24, 909

Anderson,O.L. 1966. J. Phys. Chem. Sol. 27 , 547

Anderson,P.W. and Blount, E.I. 1965. Phys. Rev., 14, 217

Asano,S. and Yamashita,Y. 1971 J.Phys. Soc. Japan 31, 1000-1015

Ashcroft,N.W. and Mermin, N.D. 1976. Solid State Physics, Holt-Saunders International Editions, Philadelphia.

Azaroff,L. 1971. Elements of X-Ray Diffraction, McGraw Hill.

Bacon,G.E., Dunmur,I.W., Smith,J.H. and Street,R.: Proc. Roy. 1957, A241, 223

Barron,T.H.K., Birch,J.A., White,G.K. 1977. J.Phy. C, Solid State Physics: vol. 10, 1617

Bateman,P.C.,1966. J. Acoust. Soc. Am., 41, 1011

Brassington,M.P., 1982. PhD Thesis, University of Bath. U.K.

Brassington,M.P. and Saunders,G.A. 1982.Phys. Rev. Lett., 48, 159

Bridgman,P.W. 1911. Proc. Amer. Aced. Arts Sci., 47, 321

Bridgman,P.V. 1940a. Proc. of The Amer. Acad. of Arts Soc, 74, 21

Brooks,M.S.S. and Glotzel,D. 1980. Physica 102B, 51

Brooks,M.S.S. 1984. J.Phys. F: Mat. Phys. 14, 639

Brown,J.G. 1966, X-Ray And Their Application, London Iliffe Book Ltd.

Brugger,K. 1964. Phys. Rev., 133, A1611

Brugger,K. 1965. Phys. Rev., 17, 6A, A1826

Brugger,K. 1965a. J.Appl. Phys. 36, 759

Brugger,K. and Fritz,T.C. 1967. Phys. Rev., 157, 524

Cade,N.A. and Young,W. 1980. J. Phys.F: Met. Phys. 10, 2035-40

Cantrell,J.H. 1980. Phys. Rev. B, 21, 4191

Cantrell,J.H., Breazeale,M.A., Nakamura,A. 1980. J. Acoust. Soc. Am. 67(5), 1477

Carlin,B. 1960. Ultrasonic, Mc Graw-Hill.

Chan, R.K., Chew, H.A. 1969. Canadian Journal of Chemistry, 47, 2249

Chung,D.Y., Gunton,D.J. and Saunders,G.A. 1976. Phys. Rev., 13, 3239

Cochran,W. 1960. Adv. Phy. 9, 387

Cousins,C.S.G. 1971. J. Phys. C, 4. 1117

Cowley,R.A. 1976. Phys. Rev. 13, 4877

Cracknell,M.F., Evan,R.G. 1970. Solid State Comm., 8, 359

Crangle,C. 1977. The Magnetic Properties of Solids, Edward Arnold Limited, London

Crangle,J. and Hallam,G.C. 1963. Proc. Roy. Soc.

(London), A272, 119

Daniels,W.B. and Smith,C.S. 1958. Phys. Rev. 111, 713.

Doring,W. 1938. Ann. Phy. 32, 465

du Plesssis,P. de V., Holden,T.M., Buyers, W.J.T., Jackman,J.A., Murray,A.F., Voon Doorn,C.F. 1985. J.Phys. C: Solid State Physics, 18, 2809

Endoh,H., Ishikawa,Y. 1971. J.Phys. Soc. Japan, 30, 1614

Endoh,Y., Noda,Y., Ishikwa,Y. 1977. Solid State Comms. 23, 951

Erdos,P. and Robinson,J.M. 1983. The Physics of Actinide Compounds, Plenum Press

Eros,S. and Retiz,J.R. 1958. J. Appl. Phys., 29, 683

Folk,R., Iro,H., Schwabl,F. 1976. Z.Phys., B25, 69

Fournier,J.M., Beille,J. and de Novion,C.H. 1979. J.Phys. (Paris) 40, C4-32

Fritz,I.J.,1974. J.Phys. Chem.Sol 35, 817

Fuller,E.R. 1973. The Study Of Covalent Bonding By Means Of Elastic Constants, PhD Thesis, Univ. of Illinois at Urban-Champaign, U.S.A.

Gay,P. 1972. The Crystalline state, Oliver and Boyd Press, Edinburgh, U.K

Greenough,R.D., Plamer,S.B. 1973. Applied Physics D, 6

Gribanov,I.F., Melnik,V.A, 1988, Journal of Magn. and Magn. Mat., 71, 219

Guillaume,C.E. 1897. Compt. Rend. Acad. Sci 125, 235

Hart,S. 1968. Brit. J. Appl. Phys. (J. Phys. D), Ser 2, 1, 1277

Hausch,G. 1973. Phys. Stat. Soln. (a) 15, 501

Hausch,G. 1974. J.Phys. Soc. Japan, 37 3, 819

Hausch,G. 1974. J.Phys. Soc. Japan, 37, 3, 824

Hausch,G. 1977, J.Phys. F: Metal Phys. 7, No.5

Hausch,G. and Torok,E. 1977. J. Mag. Magn. Mat. 6, 269

Hennion,B., Hutching,M.T., Lowde,R.D., Stringfellow,M.W. and Tocchetti D., 1976 Proc. Conf. Neutron Scatt. Ed. R.M. Moon p. 825 U.S. Department of Commerce Publication CONF-760601 P2.

Hicks,T.J., Pepper,A.R., Smith,J.H. 1968, J.Phy. C1, 1683

Hiki,Y. and Granato,A.V. 1966. Phys. Rev. 144, 441

Honda,N., Tanji,Y. and Nakagawa,Y. 1975. J. Phys. Soc. Japan, 38, 589

Honda,N., Tanji,Y., Nakagawa,Y. 1976 J.Phys. Soc. Japan, 41, 6, 1931

Huntington,H.B. 1947. Phy. Rev. 72, 321

Kamimura,T., Ido,H., Sato,M., Sutak,T.
1986, Journal of Magn. and Magn. Mat. 54-57, 939

Kennedy,S.J., Hicks,T.J. 1987. J.Phys. F: Met. Phys. 17, 1599

Kittinger,E. 1977. Ultrasonic, January, 33

Kittel,C 1986, Solid State Physics, Sixth Edition, John Wiley & Son.

Koh, A.K. 1978, MSc Thesis University of Bath, U.K.

Krasilnikov,O.M. 1977, Fiz. Tverd, Tela (Liningrad), 19, 1313

Ledbetter,H.M. 1983, Physica 119B, 115-118.

Lemmer,R.H., Viljoen,J. de P. 1977. J. Magn. and Magn. Mat. 5, 161

Liakos,J.K. 1981. MSc Thesis, University of Bath, U.K

Lowde,R.D., Harley,R.T., Saunders,G.A., Sato,M., Scherm,R. and Underhill,C. 1981. Proc. Roy. Soc. A374, 87

Mabbs,F.E., Machin,D.J. 1973. Magnetism and Transition Metal Complexs, Chapman and Hall, London

Marples,J.A.C., Simpson,C.F., Wedgwood,F.A. and Kuzneitz,M. 1975. J. Phys. C, Solid State Phys. 8, 708

Mase,G.E. 1970. Theory and Problem in Coninuum Mechanics, Mc Graw-Hill

Masumoto,H., Sawaya,S. and Kikuchi,M. 1972. Trans. Jap. Inst. Met. 13, 315

Meneghetti,D., Sidhu,S.S. 1957. Phys. Rev. 105, 1

Miller,A.J., Saunders,G.A., Yogurtchu,Y.K. 1981. Phil. Mag. A, 43, 6, 1447

Momin,A.C. and Karkhanavala,M.D. 1979. High Temp. Sci. 11, 179

Moruzzi,V.L. 1986, Phys. Rev. Lett. 57, 17, 2211

Murnaghan,F.D. 1951. Finite Deformation of an Elastic Solid. Wiley.

Murnaghan,F.D. 1944 Proc. Nat. Acad. Soc. USA, 30, 244

Muromura,T. and Tagawa,H. 1979. J.Nucl. Mater. 79, 264

Nagamiya,T., Yosida,K., Kubo,R. 1955. Phil. Mag. 4, 13, B2

Nye,J.F. 1957. Physical Properties of Crystal, Oxford Science Publication

Oguchi,T., Nishimori,H., Taguchi,Y. 1986. J. Magn. and Magn. Mat. 54-57 1353

Oner,Y., Elkhatouri,D., Senoussi,S. 1986. J. Magn. and Magn. Mat. 54, 159

Oomi,G., Mori,N. 1983. Physica 119B, 14

Overton,W.C., 1962. J. Chem. Phys. 37, 2975

Pace,N.G. 1970, PhD Thesis, University of Durham

Pace,N.G., Saunders,G.A. 1972. Proc. Roy. Soc., A326, 521

Palmer,S.B. 1975. J. Phys. F: Met. Phys. 5, 2370-2378

Papadakis,E.P. 1967. J. Acoust. Soc. Am.42, 1045

Patrick,L. 1953. Physical Review 93, 384Pollard,H.H. 1977. Sound Waves in Solids, Pion Ltd. London

Ramakarishnan,J., Kennedy,G.C. 1979. J.Phys. Chem. Sol. 41,301

Raub,E., Mahler,W : 1954. Z. Metalkunde, 45, 430

Renaud,G.P., Steinemann,S.G. 1984, J. Magn. and Magn. Mat. 45, 126

Robie,R.A., Edwards,J.L. 1966. J. App.Phys., 37, 7, 2659

Sato,M., Lowde,R.D., Saunders,G.A., Hargreave,M.M. 1981. Proc. Roy. Soc. A374, 115

Salama,K. and Alers,G.A. 1968. Paper Presented to Ultrasonic Symp. New York City. Sept.25-27.

Salleh,M.D., Mac Donald,J.E, Saunders,G.A. 1986. J. Mat. Sc. 21, 257

Salleh,M.D., Saunders, G.A., Sullivan,R.A.L. 1987. Phil. Mag. Lett., 55, 2, 81

Samara,G.A., Giardini,A.A. 1964. Rev. Sci. Inst. 35, 8, 989

Sawaoka,A., Soma,T., Saito,S., Endoh,Y. 1971. Phys. Stat. Soln. (b) 47, K99

Shanker,J., Varshney,R.K. 1982. Phys. Stat. Sol. (b) 114, K71

Steinemann,S.G., 1979. J. Magn. and Magn. Mat. 12, 191

Swenson,C.A. 1985. Phy. Rev. B, 31, 2, 1150

Tajima,K., Endoh,Y., Ishikawa,Y., Stirling,W.G. 1976. Phys. Rev. Lett. 37, 519

Tanji,Y., Nakagawa,Y., Steinemann,S.G. 1983. Physica 119B, 109

Tanner,B.K. 1979. Contemp. Phys. 20, 2, 187

Taylor,R.G.F., Pointon,A.J. 1969. Contemp. Phys., 10, 2, 159

Thakur,K.P. 1980. J. Phys. Chem. Solids 41, 465

Thurston,R.N. 1965. Proc. IEEE, 53, 132

Thurston,R.N., Brugger,K. 1964. Phy. Rev. 133, 6A, A1604

Thurston,R.N. 1965. Proc. IEEE, 53, 1320

Tino,Y. 1986. J. Mang. and Mang. Mat. 54, 1067

Truell,R., Elbaum,C., Chick, B.B., 1969. Ultrasonic Method in Solid State Physics, Acad. Press New York

Tsiuplakis,V.K.E and Kneller,E 1969. Z. Metallkde 60, 433

Tu Hailing, 1983. PhD Thesis, University of Bath, U.K

Tu Hailing, Saunders,G.A. and Bach,H. 1984. Phy. Rev. B29, 1848

Uchishiba,H. 1971. J. Phy. Soc. Japan. 31, 436

van Doorn,C.F., du Plessis P. de U. 1977. J. Magn. and Magn. Mat. 5, 164

van Vleck, 1941. J. Chem. Phys. 9, 85

Wachtmann,J.B., Tefft,W.E., Lam,D.G., Apstein, Jr and

C.S. 1961. Phys. Rev. 122, 1754

Wallace,D.C. 1972. Thermodynamic of Crystals, Wiley

Wassermann,E.E., Tieftemperaturphysik, Universitat Duisburg, 4100, Duisburg 1, FRG

Walther,K. 1967. Sol. Stat. Comm. 5,399

Weber,W. 1974. Phys. Rev. Lett. 33, 371

Weinmann,C. and Steinemann,S. 1974. Phys. Lett 47A.

Weinstein,B.A. 1977. Sol. Stat. Comm. 24, 595

Weston,W.F. and Granato,A.V. 1975. Phys. Rev.B, 12, 5355

White,G.K. 1965. Proc. Phys. Soc. 86, 159

Wohlfarth,E.P. 1972. Phys. Stat. Soln. (a) 10, K 39

Wohlfarth,E.P. 1976. J. Phys. F6, 1, 59

Yamaoka,T. 1974. J. Phys. Soc. Japan. 36, 445

Yogurtcu,Y.K. 1980. PhD Thesis, University of Bath, U.K

Yogurtcu,Y.K., Saunders,G.A. and Riedi,P.C. 1985. Phil. Mag. 52, 6, 833-846

Yoshizawa,M., Luthi,B., Goto,T., Suzuki,T., Renker,B., de Visser A., Frings,P., Franse,J.J.M. 1985. J. Magn. and Magn. mat. 52, 413

Zaky,A.A., Hawley,R. 1970. Dielectric Solid, Routledge and Kegan Paul Ed. London

Zhdanov,G.S., Crystal Physics, Oliver and Boyd Ed.

Zimmerman,J.E., Arrot,A., Sato,H. and Shinozaki,S. 1964. J. App. Phys, 35, 942